Charles University in Prague
Faculty of Science
Institute of Geology and Paleontology
Program Geology

Filip Tomek

MAGNETIC FABRIC, MAGMA FLOW AND TECTONIC DEFORMATION IN VOLCANO–PLUTONIC SYSTEMS

Ph.D. thesis

Principal advisor: Jiří Žák

Prague, 2015

STATEMENT

Herewith, I certify that I have worked on this Ph.D. thesis by myself and that I have properly cited all the relevant literature and other sources of information. I also certify that the thesis, or any substantial part of the thesis, has not been submitted elsewhere to get any other comparable degree.

In Prague, June 11th 2015

Signature

ABSTRACT

This Ph.D. thesis aims to investigate dynamics of emplacement and tectonic history of selected volcano–plutonic complexes in a continental magmatic arc and back arc setting. The thesis presents new data sets from five field areas, presented in separate chapters, which could be viewed as representing a vertical sections through upper part of an intermediate to felsic magmatic system. From top to bottom in this 'imaginary' vertical system, the examined units are: (1) andesitic lava domes and (2) sub-volcanic magma chambers (<3 km deep) of the Miocene Štiavnica volcano–plutonic complex, Western Carpathians (Slovakia), (3) Shellenbarger pluton (<3 km depth) within the mid-Cretaceous Minarets caldera, Sierra Nevada batholith in California (USA), and ~7–10 km deep granitoids of (4) Lower-Cretaceous Wallowa batholith, Blue Mountains province in Oregon (USA) and (5) Late Devonian Staré Sedlo complex, central Bohemian Massif (Czech Republic). The research incorporates extensive field and structural data, supported by analysis of igneous textures and anisotropy of magnetic susceptibility (AMS). The latter is further accompanied by detailed examination of magnetic mineralogy using thermomagnetic measurements and optical and back scattered diffraction microscopy. In addition, the third chapter contains U–Th–Pb radiometric dating obtained by laser ablation–inductively coupled plasma–mass spectrometry (LA–ICP–MS).

The key results of each of these case studies are as follows. (1) Different fabric patterns of the Štiavnica lava domes and their spatial and temporal association with collapse caldera suggest that the dome growth was controlled by caldera floor subsidence. It is inferred that each dome reflects snapshots of a continuous succession of various modes of caldera collapse from piston through trap-door to piecemeal. (2) Magnetic fabric study of the Štiavnica sub-volcanic plutons revealed contrasting mechanisms of their construction. A diorite pluton represents a steep sided-stock whereas the granodiorite was emplaced in two stages. First, a thin sill intruded along a subhorizontal basement/cover detachment, followed by piecemeal subsidence of the fractured pluton floor due to magma overpressure. (3) The Minarets caldera developed by two Plinian eruptions marked by voluminous deposits of ash-flow tuffs and caldera collapse represented by collapse mega-breccia. The whole sequence was then deformed along a ductile transpressive shear zone and intruded by resurgent Shellenbarger granite pluton within the caldera interior. Magmatic fabrics in the pluton record regional dextral transpression interpreted in terms of oblique convergence of lithospheric plates. (4) Multiple magmatic fabrics in three granodioritic to tonalitic plutons of the Wallowa batholith are interpreted as emplaced syn-tectonically and reflecting progressive deformation during oceanic terrane/continent collision and oroclinal bending in the Blue Mountains Province. (5) Coupled host-rock and magmatic to solid state fabrics of the Staré Sedlo granitoids suggest transtensional deformation which operated prior to, during, and after its emplacement. This syn-convergent transtension is an enigmatic deformation event that occurred during onset of the Variscan Orogeny in the central Bohemian Massif.

In summary, this Ph.D. thesis shows that preexisting environment and active faulting of volcano–plutonic systems may largely control emplacement of volcanic and plutonic rocks as exemplified by the dynamics of growth and construction of lava domes and subvolcanic magma chambers. Furthermore, as opposed to theoretical models, it has been demonstrated that even very shallow-level small-scale intrusions are able to record subtle tectonic strains still in magmatic state. Although the fabrics in plutons preserve only one short snapshot of the inferred instantaneous strain, detailed analysis of syntectonic plutons characterized by hypersolidus fabrics together with precise radiometric dating could unravel complex deformation histories at regional scale over a long period of time. Finally, it has been proposed that pluton fabrics may be used to decipher kinematics of lithospheric plate convergence or divergence and changes in their past relative motions.

CONTENT

ACKNOWLEDGMENT

I am deeply indebted to my principal advisor Jiří Žák for introducing me into the world of science, for his mentorship and guidance, but especially for his patience with me throughout the last four years. Dozens of thoughtful inspirations and advices by František V. Holub and Martin Chadima significantly improved quality of this dissertation thesis. Following colleagues are highly appreciated for their stimulating insights and discussions: Kryštof Verner, Jiří Sláma, Scott Paterson, Vali Memeti, Marta Chlupáčová, František Hrouda, Václav Kachlík, Jakub Trubač, Vojtěch Janoušek, and Vladislav Babuška. Kenneth Johnson and Joshua Schwartz are thanked for their contributions on the third chapter. Crew of the Institute of Geology and Paleontology, the Institute of Petrology and Structural Geology, and especially my office mate Jaroslava Hajná are thanked for friendly atmosphere during my postgraduate study. I would like to acknowledge secretaries Helena Součková, Eliška Černá, and Rudolf Trnka for running all the complicated bureaucratic paperwork and technical assistance. I also thank to the Geological Institute of the Czech Academy of Sciences, for warm welcome and support in the last two years.

This thesis was supported by the Charles University projects PRVOUK P44 and SVV261203. I further appreciate funding from the Grant Agency of the Czech Republic through grant No. P210/12/1385 (to Jiří Žák). Partial support was also provided by the Academy of Sciences of the Czech Republic Research Plan RVO67985831.

I really enjoyed beer–liqueur parties and fieldtrips with faculty mates, namely Václav Špillar, Jakub Vodička, Jan Flašar, Vít Peřestý, Jaroslav Říhošek, Kuba Kryl, Bára Hanková, Ondra Švagera, and all the rest I forgot to mention. I will always remember talks with old buddies from high school and football (Sparta), in particular their comments in sense of: ”Geology, what? Why? How? Are you crazy?”.

I would like to express my gratitude to my family: mom Jana, dad Jirka, doggie Monty and all the rest for their constant support, even during the field campaigns on the other side of the Atlantic Ocean. Most of all, I thank my wonderful girlfriend Kačka for the beautiful moments that she spent with me over last more than three years and also for her help with corrections of this thesis.

PREFACE

I started to work on my dissertation thesis in October 2011 at the Institute of Geology and Paleontology, Charles University in Prague and finished it the beginning of June 2015. The principal goal of the thesis is to examine the evolution of selected volcano–plutonic complexes with emphasis on interaction between emplacement mechanisms with regional tectonic deformation. The thesis contains new data collected during 2011–2014 in four different field areas: (1) Štiavnica volcano–plutonic complex, which belongs to back-arc Quaternary volcanic field in the Western Carpathians; (2) Sierra Nevada batholith, California; (3) Blue Mountains Province, northeastern Oregon, both are part of the North American Cordillera; and (4) Central Bohemian Plutonic Complex, a Variscan magmatic arc in the central Bohemian Massif.

The research in all study areas was based on a combination of multiple methods including field and structural mapping, which served as a basis for targeted anisotropy of magnetic susceptibility (AMS) sampling. The AMS was measured in the Laboratory of Rock Magnetism at the Institute of Geology and Paleontology and was complemented with detailed analysis of magnetic mineralogy. In addition, a large number of thin-sections were examined using optical and back scattered diffraction microscopy in order to precisely characterize volcanic and plutonic textures, the degree of their tectonic deformation, and mineral assemblages. Last but not least, the chapter three contains U–Th–Pb radiometric dating using laser ablation–inductively coupled plasma–mass spectrometry (LA–ICP–MS) obtained at the University of Bergen.

The thesis is divided into three sections. Introduction outlines principal goals of the thesis and motivation for the research and briefly summarizes current state of knowledge. The main body of the thesis then includes five chapters, three of which are based on papers already published in international peer reviewed journals (enclosed in the Appendix), and the two other chapters are papers currently under review. The last section (Summary) highlights the most important results of the thesis.

INTRODUCTION

Magmatic systems in continental magmatic arcs

Intermediate to felsic volcanoes and underlying plutons (former magma chambers) in continental magmatic arcs are in fact end products of vertically extensive (from the lithospheric mantle to the uppermost crust) magmatic systems (Fig. 1). The arcs grow as a result of protracted subduction of oceanic plates beneath the continental lithosphere (e.g., DeCelles et al., 2015, 2009; Ducea and Barton, 2007; Paterson and Ducea, 2015; Tatsumi and Kogiso, 2003; Tatsumi, 2005). Herein, magma is has intermediate compositions and is typically a product of mixing of mantle- and crustally-derived melts. The former is commonly generated from fractional crystallization of mantle-derived basalts (e.g., Annen et al., 2006) whereas the latter by partial melting of middle to lower crustal metasediments and amphibolites (e.g., Brown, 2013, 2007, 1994; Milord et al., 2001; Petford et al., 2000). The segregated buoyant magma then ascends through the crust (e.g., Cartwright and Hansen, 2006; Clemens and Mawer, 1992; Petford et al., 1993; Vigneresse and Clemens, 2000), where it may stall to form large reservoirs (e.g., Collins and Sawyer, 1996; Crawford et al., 1999; Miller and Paterson, 2001) before final high-level emplacement and/or eventually eruption (e.g., Acocella and Funiciello, 2010; Bachmann and Bergantz, 2008, 2004; Bachmann et al., 2007; Lipman, 1984; Lipman and Bachmann, 2015). In addition, the active continental margins are sites of high tectonic stress accumulation resulting from plate convergence. The tectonic stresses thus significantly influence the whole dynamics of magmatic arcs. Consequently, it is inferred that the tectonic stresses in arcs also facilitate magma ascent and may also control pluton emplacement and volcanic processes at the Earth's surface (e.g., Brown and Solar, 1998; D'Lemos et al., 1992; Rosenberg, 2004; Vigneresse, 1995a, 1995b).

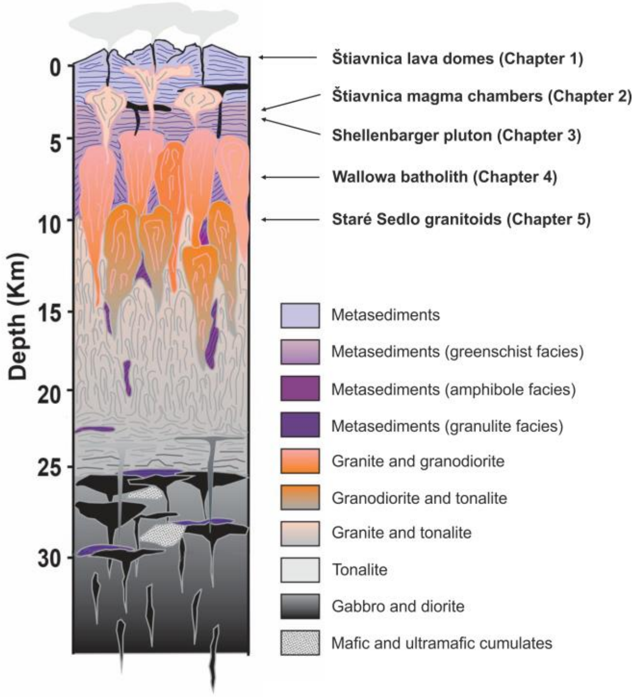

Fig. 1 Idealized cross-section through a continental magmatic arc with highlighted structural levels of examined field areas (Modified after Tibaldi et al., 2013).

Internal fabrics in volcanic and plutonic rocks

It has been well established that the structural inventory volcanic and plutonic rocks provides 'archives' of mechanical processes during lava and magma flow, emplacement, and of strain regimes recording tectonic deformation at the lithospheric scale (e.g., Pitcher and Berger, 1972; Cañón-Tapia et al., 1996, 1997; Paterson et al., 1998; Petford et al., 2000; Vernon, 2000; Petford, 2003; Benn et al., 2001; Benn, 2004; Féménias et al., 2004; Vernon and Paterson, 2006; Cao et al., 2015). These processes are generally interpreted from three-dimensional shapes of volcanic and plutonic bodies, characteristics of intrusive contacts, and internal structures such as magmatic fabrics.

Magmatic fabrics represented by foliation and lineation are defined as planar and linear shape-preferred alignment of mineral grains, aggregates, and/or microgranular enclaves, respectively (e.g., Paterson et al., 1998, 1989; Vernon et al., 2004; Vernon, 2000). Macroscopic fabrics are measured directly in the field and plotted to maps and can be further analyzed in thin-sections or using some other quantitative methods such as electron back scattered diffraction (EBSD) or computer-integrated polarization (CIP). As opposed to coarser-grained foliated plutons, volcanic rocks are commonly fine-grained and even aphyric with no apparent magmatic fabric. To obtain the internal fabrics in quasi-isotropic volcanic and also plutonic rock, the anisotropy of magnetic susceptibility (AMS) is often used as a sensitive tool capable of detecting even the weakest, macroscopically invisible fabrics.

Anisotropy of magnetic susceptibility (AMS)

The AMS technique (e.g., Hrouda, 1982; Tarling and Hrouda, 1993; Borradaile and Jackson, 2004, 2010) is based on natural capability of minerals to acquire magnetization in magnetic field, referred to as magnetic susceptibility. The magnetic susceptibility k is a second-rank tensor, described by matrix $k = M/h$, where M is vector of material magnetization and h is vector of the applied magnetic field (SI units are used throughout the thesis). The AMS is a sum of all mineral grains in a rock, each having different magnetic susceptibility in different directions.

Three groups of minerals are distinguished based on their magnetic properties. (1) Diamagnetic (e.g., quartz, calcite), which have negative magnetization against the direction of magnetic field and thus their susceptibility is negative on the order of -10^{-5}. (2) Paramagnetic minerals (e.g., biotite, amphibole, olivine) are characterized by weak positive magnetization parallel to the direction of magnetic field ranging on the orders of 10^{-2} – 10^{-4}. (3) Ferromagnetic minerals (magnetite, maghemite, and other FeTi oxides) have complex dependence between magnetic field and induced magnetization described as a hysterics loop. These minerals indicate high susceptibility on the orders of 10^{-3} to 10^{-2}. Contribution to the bulk rock susceptibility of each of these three mineral populations may vary significantly (Fig. 2): for instance 0.01 % of magnetite in rock sample corresponds to 100 % concentration of biotite (Hrouda and Kahan, 1991).

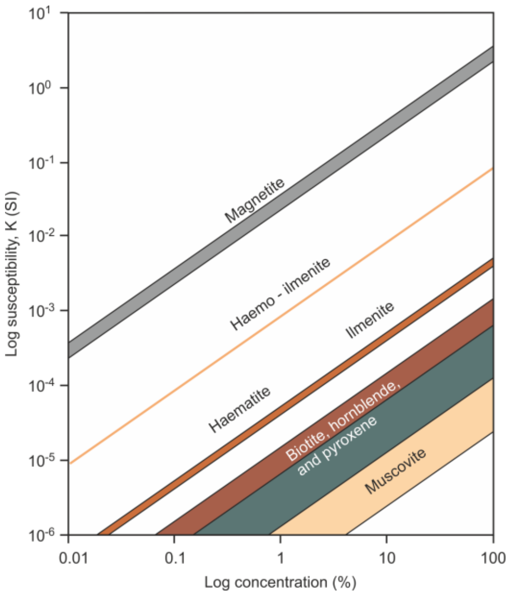

Fig. 2 Diagram of concentration of minerals with respect to contrubution to bulk rock susceptibility (after Hrouda and Kahan, 1991).

Magnetic anisotropy of minerals further differs due to their crystallographic structure. (1) Cubic minerals are characterized by shape anisotropy, where their longest, intermediate, and shortest axis correspond to maximum, intermediate, and minimum susceptibilities (k_1, k_2, and k_3, respectively; e.g., Grégoire et al., 1998). (2) Other minerals posses crystallographic anisotropy reflecting their crystal structure (e.g., Richter et al., 1993). In order to determine which phase dominates the magnetic susceptibility of a rock sample, variations of susceptibility with temperature are measured from temperature of liquid nitrogen up to 700 °C and back (thermomagnetic curves). For instance, typical curves of 'normal' magnetite have a box-like shape with Verwey transition (apparent at ca. −180 °C) and Curie temperature (at ca. 560–580 °C), whereas paramagnetic minerals show typical hyperbolic decrease of susceptibility with increasing temperature.

The AMS tensor can be visualized as an ellipsoid with the principal susceptibility axes $k1 \geq k2 \geq k3$ where the maximum susceptibility (k_1) represents magnetic lineation and the minimum susceptibility (k_3) is the normal (pole) to magnetic foliation (Fig. 3). The AMS can be further described by several parameters (Tarling and Hrouda, 1993): (1) the bulk (mean) susceptibility ($k_m = (k_1 + k_2 + k_3)/3$) which reflects the type and volume fraction of magnetic minerals, (2) the degree of anisotropy ($P = k_1/k_3$) which indicates the eccentricity of the AMS ellipsoid and may be thus related to the intensity of the shape-preferred orientation of magnetic minerals (Nagata, 1962), and (3) the shape parameter ($T = 2ln(k_2/k_3)/ln(k_1/k_3) - 1$) which describes symmetry of the AMS ellipsoid. For $-1 \leq T < 0$ the ellipsoid is prolate, for $T = 0$ neutral, and for $1 \geq T > 0$ oblate (Jelínek, 1981).

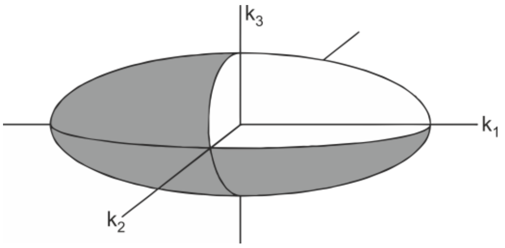

Fig. 3 Ellipsoid of magnetic susceptibility.

What can magmatic fabrics tell us?

Magmatic fabrics are those formed in melt-present hypersolidus state. A foliation is perpendicular to the maximum shortening, indicating z_i-axis of the instantaneous strain ellipsoid, and a lineation reflects the maximum stretching direction, which is parallel to the x_i-axis of the instantaneous strain ellipsoid (e.g., Hutton, 1988; Paterson et al., 1998). In many cases, magmatic fabrics are interpreted as recording last increments of strain during magma solidification, when the near solidus crystal mushes become rigid crystal–melt frameworks wherein the magma cannot move anymore. Hence, fabrics are rather poor recorders of the total strain history experienced by the flowing magma and instead they likely record only a 'frozen-in snapshot' of strain just before immediate solidification. So, what kind of processes are actually archived in igneous rocks?

In volcanic bodies (e.g., lava flow, domes, and pyroclastic deposits), fabrics are commonly associated with local lava flow end emplacement of individual parts of the volcanic edifice (e.g., Palmer et al., 1996; Ort et al., 2003, 2015; Loock et al., 2008; Petronis et al., 2013). Similarly, very shallow, small-scale plutons with fast cooling rates are inferred only to record magma flow during pluton construction as such plutons are not expected to interact with slower tectonic processes due to their rapid cooling. Hence, their construction rates are supposed to be orders of magnitude faster than regional tectonic strains. To the contrary, large-scale batholiths, which are constructed by amalgamation of several magma pulses over longer periods of time, should have comparable rates of emplacement and tectonic deformation (e.g., de Saint Blanquat et al., 2011), and thus in many cases represent excellent markers of tectonic strain.

In addition, a great challenge arises when interpreting magma flow and emplacement from magnetic fabric due to possible complexities of magnetic mineralogy. For instance, the tiny microscopic crystals (susceptibility carriers) can still rotate within the interstitial melt, whereas the surrounding crystal-rich mush is already locked, unable to move. This may cause discrepancies between magmatic and magnetic fabrics, caused by some later most likely subtle change in strain regime. Furthermore, the ferromagnetic minerals can define inverse fabric, be altered, or new magnetite may grow after the emplacement affecting the primary AMS fabric. Last but not least, the heat from magma induces hydrothermal fluid circulation, which in turn can significantly influence the AMS fabric.

Aims and goals of the thesis

Several outstanding and yet unsolved issues thus arise when studying fabric record in arc volcano–plutonic systems, which may indicate anything from local magma flow to regional tectonic deformation. The ambition of this thesis is to discuss and address the following issues:

- Can magmatic fabrics in volcanic rocks reveal mechanisms of flow and growth of various lava formations (e.g. flows, domes, necks, spines, and tuffs). What is the role of preexisting structures, active faulting, or caldera collapses during volcanic activity? Is it possible that these structures influence the emplacement of lavas, and can this be deduced from fabrics in the volcanic edifice?
- What are the mechanisms of construction and associated magma flow paths and strain patterns in shallow magma chambers beneath large volcanoes, and are they comparable to deeper plutons?
- Do the small very shallow intrusions such as sills, dikes, laccoliths, and sub-volcanic plutons really record only emplacement-related strain, or could they also record paleostrain fields still in magmatic state?
- How does magma interact in the upper continental crust with various tectonic regimes such as transtension, transpression, block rotations, and what can we learn from it?
- On the largest scale, is it possible to determine plate motion vectors and associated paleodeformation fields from strain recorded in high-level intrusions?

Field areas

The above issues were addressed on four volcano–plutonic complexes in continental arc and back arc setting. Together, these case studies can be considered as representing a vertical section through a magmatic system from surface lava domes to deeper plutons (Fig. 1). As each chapter of the thesis contains detailed information about local geological setting, here I will only briefly introduce the study areas, the summary of which is also provided in Figure 4.

(1) The first two chapters deal with lava domes and subvolcanic magma chambers of the Štiavnica volcano-plutonic complex of Neogene to Quaternary Carpathian–Pannonian Region, Western Carpathians. This complex is an erosional relic of a Miocene caldera-stratovolcano formed in an extensional back-arc setting inboard of a flysch belt and oceanic domains subducted underneath the outer Carpathian arc (Konečný et al. 1995, 2002; Lexa et al., 1999; Harangi et al. 2007; Chernyshev et al., 2013). The significant vertical relief exposes nearly complete vertical section from volcano basement, through subvolcanic intrusions and ring-fault to overlying volcanic deposits, which provides unique insights into dynamics of magma flow, emplacement, and eruption of large composite volcanoes.

(2) The mid-Cretaceous Minarets caldera discussed in Chapter 3 is a volcano–plutonic complex preserved in the roof of the Cenozoic Sierra Nevada batholith of the North American Cordillera in California (Fiske and Tobisch, 1994). The complex exposes regionally deformed syn- to post-caldera volcanic products and associated <3 km deep resurgent Shellenbarger pluton, allowing a complex study of presumably simultaneous volcanic and tectonic processes.

(3) Chapter 4 examines plutons and their host rock of the Early Cretaceous Wallowa batholith in the Blue Mountains Province, which is also part of the North American Cordillera but in notheastern Oregon (e.g., Johnson et al., 2011). The batholith was emplaced into the Blue Mountains orocline approximately at the time of collision of the Blue Mountains oceanic terranes with the North American craton. The Wallowa batholith is here examined to reveal transpressional deformation, kinematics, and temporal relations of shallow-level plutonism to the terrane/continent collisions and to oroclinal bending.

(4) Research in the Late Devonian Staré Sedlo complex, central Bohemian Massif, is presented in the last chapter. The complex comprises deformed granodiorite to tonalite of supra-subduction calc-alkaline origin in the roof of a large magmatic arc emplaced along a boundary between two lithospheric units in the Bohemian Massif (Košler et al., 1993; Janoušek et al., 2000). The structural analysis of this complex was used a basis for discussion of interplay between emplacement processes and tectonic (transtensional) deformation of deeper-seated granitic magmas.

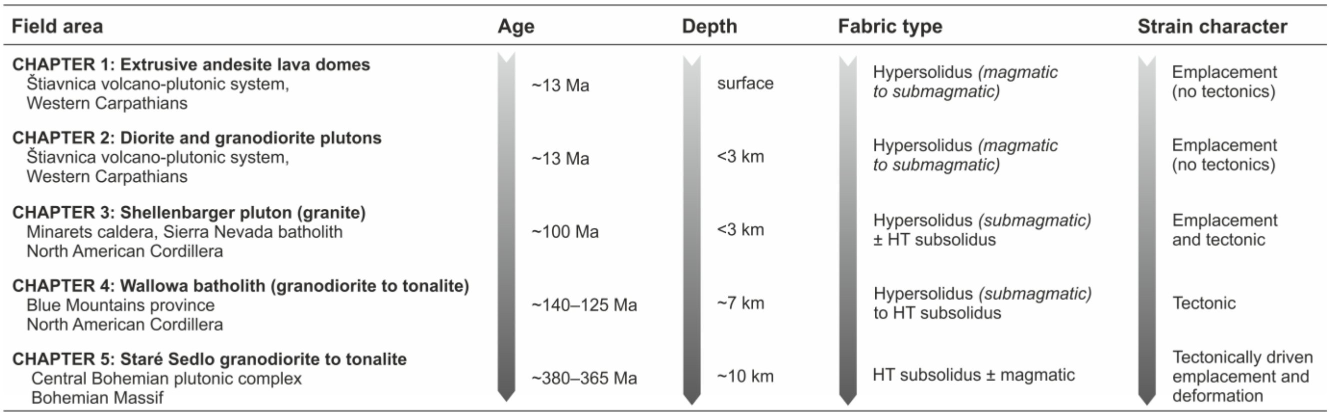

Field area	Age	Depth	Fabric type	Strain character
CHAPTER 1: Extrusive andesite lava domes Štiavnica volcano-plutonic system, Western Carpathians	~13 Ma	surface	Hypersolidus *(magmatic to submagmatic)*	Emplacement (no tectonics)
CHAPTER 2: Diorite and granodiorite plutons Štiavnica volcano-plutonic system, Western Carpathians	~13 Ma	<3 km	Hypersolidus *(magmatic to submagmatic)*	Emplacement (no tectonics)
CHAPTER 3: Shellenbarger pluton (granite) Minarets caldera, Sierra Nevada batholith North American Cordillera	~100 Ma	<3 km	Hypersolidus *(submagmatic)* ± HT subsolidus	Emplacement and tectonic
CHAPTER 4: Wallowa batholith (granodiorite to tonalite) Blue Mountains province North American Cordillera	~140–125 Ma	~7 km	Hypersolidus *(submagmatic)* to HT subsolidus	Tectonic
CHAPTER 5: Staré Sedlo granodiorite to tonalite Central Bohemian plutonic complex Bohemian Massif	~380–365 Ma	~10 km	HT subsolidus ± magmatic	Tectonically driven emplacement and deformation

Fig. 4 Schematic chart to integrate the particular studies in this thesis into a single model of a vertical magmatic system.

REFERENCES

Acocella, V., Funiciello, F., 2010. Kinematic setting and structural control of arc volcanism. Earth Planet. Sci. Lett. 289, 43–53.

Annen, C., Blundy, J.D., Sparks, R.S.J., 2006. The genesis of intermediate and silicic magmas in deep crustal hot zones. J. Petrol. 47, 505–539.

Bachmann, O., Bergantz, G.W., 2004. On the Origin of Crystal-poor Rhyolites: Extracted from Batholithic Crystal Mushes. J. Petrol. 45, 1565–1582.

Bachmann, O., Bergantz, G.W., 2008. The magma reservoirs that feed supereruptions. Elements 4, 17–21.

Bachmann, O., Miller, C.F., de Silva, S.L., 2007. The volcanic–plutonic connection as a stage for understanding crustal magmatism. J. Volcanol. Geotherm. Res. 167, 1–23.

Benn, K., 2004, Late Archaean Kenogamissi complex, Abitibi Subprovince, Ontario, Canada: doming, folding and deformation-assisted melt remobilisation during syntectonic batholith emplacement: Earth and Environmental Science Trans. Roy. Soc. Edinb. Earth. Sci. 95, 297–307.

Benn, K., Paterson, S.R., Lund, S.P., Pignotta, G.S., and Kruse, S., 2001. Magmatic fabrics in batholiths as markers of regional strains and plate kinematics: example of the Cretaceous Mt. Stuart batholith. Phys. Chem. Earth, Part A Solid Earth Geod. 26, 343–354.

Borradaile, G.J, Jackson, M., 2004. Anisotropy of magnetic susceptibility (AMS): magnetic petrofabrics of deformed rocks. Geol. Soc. London, Spec. Publ. 238, pp. 299–360.

Borradaile, G.J., Jackson, M., 2010. Structural geology, petrofabrics and magnetic fabrics (AMS, AARM, AIRM). J. Struct. Geol. 32, 1519–1551.

Brown, M., 1994. The generation, segregation, ascent and emplacement of granite magma: the migmatite-to-crustally-derived granite connection in thickened orogens. Earth-Science Rev. 36, 83–130.

Brown, M., 2007. Crustal melting and melt extraction, ascent and emplacement in orogens: mechanisms and consequences. J. Geol. Soc. 164, 709–730.

Brown, M., 2013. Granite: From genesis to emplacement. Geol. Soc. Am. Bull. 125, 1079–1113.

Brown, M., Solar, G.S., 1998. Granite ascent and emplacement during contractional deformation in convergent orogens. J. Struct. Geol. 9–10, 1365–1393.

Cañón-Tapia, E., Walker, G.P.L., Herrero-Bervera, E., 1996. The internal structure of lava flows-insights measurements I : Near-vent a‘a from AMS. J. Volcanol. Geotherm. Res. 70, 21–36

Cañón-Tapia, E., Walker, G.P.L., Herrero-Bervera, E., 1997. The internal structure of lava flows—insights from AMS measurements II: Hawaiian pahoehoe, toothpaste lava and a‘a. J. Volcanol. Geotherm. Res. 76, 19–46.

Cao, W., Paterson, S., Memeti, V., Mundil, R., Anderson, J.L., Schmidt, K., 2015. Tracking paleodeformation fields in the Mesozoic central Sierra Nevada arc: Implications for intra-arc cyclic deformation and arc tempos. Lithosphere, 1–25.

Cartwright, J., Hansen, D.M., 2006. Magma transport through the crust via interconnected sill complexes. Geology 34, 929–932.

Chernyshev, I.V., Konečný, V., Lexa, J., Kovalenker, V.A., Jeleň, S., Lebedev, V.A., Goltsman, Y.V., 2013. K-Ar and Rb-Sr geochronology and evolution of the Štiavnica Stratovolcano (Central Slovakia). Geol. Carpathica 64, 1–25.

Clemens, J.D., Mawer, C.K., 1992. Granitic magma transport by fracture propagation. Tectonics 204, 339–360.

Collins, W.J., Sawyer, E.W., 1996. Pervasive granitoid magma transfer through the lower-middle crust during non-coaxial compressional deformation. J. Metamorph. Geol. 14, 565–579.

Crawford, M.L., Klepeis, K.A., Gehrels, G., Isachsen, C., 1999. Batholith emplacement at mid-crustal levels and its exhumation within an obliquely convergent margin. Tectonophysics 312, 57–78.

D'Lemos, R.S., Brown, M., Strachan, R. A., 1992. Granite magma generation, ascent and emplacement within a transpressional orogen. J. Geol. Soc. London. 149, 487–490.

DeCelles, P.G., Ducea, M.N., Kapp, P., Zandt, G., 2009. Cyclicity in Cordilleran orogenic systems. Nat. Geosci 2, 251–257.

DeCelles, P.G., Zandt, G., Beck, S.L., Currie, C.A., Ducea, M.N., Kapp, P., Gehrels, G.E., Carrapa, B., Quade, J., Schoenbohm, L.M., 2014, Cyclical orogenic processes in the Cenozoic central Andes: Geol. Soc. Am. Memoirs 212.

de Saint Blanquat, M., Horsman, E., Habert, G., Morgan, S., Vanderhaeghe, O., Law, R., Tikoff, B., 2011. Multiscale magmatic cyclicity, duration of pluton construction, and the paradoxical relationship between tectonism and plutonism in continental arcs. Tectonophysics, 500, 20–33.

Ducea, M.N., Barton, M.D., 2007. Igniting flare-up events in Cordilleran arcs. Geology 35, 1047–1050.

Féménias, O., Diot, H., Berza, T., Gauffriau, A., Demaiffe, D. 2004. Asymmetrical to symmetrical magnetic fabric of dikes: Paleo-flow orientations and Paleo-stresses recorded on feeder-bodies from the Motru Dike Swarm (Romania). J. Struct. Geol. 26, 1401–1418.

Fiske, R., and Tobisch, O., 1994, Middle Cretaceous ash-flow tuff and caldera-collapse deposit in the Minarets caldera, east-central Sierra Nevada, California: Geolo. Soc. Am. Bull. 205, 582–593.

Grégoire, V., Darrozes, J., Gaillot, P., Nédélec, A., Launeau, P., 1998. Magnetite grain shape fabric and distribution anisotropy vs rock magnetic fabric: a three-dimensional case study. J. Struct. Geol. 20, 937–944.

Harangi, S., Downes, H., Thirlwall, M., Gmeling, K., 2007. Geochemistry, petrogenesis and geodynamic relationships of Miocene calc-alkaline volcanic rocks in the Western Carpathian Arc, Eastern Central Europe. J. Petrol. 48, 2261–2287.

Hrouda, F., 1982. Magnetic anisotropy of rocks and its application in geology and gephysics. Geophys. Surv. 5, 37–82.

Hrouda, F., Kahan, Š, 1991. The magnetic fabric relationship between sedimentary and basement nappes in the High Tatra Mountains, N. Slovakia. J. Struct. Geol. 13, 431–442.

Hutton, D.H.W., 1988. Granite emplacement mechanisms and tectonic controls: inferences from deformation studies. Earth Environ. Sci. Trans. R. Soc. Edinburgh 79, 245–255.

Janoušek, V., Bowes, D.R., Rogers, G., Farrow, C.M., Jelínek, E., 2000. Modelling diverse processes in the petrogenesis of a composite batholith: the Central Bohemian Pluton, Central European Hercynides. J. Petrol. 41, 511–543.

Jelínek V (1981) Characterization of the magnetic fabric of rocks. Tectonophysics 79, T63–T67.

Johnson, K., Schwartz, J.J., Wooden, J.L., O'Driscoll, L.J., Jeffcoat, R.C., 2011. The Wallowa batholith: new Pb/U (SHRIMP–RG) ages place constraints on arc magmatism and crustal thickening in the Blue Mountains Province, NE Oregon. Geol. Soc. Am. Abstracts with Programs 43, 5.

Konečný, P., Lexa, J., Hostričová, V., 1995. The Central Slovakia Neogene volcanic field. Acta Vulcanol. 7, 63–78.

Konečný, V., Kováč, M., Lexa, J., Šefara, J., Sefara, J., Konečný, V., Kováč, M., Šefara, J., 2002. Neogene evolution of the Carpatho–Pannonian region: an interplay of subduction and backarc diapiric uprise in the mantle. EGU Stephan Mueller Spec. Publ. Ser. 1, 105–123.

Košler, J., Aftalion, M., Bowes, D.R., 1993. Mid-late Devonian plutonic activity in the Bohemian Massif: U–Pb zircon isotopic evidence from the Staré Sedlo and Mirotice gneiss complexes, Czech Republic. Neues Jahrb. Mineral. Monatsh. 9, 417–431.

Lexa, J., Štohl, J., Konečný, V., 1999. The Banská Štiavnica ore district: relationship between metallogenetic processes and the geological evolution of a stratovolcano. Miner. Depos. 34, 639–654.

Lipman, P.W., 1984. The roots of ash flow calderas in western North America: Windows into the tops of granitic batholiths. J. Geophys. Res. 89, 8801–8840.

Lipman, P.W., Bachmann, O., 2015. Ignimbrites to batholiths: Integrating perspectives from geological, geophysical, and geochronological data. Geosphere 11, 705–743.

Loock, S., Diot, H., Van Wyk de Vries, B., Launeau, P., Merle, O., Vadeboin, F., Petronis, M.S., 2008. Lava flow internal structure found from AMS and textural data: An example in methodology from the Chaîne des Puys, France. J. Volcanol. Geotherm. Res. 177, 1092–1104.

Miller, R.B., Paterson, S.R., 2001. Construction of mid-crustal sheeted plutons: Examples from the North Cascades, Washington. Geol. Soc. Am. Bull. 113, 1423–1442.

Milord, I., Sawyer, E.W., Brown, M., 2001. Formation of diatexite migmatite and granite magma during anatexis of semi-pelitic metasedimentary rocks: An example from St. Malo, France. J. Petrol. 42, 487–505.

Nagata, T., 1962. Rock Magnetism. Maruzen, Tokyo.

Ort, M.H., Orsi, G., Pappalardo, L., Fisher, R.V., 2003. Anisotropy of magnetic susceptibility studies of depositional processes in the Campanian Ignimbrite, Italy. Bull. Volcanol. 65, 55–72.

Ort, M.H., Porreca, M., Geissman, J.W., Aquila, L., 2015. The use of palaeomagnetism and rock magnetism to understand volcanic processes: introduction. Geol. Soc. London, Spec. Publ. 396, pp. 1–11.

Palmer, H.C., MacDonald, W.D., Gromme, C.S., Ellwood, B.B., 1996. Magnetic properties and emplacement of the Bishop tuff, California. Bull. Volcanol. 58, 101–116.

Paterson, S.R., Ducea, M.N., 2015. Arc Magmatic Tempos: Gathering the Evidence. Elements 11, 91–98.

Paterson, S.R., Vernon, R.H., Tobisch, O.T., 1989. A review of criteria for the identification of magmatic and tectonic foliations in granitoids. J. Struct. Geol. 11, 349–363.

Paterson, S.R., Fowler, T.K., Schmidt, K.L., Yoshinobu, A.S., Yuan, E.S., Miller, R.B., 1998. Interpreting magmatic fabric patterns in plutons. Lithos 44, 53–82.

Pitcher, S.W., Berger, A.R., 1972. Geology of Donegal: s study of granite emplacement and unroofing. Regional Geology Series, John Wiley & Sons Inc, New York, pp. 435.

Petford, N., 2003. Rheology of granitic magmas during ascent and emplacement. Annual Review of Earth and Planetary Sciences, 31, 399–427.

Petford, N., Kerr, R., Lister, J., 1993. Dike transport of granitoid magmas. Geology 21, 845–848.

Petford, N., Cruden, A.R., McCaffrey, K.J., Vigneresse, J.L., 2000. Granite magma formation, transport and emplacement in the Earth’s crust. Nature 408, 669–73.

Petronis, M.S., Delcamp, A., van Wyk de Vries, B., 2013. Magma emplacement into the Lemptégy scoria cone (Chaîne Des Puys, France) explored with structural, anisotropy of magnetic susceptibility, and paleomagnetic data. Bull. Volcanol. 75, 753.

Richter, C., van Der Pluijm, B.A., Housen, B.A., 1993. The quantification of crystallographic preferred orientation using magnetic anisotropy. J. Struct. Geol. 15, 113–116.

Rosenberg, C.L., 2004. Shear zones and magma ascent: A model based on a review of the Tertiary magmatism in the Alps. Tectonics 23. doi:10.1029/2003TC001526

Tarling, D., Hrouda, F., 1993. Magnetic Anisotropy of Rocks. Chapman & Hall.

Tatsumi, Y., 2005. The subduction factory: How it operates in the evolving Earth. GSA Today 15, 4–10.

Tatsumi, Y., Kogiso, T., 2003. The subduction factory: its role in the evolution of the Earth’s crust and mantle. Geol. Soc. London, Spec. Publ. 219, 55–80.

Tibaldi, A.M., Otamendi, J.E., Cristofolini, E.A., Baliani, I., Walker, B.A., and Bergantz, G.W., 2013, Reconstruction of the Early Ordovician Famatinian arc through thermobarometry in lower and middle crustal exposures, Sierra de Valle Fértil, Argentina: Tectonophysics 589, 151–166.

Vernon, R.H., 2000. Review of Microstructural Evidence of Magmatic and Solid-State Flow. Vis. Geosci. 5, 1–23.

Vernon, R.H., and Paterson, S.R., 2006. Mesoscopic structures resulting from crystal accumulation and melt movement in granites. Trans. Roy. Soc. Edinb. Earth Sci. 97, 369–381.

Vernon, R.H., Johnson, S.E., Melis, E.A., 2004. Emplacement-related microstructures in the margin of a deformed pluton: the San José tonalite, Baja California, México. J. Struct. Geol. 26, 1867–1884.

Vigneresse, J.L., 1995a. Control of granite emplacement by regional deformation. Tectonophysics 249, 173–186.

Vigneresse, J.L., 1995b. Crustal regime of deformation and ascent of granitic magma. Tectonophysics 249, 187–202.

Vigneresse, J.L., Clemens, J.D., 2000. Granitic magma ascent and emplacement: neither diapirism nor neutral buoyancy. Geol. Soc. London, Spec. Publ. 174, 1–19.

Chapter *1:*

GROWTH OF INTRA-CALDERA LAVA DOMES CONTROLLED BY VARIOUS MODES OF CALDERA COLLAPSE, THE ŠTIAVNICA VOLCANO–PLUTONIC COMPLEX, WESTERN CARPATHIANS

by Filip Tomek, Jiří Žák, Fratišek V. Holub, Marta Chlupáčová and Kryštof Verner

a manuscript under review in **Journal of Volcanology and Geothermal Research**

(additional information are listed in appendix item 1)

GRAPHICAL ABSTRACT

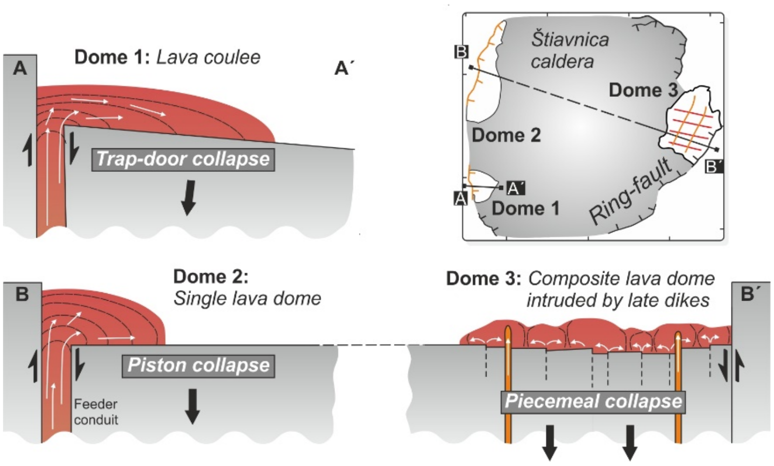

KEY WORDS

◇ Andesite

◇ Anisotropy of magnetic susceptibility (AMS)

◇ Collapse caldera

◇ Lava dome

◇ Magma flow

◇ Stratovolcano

GROWTH OF INTRA-CALDERA LAVA DOMES CONTROLLED BY VARIOUS MODES OF CALDERA COLLAPSE, THE ŠTIAVNICA VOLCANO–PLUTONIC COMPLEX, WESTERN CARPATHIANS

ABSTRACT

The Štiavnica volcano–plutonic complex is an erosional relic of a large (ca. 50 km in diameter) Miocene caldera-stratovolcano in the Western Carpathians. The complex exposes a vertical section from the volcano basement through subvolcanic intrusions and ring-fault to volcanic edifice, comprising mostly andesitic lava flows and domes. This paper examines internal structure, magnetic fabric derived from the anisotropy of magnetic susceptibility (AMS), and emplacement dynamics of three intra-caldera andesite domes (referred to as Domes 1–3 here) located near the ring-fault. Magnetic fabrics, carried by multi-domain titanomagnetite and titanomaghemite, are interpreted as recording various mechanisms of dome growth controlled by active caldera collapse. Dome 1 is explained as a lava coulee fed by conduit located along the ring-fault with a long magma outflow down the sloping caldera floor. Dome 2 represents an elongated, ring-fault-parallel dome wherein the lava flowed a short distance over a flat floor. Dome 3 is most complex, interpreted as a composite dome fed from multiple linear fissures opened at a high angle to the ring fault. Subsequently, the dome was intruded by a series of ring-fault-parallel dikes that may have potentially fed younger, now largely eroded lava domes and flows. Finally, we suggest that all domes formed during collapse of the Štiavnica caldera and the various mechanisms of their growth reflect different stages of the caldera evolution from piston (Dome 2) through trap-door (Dome 1) to piecemeal (Dome 3).

INTRODUCTION

Lava domes are near-vent accumulations of extruded highly viscous intermediate to felsic lava and thus represent a final volcanic expression of the underlying magmatic systems (Fink, 1990; Fink and Griffiths, 1998; Fink and Anderson, 2000; Ogburn et al., 2015). Lava domes have various sizes and shapes and typically occur within monogenetic fissure-aligned volcano chains (e.g., Sieh and Bursik, 1986), composite volcanoes (e.g., Clynne, 1990; Fink et al., 1990; Bourdier et al., 1997), and collapse calderas (e.g., Maeno and Taniguchi, 2006; Ashwell et al., 2013). Potential volcanic hazards associated with dome growth include highly explosive eruptions due to dome and/or flank collapse, accompanied by deadly pyroclastic flows and surges (see Ogburn et al., 2015 for overview and references). From this perspective, most studies have focused on monitoring of active domes and eruption forecasting (e.g., Jaupart and Allègre, 1991; Sparks, 1997; Voight et al., 1998, 2006; Ramsey and Fink, 1999; Barmin et al., 2002; Bonadonna et al., 2005; Hale, 2008; Major et al., 2009; Wadge et al., 2010) whereas less attention has been paid to the internal structure of and strain patterns in lava domes and mechanisms of their emplacement and flow.

Hereinafter we use the term 'flow' to describe magma movement on a small scale, whereas 'dome growth' means its large-scale emplacement.

The existing field studies and numerical and analogue models (e.g., Fink, 1983; Fink and Pollard, 1983; Anderson and Fink, 1992; Merle, 1998; Buisson and Merle, 2002, 2004; Castro et al., 2002; Závada et al., 2009; Bella Nké et al., 2014) mostly describe simple concentric 'onion-skin' fabric patterns in lava domes. On the other hand, one would expect that natural examples of lava domes will likely have a more complex structure resulting from variations in magma effusion rates, episodic multi-pulse dome growth, pre-existing local topography, active tectonic faulting in the underlying basement, and caldera collapses as documented by Ashwell et al. (2013). An outstanding question thus arises whether internal fabric of lava domes may preserve information about the dynamics of related faulting, and mode of caldera collapse.

The macroscopic structures in lava domes are mostly represented by flow banding, foliations and lineations (planar and linear shape preferred orientation of phenocrysts and vesicles), crease structures, and cooling-induced fractures including columnar joints (Fink, 1980; Anderson and Fink, 1992; Smith and Houston, 1994; Cañón-Tapia et al., 1996; Gonnermann and Manga, 2005; Hetényi et al., 2012). As opposed to coarser-grained and commonly foliated plutons, many domes consist of fine-grained aphyric lava with no apparent magmatic fabric (planar and linear shape preferred orientation of phenocrysts). Hence, the anisotropy of magnetic susceptibility (AMS) is often used as a sensitive tool capable of detecting even the weakest, macroscopically invisible fabrics in volcanic rocks (e.g., Palmer et al., 1996; Cañón-Tapia et al., 1996, 1997, 2004, 2005; Ort et al., 2003, 2015; Loock et al., 2008; Petronis et al., 2013; Cañón-Tapia and Mendoza-Borunda, 2014). Relating the AMS to magma flow and emplacement in volcano–plutonic systems requires, however, a detailed characterization of magnetic minerals to distinguish flow-related fabrics from those reflecting syn- to post- emplacement alteration and oxidation (e.g., Seaman et al., 1991; Krása and Herrero-Bervera, 2005; Silva et al. 2008). The original mineral associations may also be partly to completely modified as a result of decompression during magma ascent and eruption (e.g., Devine et al., 1998; Rutherford and Devine, 2003; Browne and Gardner, 2006).

This paper addresses some of the above issues and examines internal structure and emplacement dynamics of three intra-caldera andesite domes in the Miocene Štiavnica volcano–plutonic complex, Western Carpathians (Fig. 1a, b). After a brief introduction into local geologic setting, we concentrate on quantification of magnetic fabric parameters and orientation in each dome. The AMS study is complemented with a detailed analysis of magnetic mineralogy using thermomagnetic experiments, magnetic field vs. susceptibility measurements, and back scattered diffraction (BSD) microscopy. Our data reveal different fabric patterns in the three domes and we suggest that they record different mechanisms of lava flow and deformation during dome growth. Finally, we interpret these fabric and inferred flow patterns as reflecting various modes of caldera subsidence.

THE ŠTIAVNICA VOLCANO–PLUTONIC COMPLEX: A BRIEF OVERVIEW

The Štiavnica volcano–plutonic complex is an erosional relic of the largest (~50 km in diameter) stratovolcano and associated caldera in the Neogene to Quaternary Carpathian–Pannonian Region (Fig. 1; Lexa et al., 2010), representing an extensional back-arc setting inboard of the Western Carpathian orogenic belt (Fig. 1a, b; e.g., Konečný et al., 1995, 2002; Harangi et al., 2007). The overall composition of igneous rocks corresponds to high-K, calc-alkaline andesite. Magma origin is interpreted as resulting from decompression melting of enriched mantle during lithospheric thinning, further fractionation of the melts, and their mixing with crustally-derived magmas (see Konečný et al., 2002 and Lexa et al., 2010, and references herein).

The Štiavnica volcano–plutonic complex developed in three stages (Fig. 1c; Konečný, 1971; Konečný et al., 1995; Lexa et al., 1999; Koděra et al., 2004, 2005; Chernyshev et al., 2013). (1) The pre-caldera stage (~15.0–13.5 Ma) is characterized by growth of the stratovolcano on Variscan basement covered by Late Paleozoic siliciclastic and Mesozoic carbonate successions. The initial volcanic activity involved pyroxene and amphibole–pyroxene andesite lava flows, domes, pyroclastic deposits, and epiclastic breccias. The central portion of the stratovolcano was then

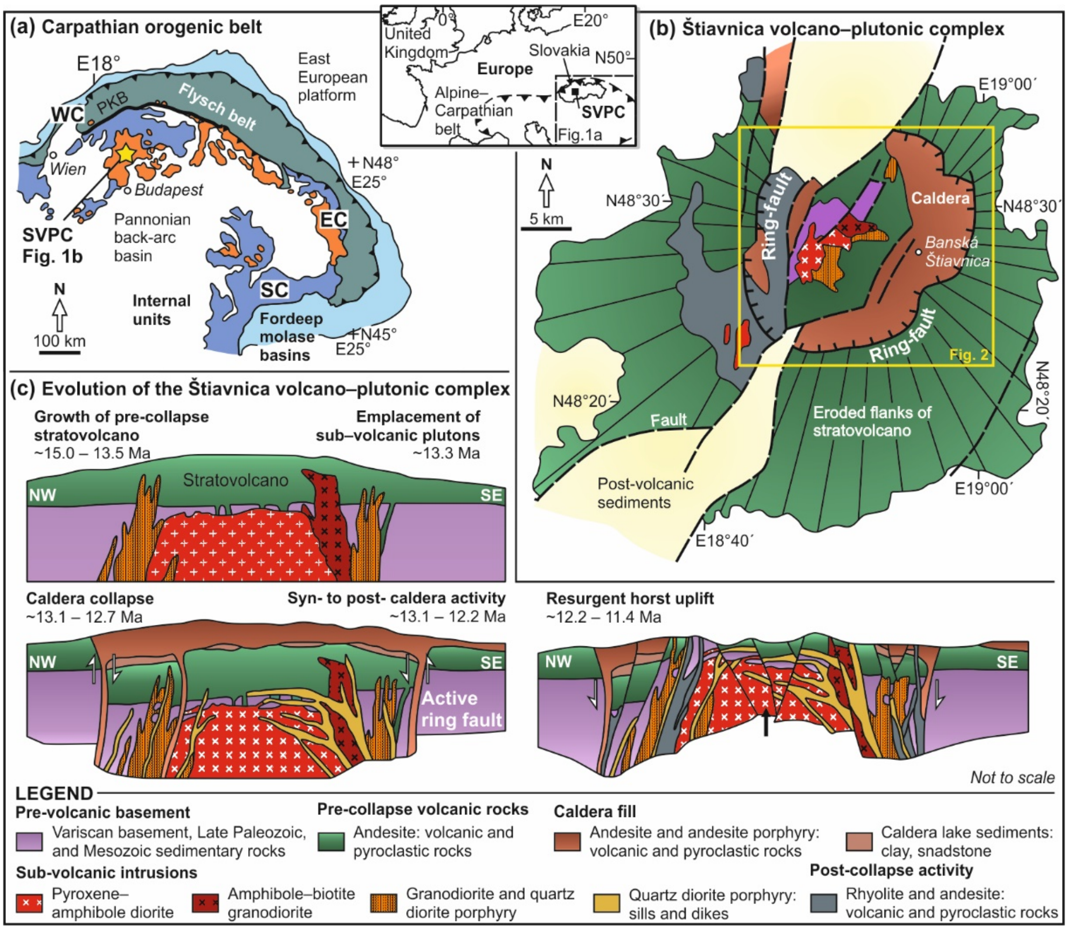

Fig. 1. (a) Simplified tectonic map of the Carpathian orogenic belt (see inset for its location in Europe); modified after Lexa et al. (1999), Plašienka (2003), and Pécskay et al. (2006). (b) Geologic map of the Štiavnica volcano–plutonic complex (modified after Lexa et al., 1999; and Chernyshev et al., 2013). (c) Simplified evolution of the Štiavnica volcano–plutonic complex (modified after Lexa et al., 1999; and Chernyshev et al., 2013).

intruded by andesite porphyry sills, dikes, and laccoliths followed by a period of quiescence and erosion. Subsequently, a voluminous bell-jar granodiorite pluton (13.4 ± 0.2 Ma and 13.3 ± 0.6 Ma; Rb–Sr whole rock) and a steep-sided diorite stock (13.3 ± 0.2 Ma; Rb–Sr whole rock) were emplaced at a very shallow level (~2–3 km) into the central part of the stratovolcano. The granodiorite pluton was accompanied by intrusion of minor stocks and dikes of granodiorite and quartz diorite porphyry (Fig. 1c). (2) Next, subsidence of an extensive collapse caldera in the central portion of the stratovolcano triggered extrusion of differentiated biotite–amphibole andesitic and dacitic lava domes, flows, and pyroclastic density currents (~13.1–12.7 Ma). The caldera depression was then filled with siliciclastic sediments, epiclastic breccias, and andesitic to dacitic volcanic rocks and later intruded by sub-volcanic quartz diorite porphyry sills, and dikes (~12.7–12.2 Ma; Fig. 1c). (3) The final post-caldera stage (~12.2–11.4 Ma) is marked by renewed volcanic activity from eruptive centers scattered along the eroded caldera stratovolcano slopes and by uplift of an asymmetric resurgent horst in the central part of the complex (Fig. 1c). This uplift was accompanied by rhyolitic volcanism and emplacement of granite porphyry dikes (11.8–8.2 Ma).

ANDESITE LAVA DOMES

Geological setting

The three extrusive domes, referred here to as Domes 1–3 (Fig. 2), were originally mapped by Konečný et al. (1998a) and interpreted as part of the 'Middle structural unit, caldera fill' by Lexa et al. (1999) and Chernyshev et al. (2013). This unit comprises a suite of pumice tuffs, pyroclastic deposits, lava domes, flows, and epiclastic breccias deposited both inside and outside the caldera depression, but all were presumably fed from vents along the active caldera ring-fault (Fig. 2; Lexa et al., 1999). Their composition ranges from basaltic andesite through trachyandesite and andesite (most common) to dacite (Konečný et al., 1998b; Chernyshev et al., 2013). Domes 1–3 have not been dated, but the existing radiometric ages of comparable volcanic rocks of the caldera fill include K–Ar ages of 13.1 ± 0.3 Ma (groundmass), 12.8 ± 0.3 Ma (biotite), and 13.0 ± 0.4 Ma (plagioclase), and Rb–Sr ages of 12.4 ± 0.1 and 12.9 ± 0.5 Ma (whole rock and monomineral samples; Chernyshev et al., 2013).

Dome 1 is located at the southeastern caldera rim (Fig. 2) and is about 3 km long and 2.5 km wide (~6 km2 in plan view). The adjacent rocks comprise older, Stage 1 andesites to the west of the ring-fault, interpreted as remnants of the original stratovolcano. The remainder of the dome is overlain by younger post-caldera volcanic products.

Dome 2 in the northwestern sector of the caldera is about 10 km long and ~3 km wide (~17 km2 in plan view) and is elongated in a NNE–SSE direction parallel to the local segment of the ring-fault (Fig. 2). The western and northwestern portions of the dome are in contact with both pre- and post-caldera volcanics whereas the eastern and southern portions are overlain by Upper Miocene sediments filling the Hron River valley. A comparable small lava body assigned to the

'Middle structural unit' is also exposed south of the river, however, its relation to Dome 2 is uncertain (Fig. 2).

The largest Dome 3 (7.5 × 5.3 km, ~27 km2 in plan view) is located at the eastern margin of the caldera. To the SE, the dome terminates against the ring-fault but elsewhere is in contact with broadly coeval syn-caldera volcanics (Fig. 2).

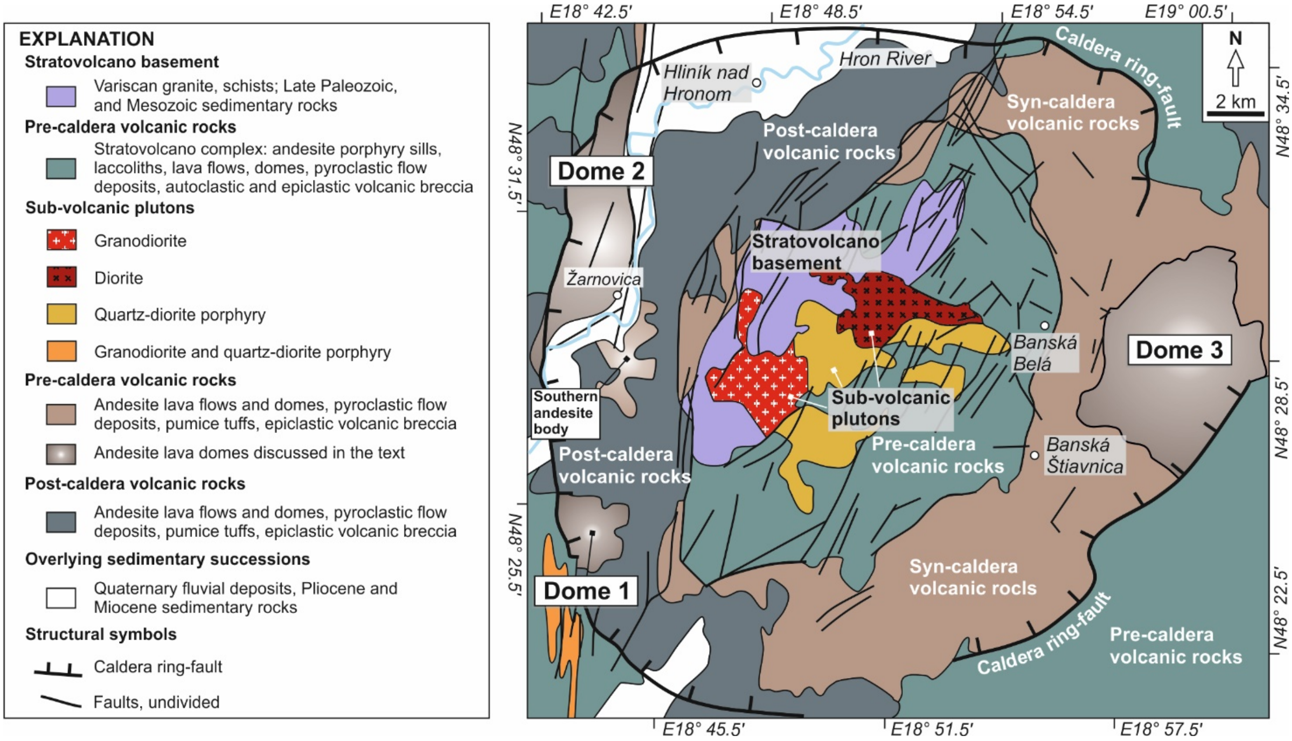

Fig. 2. Detailed geologic map of the central portion of the Štiavnica volcano–plutonic complex. The extrusive Domes 1–3 are located near the caldera ring-fault (redrafted from Konečný et al., 1998a; and Chernyshev et al., 2013).

Internal structure and textures of the andesite domes

The andesites in all domes have dark grayish green to gray color, are medium-grained and porphyritic with pyroxene, amphibole, and plagioclase phenocrysts up to 5 mm in size (Fig. 3a–d). On outcrops, Domes 1–2 typically exhibit no significant macroscopic compositional or textural variations, whereas Dome 3 is somewhat more complex. First, the andesites show various degree of alteration ranging from pervasive to localized along fractures (Fig. 3a, b). Most of the andesites, however, appear macroscopically unaltered (Fig. 3c, d). Second, detailed mapping by Konečný et al. (1998a) revealed several up to 1 km long domains of extrusive breccia (Fig. 4). Third, Dome 3 also preserves a weak magmatic foliation defined by shape-preferred orientation of amphibole, plagioclase, and pyroxene phenocrysts (Figs. 3a, c, 5d). The foliation dips moderately to steeply but displays two distinct orientations. In the bulk of the dome, foliation strikes ~NW–SE to ~NNW–SSE and is thus at a high angle to the present-day (erosional) dome margin and to the caldera ring-fault (Fig. 4). In contrast, foliation strikes ~N–S to ~NNE–SSW in three ~100–200 meters wide zones that seem to cut across the earlier foliation (Fig. 4). Magmatic lineation is not readily discernible.

On the microscale, the andesites contain largely devitrified glassy groundmass (~50–60 %) with crystallites and rare spherulites, surrounding abundant subhedral phenocrysts of clino- and orthopyroxene, green hornblende, brown biotite, and plagioclase (Fig. 5a–d). In all domes, the andesites exhibit two different mineral assemblages: 'dry', without amphibole, and 'wet', with amphibole (Fig. 5a). The plagioclase phenocrysts have either clear or sieve texture (Fig. 5d). In addition, abundant euhedral microphenocrysts of orthopyroxene (enstatite), biotite, and magnetite are interspersed within the matrix (Fig. 5e). Some samples also include glomerocrysts of clino- and orthopyroxene, plagioclase, and rare amphibole (Fig. 5f). Especially in Domes 2 and 3, pyroxene phenocrysts are partly or completely decomposed and have thick opacite rims (Fig. 5g). Similarly, amphibole and partly also biotite phenocrysts are opacitized in a pseudomorphs of secondary magnetite, pyroxene, and new generation of amphibole (opacite; Fig. 5a, d, h).

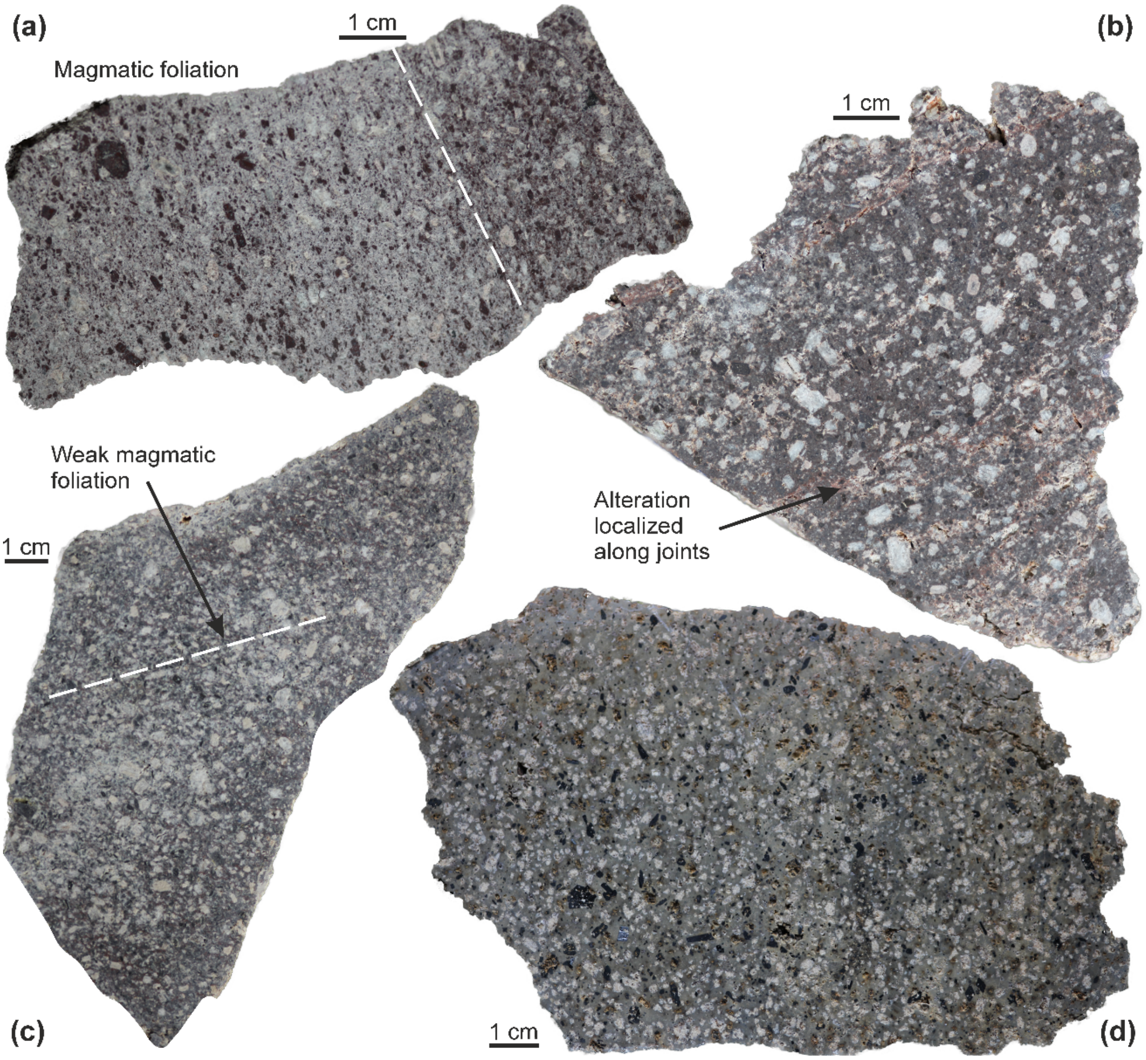

Fig. 3. Photographs of rock slabs of representative andesite samples. (a) Pyroxene andesite, note the alteration localized along fractures, sample JZ44 (Dome 3); coordinates: N48°29'59.5", E18°59'07.5". (b) Foliation-perpendicular and lineation-parallel (kinematic) section of porphyritic amphibole–biotite–pyroxene andesite, note the magmatic foliation and reddish color caused by oxidation, sample JZ43 (Dome 3); coordinates: N48°29'36.2", E18°58'54.6". (c) Amphibole–biotite–pyroxene andesite, sample FT76 (Dome 1); coordinates: N48°25'06.2", E18°42'39.1". (d) Biotite–pyroxene andesite, sample FT116 (Dome 3); coordinates: N48°27'19.0", E18°58'52.2". All coordinates are referenced to the WGS84 datum.

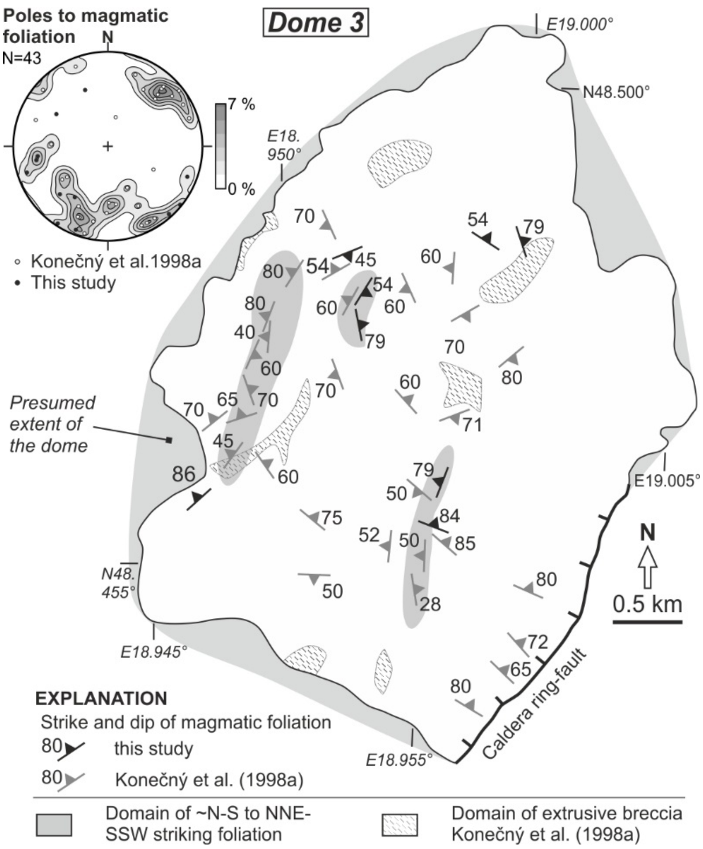

Fig. 4. Map of magmatic foliation in the Dome 3 showing two discordant fabrics (Type 1 and 2 as defined in the text) and domains of extrusive breccia (after Konečný et al., 1998a). Stereonet is equal are projection on lower hemisphere.

ANISOTROPY OF MAGNETIC SUSCEPTIBILITY (AMS)

Methodology

We use the anisotropy of magnetic susceptibility (AMS; see Hrouda, 1982; Tarling and Hrouda, 1993; Borradaile and Jackson, 2010 for reviews and principles) to quantify magnetic fabrics and parameters in the three andesite lava/flow domes. The sampling strategy involved drilling of rock cores using a hand-held gasoline drill on outcrops or taking oriented blocks. The blocks were then drilled in the laboratory, rotated back to their original (in situ) position, and the orientation of the drilled cores was measured using the standard orientation table. Samples were collected at 20, 15, and 34 stations in Domes 1 to 3, respectively. In total, the cores yielded 820 standard cylindrical specimens, each approximately 10 cm3 in volume, which corresponds to an average of 12 specimens per station.

The AMS was measured with a MFK1-A Kappabridge in the Laboratory of Rock Magnetism, Institute of Geology and Paleontology, Charles University in Prague. A statistical analysis of the data was treated using the ANISOFT software package (www.agico.com). The measured data and parameters are presented in Figs. 6–9 and listed in full in the Appendix items 1/1–1/4.

The AMS tensor is represented by an ellipsoid with the principal susceptibility axes $k_1 \geq k_2 \geq k_3$ where the maximum susceptibility (k_1) represents magnetic lineation and the minimum susceptibility (k_3) characterize the pole to magnetic foliation. The AMS can be further described by several parameters (Tarling and Hrouda, 1993) from which we use (1) the bulk (mean) susceptibility ($k_m = (k_1 + k_2 + k_3)/3$) which reflects the type and volume fraction of magnetic minerals, (2) the degree of anisotropy ($P = k_1/k_3$) which indicates the eccentricity of the AMS ellipsoid and may be thus related to the intensity of the shape-preferred orientation of magnetic minerals (Nagata, 1962), and (3) the shape parameter ($T = 2\ln(k_2/k_3)/\ln(k_1/k_3) - 1$) which

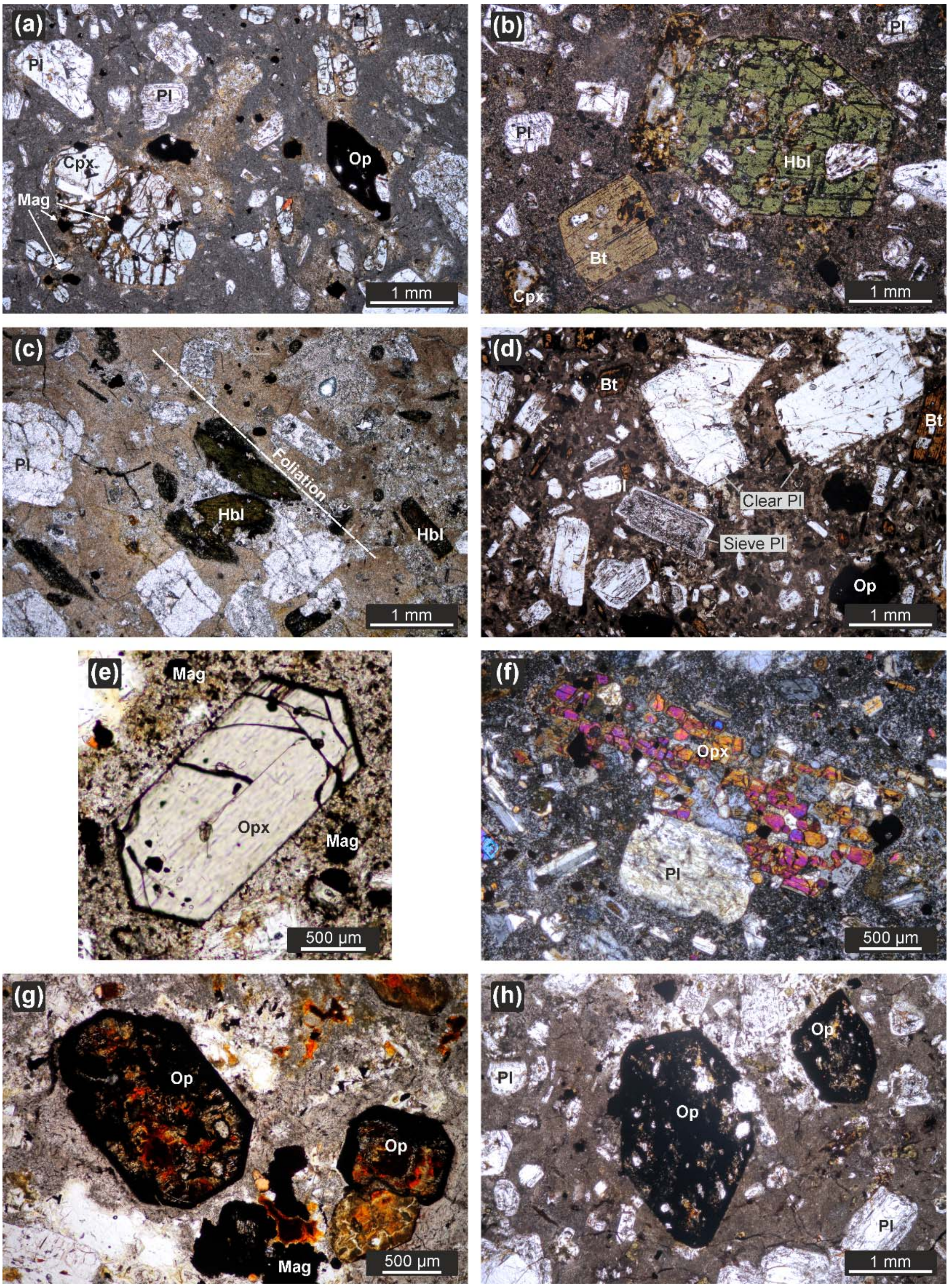

Fig. 5. (on previous page) Plane polarized (a–e, g, h) and cross polarized light (f) photomicrographs in kinematic section perpendicular to magnetic foliation and parallel to magnetic lineation. (a) Porphyritic biotite–pyroxene andesite (dry mineral assemblage), amphibole is completely opacitized, specimen FT75 (Dome 1); coordinates: N48°24'59.6", E18°43'06.4". (b) Amphibole–biotite–pyroxene andesite, note the basal section through the amphibole phenocryst, no opacitization, specimen JZ26 (Dome 1); coordinates: N48°29'59.5", E18°59'07.5". (c) Amphibole–biotite–pyroxene andesite with shape-preferred orientation of plagioclase and hornblende phenocrysts (foliation), specimen FT112 (Dome 3); coordinates: N48°27'29.8", E18°57'23.6". (d) Amphibole–biotite andesite (no pyroxene), amphibole is locally opacitized, note the two populations of plagioclase phenocrysts, specimen FT99 (Dome 3); coordinates: N48°29'21.6", E18°59'10.4". (e) Detail of euhedral enstatite microphenocryst from the biotite–pyroxene–amphibole andesite, specimen KV10 (Dome 2); coordinates: N48°31'57.4", E18°42'56.7". (f) Plagioclase–orthopyroxene glomerocryst in the biotite–pyroxene–amphibole andesite (wet assemblage), specimen KV10 (Dome 2); coordinates: N48°31'57.4", E18°42'56.7". (g) Completely decomposed pyroxene phenocryst with a thick opacite rim, specimen FT84 (Dome 2); coordinates: N48°30'16.0", E18°43'24.2". (h) Opacite pseudomorphs after hornblende crystals, amphibole–biotite andesite, specimen FT72 (Dome 2); coordinates: N48°24'43.0", E18°43'48.4". All coordinates are referenced to the WGS84 datum. Hbl – hornblende, Cpx – clinopyroxene, Op – opacite, Opx –

describes symmetry of the AMS ellipsoid. For $-1 \leq T < 0$ the ellipsoid is prolate, for $T = 0$ neutral, and for $1 \geq T > 0$ oblate (Jelínek, 1981). The orientations of the magnetic lineations (k_1) and magnetic foliation poles (k_3) are presented in stereonets in the geographic coordinates and as mean values for individual stations on the maps.

Magnetic mineralogy

Bulk susceptibility

The bulk (mean) susceptibility of all andesite specimens ranges from 1.47 × 10–4 to 3.80 × 10^{-2} (Fig. 6a; SI units are used throughout this paper). Domes 1 and 2 are dominated by high-susceptibility andesites with k_m of 10^{-3} and 10^{-2} (100 % and 99 % of the measured specimens, respectively), whereas 16 % of specimens in Dome 3 have low susceptibilities on the order of 10^{-4} (Fig. 6a). The overall high susceptibility of the andesites suggests that the AMS is carried by ferromagnetic minerals (e.g., Bouchez, 1997; Hrouda and Kahan, 1991). Spatial distribution of the bulk susceptibility does not reveal any systematic pattern in neither of the domes (Appendix item 1/2).

Thermomagnetic experiments

In order to better constrain the AMS carriers, we measured thermomagnetic curves (susceptibility variations with temperature) on seven representative coarsely powdered specimens. The specimens were chosen based on (1) their specific location within each dome (next to the ring-fault, dome center and margin); (2) magnetic fabric orientation and P and T parameters, and (3) the magnetic susceptibility magnitude. The specimens were measured using an Agico MFK1-FA Kappabridge connected to a CS4 non-magnetic Furnace and CS-L Cryostat units. Thermomagnetic curves in the range of –196 °C to 700 °C were acquired in two steps. First, samples were cooled down to the temperature of liquid nitrogen (ca. –196 °C) and heated to the room temperature (ca. 20 °C). Second, samples were heated up from the room temperature to 700 °C and cooled back at a rate of ~14 °C/min. The thermomagnetic curves were analyzed using the Cureval 8 program (freely available from http://www.agico.com) which utilizes a method developed by Hrouda (2003), Hrouda et al. (1997), and Petrovský and Kapička (2006). Furthermore, the thermomagnetic experiments were complemented with measurements of susceptibility dependence on magnetic field intensity, and optical and back-scattered diffraction (BSD) microscopy.

Dome 1. Thermomagnetic curves were obtained on specimens KV2/2/2 (k_m = 1.76 × 10^{-2}) and FT71/2/2 (k_m = 3.54 × 10^{-3}). During heating, specimen KV2/2/2 shows no Verwey transition (T_V) and a pronounced susceptibility peak indicates the presence of a Ti-rich Fe oxide (T_C = –130 °C; Curie temperature), followed by further susceptibility increase to ~350 °C and almost constant susceptibility until 512 °C, where it abruptly drops. The T_C of 544 °C reveals very likely magnetite slightly Ti substituted and oxidized to be the main ferromagnetic mineral (Fig. 6b). In addition, high T_C of 584 °C and 627 °C indicate minor contribution of Ti-maghemite. During cooling, the bulk susceptibility decreases due to unstable magnetite changing to hematite (Fig. 6b).

Specimen FT71/2/2 is characterized by the Verwey transition in the beginning of the heating curves (ca. –165°C), then by a slight increase of susceptibility from ca. 150 °C to higher temperatures, and by pronounced T_C of about 570 °C. These susceptibility variations correspond to pure magnetite, possibly partly oxidized to maghemite (Fig. 6b). This specimen also contains other minerals with higher T_C (584 °C and 648 °C), representing high-temperature oxidation products of the original Ti-magnetite. The cooling part of the susceptibility–temperature curve is almost identical to the heating part.

Dome 2. Thermomagnetic curves of specimens FT78/2/1 (k_m = 1.36 × 10^{-3}) and FT81/1/6 (k_m = 1.70 × 10^{-2}) also display no Verwey transitions. Specimen FT78/2/1 contains a Ti-rich Fe oxide with T_C = –100 °C, slightly substituted magnetite with T_C 560 °C, and both low- and high-temperature maghemite (T_C = 624 °C; Fig. 6b). The susceptibility decrease on the cooling curve most likely represents unstable maghemite changing to hematite (Fig. 6b).

The heating curve of specimen FT81/1/6 is characterized by a susceptibility peak at –166 °C, likely reflecting a Ti-rich Fe-oxide grown due to high-temperature oxidation. The dominant AMS carrier is magnetite, weakly substituted by Ti (T_C = 505 °C and 544 °C), but there is also a trace of high-temperature maghemite (T_C = 583 °C and 640 °C). The cooling curve follows the heating one (Fig. 6b).

Dome 3. Thermomagnetic curves were measured on specimens FT93/1/1 (k_m = 4.80 × 10^{-4}), FT115/3/3 (k_m = 7.46 × 10^{-3}), and JZ48/2/2 (k_m = 1.05 × 10^{-2}). The course of the specimen FT93/1/1 heating curve suggests dominant role of slightly substituted Ti-magnetite (T_C = 544 °C), with a minor contribution of low- and high temperature maghemite with T_C = 573 °C and 606 °C, respectively. The cooling curve shows almost reversible behavior (Fig. 6b). The calculation of resolution of ferromagnetic and paramagnetic minerals using a method developed by Hrouda et al. (1997) indicates 92 % of a ferromagnetic component.

The low-temperature heating curve of specimen FT115/3/3 has a small bump at the beginning, which may reflect either weak Verwey transition of magnetite or a volumetrically minor Ti-rich oxide with T_C = –162 °C. The susceptibility then increases on the high-temperature heating curve, followed by two drops at 394 °C and 538°C. This could be explained as low-temperature maghemite and weakly substituted magnetite. There is also a minor contribution of high-temperature maghemite with T_C = 622 °C. The susceptibility decrease on the cooling curve represents unstable magnetite changing to hematite.

Specimen JZ48/2/2 has no T_V and displays a continuous susceptibility increase up to ~500 °C (Fig. 6b) due to presence of a slightly thermally unstable Fe–Ti-oxide with T_C = 510 °C. A slight bump at ca. 380 °C and T_C = 607 °C probably correspond to low- and high-temperature maghemite, respectively.

Further analysis of ferromagnetic minerals

In thin-sections and BSD images, two distinct populations of magnetite grains and aggregates were distinguished, both with similar average size of individual grains (~100–500 μm; Fig. 6c).

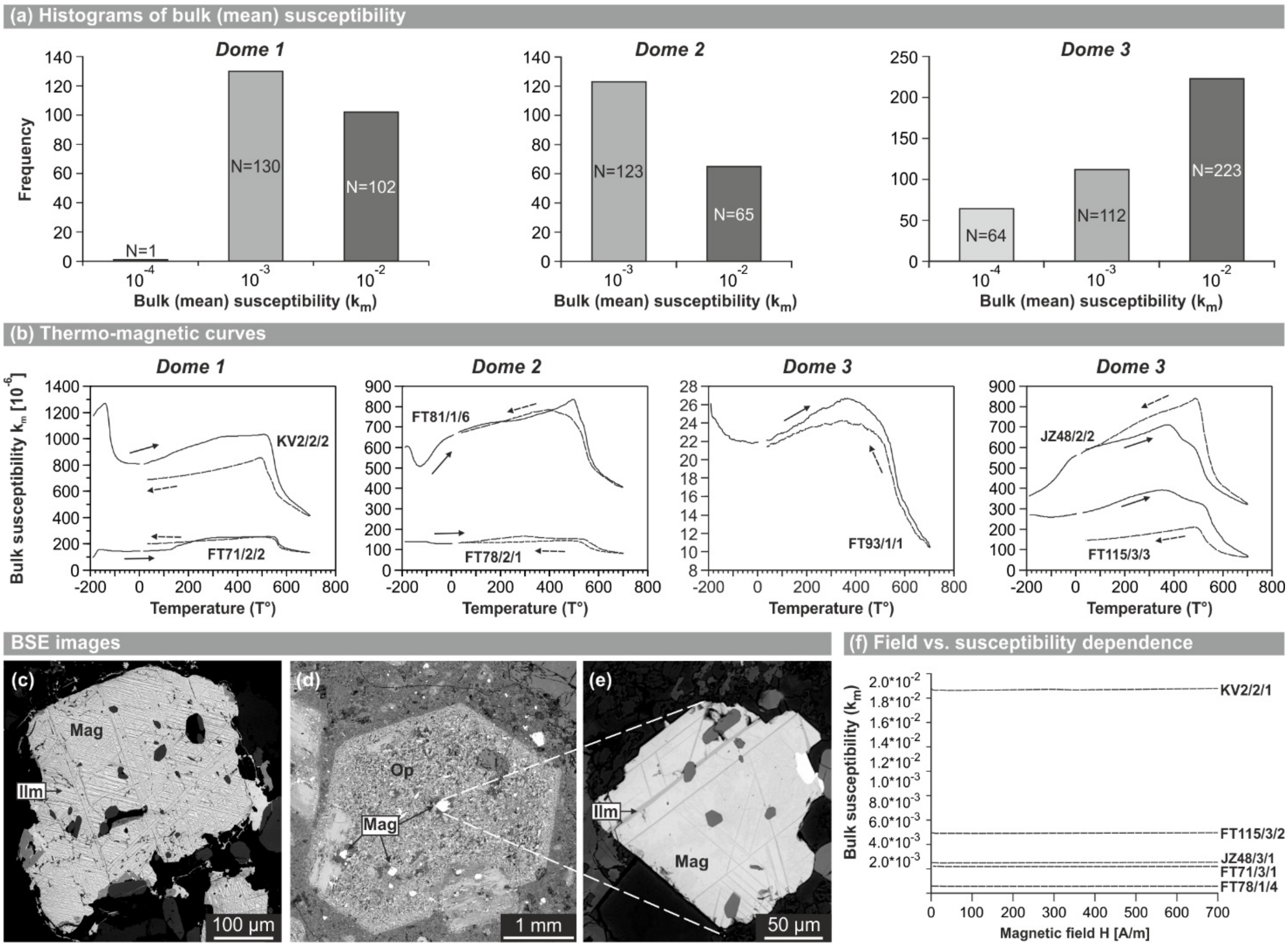

Fig. 6. (a) Histograms of the bulk susceptibility (km) summarizing all the measured AMS specimens from Domes 1–3. (b) Thermomagnetic curves for representative specimens from Domes 1–3. Back scattered diffraction images of (c) subhedral magnetite with ilmenite lamellae, (d) completely opacitized hornblende phenocrysts, and (e) secondary magnetite within opacite. (f) Graphs showing linear dependence of the bulk susceptibility on the magnetic field intensity for five selected specimens from Domes 1–3.

One population includes magmatic microphenocrysts of magnetite scattered within the glassy matrix, a typical feature of all andesite samples (Fig. 6c). The other population, found in most of the andesites, contains variable amount of late, post-magmatic magnetite in opacitized hornblende ± biotite phenocrysts or pseudomorphs (Fig. 6d, e). Both populations also show apparent lamellae. Furthermore, the BSD analysis revealed that both magnetite populations contains only up to ~16 % of Ti (Appendix item 1/3). Such a low Ti content was further corroborated by measurements of dependence of the bulk susceptibility on applied magnetic field. Measurements on five representative specimens showed virtually no change in the bulk susceptibility with increasing magnetic field intensity, suggesting that they are dominated by nearly pure magnetite (Fig. 6f).

Degree of anisotropy and shape parameter

The degree of anisotropy (*P*) of Dome 1 is generally low, ranging from 1.004 to 1.081 (0.4–8% anisotropy), with one significant data peak between 1.010–1.025. An average of all data is 1.022 (2.2% anisotropy; Fig. 7a). Similarly, Dome 2 is characterized by a weak anisotropy between 1.003 and 1.082 with most of the data clustered within an interval of 1.020–1.030 and an average of 1.021 (2.1% anisotropy; Fig. 7b). The *P* parameter is relatively highest in the Dome 3, varying between 1.009 and 1.257, with a peak between 1.030–1.040 and an all-data average of 1.036 (3.6% anisotropy; Fig. 7c).

The shape parameter (*T*) ranges from −0.916 to 0.959 in Dome 1, with oblate AMS ellipsoids slightly prevailing (57 %; Fig. 7a). In Dome 2, the *T* parameter ranges between −0.877 and 0.956, with 62 % of oblate ellipsoids (Fig. 7b). In Dome 3, most of the AMS ellipsoids are oblate (77 %), varying from −0.850 to 0.983 (Fig. 7c).

In the map, station-means of the *P* parameter reveal no obvious pattern in neither of the domes (Fig. 8a). To the contrary, spatial distribution of station-means of the *T* parameter in Domes 1 and 2 define a prominent zone of prolate to neutral AMS ellipsoids near the westerly ring-fault, whereas oblate ellipsoids tend to occur farther away from the fault, i.e., towards the opposite dome margins (Fig. 8b). Fabric is mostly oblate in Dome 3, except on several stations with neutral AMS ellipsoids in its eastern portion and in a roughly N–S-trending zone with prolate fabric in the dome center (Fig. 8b).

Magnetic fabric orientation

Despite the low degree of anisotropy, principal susceptibilities of individual specimens are well clustered about their respective mean directions on most stations (Appendix items 1/4–1/6). The few exceptions with large data scatter are stations KV6 and JZ27 in Dome 1 and stations JZ50 and FT104 in Dome 3.

Fig. 7. (a–c) Plots of the shape parameter (T) against the degree of anisotropy (P) for all the measured AMS specimens from Domes 1–3.

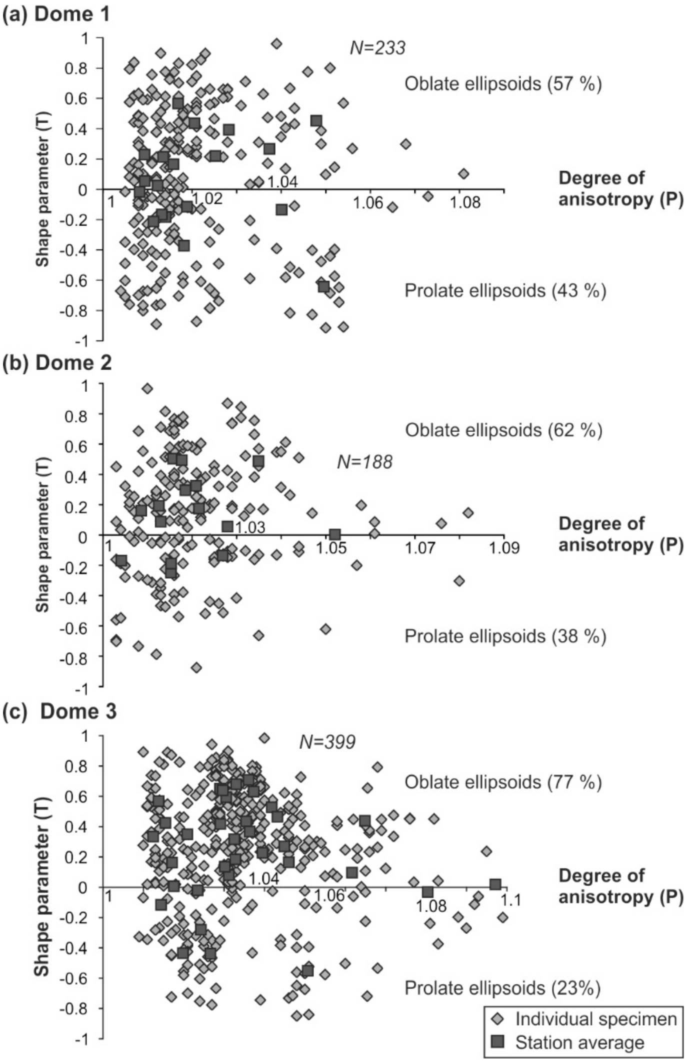

Dome 1

In the map, magnetic fabric in Dome 1 defines a pronounced arcuate pattern, which seems to extend from the westerly ring-fault to the SE. Along the NE and SW dome margins, magnetic foliations dip moderately to steeply to the ~NE or ~SW and then reorient to a ~NE–SW strike in the dome center (Fig. 9a). The associated magnetic lineations are mostly subhorizontal to moderately plunging and follow the same arcuate pattern (Fig. 9b). The exceptions are stations KV5, KV6, and FT72 where magnetic foliations and/or lineations are at a high angle to this overall trend.

Dome 2

Magnetic fabric trajectories in Dome 2 are roughly parallel both to the adjacent ~NNE–SSW-trending segment of the ring-fault and to the outer dome margin. Magnetic foliations dip at shallow to moderate angles and strike ~WNW–SSE in the southernmost portion of the dome and reorient to ~NNE–SSW direction in the remainder of the dome (Fig. 9). Magnetic lineations plunge shallowly to moderately and follow approximately the foliation trend (Fig. 9). The exceptions are stations FT86 and FT77 where the foliation and/or lineations are at a high angle to the dome margin or to the fabric trend (Fig. 9). The significance of magnetic fabric on the outlying station FT117 (Fig. 9) remains uncertain as it is located in the southern andesite body separated from the main dome by the Hron River valley (Figs. 2, 9).

Dome 3

Based on two distinct orientations of magnetic foliations and lineations, two fabric types (referred here to as the Type 1 and 2) were distinguished in Dome 3. The Type 1 fabric occurs in the bulk of the dome and is characterized by subhorizontal to steep ~WNW–ESE foliations dipping mostly to the ~SSW and by ~N–W to ~WNW–ESE-trending subhorizontal to moderately plunging lineations (Fig. 9a–c). The fabric is thus generally at a high angle to the caldera ring-fault and transverse to the dome elongation. The Type 2 fabric defines two narrow, roughly NNE–SSW-trending zones characterized by ~N–S to ~NNE–SSW-striking foliations which dip both to ~E and ~W. The attitude of magnetic foliations is steep in the eastern zone, whereas those in the western zone dip at both subhorizontal and steep angles (Fig. 9a, c). Magnetic lineations trend ~N–S to ~NNE–SSW, however, as compared to foliations, the lineation plunge is both steep and subhorizontal in the eastern zone and generally subhorizontal to moderate in the western zone (Fig. to both the nearby margin but also to either of the two fabrics, lineations consistently plunge

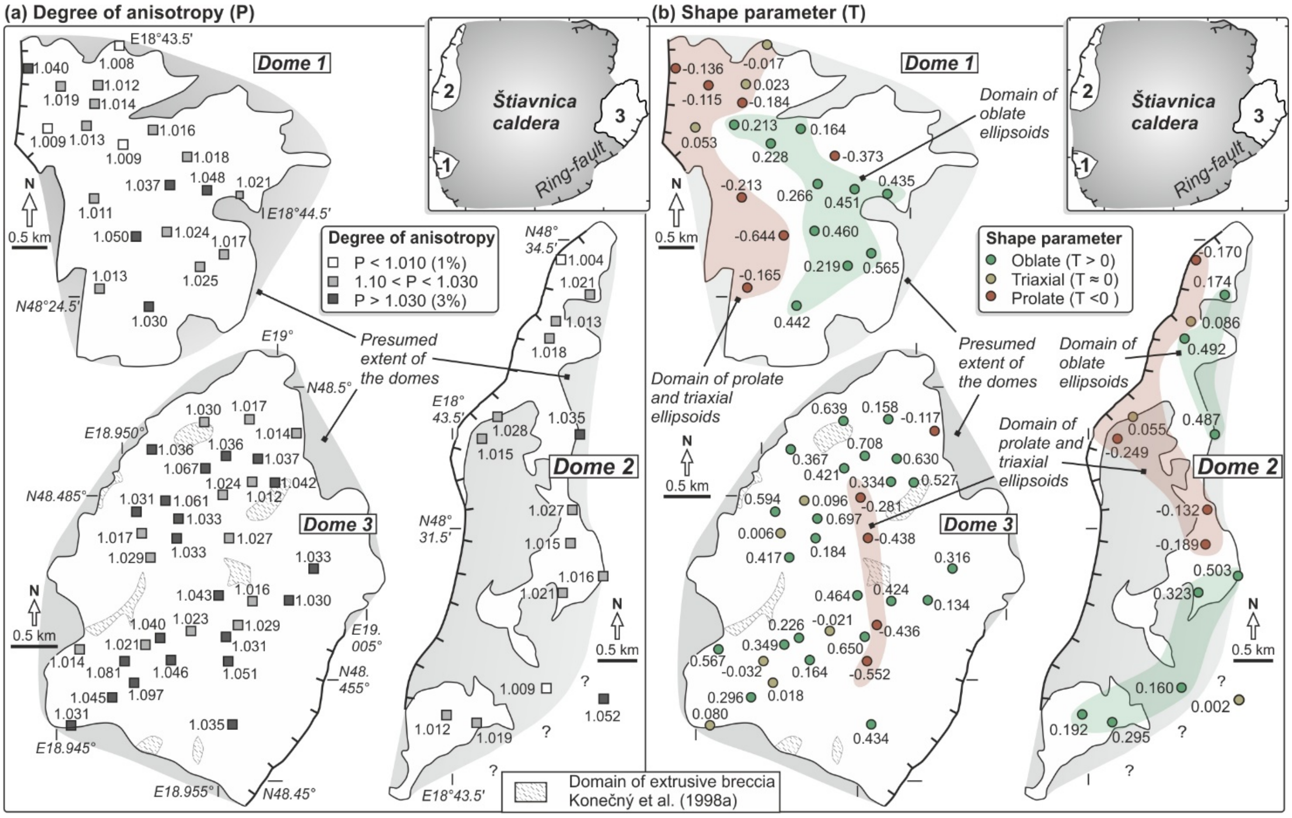

Fig. 8. Maps of spatial distribution of station-average of (a) the degree of anisotropy (P) and (b) the shape parameter (T) in Domes 1–3.

outward at variable angles (Fig. 9a, b).

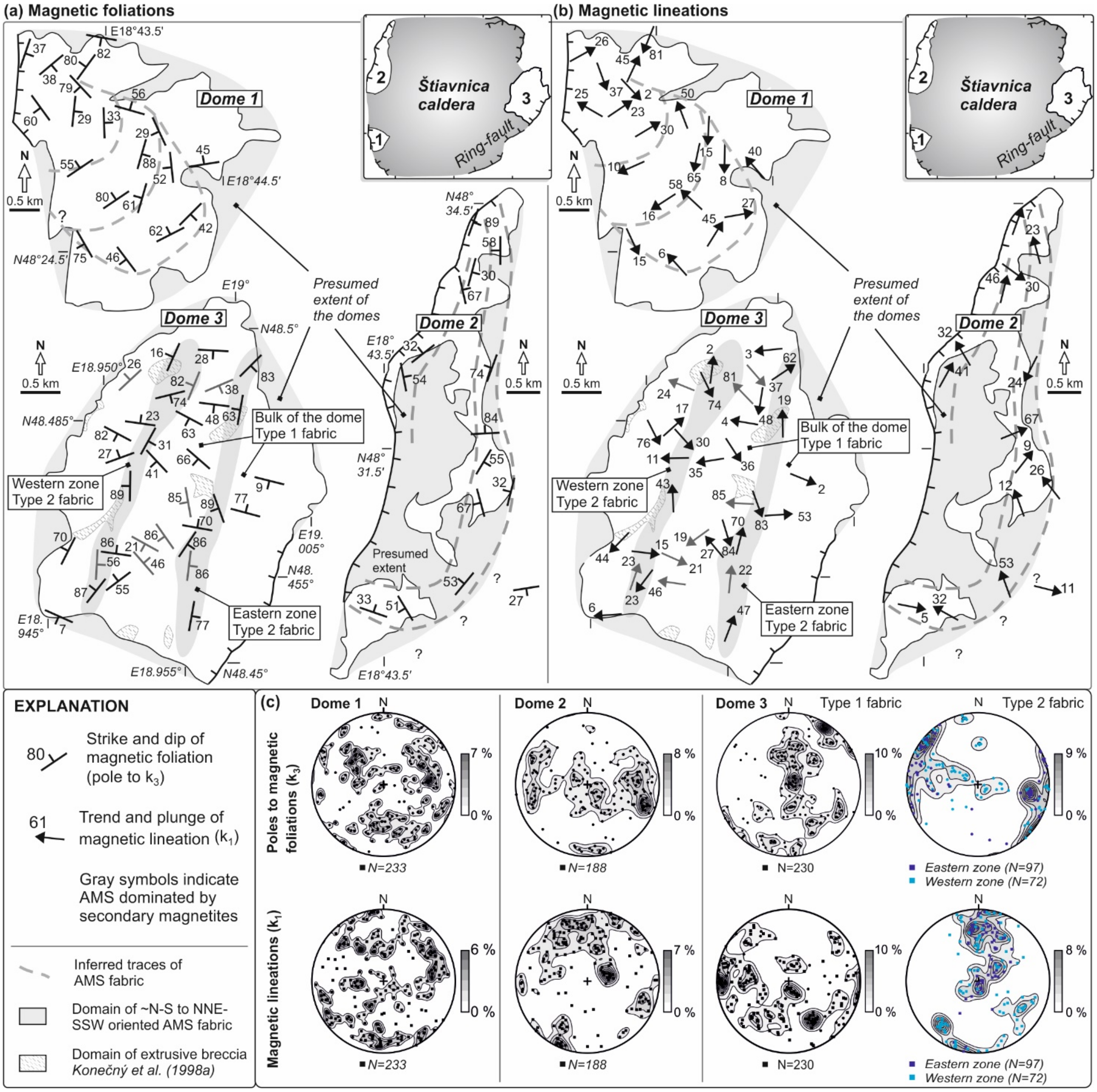

Fig. 9. Maps showing orientation of (a) magnetic foliations and (b) magnetic lineations in Domes 1–3.

DISCUSSION

Interpretation of magnetic mineralogy

Thermomagnetic measurements indicate that the dominant AMS carrier in andesites of all domes is a mineral with T_C above ~500 °C, most likely titanomagnetite, and/or titanomaghemite; contribution of paramagnetic minerals is negligible (Fig. 6a, b). As the Ti content in magnetite is low, we interpret the magnetic fabric as representing shape and distribution anisotropy of low-Ti titanomagnetite and low-Ti titanomaghemite grains with a minor contribution of cubic maghemite. Magnetite is likely multi domain as indicated by its relatively large grain size (Fig. 6c–e).

In addition, we documented late-magmatic magnetite grains that grew in reaction rims of amphibole phenocrysts due to opacitization. This oxidation process is a result of decompression during magma ascent and eruption, in which exsolution of water causes breakdown of amphibole into pseudomorphs of pyroxene and opaque minerals including magnetite (e.g., Rutherford and Devine, 2003; Plechov et al., 2008; De Angelis et al., 2013). The apparent lamellae in both magnetite populations (Fig. 6e) cause the observed variation in Ti content and may represent either Ti-rich titanomagnetite or ilmenite. The former is evidenced by thermomagnetic measurements, whereas the latter cannot be detected, as T_C of ilmenite is bellow –200 °C (O'Reilly, 1984).

Interpretation of fabric patterns in the andesite domes

No tectonic fabric overprint was identified in the andesites and we thus interpret the magnetic fabrics as recording magmatic strain and possibly also flow patterns during dome growth. It has been well established that fabrics are poor recorders of the total strain history experienced by the flowing magma and instead they likely record only a late snapshot of strain before final solidification (e.g., Paterson et al., 1998; Launeau and Cruden, 1998; Cañón-Tapia and Castro, 2004; Féménias et al., 2004; Schultz et al., 2008). This may also apply to the three lava domes examined here, as the andesites are non-banded, thus mechanically quasi-isotropic, and they do not develop complex sets of superposed structures (e.g., Smith, 2002; Cioni and Funedda, 2005). Hence, in agreement with the generally low degree of anisotropy (Fig. 7), the measured fabrics are interpreted as recording only final increments of strain during magma freezing. These inferences are indirectly supported by theoretical models, predicting that fabrics in flowing low-viscosity Newtonian lava should form at every instant with periodically oscillating intensity and orientation (see Arbaret et al., 2000 for an overview). This mechanism would likely produce random fabric orientations in each dome. In contrast, magnetic foliations and lineations reported here define systematic dome-wide patterns, suggesting that they formed through straining of a stiff crystal-rich magma mush during relatively fast cooling and solidification.

In the following text, we thus assume that the principal AMS axes (k1, k2, k3) correspond to principal axes of instantaneous strain (Xi, Yi, Zi) of actively deforming magma which, however, do not have to coincide with the actual flow planes and lines (see Paterson et al., 1998 for detailed discussion). In particular, this applies for a divergent flow regime where the maximum (Xi) and minimum (Zi) instantaneous strain axes (lineation and foliation, respectively) are at a high angle to the flow planes and flow lines. Similarly, in simple shear flows expected in dikes and lavas, instantaneous strain axes are at variable angle to the flow planes and flow lines depending on the position along the velocity profile (see Ort et al., 2015 for overview and references).

The exception to the synmagmatic strain interpretation of the measured AMS could be Dome 3 where andesites on 7 stations contained larger proportions of late post-magmatic magnetite grains (gray symbols in Fig. 9a). However, magnetic foliations and lineations on these stations show regionally consistent orientations and fit well into general fabric trends in the dome (Fig. 9a, b). This may suggests a mimetic growth of late magnetite that only enhanced an earlier silicate-dominated flow fabric (e.g., Trindade et al., 2001).

Dome 1: a lava coulee

The pronounced arcuate, ~NW–SE elongated fabric pattern in Dome 1 (Fig. 9; Section 4.4.1) is comparable to ‘onion-skin’ fabrics in natural lava domes and analogue experiments (e.g., Fink, 1983; Fink and Pollard, 1983; Buisson and Merle, 2004; Hrouda et al., 2005; Závada et al., 2009; Bella Nké et al., 2014). Based on this comparison, we infer that the present-day level of exposure, characterized by moderately- to steeply-dipping magnetic foliations, represents a lower to middle section through a dome core (Fig. 10a). The inferred magnetic foliation and lineation trajectories indicate that the feeder conduit was located along the ring-fault, from which the lava flowed laterally in the SE direction towards the caldera interior (Fig. 10a). The observed arcuate fabric pattern may thus mimic a simple shear-dominated velocity gradient flow typical of lava and pyroclastic flows (e.g., Cañón-Tapia et al., 1995, 1996; Ort et al., 2003; Giordano et al., 2008). The prolate to neutral AMS ellipsoids close to the ring-fault indicate that the lava was horizontally stretched whereas the strongly oblate AMS ellipsoids near the southeastern dome margin suggest magma shortening as the flow front zone slowed down or even stopped (Fig. 10a). The elongated arcuate fabric pattern also indicates relatively long magma outflow and the Dome 1 can thus be interpreted as a lava coulee, i.e., a hybrid between a true dome and flow (e.g., Fink and Anderson, 2000). Accordingly, we envision that the lava flowed down a paleotopographic slope: was the crystal-rich, viscous andesite extruded on a flat bottom, it would rather accumulate near the vent.

Dome 2: a single lava dome

The narrow Dome 2 has magnetic foliations subparallel both to the nearby ring-fault and to the dome elongation. Similarly to Dome 1, the stretching component in the flowing lava was greater alongside the vent (prolate to neutral AMS ellipsoids) than near the outer dome margin (oblate AMS ellipsoids; Fig. 10b). On the other hand, the foliations suggest uniform ring-fault-perpendicular shortening across much of the dome. The shape of the dome and the magnetic fabrics are thus interpreted as reflecting only short lava transport which was arrested near the ring-fault and thus did not evolve into the arcuate flow pattern. By analogy with Dome 1, we infer a flat floor in this portion of the Štiavnica caldera (Fig. 10b).

Dome 3: a composite dome intruded by dikes

The Dome 3 exhibits a complex fabric pattern with two discordant fabrics (Type 1 and 2; Fig. 9a–c). We suggest that the Type 1 fabric is relatively earlier and reflects the bulk dome growth, characterized by homogeneous, dome-wide ~NE–SW to ~NNE–SSW shortening and mostly oblate AMS ellipsoids (Fig. 10c). This fabric is explained as resulting from magma flow from multiple linear fissure-vents in fractured caldera floor, which were oriented at a high angle to the ring-fault (Figs. 2, 10c). We envisage that as the magma extruded from the ~NW–SE to ~WNW–ESE-trending fissures, it pushed against the neighboring pulses and was shortened in a fissure-perpendicular direction (oblate AMS ellipsoids; Fig. 8b).

The prominent ~NNE–SSW-trending zones with the Type 2 fabric, which seem to cut across the Type 1 fabric, are interpreted as remnants of steep, ring-fault-parallel lava sheets (dikes) which intruded into the already emplaced and largely solidified dome. Potentially, these dikes may have also acted as feeders for some late lava domes and flows which either have been largely eroded or now overlap the northeastern segment of the ring-fault (Fig. 2). Magnetic lineations in the eastern conduit are compatible with moderately inclined to subvertical magma flow, whereas in the western conduit they indicate mostly ~N–S-oriented subhorizontal flow (Figs. 9a–c; 10d). Interestingly, the dikes are also spatially associated with domains of extrusive breccia (Fig. 4; Konečný et al., 1998a) which may represent relics of feeder walls. In a few other cases where the breccias occur near the dome margin (away from the dikes) they may be interpreted as autobreccias formed along the boundary between individual lava lobes (e.g., Fisher, 1960; Christiansen and Lipman, 1966; Manley and Fink, 1987).

Finally, we conclude that Dome 3 is composite and was also emplaced during the caldera collapse, but its growth was largely controlled by a network of brittle fractures in the caldera floor.

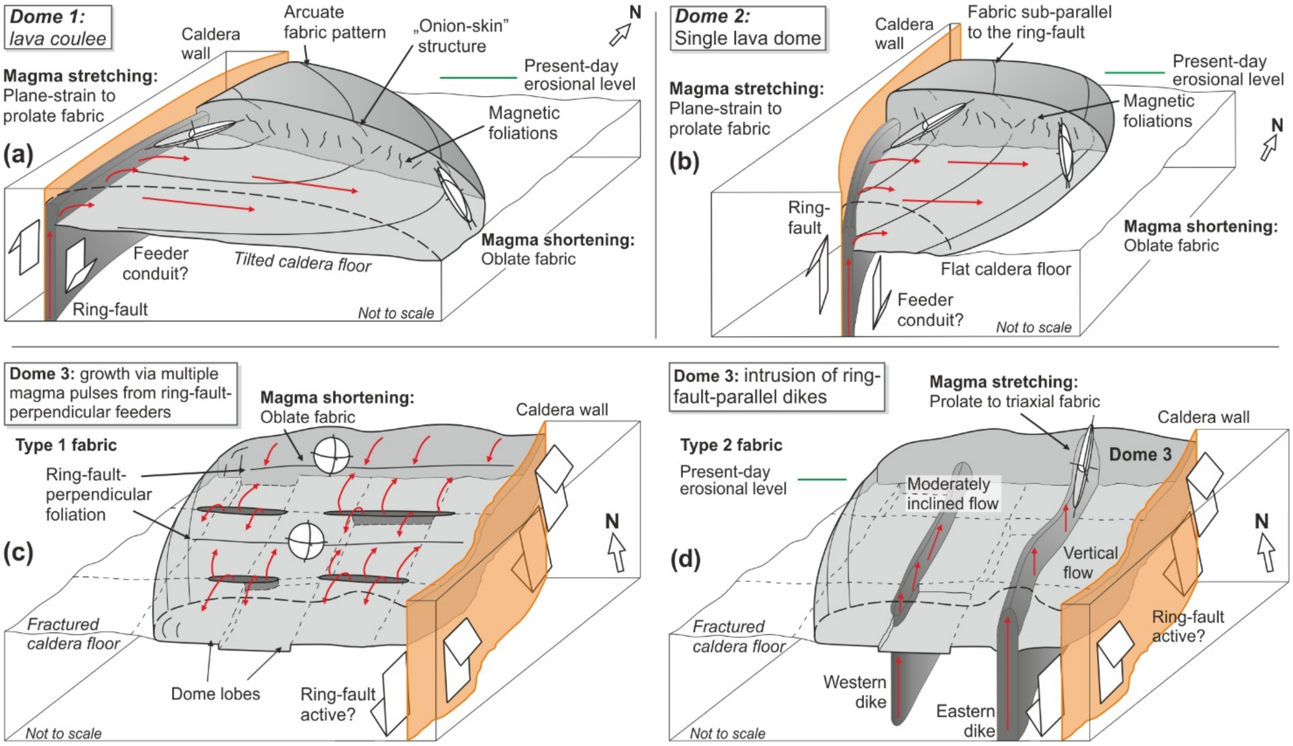

Fig. 10. Interpretative blockdiagrams to explain the measured fabrics in Domes 1–3. The fabric patterns in each dome (a–d) are interpreted as representing different magma flow paths, influenced by the original paleotopography and geometry of feeder conduits. See the text for discussion.

General implications: relating fabric and flow patterns in syn-collapse extrusive domes to caldera collapse mechanisms

Field relations suggest that emplacement of the three intra-caldera lava domes were broadly coeval with the caldera collapse (Lexa et al., 1999; Chernyshev et al., 2013). Given the close spatial association of the lava domes with the caldera ring-fault and their internal fabric patterns indicating outflow of magma from the lateral ring-fault feeders (Domes 1 and 2) or from the fractured caldera floor, we propose that the different flow patterns in each dome may be explained as reflecting different modes of the caldera collapse. (1) The long outflow of Dome 1 could imply a trap-door mode where andesite lava flowed down the hinged caldera floor (Fig. 1). (2) The short outflow of the Dome 2 indicates a flat caldera floor in the immediate vicinity of the ring-fault and thus suggests a piston collapse (Fig. 11). (3) The two-stage evolution of Dome 3 is explained as resulting from initial exogenous growth of a composite lava dome from multiple ring-fault-perpendicular feeder fractures, followed by intrusion of ring-fault-parallel dikes. The complex dome growth thus records a piecemeal caldera collapse where the caldera floor was cross cut by two nearly orthogonal sets of fractures (Fig. 11).

Were the above inferences correct, some important additional questions arise: (1) what are the temporal relations between dome emplacement and caldera collapse and (2) what are the rates of dome growth with respect to caldera collapse? The reported time spans of lava dome growth range from weeks to several years (e.g., Swanson et al., 1987; Watts et al., 2002; Harris et al., 2003; Diefenbach et al., 2013). Although only a few small-magnitude caldera collapses were directly monitored, it seems that rates of caldera collapse are faster and the collapses occur within a few days (e.g., Geshi et al., 2001; Michon et al., 2007). On the other hand, the proposed models for large calderas suggest that their growth may also have been incremental (e.g., Walker, 1984; Skilling, 1993), and thus extending over larger time spans. In summary, the caldera collapse and collapse-triggered extrusion of lava domes may still be closely temporally and kinematically coupled: sudden caldera collapse may generate overpressure in the underlying chamber which, in turn, triggers slower dome extrusion.

In the absence of high-precision radiometric ages, we may only speculate that Domes 1–3 were emplaced either simultaneously as a direct response to the caldera collapse or that they were emplaced successively, shortly after the collapse. Assuming that the former hypothesis is valid, the Štiavnica caldera would have then collapsed by three different collapse modes operating in different parts of the caldera. Alternatively, recent models (e.g., Acocella, 2006, 2007) suggest that the end-member caldera collapse modes (i.e., downsag, funnel, piston, piecemeal, and trapdoor; Lipman, 1997; Cole et al., 2005) rather represent frozen snapshots of a continuous caldera evolution (Fig. 11). Hence, we favor the latter hypothesis and envision that the Štiavnica caldera has successively gone through most of the collapse stages: Dome 2 is the oldest, recording initial piston collapse, followed by Dome 1 reflecting trap-door collapse and, finally, by the youngest Dome 3 the emplacement of which was controlled by piecemeal collapse (Fig. 11).

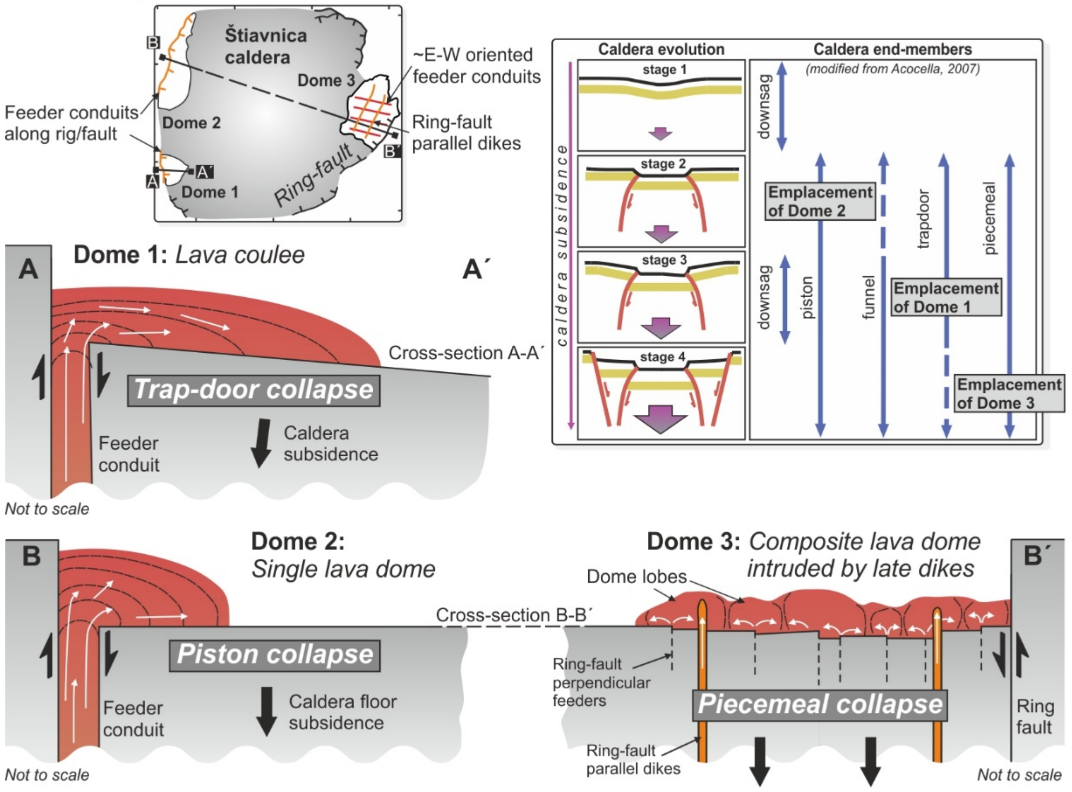

Fig. 11. Interpretative cross-sections through parts of the Štiavnica caldera showing the various inferred modes of dome growth controlled by different mechanisms of caldera collapse. The dome growth modes are interpreted as recording transient stages in a continuous evolution of the caldera. See the text for discussion. Right top panel modified after Acocella (2007).

CONCLUSIONS

The intra-caldera andesitic Domes 1–3 of the Štiavnica volcano–plutonic complex exhibit different magnetic fabric and inferred magma flow patterns. The internal structure of the domes is interpreted as recording various mechanisms of their growth and we also suggest that they were coeval with and directly linked to various modes of caldera collapse. Dome 1 was fed by a conduit located along the ring-fault and is interpreted as a lava coulee which flowed down the hinged floor of a trap-door caldera. Dome 2 represents a single elongated, ring-fault-parallel dome with short lava outflow emplaced on a flat floor during piston collapse. The most complex Dome 3 was fed by multiple ~NW–SE to ~WNW–ESE linear fissures (at a high angle to the ring fault) in the collapsing caldera floor. After this main stage of dome growth, narrow ring-fault-parallel dikes intruded into the largely solidified dome, representing potential feeders for younger lava domes and flows. Finally, we envision that all the three domes were emplaced successively and record snapshots of different stages of the caldera evolution from piston (Dome 2) through trap-door (Dome 1) to piecemeal collapse (Dome 3).

ACKNOWLEDGEMENTS

František Hrouda, Martin Chadima, Ondrej Lexa, Prokop Závada, and Jakub Trubač are thanked for valuable discussions and Valerio Acocella for providing part of the last figure. Matěj Machek, Jaroslava Hajná, and Šárka Kubínová are acknowledged for technical assistance. Funding was provided by the Grant Agency of the Czech Republic through grant P210/12/1385 (to Jiří Žák). This study is part of the Ph.D. research of Filip Tomek. We appreciate support from the Charles University projects PRVOUK P44 and SVV261203 and by the Academy of Sciences of the Czech Republic Research Plan RVO 67985831.

REFERENCES

Acocella, V., 2007. Understanding caldera structure and development: an overview of analogue models compared to natural calderas. Earth Sci. Rev. 85, 125–160. doi: 10.1016/j.earscirev.2007.08.004.

Acocella, V., 2006. Caldera types: how end-members relate to evolutionary stages of collapse. Geophys. Res. Lett. 33, L18314, doi: 10.1029/2006GL027434.

Anderson, S.W., Fink, J.H., 1992. Crease structures: indicators of emplacement rates and surface stress regimes of lava flows. Geol. Soc. Am. Bull. 104, 615–625, doi: 10.1130/0016-7606(1992)104<0615:CSIOER>2.3.CO;2.

Arbaret, L., Fernandez, A., Ježek, J., Ildefonse, B., Launeau, P., Diot, H., 2000. Analogue and numerical modelling of shape fabrics: application to strain and flow determination in magmas. Trans. Roy. Soc. Edin. Earth Sci. 90, 97–109. doi: 10.1130/0-8137-2350-7.97.

Ashwell, P. A., Kennedy, B.M., Gravley, D.M., von Aulock, F.W., Cole, J.W., 2013. Insights into caldera and regional structures and magma body distribution from lava domes at Rotorua Caldera, New Zealand. J. Volcanol. Geotherm. Res. 258, 187–202. doi: 10.1016/j.jvolgeores.2013.04.014.

Barmin, A., Melnik, O., Sparks, R.S.J., 2002. Periodic behavior in lava dome eruptions. Earth Planet. Sci. Lett. 199, 173–184. doi: 10.1016/S0012-821X(02)00557-5.

Bella Nké, B.E., Njanko, T., Kwékam, M., Njonfang, E., Naba, S., Tcheumenak, K.J., Gountié, M., Rochette, P., Nédélec, A., 2014. Structural study of the Foréké-Dschang trachytic dome (Mount Bambouto, West Cameroon): an anisotropy of magnetic susceptibility (AMS) approach. J. African Earth Sci. 95, 63–76. doi: 10.1016/j.jafrearsci.2014.02.014.

Bonadonna, C., Connor, C.B., Houghton, B.F., Connor, L., Byrne, M., Laing, A., Hincks, T.K., 2005. Probabilistic modeling of tephra dispersal: hazard assessment of a multiphase rhyolitic eruption at Tarawera, New Zealand. J. Geophys. Res. 110, 1–21. doi: 10.1029/2003JB002896.

Borradaile, G.J., Jackson, M., 2004. Anisotropy of magnetic susceptibility (AMS): magnetic petrofabrics of deformed rocks. In: Martín-Hernández, F., Luneburg, C.M., Aubourg, C., Jackson, M. (Eds.), Magnetic Fabric: Methods and Applications. Geol. Soc., London, Spec. Publ., 238, pp. 299–360. doi: 10.1144/GSL.SP.2004.238.01.18.

Borradaile, G.J., Jackson, M., 2010. Structural geology, petrofabrics and magnetic fabrics (AMS, AARM, AIRM). J. Struct. Geol. 32, 1519–1551. doi: 10.1016/j.jsg.2009.09.006.

Bouchez, J.L., 1997. Granite is never isotropic: an introduction to AMS studies of granitic rocks. In: Bouchez, J.L., Hutton, D.H.W., Stephens, W.E. (Eds.), Granite: From Segregation of Melt to Emplacement Fabrics. Springer Netherlands, pp. 95–112. doi: 10.1007/978-94-017-1717-5_6.

Bourdier, J.L., Pratomo, I., Thouret, J.C., Boudon, G., Vincent, P.M., 1997. Observations, stratigraphy and eruptive processes of the 1990 eruption of Kelut volcano, Indonesia. J. Volcanol. Geotherm. Res. 79, 181–203. doi: 10.1016/S0377-0273(97)00031-0.

Browne, B.L., Gardner, J.E., 2006. The influence of magma ascent path on the texture, mineralogy, and formation of hornblende reaction rims. Earth Planet. Sci. Lett. 246, 161–176. Doi: 10.1016/j.epsl.2006.05.006.

Buisson, C., Merle, O., 2002. Experiments on internal strain in lava dome cross sections. Bull. Volcanol. 64, 363–371. doi: 10.1007/s00445-002-0213-6.

Buisson, C., Merle, O., 2004. Numerical simulation of strain within lava domes. J. Struct. Geol. 26, 847–853. doi: 10.1016/j.jsg.2003.11.017.

Cañón-Tapia, E., 2004. Anisotropy of magnetic susceptibility of lava flows and dykes: a historical account. In: Martín-Hernández, F., Luneburg, C.M., Aubourg, C., Jackson, M. (Eds.), Magnetic Fabric: Methods and Applications. Geol. Soc., London, Spec. Publ., 238, pp. 205–225. doi: 10.1144/GSL.SP.2004.238.01.14.

Cañón-Tapia, E., 2005. Uses of anisotropy of magnetic susceptibility in the study of emplacement processes of lava flows. In: Manga, M., Ventura. G. (Eds.), Kinematics and dynamics of lava flows. Geol. Soc. Am. Spec. Pap. 396, pp. 29–46. doi: 10.1130/0-8137-2396-5.29.

Cañón-Tapia, E., Mendoza-Borunda, R., 2014. Magnetic petrofabric of igneous rocks: lessons from pyroclastic density current deposits and obsidians. J. Volcanol. Geotherm. Res. 289, 151–169. doi: 10.1016/j.jvolgeores.2014.11.006.

Cañón-Tapia, E., Walker, G.P.L., Herrero-Bervera, E., 1995. Magnetic fabric and flow direction in basaltic Pahoehoe lava of Xitle volcano, Mexico. J. Volcanol. Geotherm. Res. 65, 249–263. doi: 10.1016/0377-0273(94)00110-3.

Cañón-Tapia, E., Walker, G.P.L., Herrero-Bervera, E., 1996. The internal structure of lava flows – insights from AMS measurements I: near-vent a'a. J. Volcanol. Geotherm. Res. 0273. doi: doi: 10.1016/0377-0273(95)00050-X.

Cañón-Tapia, E., Walker, G.P.L., Herrero-Bervera, E., 1997. The internal structure of lava flows – insights from AMS measurements II: Hawaiian pahoehoe, toothpaste lava and 'a'ā. J. Volcanol. Geotherm. Res. 76, 19–46. doi: 10.1016/S0377-0273(96)00073-X.

Castro, J., Manga, M., Cashman, K., 2002. Dynamics of obsidian flows inferred from microstructures: insights from microlite preferred orientations. Earth Planet. Sci. Lett. 199, 211–226. doi: 10.1016/S0012-821X(02)00559-9.

Cioni, R., Funedda, A., 2005. Structural geology of crystal-rich, silicic lava flows: a case study from San Pietro Island (Sardinia, Italy). In: Manga, M., Ventura. G. (Eds.), Kinematics and Dynamics of Lava Flows. Geol. Soc. Am. Spec. Pap. 396, pp. 1–14. doi: 10.1130/0-8137-2396-5.1.

Clynne, M.A., 1990. Stratigraphic, lithologic, and major element geochemical constraints on magmatic evolution at Lassen Volcanic Center, California. J. Geophys. Res. 95, 19651–19669. doi: 10.1029/JB095iB12p19651.

Cole, J., Milner, D., Spinks, K., 2005. Calderas and caldera structures: a review. Earth Sci. Rev. 69, 1–26. doi: 10.1016/j.earscirev.2004.06.004.

De Angelis, S.H., Larsen, J., Coombs, M., 2013. Pre-eruptive magmatic conditions at augustine volcano, Alaska, 2006: evidence from amphibole geochemistry and textures. J. Petrol. 54, 1939–1961. doi: 10.1093/petrology/egt037.

Devine, J.D., Murphy, M.D., Rutherford, M.J., Barclay, J., Sparks, R.S.J., Carroll, M.R., Young, S.R., Gardner, J.E., 1998. Petrologic evidence for pre-eruptive pressure-temperature conditions, and recent reheating, of andesitic magma erupting at the Soufriere Hills Volcano, Montserrat, W.I. Geophys. Res. Lett. 25, 3669-3672. doi: 10.1029/98GL01330.

Diefenbach, A.K., Bull, K.F., Wessels, R.L., McGimsey, R.G., 2013. Photogrammetric monitoring of lava dome growth during the 2009 eruption of Redoubt Volcano. J. Volcanol. Geotherm. Res. 259, 308–316. doi: doi: 10.1016/j.jvolgeores.2011.12.009.

Féménias, O., Diot, H., Berza, T., Gauffriau, A., Demaiffe, D., 2004. Asymmetrical to symmetrical magnetic fabric of dikes: paleo-flow orientations and paleo-stresses recorded on feeder-bodies from the Motru Dike Swarm (Romania). J. Struct. Geol., 26, 1401–1418. doi: 10.1016/j.jsg.2003.12.003.

Fink, J.H, 1980. Surface folding and viscosity of rhyolite flows. Geology 8, 250–254. doi: 10.1130/0091-7613(1980)8<250:SFAVOR>2.0.CO;2.

Fink, J.H, 1983. Structure and emplacement of a rhyolitic obsidian flow: Little Glass Mountain, Medicine Lake Highland, northern California. Geol. Soc. Am. Bull. 94, 362–380. doi:10.1130/0016-7606(1983)94<362:SAEOAR>2.0.CO;2.

Fink, J.H., 1990. Lava Flows and Domes: Emplacement Mechanisms and Hazard Implications. IAVCEI Proc. Volc, 2., Springer-Verlag, 249 p.

Fink, J.H., Pollard, D.D., 1983. Structural evidence for dikes beneath silicic domes, Medicine Lake Highland Volcano, California (USA). Geology 11, 458–461. doi: 10.1130/0091-7613(1983)11<458:SEFDBS>2.0.CO;2.

Fink, J.H., Griffiths, R.W., 1998. Morphology, eruption rates, and rheology of lava domes: insights from laboratory models. J. Geophys. Res. 103, 527–545. doi: 10.1029/97JB02838.

Fink, J.H., Anderson, S.W., 2000. Lava domes and coulees. In: Sigurdsson, H. (Ed.), Encyclopedia of Volcanoes. Academic Press, pp. 307–319.

Fink, J.H., Malin, M.C., Anderson, S.W., 1990. Intrusive and extrusive growth of the Mount St. Helens lava dome. Nature 348, 435–437. doi: 10.1038/348435a0.

Fisher, R.V., 1960. Classification of volcanic breccias. Geol. Soc. Am. Bull. 71, 973–982. doi: 10.1130/0016-7606(1960)71[973:COVB]2.0.CO;2 .

Geshi, N., Shimano, T., Chiba, T., Nakada, S., 2001. Caldera collapse during the 2000 eruption of Miyakejima Volcano, Japan. Bull. Volcanol. 64, 55–68. doi: 10.1007/s00445-001-0184-z.

Giordano, G., Porreca, M., Musacchio, P., Mattei, M., 2008. The Holocene Secche di Lazzaro phreatomagmatic succession (Stromboli, Italy): evidence of pyroclastic density current origin deduced by facies analysis and AMS flow directions. Bull. Volcanol. 70, 1221–1236. doi: 10.1007/s00445-008-0198-x.

Gonnermann, H.M., Manga, M., 2005. Flow banding in obsidian: a record of evolving textural heterogeneity during magma deformation. Earth Planet. Sci. Lett. 236, 135–147. doi: 10.1016/j.epsl.2005.04.031.

Hale, A.J., 2008. Lava dome growth and evolution with an independently deformable talus. Geophys. J. Int. 174, 391–417. doi: 10.1111/j.1365-246X.2008.03806.x.

Harangi, S., Downes, H., Thirlwall, M., Gméling, K., Gmeling, K., 2007. Geochemistry, petrogenesis and geodynamic relationships of Miocene calc-alkaline volcanic rocks in the Western Carpathian Arc, eastern Central Europe. J. Petrol. 48 , 2261–2287. doi: 10.1093/petrology/egm059.

Harris, A.J.L., Rose, W.I., Flynn, L.P., 2003. Temporal trends in lava dome extrusion at Santiaguito 1922–2000. Bull. Volcanol. 65, 77–89. doi: 10.1007/s00445-002-0243-0.

Hetényi, G., Taisne, B., Garel, F., Médard, É., Bosshard, S., Mattsson, H.B., 2012. Scales of columnar jointing in igneous rocks: field measurements and controlling factors. Bull. Volcanol. 74, 457–482. doi: 10.1007/s00445-011-0534-4.

Hrouda, F., 1982. Magnetic anisotropy of rocks and its application in geology and geophysics. Geophys. Surv. 5, 37–82. doi: 10.1007/BF01450244.

Hrouda, F., 2003. Indices for numerical characterization of the alteration processes of magnetic minerals taking place during investigation of temperature variation of magnetic susceptibility. Stud. Geophys. Geod. 47, 847–861. doi: 10.1023/A:1026398920172.

Hrouda, F., Kahan, Š., 1991. The magnetic fabric relationship between sedimentary and basement nappes in the High Tatra Mountains, N. Slovakia. J. Struct. Geol. 13, 431–442. doi: doi: 10.1016/0191-8141(91)90016-C.

Hrouda, F., Jelínek, V., Zapletal, K., 1997. Refined technique for susceptibility resolution into ferromagnetic and paramagnetic components based on susceptibility temperature-variation measurement. Geophys. J. Int. 129, 715–719. doi: 10.1111/j.1365-246X.1997.tb04506.x.

Hrouda, F., Chlupáčová, M., Schulmann, K., Šmíd, J., Závada, P., 2005. On the effect of lava viscosity on the magnetic fabric intensity in alkaline volcanic rocks. Stud. Geophys. Geod. 49, 191–212. doi: 10.1007/s11200-005-0005-5.

Chernyshev, I.V., Konečný, V., Lexa, J., Kovalenker, V.A., Jeleň, S., Lebedev, V.A., Goltsman, Y.V., 2013. K–Ar and Rb–Sr geochronology and evolution of the Štiavnica Stratovolcano (Central Slovakia). Geol. Carpath. 64, 1–25. doi: 10.2478/geoca-2013-0023.

Christiansen, R.L., Lipman, P.W., 1966. Emplacement and thermal history of a rhyolite lava flow near Fortymile Canyon, southern Nevada. Geol. Soc. Am. Bull. 77, 671–684. doi: 10.1130/0016-7606(1966)77[671:EATHOA]2.0.CO;2.

Jaupart, C., Allègre, C.J., 1991. Gas content, eruption rate and instabilities of eruption regime in silicic volcanoes. Earth Planet. Sci. Lett. 102, 413–429. doi: 10.1016/0012-821X(91)90032-D.

Jelínek, V., 1981. Characterization of the magnetic fabric of rocks. Tectonophysics 79, T63–T67. doi: doi: 10.1016/0040-1951(81)90110-4.

Koděra, P., Lexa, J., Rankin, A.H., Fallick, A.E., 2004. Fluid evolution in a subvolcanic granodiorite pluton related to Fe and Pb–Zn mineralization, Banská Štiavnica ore district, Slovakia. Econ. Geol. 99, 1745–1770.

Koděra, P., Lexa, J., Rankin, A.H., Fallick, A.E., 2005. Epithermal gold veins in a caldera setting: Banská Hodruša, Slovakia. Mineral. Depos. 39, 921–943. doi: 10.1007/s00126-004-0449-5.

Koděra, P., Lexa, J., Fallick, A.E., 2010. Formation of the Vysoká–Zlatno Cu–Au skarn–porphyry deposit, Slovakia. Mineral. Depos. 45, 817–843. doi: 10.1007/s00126-010-0304-9.

Konečný, P., Lexa, J., Hostričová, V., 1995. The Central Slovakia Neogene volcanic field. Acta Vulcanol. 7, 63–78.

Konečný, V., 1971. Evolutionary stages of the Banská Stiavnica caldera and its post-volcanic structures. Bull. Volcanol. 35, 95–116. doi: 10.1007/BF02596810.

Konečný, V., Lexa, J., Halouzka, R., Dublan, L., Šimon, L., Stolár, M., Nagy, A., Polák, M., Vozár, J., Havrila, M., Pristaš, J., 1998a. Geologic map of Štiavnické vrchy and Pohronský Inovec mountain ranges 1:50,000. State Geological Institute of Dionýz Štúr, Bratislava.

Konečný, V., Lexa, J., Halouzka, R., Hók, J., Vozár, J., Dublan, L., Nagy, A., Šimon, L., Havrila, M., Ivanička, J., Hojstričová, V., Mihaliková, A., Vozárová, A., Konečný, P., Kováčiková, M., Filo, M., Marcin, D., Klukanová, A., Liščák, P., Žáková 1998b. Explanations to the geological map of the Štiavnické vrchy and Pohronský Inovec mountain ranges (Štiavnica stratovolcano). State Geological Institute of Dionýz Štúr, Bratislava, 473 p.

Konečný, V., Kováč, M., Lexa, J., Šefara, J., 2002. Neogene evolution of the Carpatho–Pannonian region: an interplay of subduction and backarc diapiric uprise in the mantle. EGU Stephan Mueller Spec. Publ. Ser. 1, 105–123.

Kovalenker, V.A., Naumov, V.B., Prokofev, V.Y., Jelen, S., Gaber, M., 2006. Compositions of magmatic melts and evolution of mineral-forming fluids in the Banská Stiavnica epithermal Au–Ag–Pb–Zn deposit, Slovakia: a study of inclusions in minerals. Geochem. Int. 44, 118–136. doi: 10.1134/S0016702906020029.

Krása, D., Herrero-Bervera, E., 2005. Alteration induced changes of magnetic fabric as exemplified by dykes of the Koolau volcanic range. Earth Planet. Sci. Lett. 240, 445–453. doi: 10.1016/j.epsl.2005.09.028.

Lexa, J., Štohl, J., Konečný, V., 1999. The Banská Štiavnica ore district: relationship between metallogenetic processes and the geological evolution of a stratovolcano. Mineral. Depos. 34, 639–654. doi: 10.1007/s001260050225

Lexa, J., Seghedi, I., Németh, K., Szakács, A., Konečný, V., Pécskay, Z., Fülöp, A., Kovács, M., 2010. Neogene–Quaternary Volcanic forms in the Carpathian–Pannonian Region: a review. Cent. Eur. J. Geosci. 2, 207–270. doi: 10.2478/v10085-010-0024-5.

Lipman, P.W., 1997. Subsidence of ash-flow calderas: relation to caldera size and magma-chamber geometry. Bull. Volcanol. 59, 198–218. doi: 10.1007/s004450050186.

Loock, S., Diot, H., Van Wyk de Vries, B., Launeau, P., Merle, O., Vadeboin, F., Petronis, M.S., 2008. Lava flow internal structure found from AMS and textural data: an example in methodology from the Chaîne des Puys, France. J. Volcanol. Geotherm. Res. 177, 1092–1104. doi: 10.1016/j.jvolgeores.2008.08.017.

Launeau, P., Cruden, A.R., 1998. Magmatic fabric acquisition in a syenite: results of a combined anisotropy of magnetic susceptibility and image analysis study. J. Geophys. Res. 103, 5067–5089. doi: 10.1029/97JB02670.

Maeno, F., Taniguchi, H., 2006. Silicic lava dome growth in the 1934–1935 Showa Iwo-jima eruption, Kikai caldera, south of Kyushu, Japan. Bull. Volcanol. 68, 673–688. doi: 10.1007/s00445-005-0042-5.

Major, J.J., Dzurisin, D., Schilling, S.P., Poland, M.P., 2009. Monitoring lava-dome growth during the 2004–2008 Mount St. Helens, Washington, eruption using oblique terrestrial photography. Earth Planet. Sci. Lett. 286, 243–254. doi: 10.1016/j.epsl.2009.06.034.

Manley, C.R., Fink, J.H., 1987. Internal textures of rhyolite flows as revealed by research drilling. Geology 15, 549–552. doi: 10.1130/0091-7613(1987)15<549:ITORFA>2.0.CO;2.

Merle, O., 1998. Internal strain within lava flows from analogue modelling. J. Volcanol. Geotherm. Res. 81, 189–206. doi: 10.1016/S0377-0273(98)00009-2.

Michon, L., Staudacher, T., Ferrazzini, V., Bachèlery, P., Marti, J., 2007. April 2007 collapse of Piton de la Fournaise: a new example of caldera formation. Geophys. Res. Lett. 34, L21301. doi: 10.1029/2007GL031248.

Nagata, T., 1962. Rock Magnetism. Maruzen, Tokyo.

Nemčok, M., Konečný, P., Lexa, O., 2000. Calculation of tectonic, magmatic, and residual stress in the Štiavnica stratovolcano, Western Carpathians: implications for mineral precipitation paths. Geol. Carpath. 51, 19–36.

Ogburn, S.E., Loughlin, S.C., Calder, E.S., 2015. The association of lava dome growth with major explosive activity (VEI□≥□4): DomeHaz, a global dataset. Bull. Volcanol. 77, 40. doi: 10.1007/s00445-015-0919-x.

Ort, M.H., Orsi, G., Pappalardo, L., Fisher, R.V., 2003. Anisotropy of magnetic susceptibility studies of depositional processes in the Campanian Ignimbrite, Italy. Bull. Volcanol. 65, 55–72. doi: 10.1007/s00445-002-0241-2.

Ort, M.H., Porreca, M., Geissman, J.W., 2015. The use of palaeomagnetism and rock magnetism to understand volcanic processes: introduction. In: Ort, M.H., Porreca, M., Geissman, J.W. (Eds.), The Use of Palaeomagnetism and Rock Magnetism to Understand Volcanic Processes. Geol. Soc., London, Spec. Publ. 396, pp. 1–11. doi: 10.1144/SP396.17.

O'Reilly, W., 1984. Rock and mineral magnetism. Blackie and Son Ltd. doi:10.1007/978-1-4684-8468-7.

Palmer, H.C., MacDonald, W.D., Grommé, C.S., Ellwood, B.B., 1996. Magnetic properties and emplacement of the Bishop tuff, California. Bull. Volcanol. 58, 101–116. doi: 10.1007/s004450050129 .

Paterson, S.R., Fowler, T.K., Schmidt, K.L., Yoshinobu, A.S., Yuan, E.S., Miller, R.B., 1998. Interpreting magmatic fabric patterns in plutons. Lithos 44, 53–82. doi: 10.1016/S0024-4937(98)00022-X

Pécskay, Z., Lexa, J., Szakacs, A., Seghedi, I., Balogh, K., Konečný, V., Zelenka, T., Kovács, M., Poka, T., Fülöp, A., Márton, E., Panaiotu, C., Cvetković, V., 2006. Geochronology of Neogene magmatism in the Carpathian arc and intra-Carpathian area. Geol. Carpath. 57, 511–530.

Petronis, M.S., Delcamp, A., van Wyk de Vries, B., 2013. Magma emplacement into the Lemptégy scoria cone (Chaîne Des Puys, France) explored with structural, anisotropy of magnetic susceptibility, and paleomagnetic data. Bull. Volcanol. 75, 753. doi: 10.1007/s00445-013-0753-y.

Petrovský, E.D., Kapička, A., 2006. On determination of the Curie point from thermomagnetic curves. J. Geophys. Res. 111, 1–10. doi: 10.1029/2006JB004507.

Philpotts, A.R., Philpotts, D.E. 2007. Upward and downward flow in a camptonite dike as recorded by deformed vesicles and the anisotropy of magnetic susceptibility (AMS). J. Volcanol. Geotherm. Res. 161, 81–94. doi: 10.1016/j.jvolgeores.2006.11.006.

Plašienka, D., 2003. Development of basement-involved fold and thrust structures exemplified by the Tatric–Fatric–Veporic nappe system of the Western Carpathians (Slovakia). Geodin. Acta 16, 21–38. doi: doi: 10.1016/S0985-3111(02)00003-7.

Plechov, P.Y., Tsai, A.E., Shcherbakov, V.D., Dirksen, O.V., 2008. Opacitization conditions of hornblende in Bezymyannyi volcano andesites (March 30, 1956 eruption). Petrology 16, 19–35. doi: 10.1007/s11495-008-1002-4.

Ramsey, M.S., Fink, J.H., 1999. Estimating silicic lava vesicularity with thermal remote sensing: a new technique for volcanic mapping and monitoring. Bull. Volcanol. 61, 32–39. doi: 10.1007/s004450050260.

Rutherford, M.J., Devine, J.D., 2003. Magmatic conditions and magma ascent as indicated by hornblende phase equilibria and reactions in the 1995–2002 Soufriére Hills magma. J. Petrol. 44, 1433–1454. doi: 10.1093/petrology/44.8.1433.

Schultz, R.A, Mège, D., Diot, H., 2008. Emplacement conditions of igneous dikes in Ethiopian Traps. J. Volcanol. Geotherm. Res. 178, 683–692. doi: 10.1016/j.jvolgeores.2008.08.012.

Seaman, S.J., McIntosh, W.C., Geissman, J.W., Williams, M.L., Elston, W.E., 1991. Magnetic fabrics of the Bloodgood Canyon and Shelley Peak Tuffs, southwestern New Mexico: implications for emplacement and alteration processes. Bull. Volcanol. 53, 460–476. doi: 10.1007/BF00258185.

Sieh, K., Bursik, M., 1986. Most recent eruption of the Mono Craters, eastern central California. J. Geophys. Res. 91, 12539–12571. doi: 10.1029/JB091iB12p12539.

Silva, P.F., Henry, B., Marques, F.O., Font, E., Mateus, A., Vegas, R.R., Miranda, J.M., Palomino, R., Palencia-Ortas, A.,

2008. Magma flow, exsolution processes and rock metasomatism in the Great Messejana-Plasencia dyke (Iberian Peninsula). Geophys. J. Int. 175, 806–824. doi: 10.1111/j.1365-246X.2008.03920.x.

Skilling, I.P., 1993. Incremental caldera collapse of Suswa volcano, Gregory Rift Valley, Kenya. J. Geol. Soc. London. 150, 885–896. doi: 10.1144/gsjgs.150.5.088.

Smith, J.V, Houston, E.C., 1994. Folds produced by gravity spreading of a banded rhyolite lava flow. J. Volcanol. Geotherm. Res. 63, 89–94. doi: 10.1016/0377-0273(94)90019-1.

Sparks, R.S.J., 1997. Causes and consequences of pressurisation in lava dome eruptions. Earth Planet. Sci. Lett. 150, 177–189. doi: 10.1016/S0012-821X(97)00109-X.

Swanson, D.A., Dzurisin, D., Holcomb, R.T., Iwatsubo, E.Y., Chadwick, W.W., Casadevall, Ewert, J.W., Heliker, C.C., 1987. Growth of the lava dome at Mount St. Helens, Washington, (USA), 1981–1983. In: Fink, J.H. (Ed.), The Emplacement of Silicic Domes and Lava Flows. Geol. Soc. Am. Spec. Pap., 212, 1–16. doi: 10.1130/SPE212-p1.

Tarling, D., Hrouda, F., 1993. Magnetic Anisotropy of Rocks. Chapman & Hall.

Trindade, R., Bouchez, J., Bolle, O., Nédélec, A., Peschler, A., Poitrasson, F., 2001. Secondary fabrics revealed by remanence anisotropy: methodological study and examples from plutonic rocks. Geophys. J. Int. 147, 310–318. doi: 10.1029/2001GL013218.

Voight, B., Hoblitt, R.P., Clarke, A.B., Lockhart, A.B., Miller, A.D., Lynch, L., McMahon, J., 1998. Remarkable cyclic ground deformation monitored in real-time on Montserrat, and its use in eruption forecasting. Geophys. Res. Lett. 25, 3405–3408. doi: 10.1029/98GL01160.

Voight, B., Linde, A.T., Sacks, I.S., Mattioli, G.S., Sparks, R.S.J., Elsworth, D., Hidayat, D., Malin, P.E., Shalev, E., Widiwijayanti, C., Young, S.R., Bass, V., Clarke, A., Dunkley, P., Johnston, W., McWhorter, N., Neuberg, J., Williams, P., 2006. Unprecedented pressure increase in deep magma reservoir triggered by lava-dome collapse. Geophys. Res. Lett. 33, 8–11. doi: 10.1029/2005GL024870.

Wadge, G., Herd, R., Ryan, G., Calder, E.S., Komorowski, J.C., 2010. Lava production at Soufriére Hills Volcano, Montserrat: 1995–2009. Geophys. Res. Lett. 37, 1–5. doi: 10.1029/2009GL041466.

Walker, G.P.L., 1984. Downsag calderas, ring faults, caldera sizes, and incremental caldera growth. J. Geophys. Res. 89, 8407–8416. doi: 10.1029/JB089iB10p08407.

Watts, R.B., Herd, R.A., Sparks, R.S.J., Young, S.R., 2002. Growth patterns and emplacement of the andesitic lava dome at Soufriére Hills volcano, Montserrat. In: Druitt, T.H., Kokelaar, B.P. (Eds.), The eruption of Soufrière Hills volcano, Montserrat, from 1995-1999. Geol. Soc. London Mem. 21, 115–152. doi: 10.1144/GSL.MEM.2002.021.01.06.

Whitney, D.L., Evans, B.W., 2010. Abbreviations for names of rock-forming minerals. Am. Mineral. 95, 185–187. doi: 10.2138/am.2010.3371.

Závada, P., Kratinová, Z., Kusbach, V., Schulmann, K., 2009. Internal fabric development in complex lava domes. Tectonophysics 466, 101–113. doi: 10.1016/j.tecto.2008.07.005.

Chapter *2:*

MAGMA FLOW PATHS AND STRAIN PATTERNS IN MAGMA CHAMBERS GROWING BY FLOOR SUBSIDENCE: A MODEL BASED ON MAGNETIC FABRIC STUDY OF SHALLOW-LEVEL PLUTONS IN THE ŠTIAVNICA VOLCANO–PLUTONIC COMPLEX, WESTERN CARPATHIANS

by Filip Tomek, Jiří Žák, and Martin Chadima

a paper published in **Bulletin of Volcanology** (2014) 76: article No. 873

(additional information are listed in supplementary material part 1 and appendix item 2)

KEY WORDS

◇ Anisotropy of magnetic susceptibility (AMS)

◇ Caldera

◇ Intrusive strain

◇ Magma emplacement

◇ Pluton floor subsidence

◇ Stratovolcano

MAGMA FLOW PATHS AND STRAIN PATTERNS IN MAGMA CHAMBERS GROWING BY FLOOR SUBSIDENCE: A MODEL BASED ON MAGNETIC FABRIC STUDY OF SHALLOW-LEVEL PLUTONS IN THE ŠTIAVNICA VOLCANO–PLUTONIC COMPLEX, WESTERN CARPATHIANS

ABSTRACT

The Miocene Štiavnica volcano–plutonic complex, Western Carpathians, exposes two nearly coeval intra-caldera plutons, their roof (basement of a stratovolcano), and associated volcanic rocks. The complex thus provides insights into mechanisms of magma chamber growth beneath large volcanoes. As inferred from the anisotropy of magnetic susceptibility (AMS), these plutons were emplaced through significantly different processes: the diorite as a discordant stock with steep fabric and the granodiorite as a tabular, bell-jar pluton. In detail, we interpret that the latter was assembled in two stages. First, an upper 'layer' intruded as a thin sill along a major subhorizontal basement/cover detachment. The subhorizontal magnetic fabric and strongly oblate AMS ellipsoid in this layer record intrusive strain where the magma flow paths were subparallel to the pluton roof. Second, in the lower 'layer' of the pluton, magnetic foliations dip moderately to the ~NW and ~WNW to vertical and are associated with down-dip to subhorizontal lineations and prolate to weakly oblate shapes of the AMS ellipsoids. Such fabric patterns are compatible with piecemeal floor subsidence, where magma flowed along multiple subsiding fault-bounded blocks.

Based on this case example, we develop a conceptual model for magma flow paths and strain patterns for four main modes of floor subsidence: (1) piston (cauldron) subsidence is characterized by convergent flow and radial principal stretching above the magma chamber floor; (2) the piecemeal floor subsidence leads to steep to inclined magma flow paths in conduits along fault-bounded blocks; (3) asymmetric (trap-door) subsidence produces first divergent flow paths near the conduit sides, changing into convergent paths in the narrower space near the kinematic hinge; and (4) symmetric cantilever (funnel) subsidence will lead to divergent flow from a central feeder and thus circumferential principal stretching of the magma. If the growing pluton develops a 'two-layer' structure, all the flow paths and associated strains are affected by the flat-lying pluton roof and will convert into horizontal flattening as the roof is approached.

INTRODUCTION

High-level plutons representing 'fossil' magma chambers once connected to their volcanic edifice play an important role in evolution of volcano–plutonic systems. Despite extensive research into petrologic, geochemical, and geophysical aspects of such plutons and active magma chambers below volcanoes (e.g., Seager and McCurry 1988; Furman et al. 1992; Huges et al. 1996; Wyss et al. 1997; Nelson et al. 1999; Canales et al. 2009; Nagaoka et al. 2012), lack of modern structural data leaves magma-emplacement mechanisms and flow patterns before, during, and after volcanic eruptions poorly understood. Exposures of high-level plutons directly linked to their volcanic equivalents are rather rare and most available studies have focused on establishing the geometry of contacts and then inferred on the three-dimensional pluton shapes. A few exposed caldera-related and sub-volcanic plutons have been reported, for instance, from the North American volcanic provinces, Iceland, and South American Andes (e.g., Cobbing and Pitcher 1972; Myers 1975; Lipman 1984, 2007; Nelson et al. 1999; Gudmundsson 2012) and show that larger plutons (up to 20 × 40 km in size) have generally plug-like, weakly elliptical shapes, steep sharp contacts, and flat to shallowly dipping roofs. Smaller plutons tend to have more variable shapes including elongated plugs, sills, and laccoliths with a dome-like roof (e.g., Roobol 1974; Corry 1988; McIntosh and Chapin 2004; Lipman 2007; Petronis and O´Driscoll 2013). In terms of the inferred growth mechanisms, the observed variability of subvolcanic plutons can be generalized into two end-member emplacement models. (1) Tabular plutons that have generally sill-like, laccolithic, or lopolithic shapes formed as an intruding magma displaces overlying or the underlying rocks, respectively (e.g., Myers 1975; Corry 1988; Cruden 1998; Bonin et al. 2004; Petronis et al. 2004; Cruden and McCaffrey 2001; O'Driscoll et al. 2006; Grocott et al. 2009; Gudmundsson 2011, 2012). (2) As opposed to the above, cylindrical, vertically extensive plutons are constructed through multiple visco–elastic processes including stoping and downward return flow of wall rocks (e.g., Paterson et al. 1996; Miller and Paterson 1999; Yoshinobu et al. 2003; Paterson and Farris 2008; He et al. 2009).

This paper compares contrasting emplacement mechanisms of two high-level, nearly coeval diorite and granodiorite plutons of the Miocene Štiavnica volcano–plutonic complex, Western Carpathians (Fig. 1; Lexa et al. 1999; Kodĕra et al. 2004). After a brief introduction to the local geologic setting and evolution of the volcano–plutonic complex, we concentrate on quantification of fabric parameters and orientation as derived from the anisotropy of magnetic susceptibility (AMS). The AMS data indicate contrasting fabrics in the two plutons, interpreted as resulting from different emplacement processes. Furthermore, the granodiorite pluton reveals a complicated fabric pattern compatible with a piecemeal subsidence of the pluton floor. Based on this specific case example, we finally develop a general model for intrusive fabric development and strain patterns in shallow-level plutons for different modes of floor subsidence.

GEOLOGIC BACKGROUND

The Štiavnica volcano–plutonic complex is an erosional relic of a stratovolcano, ~50 km in diameter, and a central caldera underlain by two main plutons intruded by numerous dikes (Figs. 1, 2, 3, and 4). The present-day level of exposure is characterized by significant topography and vertical relief of ~800 m, cutting across the pluton roof (the volcano basement) and partly eroded overlying volcanic rocks. The volcanic rocks generally have medium- to high-K calc-alkaline andesitic to rhyolitic compositions and were interpreted as having formed in an extensional back-

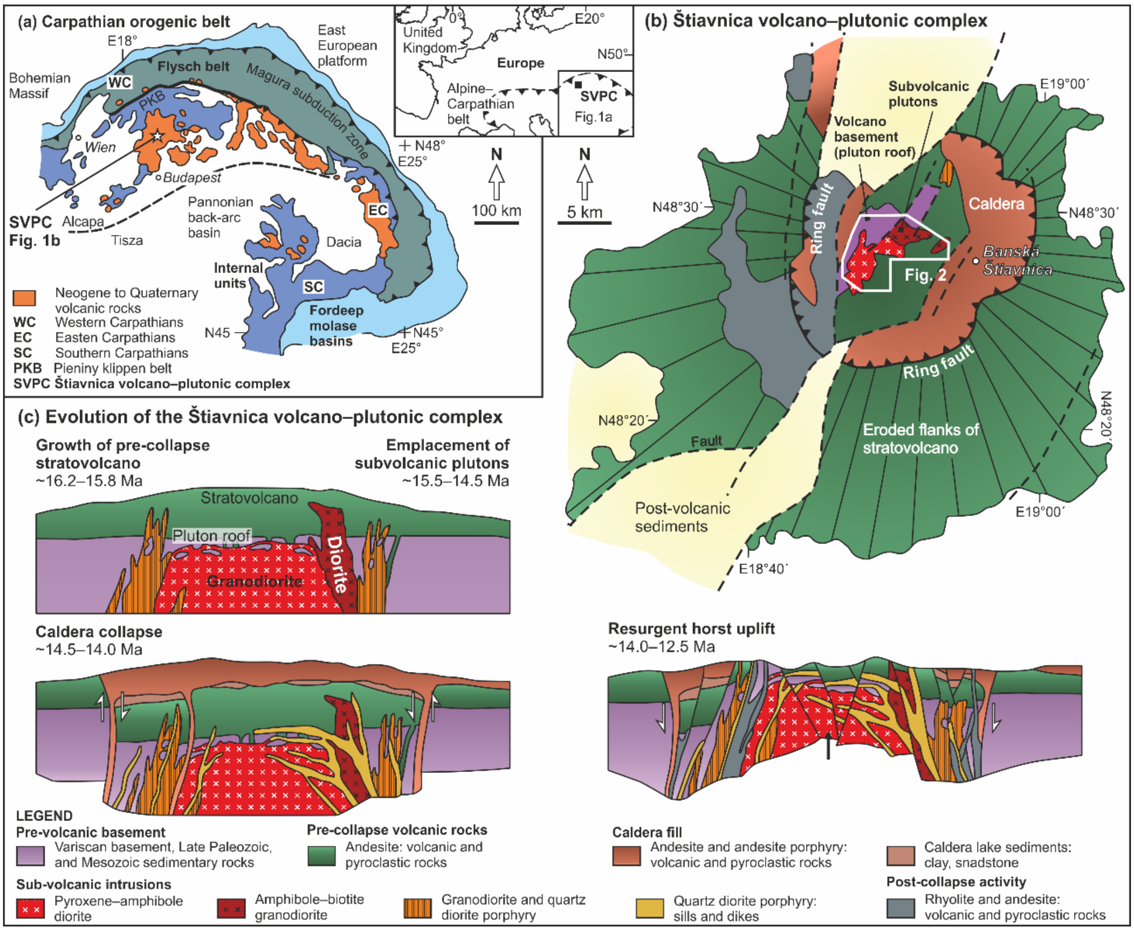

Fig. 1 (a) Simplified tectonic map of the Carpathian orogenic belt (see inset for its location in Europe). The Štiavnica volcano–plutonic complex (SVPC) developed in a back-arc setting with respect to the outer Magura subduction zone (after Lexa et al. 1999; Plašienka 2003; Pecskay et al. 2006). (b) Geologic map of the Štiavnica volcano–plutonic complex (after Lexa et al. 1999 and Koděra et al. 2005). (c) A model for evolution of the Štiavnica volcano–plutonic complex (after Lexa et al. 1999 and Koděra et al. 2005)

arc setting inboard of a flysch belt and oceanic domains subducted underneath the outer Carpathian arc (Fig. 1a; e.g., Konečný et al. 1995, 2002; Harangi et al. 2007).

The complex was built on Variscan greenschist-facies metagranitoids and schists covered by Late Paleozoic siliciclastic and Mesozoic chiefly carbonate successions (Konečný 1971; Konečný et al. 1998b; Lexa et al. 1999). Both the Variscan rocks and their cover were overprinted by the mid-Cretaceous Alpine collision resulting in an overall nappe architecture (e.g., Plašienka 2003; Bielik et al. 2004; Froitzheim et al. 2008) and in the development of a subhorizontal basement–cover detachment (Lexa et al. 1999).The Štiavnica volcano–plutonic complex evolved in three stages (Fig. 1c; Konečný 1971; Konečný et al. 1995; Lexa et al. 1999; Koděra et al. 2004, 2005). (1) The pre-caldera stage (~16.2–15.8 Ma) is characterized by growth of the stratovolcano through pyroxene and amphibole–pyroxene andesite lava flows, domes, pyroclastic deposits, and epiclastic breccias. The central portion of the stratovolcano was then intruded by andesite porphyry sills, dikes, and laccoliths followed by a period of quiescence and erosion. Subsequently, a diorite stock and a younger-yet, voluminous, granodiorite pluton were emplaced at a very shallow level into the central part of the stratovolcano (~15.5–14.5 Ma). It is inferred that both plutons were fed from a

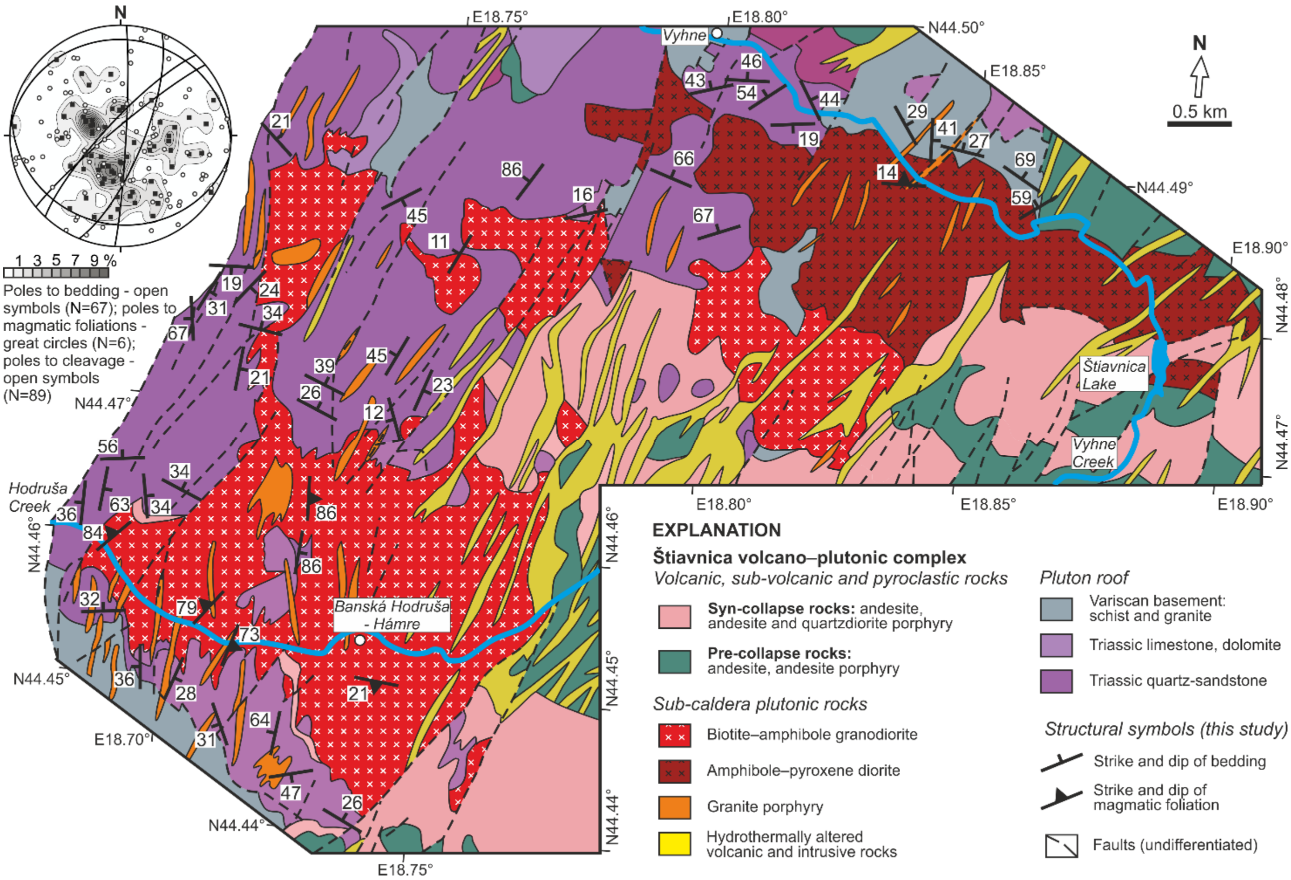

Fig. 2 Detailed geologic map of the central portion of the Štiavnica volcano–plutonic complex with two sub-volcanic diorite and granodiorite plutons (simplified after Konečný et al. 1998a). Stereonet (equal-area, lower hemisphere) shows orientation of main structural elements (this study)

deeper differentiated magma chamber (at ~6–10 km depth; Konečný 2002; P. Koděra, written communication, 2012). Emplacement of the granodiorite was also accompanied by intrusion of minor stocks and dikes of granodiorite and quartz diorite porphyry (Fig, 1c). (2) An extensive collapse caldera, incorporating the two shallow sub-volcanic plutons, subsided into the deeper magma chamber and triggered extrusion of differentiated biotite–amphibole andesites and dacites (~14.5–14 Ma). The caldera depression was filled by siliciclastic sediments, reworked tuffs, and andesite to dacite volcanic rocks, and later intruded by sub-volcanic quartz diorite porphyry sills, dikes, and ring dikes (Fig. 1c). (3) The final post-caldera stage (~14–2.5 Ma) was marked by renewed volcanic activity from eruptive centers scattered along the eroded volcano slopes and by uplift of an asymmetric resurgent horst in the central part of the complex (including the sub-volcanic plutons). This uplift was accompanied by rhyolitic volcanism and emplacement of granite porphyry dikes (Fig. 1c).

The sub-volcanic plutons

The diorite is a steep-sided, ~4.5 km2 in plan view, ~WNW–ESE elongated stock that pierced the Variscan basement, overlying nappes, and pre-caldera volcanic rocks (Lexa et al., 1999). The outer diorite contacts are irregular, sharply intrusive or faulted, and discordant to the host rock bedding and cleavage (Fig. 2). The exposed portion of the pluton is composed of equigranular, fine to medium grained pyroxene–amphibole diorite showing neither apparent textural nor compositional variations and lacking magmatic sheets, microgranular enclaves, and host rock xenoliths. On the micro-scale, the diorite exhibits solely magmatic texture with no evidence of recrystallization or solid state deformation (using criteria summarized in Vernon 2000, Vernon et al. 2004). The texture is defined by chiefly subhedral plagioclase laths and pyroxene grains, up to 1 mm in size, and abundant smaller grains of magnetite (up to 0.3 mm in size) interspersed within the matrix (Fig. 3a).

To the southwest, the diorite is intruded by the equigranular amphibole–biotite granodiorite (~9.5 km2 in surface exposure; Fig. 2). The granodiorite pluton has a bell-jar shape with a generally flat roof rolling over into steep outward-dipping margins (Lexa et al. 1999). The total thickness of the granodiorite is unknown but likely exceeds 2.5 km based on borehole data (Štohl et al. 1990). The pluton encloses several roof pendants with the longest dimension up to 1 km and is cross-cut by numerous porphyry dikes and faults containing Au–Ag, Pb–Zn, and Cu–Bi–W

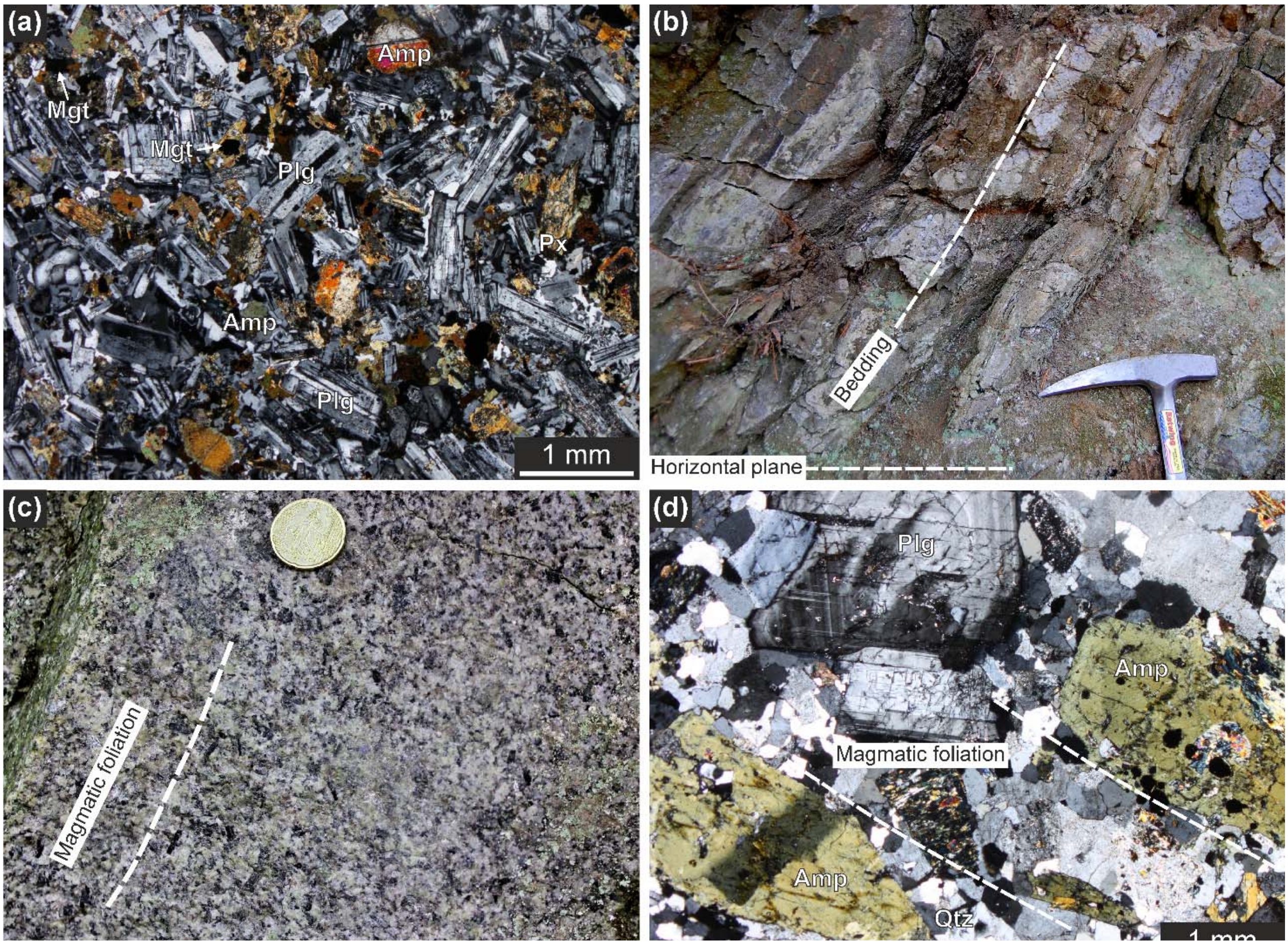

Fig. 3 Field and textural characteristics of the sub-volcanic plutons and their host rocks. (a) Photomicrograph of the diorite. Coordinates: N48.49159°, E18.84567°. (b) Bedded Triassic limestones; hammer for scale. Coordinates: N48.48781°, E18.85690°. (c) Amphibole–biotite granodiorite with a weak magmatic foliation defined by the shape-prefered orientation of mafic minerals. Coordinates: N48.45352°, E18.77993°. (d) Photomicrograph of the granodiorite with weak magmatic foliation defined by the shape-prefered orientation of the amphibole grains. Coordinates: N48.46348°, E18.78902°; (all coordinates are referenced to WGS84 datum)

mineralization (Fig. 2). A recent interpretation based on Al-in hornblende geobarometry suggests that the pluton was emplaced at a shallow depth of about 2.5–4 km and was fed from a deep seated magma reservoir. The granodiorite thus represents an upper part of a vertically extensive magma plumbing system (Konečný 2002).

The granodiorite pluton/roof contact is highly irregular in map view, but this is largely an apparent geometry caused by topographic cut effects (Fig. 4). In outcrops, the Late Paleozoic and Triassic sedimentary roof rocks are frequently bedded with the bedding attitude varying from gently to steeply dipping (Figs. 2, 3b). No evidence for widespread syn-emplacement bedding reorientation or ductile strain was found in the roof rocks.

In the accessible part of the pluton, the granodiorite is macroscopically uniform in texture and composition (non-sheeted), equigranular and medium- to coarse-grained, with scattered microgranular enclaves without shape preferred orientation. In some places, the granodiorite displays relatively weak, steep ~NNE–SSW magmatic foliation defined mainly by the shape-preferred orientation of amphibole and biotite (Fig. 3c), whereas most of the pluton is macroscopically isotropic. Weak shape preferred orientation of plagioclase can also be observed in thin-sections. Microstructures corroborate that this fabric is clearly magmatic with no solid state overprint (Fig. 3d).

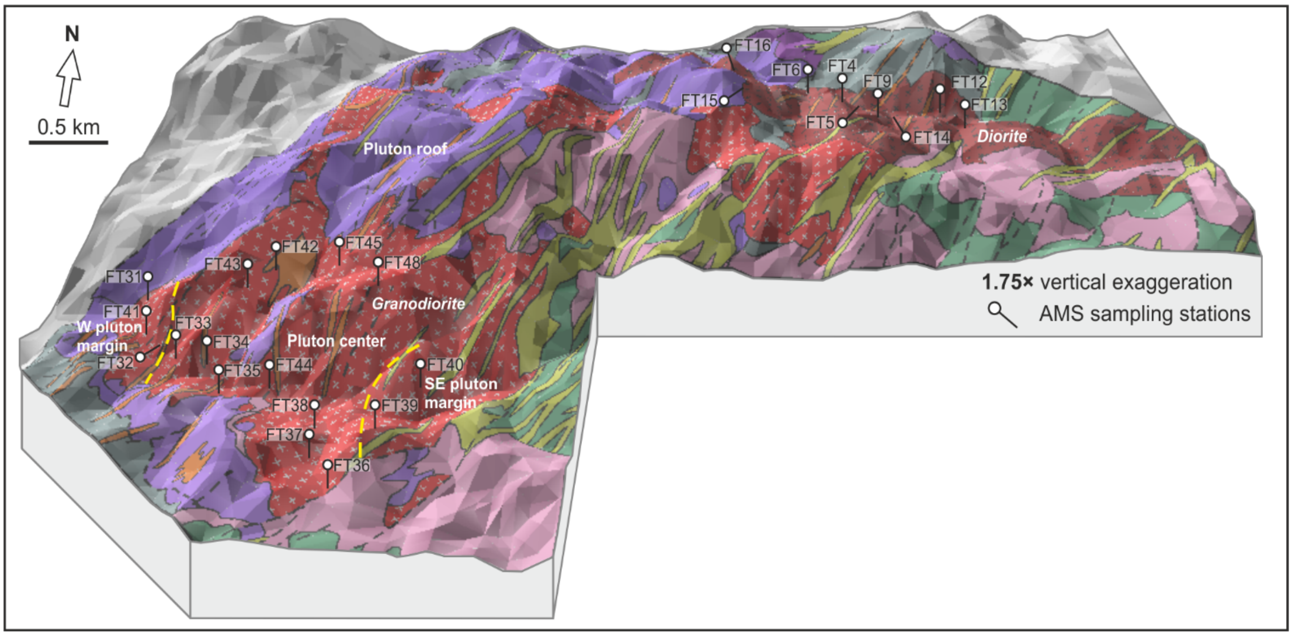

Fig. 4 Digital elevation model of the central portion of the Štiavnica volcano–plutonic complex showing location of the AMS stations. The base of the 1:50,000 topographic DEM of Slovakia is freely available at http://www.gisat.cz/content/en, geologic map layer is taken from Fig. 2

ANISOTROPY OF MAGNETIC SUSCEPTIBILITY

The anisotropy of magnetic susceptibility (AMS) technique was used to quantify the internal structure of both plutons (see Hrouda 1982; Tarling and Hrouda 1993; Borradaile and Henry 1997; Borradaile and Jackson 2010 for reviews and principles of the method). A total of 56 oriented cores were collected using a hand-held gasoline drill at 9 stations in the diorite and 16 stations in the granodiorite (we have sampled nearly all available surface outcrops). The cores yielded 131 and 233 standard cylinder-shaped specimens of the diorite and granodiorite (9–20 specimens per station), respectively, each approximately 10 cm3 in volume. The AMS was measured using a MFK1-A Kappabridge in the Laboratory of Rock Magnetism, Institute of Geology and Paleontology, Charles University in Prague. Statistical analysis of the data was carried out using the ANISOFT software package (www.agico.com, Chadima and Jelínek 2009). The measured data and parameters are presented in Figures 5–9 and listed full in Appendix items 2/1 and 2/2.

Hereinafter we use three parameters to characterize the magnetic fabric: (1) the bulk susceptibility, $km = (k_1 + k_2 + k_3)/3$, reflecting the magnetic mineral species and their fraction, (2) the degree of anisotropy, $P = k_1/k_3$, which expresses the eccentricity of the AMS ellipsoid (Nagata 1962), and (3) the shape parameter, $T = 2ln(k_2/k_3)/ln(k_1/k_3) - 1$, which describes symmetry of the AMS ellipsoid; for $-1 \leq T < 0$ the ellipsoid is prolate, for $T = 0$ triaxial, and for $1 \geq T > 0$ oblate (Jelínek 1981). The maximum, intermediate, and minimum susceptibility axes are k_1, k_2, and k_3, respectively. The maximum principal susceptibility (k_1) represents magnetic lineation, the minimum principal susceptibility (k_3) represents pole to the magnetic foliation plane. Orientations of magnetic foliations and lineations are visualized in stereograms and by plotting the station mean directions on the map.

Magnetic mineralogy

The diorite has a bimodal distribution of bulk susceptibilities (k_m) on the order of 10^{-3} and 10^{-2} (60 % of specimens; SI units are used throughout this paper). The granodiorite yields susceptibilities on the order of 10^{-2} (96 % of specimens; Fig. 5a; Appendix item 2/1). Such high susceptibilities are typical of ferromagnetic granites and suggest that the magnetic signal is dominated by a magnetite-like mineral (e.g., Hrouda and Kahan 1991). In order to determine the AMS carriers, the bulk magnetic susceptibility of representative coarsely powdered specimens was measured as a function of temperature using an MFK1-FA Kappabridge with the CS-4 and CS-L temperature control units in the laboratory of Agico, Inc., Brno. Complete thermomagnetic curves (from −196 °C to 700 °C and back) were obtained in three steps. First, samples were cooled down to the temperature of liquid nitrogen (ca. −196 °C) and heated to room temperature, magnetic susceptibility was measured approximately every minute. Second, samples were heated up from room temperature to 700 °C and cooled back (in argon atmosphere to minimize mineral changes due to oxidation) at an approximate rate of 14 °C/min. Third, samples were cooled down to the temperature of liquid nitrogen and heated to the room temperature (Fig. 5b). The thermomagnetic measurements confirm that the magnetic mineralogy of both the diorite and granodiorite (specimens FT05/1/8, FT15/1/5, FT32/1/8, FT35/3/4) is uniform and controlled exclusively by titanomagnetite. This is demonstrated by a susceptibility decrease at −170 °C and by an abrupt susceptibility drop at ~580 °C on both the cooling and heating curves, corresponding to the Verwey transition and Curie temperature, respectively. The heating and cooling curves also follow nearly the same trends implying no rock alteration or magnetite growth during the experiment (Fig. 5b). A small "bump" on the heating curves of specimens FT15/1/5 and FT35/3/4 at ~250–350 °C (not present on the respective cooling curves) most probably reflects the presence of low temperature maghemite.

Magnetic fabric parameters and orientation

Unlike their uniform magnetic mineralogy, the diorite and granodiorite plutons exhibit significantly different magnetic fabrics. The diorite yields weakly anisotropic fabric, the P parameter ranges from 1.028 to 1.099 with two data peaks clustered around P = 1.050 and 1.090 (Fig. 6a; Appendix item 2/2; corresponding to 5% and 9% anisotropy, respectively). The distribution of station averages with relatively weak or strong anisotropy ranging from 1.037 to 1.089 shows no apparent spatial pattern (Fig. 7a; Appendix item 2/2). The T parameter shows a large spatial variation from –0.933 to 0.738 and almost evenly distributed shapes to the AMS ellipsoids with 52 % prolate specimens (Fig. 6a; Appendix item 2/2). In map view, five stations with prolate fabric (FT06, FT13, FT14, FT15, and FT16; station averages range from –0.667 to –0.222) occur along the pluton/roof contact, whereas stations characterized by oblate shape AMS

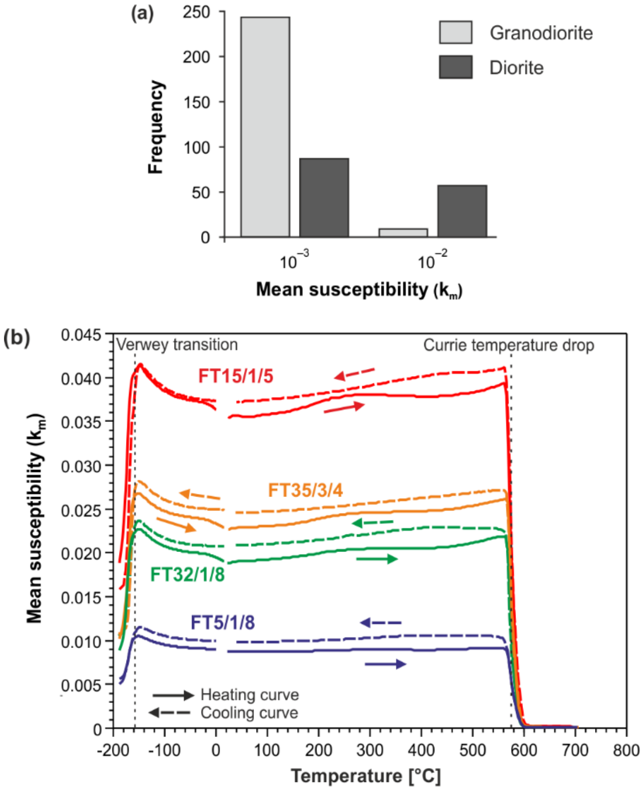

Fig. 5 (a) Histogram of the bulk (mean) susceptibilities of all measured AMS specimens in diorite and granodiorite. (b) Magnetic susceptibility as a function of temperature for selected diorite (FT05, FT15) and granodiorite (FT32, FT35) specimens

(a) Diorite

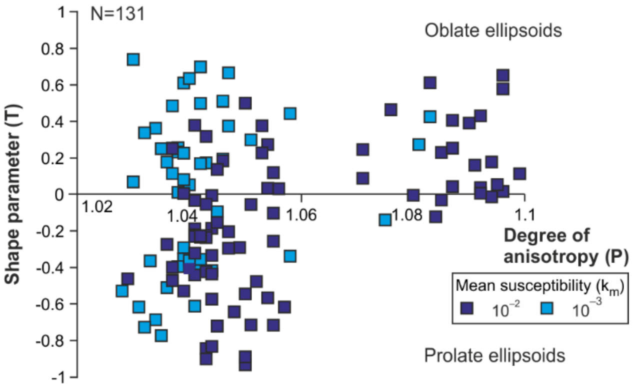

(b) Granodiorite

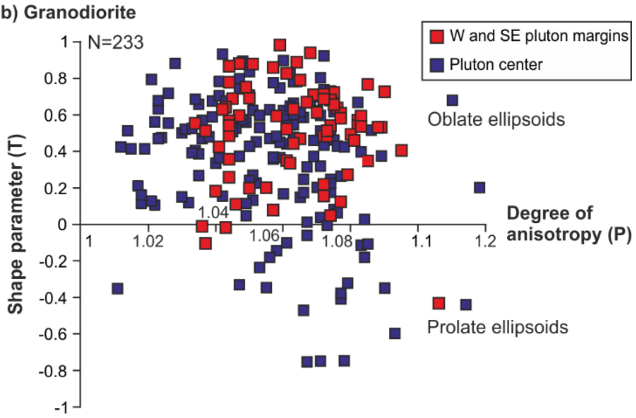

Fig. 6 Magnetic anisotropy P–T plots summarizing all data for (a) diorite, and (b) granodiorite. Data outliers above P = 1.120 are not shown

ellipsoid (FT04, FT05, FT09, FT12; station averages range 0.121 to 0.525) are found closer to the pluton center (Fig. 7b; Appendix item 2/2). The diorite is characterized by steep magnetic foliations that are subparallel to the local roof margin, except at stations FT06 and FT15 where foliations are almost margin-perpendicular (Figs. 8a, 9a; Appendix item 2/2). Regardless the foliation strike, magnetic lineations plunge at moderate to steep angles and, in most cases, lie close to the dip direction of the associated magnetic foliation (Figs. 8a, 9; Appendix item 2/2). The exception is station FT05 which yields sub-horizontal ~E–W lineations parallel to the foliation strike.

By contrast, the granodiorite yields a larger scatter in the P parameter from 1.011 to 1.169, but most data are clustered between ~1.040 and ~1.090 (4–9% anisotropy; Fig. 6b; Appendix item 2/2). In map view, the station average P parameters of the granodiorite loosely define ~N–S to ~NNE–SSW elongated domains, each with comparable P values (Fig. 7c). Though the shape parameter varies greatly from −0.757 to 0.988, the granodiorite exhibits overall oblate-shaped AMS ellipsoids (89 %) at all but one station (FT42; Figs. 6b, 7d; Appendix item 2/2). In detail, prolate (station FT42) to weakly oblate ellipsoids (T<0.500) characterize the pluton center (deeper structural level) whereas strongly oblate ellipsoids (T>0.500) were revealed at stations close to the western and southeastern pluton margin (near the roof; Fig. 7d; Appendix item 2/2).

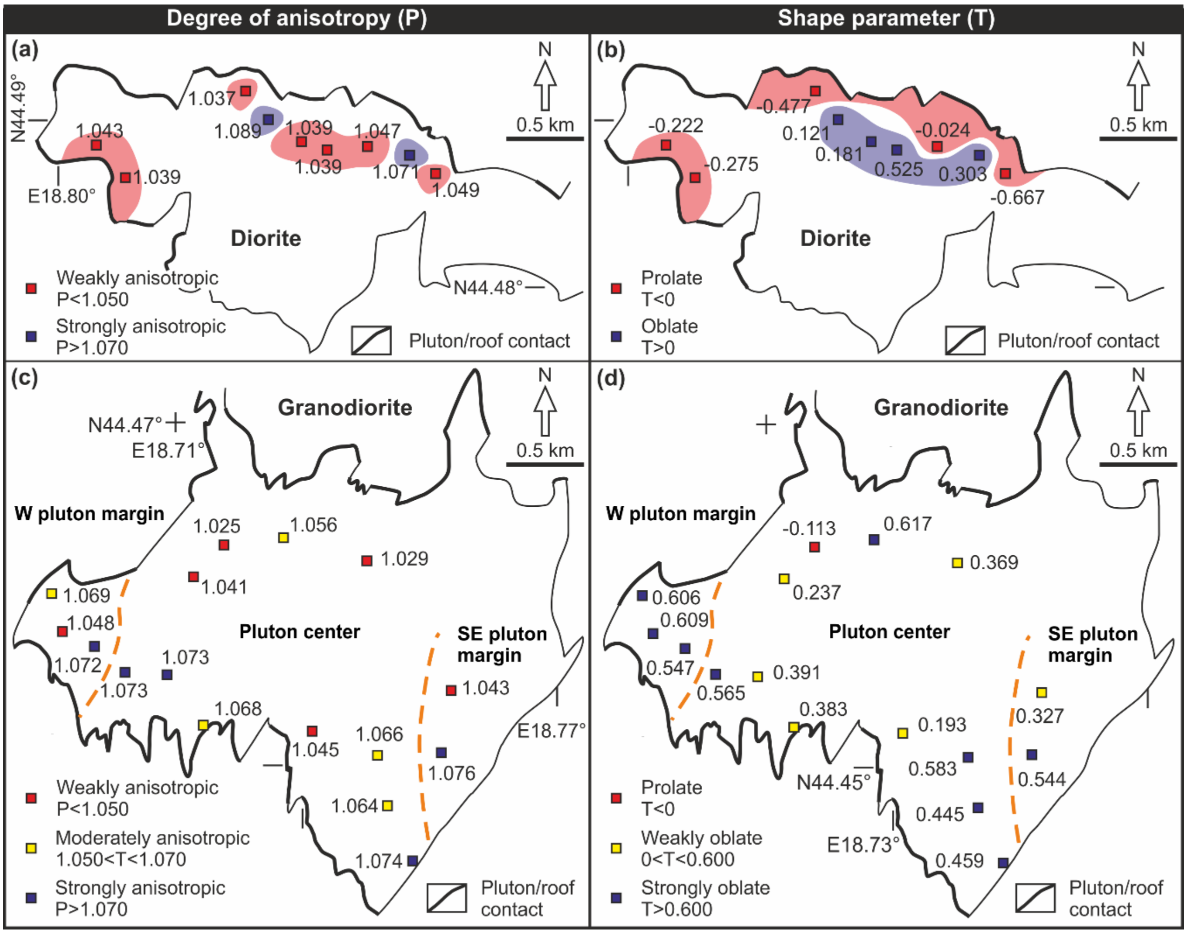

Fig. 7 Maps of spatial distribution of average degree of anisotropy (P) and shape parameter (T) in the diorite (a, b) and the granodiorite (c, d)

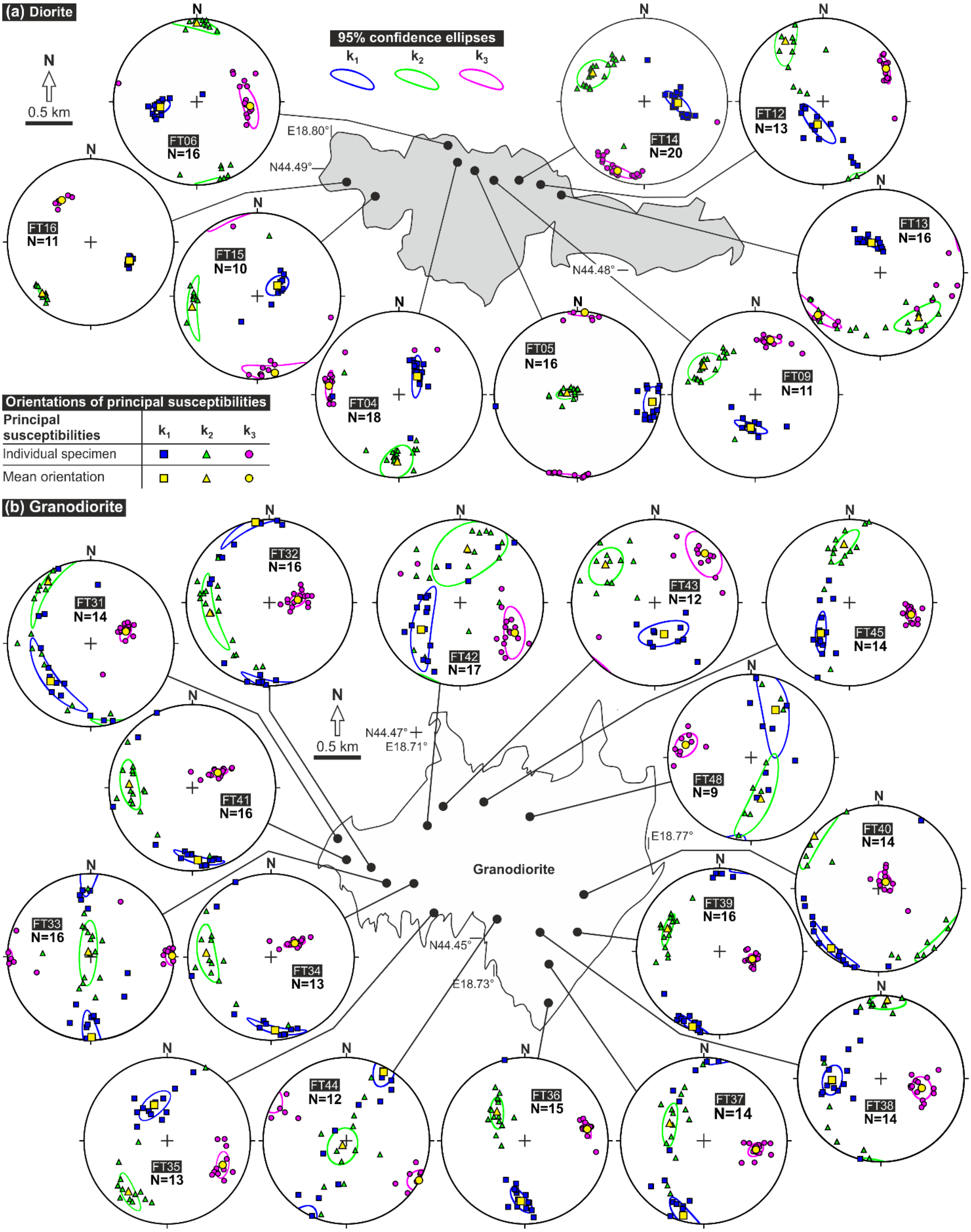

Fig. 8 Maps showing orientation of the principal susceptibilities in the (a) diorite and (b) granodiorite. Stereonets (equal-area, lower hemisphere) show orientation of the principal susceptibilities

Based on orientation of magnetic foliations, two distinct domains ('layers') can be identified in the pluton. Magnetic foliations in the pluton center (a lower 'layer') strike ~N–S to ~NNE–SSW and dip at moderate to steep angle to the ~W and ~WNW whereas foliations near the western and southeastern margins of the pluton (an upper 'layer') are almost perpendicular, ~NW–SE-striking. The latter dip shallowly to moderately to the southwest (stations FT31, FT32, FT39, FT40, and FT41) and to the ~WNW (station FT39; Figs. 8b, 9a; Appendix item 2/2). The exception to the above is the ~NNE–SSW-striking foliation at station FT39. Magnetic lineations of both domains vary from down-dip to predominantly subhorizontal, i.e., parallel to the foliation strike. The mean lineation trend and plunge calculated from all data is 191° and 12°, respectively (Fig. 9b).

Further analysis of the data shows that the degree of anisotropy and the oblateness of the AMS ellipsoids relate to the dip of magnetic foliations. Two data groups can be discriminated on the P and T vs. foliation dip diagrams. One group includes data from stations in the pluton center (the lower 'layer'; Fig. 4) and is characterized by greater foliation dip (>40°), larger scatter of the P parameters (from 1.011 to 1.169), and both prolate- and oblate-shaped AMS ellipsoid (Fig. 10;

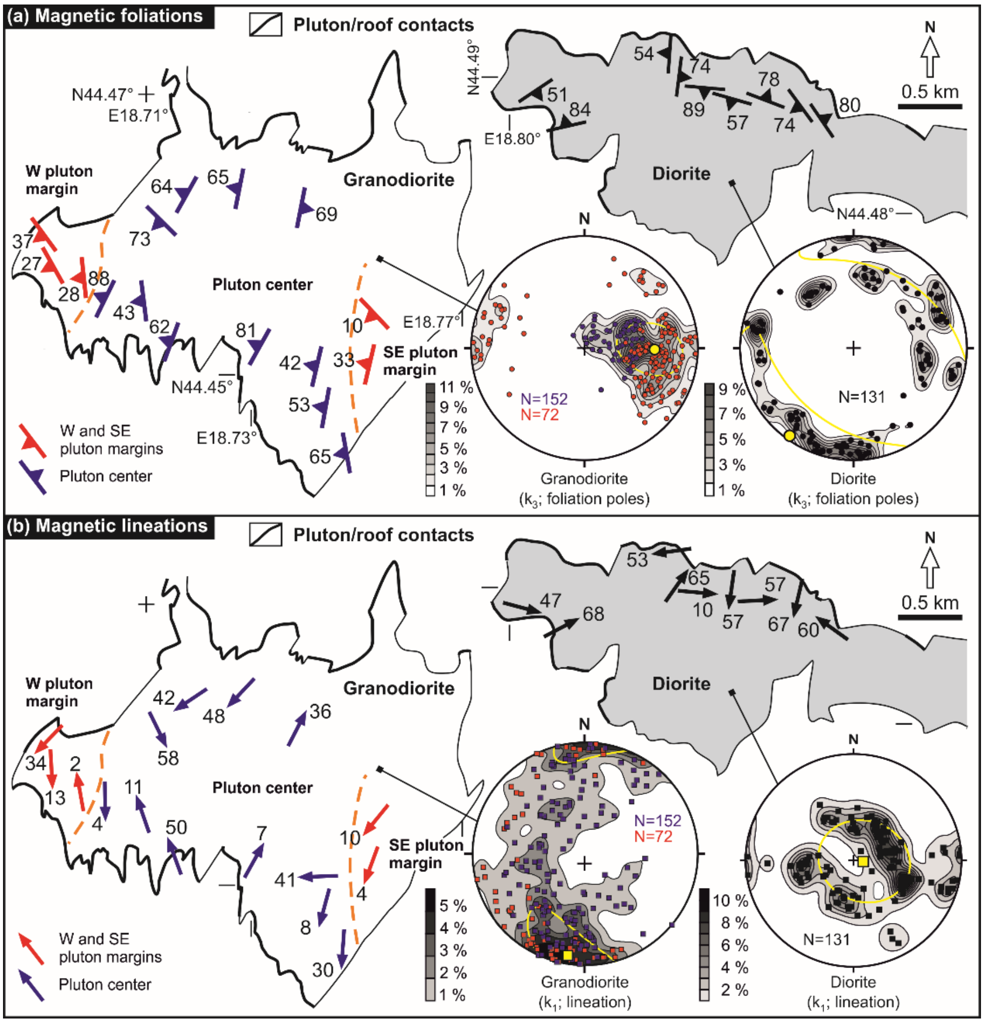

Fig. 9 Maps showing orientation of (a) magnetic foliations and (b) magnetic lineations in the diorite and granodiorite. Stereonets (equal-area, lower hemisphere) show orientation of the principal susceptibilities. Specimens from the W and SE pluton margins and pluton center are highlighted in red and blue, respectively. Yellow symbols indicate mean directions and yellow lines represent 95% confidence ellipses

Appendix item 2/2). In contrast, the other group includes data from stations along the western and southeastern margins (near the roof; Fig. 4) and is characterized by shallower dips (<40°), a more restricted range of the P parameter (1.034–1.106), and mostly oblate susceptibility ellipsoids (Fig. 10; Appendix item 2/2).

Fig. 10 Diagrams showing distributions of (a) degree of anisotropy, and (b) shape parameter against the magnetic foliation dip.

(a) P *vs.* foliation dip (granodiorite)

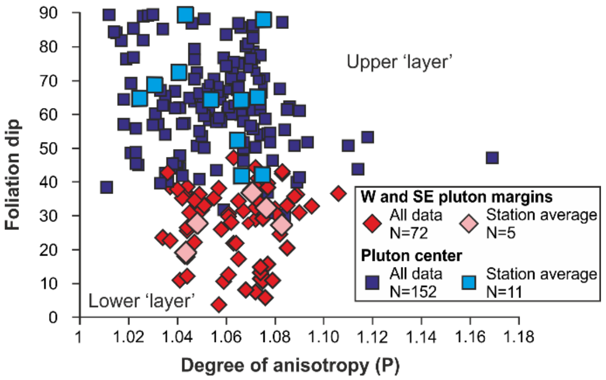

(b) T *vs.* foliation dip (granodiorite)

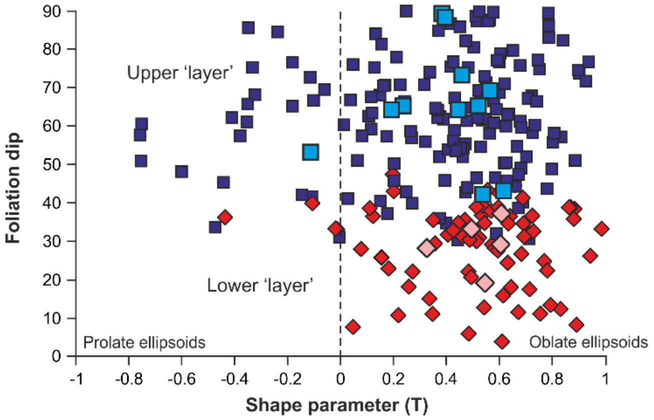

DISCUSSION

Intrusive strain and emplacement mode of the diorite

The subvertical margin-parallel magnetic foliations and steeply plunging lineations (Figs. 8a, 9a) provide an independent argument to support the stock shape of the pluton. Given that the fabrics observed in the pluton are magmatic (e.g., Fig. 3a), we interpret this magnetic fabric to record intrusive strain during magma emplacement where the principal stretching direction was subvertical and the overall principal shortening was perpendicular or at a high angle to the pluton margin. As documented by high bulk susceptibilities and thermomagnetic curves (Fig. 5a, b), this fabric records shape-preferred orientation or distribution anisotropy of magnetite grains in the dioritic magma (the same applies for the granodiorite). Interestingly, the AMS ellipsoid shapes in the diorite indicate significant magma stretching along margins passing inwards into a zone of flattening (Fig. 7b), exactly opposite to many examples and models of steep-sided intrusions (e.g., Cogné and Perroud 1988; Hrouda and Lanza 1989; Ramsay 1989; Cruden 1990, Paterson and

Vernon 1995; Miller and Paterson 1999). We may only speculate that the vertical stretching resulted from magma flow past an irregular rigid wall (e.g., Geoffroy et al. 2002; Callot and Guichet 2003; Philpotts et al. 2007).

In summary, the emplacement of the diorite stock represents initial, small-volume intrusion of hot magma into the future caldera floor (volcano basement) and pre-collapse andesites (Figs. 1c, 2) and marks the onset of major plutonic growth beneath the Štiavnica stratovolcano (Fig. 11a).

Intrusive strain and emplacement mode of the granodiorite

Emplacement of the diorite was followed by intrusion of voluminous granodiorite which was interpreted as a bell-jar pluton emplaced by cauldron subsidence (Lexa et al. 1999). Our magnetic fabric study provides deeper insights into this emplacement mechanism. We have shown that the exposed crestal part of the granodiorite pluton exhibits a 'layered' internal structure defined by magnetic fabric (Figs. 6b, 7c, d, 8, 9). The flat-lying magnetic fabric near its western and southeastern margins (the 'upper layer') may be explained as resulting from roof-perpendicular shortening and roof-parallel spreading of magma during emplacement (e.g., Cruden et al. 1999; Fig. 11b). In contrast, as no vertical sheets were observed in the pluton, we interpret the alternating foliation dip domains in the pluton center (the 'lower layer') as reflecting strain during magma flow along multiple variably subsiding fault-bounded blocks elongated ~NNE–SSW to ~NE–SW (Fig. 11c). Magma flow is assumed to have been generally upward along the inclined fault planes,

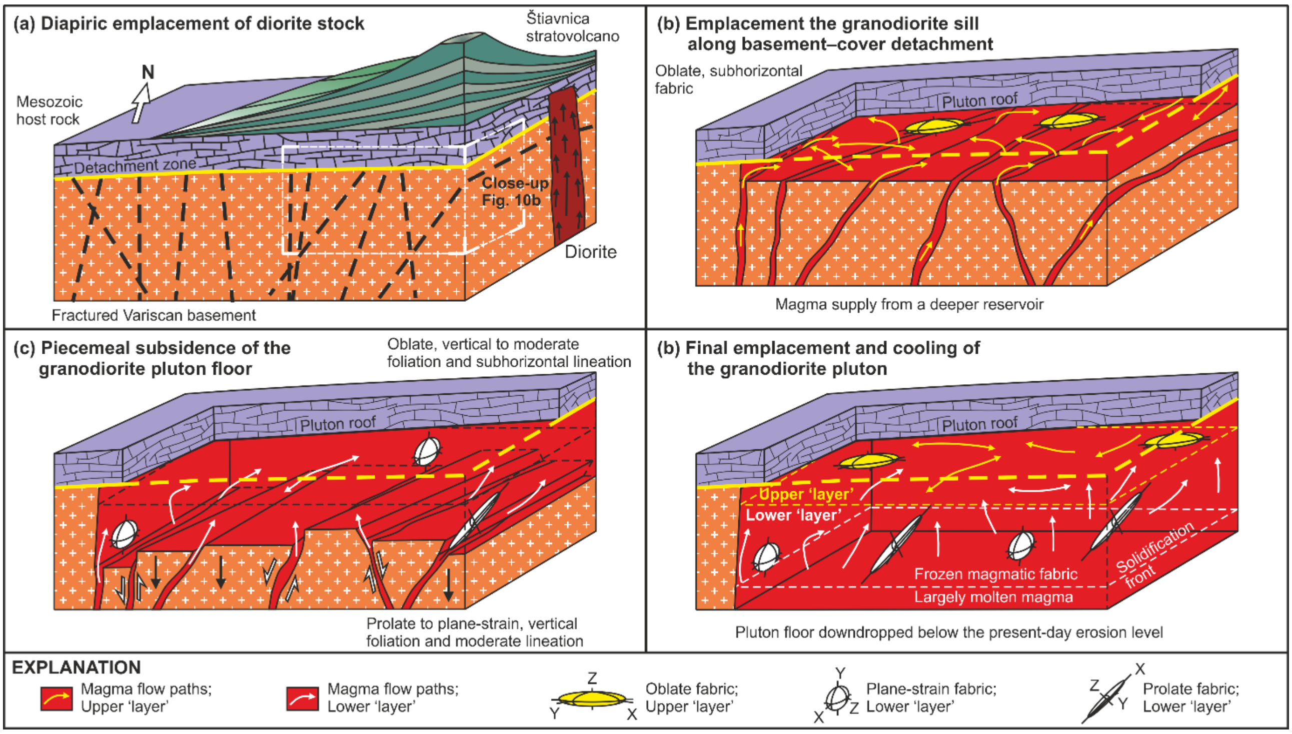

Fig. 11 Interpretive block-diagrams (not to scale) illustrating the emplacement mechanism and the inferred magma flow paths and associated strains in the Štiavnica subvolcanic plutons. (a) Intrusion of steep-sided discordant diorite stock. (b) Initial stage of the granodiorite emplacement as a thin sill emplaced along a major basement–cover detachment zone. (c) Subsidence of the individual fault-bounded blocks in the pluton floor accommodates thickening of the sill. (d) A thickly tabular bell-jar pluton with a 'layered' internal structure develops during continued floor subsidence. Downward migration of the solidification front captures different fabrics below the pluton roof and above its floor

continuously passing into lateral spreading in the upper layer below the roof (Fig. 11c). This transition in overall magma flow direction was associated with intrusive strain changing from prolate (station FT42) to weakly oblate (Fig. 7d), in presumably narrow conduits between fault-bounded blocks, to strongly oblate below the roof (Figs. 7d, 10c).

The magnetic fabric data thus suggest that the granodiorite pluton was not emplaced via a 'classic-type' cauldron subsidence where the space for intruding magma was created by downdrop of a single piston-shaped block (e.g., Clough et al. 1909; Myers 1975). Instead, we envision that the subsidence was piecemeal and took place in two stages. First, the magma intruded along steep fracture-bounded narrow conduits in the crystalline basement and then spread laterally parallel to a major flat-lying basement–cover detachment to form a thin sill (Fig. 11b; see also Lexa et al. 1999). Second, the sill floor composed of multiple blocks continued to subside differentially to accommodate arrival of new, more voluminous magma batches forming a tabular pluton (Fig. 11c). This emplacement mechanism may explain the 'layered' internal structure of the pluton with prolate to weakly oblate steeper fabric in and above the conduits and oblate flat-lying fabric below the pluton roof (Fig. 11d).

Magma flow paths and strain patterns in sub-volcanic magma chambers growing by floor subsidence

Generalizing our data and inferences from the Štiavnica volcano–plutonic complex, we develop here an idealized model for the magma flow paths and associated strain patterns in shallow chambers growing by floor downdrop beneath large volcanoes. We follow the concept and terminology of Paterson et al. (1998), assuming that magmatic (and magnetic) foliations and lineations represent the XY plane and the X axis of the local strain ellipsoid, respectively, which however do not have to coincide, or even may be perpendicular to, the flow planes and flow lines of the flowing magma. Our model also presumes a 'two-layer' structure of the plutons, with a near-roof layer characterized by roof-parallel fabric and flattening strains and the lower layer that differs according to a particular mode of the pluton floor downdrop (Fig. 12). These main modes of pluton floor subsidence, elaborated by Cruden (1998), Cruden and McCaffrey (2001), and McNulty et al. (2000), include piston, symmetric and asymmetric cantilever, and piecemeal.

(1) During piston (cauldron) floor subsidence (e.g., Clough et al. 1909; Bonin et al. 2004; Burchardt et al. 2012), magma flow is inferred to have been vertical in the ring fracture and along the pluton wall, changing into subhorizontal convergent flow towards the pluton center above the subsiding block (Fig. 12a; e.g., Karell et al. 2009). The convergent flow is inferred to have resulted in radial stretching of the magma and in an overall constrictional regime (e.g., Paterson et al. 1998; Twiss and Moores, 1992, p. 490).

(2) During the piecemeal collapse, magma flow paths are inferred to have varied along each fault-bounded floor block, but generally were inclined to steep in planar conduits between the blocks and were reoriented into horizontal below the pluton roof. This change in orientation was accompanied by increased flattening of the associated strain ellipsoid (Fig. 12b; McNulty et al. 2000; this study).

(3) Wedge-shaped plutons formed in an asymmetric cantilever (trapdoor) mode (Cruden 1998; Cruden and McCaffrey 2001) should be characterized by magma flow paths first diverging from the steep conduit (e.g., Petronis et al. 2004) and then converging as the narrower part of the opening space is approached. The principal stretching would thus change from vertical in and near the conduit through subhorizontal and flow-perpendicular to flow-parallel (Fig. 12c).

(4) Funnel-shaped chambers growing by a symmetric cantilever mechanism (Cruden 1998; Cruden and McCaffrey 2001) will display vertical magma flow and prolate and triaxial strains in a central conduit (if it is pipe-shaped or sheet-like, respectively), changing to radially divergent magma flow (e.g., Petronis et al. 2004) with the principal stretching oriented parallel to the pluton margin (opposite to case 1; Fig. 12d). The circumferential stretching is also likely to be associated with constrictional strain, at least in the narrower space near the pluton margin.

In summary, we suggest that each mode of floor subsidence should leave behind a characteristic flow and fabric pattern in the solidified pluton (Fig. 12), provided it is not subsequently obliterated by convection, extensive magma chamber replenishment, or syn- to post-emplacement regional tectonics. Hence, fabrics, and especially the AMS, may help to unravel the mechanical processes that lead to the growth of magma chambers beneath volcanoes. An important

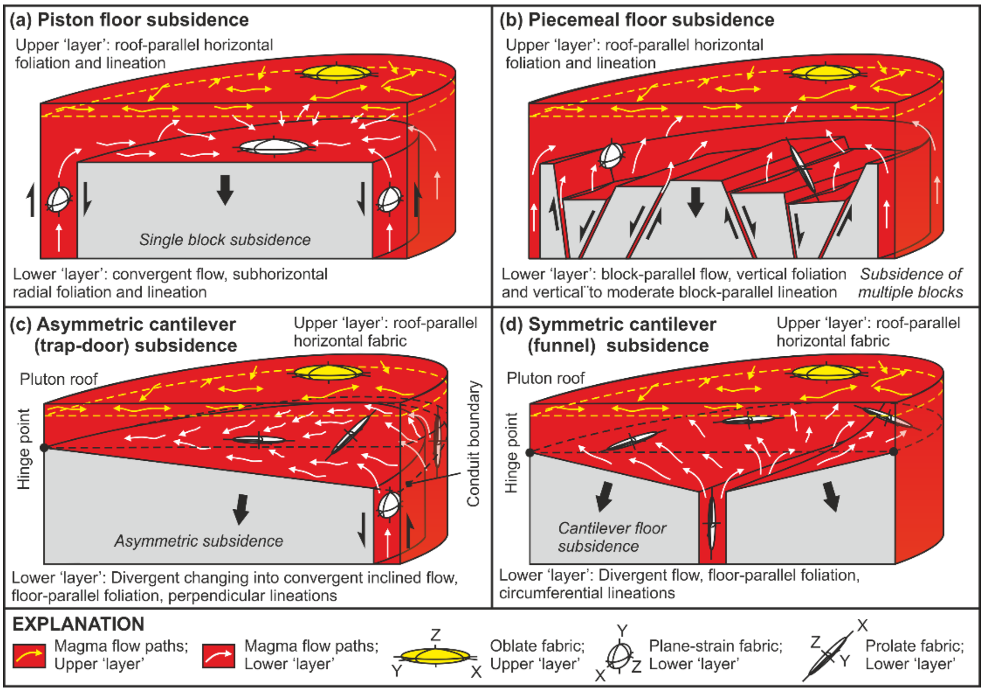

Fig. 12 Presumed magma flow paths and strain patterns for main modes (piston, piecemeal, asymmetric trap-door, symmetric cantilever) of pluton floor subsidence. See text for discussion

limitation of our conceptual model is that only simple geometric cases are considered whereas more complicated pluton filling patterns are likely in nature.

CONCLUSIONS

Magnetic fabric indicates contrasting emplacement mechanisms of sub-volcanic diorite and granodiorite plutons in the Štiavnica volcano–plutonic complex. The older small-volume diorite was emplaced as a steep-sided, ~WNW–ESE elongated stock cutting across the host rock structures. In contrast, the younger, more voluminous granodiorite reveals a complex fabric pattern interpreted in terms of a 'layered' architecture suggesting emplacement in two stages. First, the upper 'layer' was emplaced as a thin sill along a major sub-horizontal basement/cover detachment. Second, the pluton floor differentially subsided along ~NNE–SSW to ~NE–SW faults, creating space for a lower 'layer' and allowing the sill to thicken into the tabular pluton. This two-stage emplacement is thus interpreted as being entirely controlled by a piecemeal pluton floor subsidence.

A conceptual model for magma flow paths and strain patterns was developed for four main modes of floor subsidence: (1) piston (cauldron) subsidence is characterized by convergent flow and radial principal stretching above the magma chamber floor; (2) piecemeal floor subsidence leads to steep to inclined magma flow paths in conduits along fault-bounded blocks; (3) asymmetric (trapdoor) subsidence produces first divergent flow paths near the conduit, changing into convergent paths in the narrower space near the kinematic hinge; and (4) symmetric cantilever (funnel) subsidence will lead to divergent flow from a central feeder and thus circumferential principal stretching of the magma. If the growing pluton develops a two-layer structure, all the flow paths and associated strains are modified by the flat-lying pluton roof and will convert into horizontal flattening as the roof is approached.

ACKNOWLEDGEMENTS

Constructive comments to the original manuscript by Michael S. Petronis, Alexander R. Cruden and Bernard Henry, as well as careful editorial handling by Agust Gudmundsson and James D. L. White are highly appreciated. František Hrouda, Peter Koděra, and František V. Holub are thanked for valuable discussions and Jan Flašar for help with the digital elevation model. This study is part of the Ph.D. research of Filip Tomek, supported by the Charles University projects PRVOUK P44, SVV261203, Grant Agency of the Czech Republic Grant No. P210/12/1385 (to Jiří Žák) and Academy of Sciences of the Czech Republic Research Plan RVO 67985831.

REFERENCES

Bielik M, Šefara J, Kováč M, Bezák V, Plašienka D (2004) The Western Carpathians – interaction of Hercynian and Alpine processes. Tectonophysics 393:63–86. doi:10.1016/j.tecto.2004.07.044

Bonin B, Ethien R, Gerbe MC, Cottin JY, Feraud G, Gagnevin D, Giret A, Michon G, Moine B (2004) The Neogene to recent Rallier-du-Baty nested ring complex, Kerguelen Archipelago (TAAF, Indian Ocean): stratigraphy revisited, implications for cauldron subsidence mechanisms. In: Breitkreuz C, Petford N (eds) Physical geology of high-level magmatic systems. Geol Soc London Spec Pub 234:125–149. doi:10.1144/GSL.SP.2004.234.01.08

Borradaile GJ, Henry B (1997) Tectonic applications of magnetic susceptibility and its anisotropy. Earth Sci Rev 42:49–93. doi:10.1016/S0012-8252(96)00044-X

Borradaile GJ, Jackson M (2010) Structural geology, petrofabrics and magnetic fabrics (AMS, AARM, AIRM). J Struct Geol 32:1519–1551. doi:10.1016/j.jsg.2009.09.006

Burchardt S, Tanner D, Krumbholz M (2012) The Slaufrudalur pluton, southeast Iceland – an example of shallow magma emplacement by coupled cauldron subsidence and magmatic stoping. Geol Soc Am Bull 124:213–227. doi:10.1130/B30430.1

Callot JP, Guichet X (2003) Rock texture and magnetic lineation in dykes: a simple analytical model. Tectonophysics 366:207–222. doi: 10.1016/S0040-1951(03)00096-9

Canales JP, Nedimovic MR, Kent GM, Carbotte SM, Detrick RS (2009) Seismic reflection images of a near-axis melt sill within the lower crust at the Juan de Fuca ridge. Nature 460:89–93. doi:10.1038/nature08095

Chadima M, Jelínek V. (2009) Anisoft 4.2: Anisotropy Data Browser for Windows." Agico, Inc.

Clough CT, Maufe HB, Bailey EB (1909) The cauldron subsidence of Glen Coe and the associated igneous phenomena. Q J Geol Soc London 65:611–678. doi: 10.1144/GSL.JGS.1909.065.01-04.35

Cobbing EJ, Pitcher WS (1972) The Coastal Batholith of central Peru. J Geol Soc London 128:421–454. doi: 10.1144/gsjgs.128.5.0421

Cogné JP, Perroud H (1988) Anisotropy of magnetic susceptibility as a strain gauge in the Flamanville granite, NW France. Phys Earth Planet Int 51:264–270. doi: http://dx.doi.org/10.1016/0031-9201(88)90068-4

Corry CE (1988) Laccoliths; Mechanics of emplacement and growth. Geol Soc Am Spec Paper 220:1–114. doi: 10.1130/SPE220-p1

Cruden AR (1990) Flow and fabric development during the diapiric rise of magma. J Geol 98:681–698

Cruden AR (1998) On the emplacement of tabular granites. J Geol Soc London 155:853–862. doi: 10.1144/gsjgs.155.5.0853

Cruden AR, Tobisch OT, Launeau P (1999) Magnetic fabric evidence for conduit-fed emplacement of a tabular intrusion: Dinkey Creek Pluton, central Sierra Nevada batholith, California. J Geophys Res Solid Earth 104:10511–10530. doi: 10.1029/1998JB900093

Cruden AR, McCaffrey KJW (2001) Growth of plutons by floor subsidence: implications for rates of emplacement, intrusion spacing and melt-extraction mechanisms. Phys Chem Earth, Part A Solid Earth Geod 26:303–315. doi: 10.1016/S1464-1895(01)00060-6

Furman T, Meyer PS, Frey F (1992) Evolution of Icelandic central volcanoes – evidence from the Austurhorn intrusion, southeastern Iceland. Bull Volcanol 55:45–62. doi: 10.1007/BF00301119

Froitzheim N, Plašienka D, Schuster R (2008) Alpine tectonics of the Alps and Western Carpathians. In: McCann T (ed) The geology of Central Europe. Volume 2: Mesozoic and Cenozoic. Geological Society Publishing House, London

Geoffroy L, Callot JP, Aubourg C, Moreira M (2002) Magnetic and plagioclase linear fabric discrepancy in dykes: a new way to define the flow vector using magnetic foliation. Terra Nova 14:183–190. doi: 10.1046/j.1365-3121.2002.00412.x

Grocott J, Arevalo C, Welkner D, Cruden A (2009) Fault-assisted vertical pluton growth: Coastal Cordillera, north Chilean Andes. J Geol Soc London 166:295–301. doi: 10.1144/0016-76492007-165

Gudmundsson A (2011) Deflection of dykes into sills at discontinuities and magma-chamber formation. Tectonophysics 500:50–64. doi: 10.1016/j.tecto.2009.10.015

Gudmundsson A (2012) Magma chambers: formation, local stresses, excess pressures, and compartments. J Volcanol Geotherm Res 237–238:19–41. doi: 10.1016/j.jvolgeores.2012.05.015

Harangi S, Downes H, Thirlwall M, Gmeling K (2007) Geochemistry, petrogenesis and geodynamic relationships of Miocene calc-alkaline volcanic rocks in the Western Carpathian Arc, Eastern Central Europe. J Petrol 48:2261–2287. doi:10.1093/petrology/egm059

He B, Xu YG, Paterson S (2009) Magmatic diapirism of the Fangshan pluton, southwest of Beijing, China. J Struct Geol 31:615–626. doi: 10.1016/j.jsg.2009.04.007

Hrouda F (1982) Magnetic anisotropy of rocks and its application in geology and geophysics. Geophys Surv 5:37–82. doi: 10.1007/BF01450244

Hrouda F, Kahan Š (1991) The magnetic fabric relationship between sedimentary and basement nappes in the High Tatra Mountains, N. Slovakia. J Struct Geol 13:431–442. doi: 10.1016/0191-8141(91)90016-C

Hrouda F, Lanza R (1989) Magnetic fabric in the Biella and Traversella stocks (Periadriatic Line): implications for the mode of emplacement. Phys Earth Planet Inter 56:337–348. doi: 10.1016/0031-9201(89)90168-4

Huges RA, Evans JA, Noble SR, Rundle CC (1996) U–Pb chronology of the Ennerdale and Eskdale intrusions supports sub-volcanic relationships with the Borrowdale Volcanic Group (Ordovician, English Lake District). J Geol Soc London 153:33–38. doi: 10.1144/gsjgs.153.1.0033

Jelínek V (1981) Characterization of the magnetic fabric of rocks. Tectonophysics 79:T63–T67

Karell F, Ehlers C, Airo ML, Selonen O (2009) Intrusion mechanisms and magnetic fabrics of the Vehmaa rapakivi granite batholith in SW Finland. Geotect Res 96:53–68. doi: 10.1127/1864-5658/09/96-0053

Koděra P, Lexa J, Rankin AH, Fallick AE (2004) Fluid evolution in a subvolcanic granodiorite pluton related to Fe and Pb–Zn mineralization, Banská Štiavnica ore district, Slovakia. Econ Geol 99:1745–1770. doi: 10.2113/gsecongeo.99.8.1745

Koděra P, Lexa J, Rankin AH, Fallick AE (2005) Epithermal gold veins in a caldera setting: Banská Hodruša, Slovakia. Miner Deposita 39:921–943. doi: 10.1007/s00126-004-0449-5

Konečný P, Lexa J, Hostričová V (1995) The Central Slovakia Neogene Volcanic Field: a review. Acta Vulcanol 7:63–78

Konečný P (2002) Evolution of magmatic reservoir underneath the Štiavnica stratovolcano; in Slovak. Dissertation, Comenius University, Bratislava

Konečný V (1971) Evolutionary stages of the Banská Štiavnica caldera and its post-volcanic structures. Bull Volcanol 35:95–116. doi: 10.1007/BF02596810

Konečný V, Lexa J, Halouzka R, et al. (1998a) Explanations to the geological map of the Štiavnické vrchy and Pohronský Inovec mountain ranges (Štiavnica stratovolcano); in Slovak, State Geol Inst of Dionýz Štúr, Bratislava

Konečný V, Lexa J, Halouzka R, et al. (1998b) Geologic map of Štiavnické vrchy a Pohronský Inovec mountain ranges 1: 50,000; in Slovak. State Geol Inst of Dionýz Štúr, Bratislava

Konečný V, Kováč M, Lexa J, Šefara J (2002) Neogene evolution of the Carpatho–Pannonian region: an interplay of subduction and back-arc diapiric uprise in the mantle. EGU Stephan Mueller Spec Publ Ser 1:105–123

Lexa J, Štohl J, Konečný V (1999) The Banská Štiavnica ore district: relationship between metallogenetic processes and the geological evolution of a stratovolcano. Miner Deposita 34:639–654. doi: 10.1007/s001260050225

Lipman PW (1984) The roots of ash flow calderas in Western North America: windows into the tops of granitic batholiths. J Geophys Res 89:8801–8841. doi: 10.1029/JB089iB10p08801

Lipman PW (2007) Incremental assembly and prolonged consolidation of Cordilleran magma chambers: evidence from the Southern Rocky Mountain volcanic field. Geosphere 3:42–70. doi: 10.1130/GES00061.1

McIntosh WC, Chapin CE (2004) Geochronology of the central Colorado volcanic field. New Mexico Bureau of Geology and Mineral Resources Bulletin 16:205–238

McNulty BA, Tobisch OT, Cruden AR, Gilder S (2000) Multistage emplacement of the Mount Givens pluton, central Sierra Nevada batholith, California. Geol Soc Am Bull 112:119–135. doi: 10.1130/0016-7606(2000)112<119:MEOTMG>2.0.CO;2

Miller RB, Paterson SR (1999) In defense of magmatic diapirs. J Struct Geol 21:1161–1173. doi: 10.1016/S0191-8141(99)00033-4

Myers JS (1975) Cauldron subsidence and fluidization: mechanisms of intrusion of the Coastal Batholith of Peru into its own volcanic ejecta. Geol Soc Am Bull 86:1209–1220. doi: 10.1130/0016-7606(1975)86<1209:CSAFMO>2.0.CO;2

Nagaoka Y, Nishida K, Aoki Y, Takeo M, Ohminato T (2012) Seismic imaging of magma chamber beneath an active volcano. Earth Planet Sci Lett 333–334:1–8. doi: 10.1016/j.epsl.2012.03.034

Nagata T (1962) Rock magnetism. Maruzen, Tokyo

Nelson ST, Davidson JP, Heizler MT, Kowallis BJ (1999) Tertiary tectonic history of the southern Andes: the subvolcanic sequence to the Tatara–San Pedro volcanic complex, lat 36°S. Geol Soc Am Bull 111: 1387–1404. doi: 10.1130/0016-7606(1999)111<1387:TTHOTS>2.3.CO;2

O’Driscoll B, Troll VR, Reavy RJ, Turner P (2006) The Great Eucrite intrusion of Ardnamurchan, Scotland: reevaluating the ring-dike concept. Geology 34:189–192. doi: 10.1130/G22294.1

Paterson S, Vernon R (1995) Bursting the bubble of ballooning plutons: a return to nested diapirs emplaced by multiple processes. Geol Soc Am Bull 107:1356–1380. doi: 10.1130/0016-7606(1995)107<1356:BTBOBP>2.3.CO;2

Paterson SR, Farris DW (2008) Downward host rock transport and the formation of rim monoclines during the emplacement of Cordilleran batholiths. Trans Roy Soc Edinb Earth Sci 97:397–413. doi: 10.1017/S026359330000153X

Paterson SR, Fowler TK, Miller RB (1996) Pluton emplacement in arcs: a crustal-scale exchange process. Geol Soc Am Spec Paper 315, 115–123. doi: 10.1130/0-8137-2315-9.115

Paterson SR, Fowler TK, Schmidt KL, Yoshinobu, AS, Yuan, ES, Miller, RB (1998) Interpreting magmatic fabric patterns in plutons. Lithos 44:53–82. doi: 10.1016/S0024-4937(98)00022-X

Pecskay Z, Lexa J, Szakács A, Seghedi I, Balogh K, Zelenka T, Kovacs M, Poka T, Fulop A, Marton E, Panaiotu C, Cvetkovic V (2006) Geochronology of Neogene magmatism in the Carpathian arc and intra-Carpathian area. Geol Carpathica 57:511–530.

Petronis MS, Hacker DB, Holm DK, Geissman JW, Harlan SS (2004) Magmatic flow paths and palaeomagnetism of the Miocene Stoddard Mountain laccolith, Iron Axis region, Southwestern Utah, USA. In: Martín-Hernández F, Lüneburg CM, Aubourg C, Jackson M (eds) Magnetic fabric: methods and application. Geol Soc London Spec Publ 238:251–283. doi:10.1144/GSL.SP.2004.238.01.16

Petronis MS, O'Driscoll B (2013) Emplacement of the early Miocene Pinto Peak intrusion, Southwest Utah, USA. Geochemistry, Geophys Geosystems 14:5128–5145. doi: 10.1002/2013GC004930

Philpotts AR, Philpotts DE (2007) Upward and downward flow in a camptonite dike as recorded by deformed vesicles and the anisotropy of magnetic susceptibility (AMS). J Volcanol Geotherm Res 161:81–94. doi: 10.1016/j.jvolgeores.2006.11.006

Plašienka D (2003) Development of basement-involved fold and thrust structures exemplified by the Tatric–Fatric–Veporic nappe system of the Western Carpathians (Slovakia). Geodin Acta 16:21–38. doi: 10.1016/S0985-3111(02)00003-7

Ramsay JG (1989) Emplacement kinematics of a granite diapir: the Chindamora batholith, Zimbabwe. J Struct Geol 11:191–209. doi: http://dx.doi.org/10.1016/0191-8141(89)90043-6

Roobol MJ (1974) The geology of the Vesturhorn intrusion, SE Iceland. Geol Mag 111:273–286. doi: 10.1017/S001675680003867X

Seager WR, McCurry M (1988) The cogenetic Organ cauldron and batholith, South Central New Mexico: evolution of a large-volume ash flow cauldron and its source magma chamber. J Geophys Res 93:4421–4433. doi: 10.1029/JB093iB05p04421

Štohl J, Hojstričová V, Lexa J, Rojkovičová L, Žáková E, Gargulák M, Staňa Š, Kantor J, Ďurkovičová J (1990) Evaluation of the bore hole B-1/2000 m, Horná Roveň. Open file report. State Geol Inst of Dionýz Štúr, Bratislava

Tarling DH, Hrouda F (1993) Magnetic anisotropy of rocks. Chapman and Hall, London

Twiss RJ, Moores EM (1992) Structural Geology. WH Freeman and Company, New York.

Vernon RH (2000) Review of microstructural evidence of magmatic and solid-state flow. Electronic Geosci 5:1–23. doi: 10.1007/s10069-000-0002-3

Vernon RH, Johnson SE, Melis EA (2004) Emplacement-related microstructures in the margin of a deformed pluton: the San José tonalite, Baja California, México. J Struct Geol 26: 1867–1884

Wyss M, Shimazaki K, Wiemer S (1997) Mapping active magma chambers by b values beneath the off-Ito volcano, Japan. J Geophys Res 102:20413–20422. doi: 10.1029/97JB01074

Yoshinobu AS, Fowler TK, Paterson SR, Llambias E, Tickyj H, Sato AM (2003) A view from the roof: magmatic stoping in the shallow crust, Chita pluton, Argentina. J Struct Geol 25:1037–1048. doi: 10.1016/S0191-8141(02)00149-9

Chapter *3:*

VOLCANO–TECTONIC INTERACTIONS, CRUSTAL STRAIN, AND PLATE KINEMATICS DURING LATE CRETACEOUS SHUTDOWN OF THE SIERRA NEVADA MAGMATIC ARC, CALIFORNIA

by Filip Tomek, Jiří Žák, Kryštof Verner, František V. Holub, Jiří Sláma, Scott R. Paterson, Valbone Memeti

a manuscript under review in **Geological Society of America Bulletin**

(additional information are listed in appendix item 3)

KEY WORDS

◇ Anisotropy of magnetic susceptibility (AMS)

◇ Pluton emplacement

◇ Sierra Nevada batholith

◇ Tectonic strain

◇ U–Pb zircon geochronology

VOLCANO–TECTONIC INTERACTIONS, CRUSTAL STRAIN, AND PLATE KINEMATICS DURING LATE CRETACEOUS SHUTDOWN OF THE SIERRA NEVADA MAGMATIC ARC, CALIFORNIA

ABSTRACT

The mid-Cretaceous Minarets caldera is a volcano–plutonic complex in the central Sierra Nevada batholith, California, that greatly exemplifies the complex interactions among continental-margin arc volcanism, tectonic deformation of the magma–host rock system, and changes in plate motions during subduction of oceanic lithosphere. The caldera development commenced with emplacement of voluminous, pre-collapse rhyolitic ash-flow tuff, possibly a product of a large Plinian eruption at ~101 Ma. Extensive overlying collapse breccia marks the caldera downdrop, followed by deposition of rhyodacitic ash-flow tuff. Subsequently, the sequence was deformed and tilted along the Bench Canyon transpressional shear zone in the western part of the caldera. Our new high-precision U–Pb zircon ages suggest caldera resurgence at ~100 Ma, associated with emplacement of the steep-sided Shellenbarger granite pluton into the caldera center. Ductile strain during pluton emplacement caused steepening of the shear zone foliation and constrains the age of shearing to >100 Ma. The post-caldera volcanic activity continued at least until ~96.7 Ma.

Our structural and anisotropy of magnetic susceptibility (AMS) data indicate that the Shellenbarger pluton was overprinted by ~NNE–SSW horizontal shortening and subvertical stretching during both late stages of magma crystallization and postmagmatic alteration from hydrothermal fluid flow focused to the pluton center. The same horizontal shortening has also been documented in several other Late Cretaceous syntectonic plutons of the central Sierra Nevada. However, they record two principal stretching directions: near-vertical magmatic stretching in ~102–86 Ma plutons and subhorizontal late magmatic to subsolidus stretching in ~87–86 Ma plutons. It is inferred that the rotation of the principal stretching direction at around 87–86 Ma reflects a continuous change in plate kinematics and resulting arc deformation from pure shear-dominated transpression to wrench-dominated dextral transpression. This major kinematic switch is compatible with increased obliquity of convergence of the Farallon plate subducting beneath the North American plate and also coincided with the abrupt cessation of the Late Cretaceous flare-up period in the Sierra Nevada magmatic arc. From this time on, the magmatic front migrated towards the interior of the North American plate, perhaps as a result of combined high convergence obliquity, the shortening distance to the slab, and thickening of the arc root.

INTRODUCTION

Large silicic volcano–plutonic systems in the continental-margin arcs are direct products of protracted subduction of oceanic plates beneath continental edges (e.g., Hamilton, 1969; Tatsumi and Eggins, 1985; Silver and Chappell, 1988; Brandon and Smith, 1994; Tatsumi and Kogiso, 2003;

Tatsumi, 2005; Haschke at al., 2006; Paterson and Ducea, 2015; DeCelles et al., 2015; Ducea et al., 2015). It has long been established that the petrogenesis of arc magmas can be used to track the tectonic evolution of arc systems, reflecting changes in relative plate kinematics, subduction zone geometry, slab window formation and break-off, and building and foundering of arc roots (e.g., Jordan et al., 1983; Pilger, 1984; Davies and von Blanckenburg, 1995; Pearce and Peate, 1995; Thorkelson, 1996; Gorton and Schandl, 2000; Heuret et al., 2007; Becker and Faccena, 2009; Karlstrom et al., 2014; Currie et al., 2015). In addition, it has been increasingly recognized that the structural inventory of granitoid plutons is also an excellent ʽarchive' of mechanical processes in arcs (e.g., Paterson et al., 1998; Petford et al., 2000; Vernon, 2000; Petford, 2003; Benn, 2004; Vernon and Paterson, 2006; Paterson, 2009). Arc plutons commonly display internal hypersolidus fabrics (foliations and lineations), defined by planar and linear shape-preferred alignment of mineral grains, aggregates, and microgranular enclaves, respectively, formed in the presence of melt (e.g., Paterson et al., 1989). Since the 1970s, following the seminal work of Pitcher and Berger (1972), a large body of literature documented that pluton fabrics may record not only magma flow in a chamber or its emplacement into the Earth's crust but also regional tectonic strain. The underlying assumption is that a magmatic foliation forms perpendicular to the maximum shortening (and thus represents the z-axis of the strain ellipsoid), whereas a lineation indicates the maximum stretching direction, i.e., is parallel to the x-axis of the strain ellipsoid (e.g., Hutton, 1988; Paterson et al., 1998). The synmagmatic tectonic strain of plutons is inferred to have been imposed on the near-solidus, stiff crystal mushes to rigid crystal–melt frameworks (e.g., Marsh, 1981; Bachmann and Berghanz, 2004, 2008; Hildreth, 2004; Miller et al., 2011) wherein the magma cannot flow but the individual melt-lubricated crystals are still capable of sliding past each other to realign into a new fabric (e.g., Park and Means, 1996). These fabrics are assumed to rapidly 'freeze-in' along crystallization fronts, thus recording increments of tectonic strain at an instant of geologic time (e.g., Paterson et al., 1998). This recognition was a major advance in understanding the ʽstructural archives' of arc plutons and promoted an on-going extensive use of pluton fabrics as markers of even subtle temporal changes in the paleodeformation fields (e.g., Snow and Wernicke, 2000; Chardon, 2003; Callahan and Markley, 2003; Cao et al., 2015).

Tectonic strains along plate margins are commonly generated by stress resulting from plate convergence, thus the question arises whether pluton fabrics can also be used to interpret past plate motions. Though the relationship among fabric and inferred strain axes in granitoid plutons and plate kinematics may not be straightforward, especially in the upper crust, due to heterogeneous deformation and strain partitioning, several studies argued that normals to magmatic foliations may possibly match the plate motion vectors (e.g., Benn et al., 2001; Cao et al., 2015). Another related, yet largely unresolved issue is whether volcanics and plutons in the uppermost portions of magmatic arc systems may also be used as tectonic strain (and plate motion?) markers or whether they cool too fast with respect to generally ʽslower' tectonic deformation. Indeed, many high-level, subvolcanic intrusions display only weak mineral alignments or even appear macroscopically isotropic, which contrasts with deeper sections through arc plutons, which commonly display well recognizable fabric.

This paper attempts to address the above issues and deals with the complex interactions among volcanic, magmatic, and tectonic processes in the mid-Cretaceous Minarets caldera and its resurgent intrusion, the Shellenbarger pluton, in the central Sierra Nevada, California (Fig. 1A, B). Based on detailed field and structural data supported by U–Th–Pb in-situ LA ICP-MS zircon dating, we present a refined model for evolution of the Minarets volcano–plutonic complex. Furthermore, using the anisotropy of magnetic susceptibility (AMS) as an extremely sensitive technique capable of detecting even 'invisible' fabrics in fine-grained volcanic rocks (e.g. Tarling and Hrouda, 1993; Borradaile and Henry, 1997; Bouchez, 1997; Borradaile and Jackson, 2004, 2010; Lock et al., 2008; Petronis et al., 2013), we infer paleostrain orientation during caldera collapse and resurgence. These data are then compared with the existing structural and geochronological data from other plutons and metamorphic rocks in the central Sierra Nevada magmatic arc to discuss paleostrain field changes and their possible relation to convergence of the Farallon and North American plates. We conclude that fabrics in subvolcanic intrusions recorded a major switch in plate kinematics, which may have been one of the geodynamic factors associated with termination of voluminous arc plutonism in the Sierra Nevada during the Late Cretaceous.

GEOLOGIC SETTING

The Minarets caldera

The mid-Cretaceous Minarets caldera (~30 × 22 km) preserves a tilted section through Lower Cretaceous meta-volcanic caldera basement (~144–127 Ma, U–Pb on zircons; Fiske and Tobisch, 1978, 1994; Tobisch and Fiske, 2000), up to 5 km thick collapse deposits, and a post-collapse intrusion represented by the Shellenbarger pluton (Fig. 1A). To the E and NE, the caldera is bordered by a subvertical ring fault that is intruded by a late dolerite porphyry (Fig. 1A, B; Fiske and Tobisch, 1994).

From bottom to top, the volcanic succession of the Minarets caldera comprises four main units. (1) A basal sequence of variable thickness controlled by paleorelief and consisting of glassy porphyritic volcanic rocks and conglomerates to breccias containing tuff and lava clasts (Fiske and Tobisch, 1978, 1994). (2) An overlying ash-flow tuff, which is up to 2.2 km thick and is composed of rhyolite to rhyodacite. (3) The up to 2 km thick caldera collapse deposit is composed of a coarse tuff-breccia containing volcanic clasts or blocks ranging in size from a few centimeters up to 1.8 km (Fiske and Tobisch, 1994). The clast compositions include juvenile rhyolitic to dacitic pumice tuff, lava and lithic volcanic rocks of the host caldera. The collapse deposits grade upward into fine-grained rhyolitic tuff and (4) a post-collapse sequence of rewashed, bedded lapilli tuff and tuff-breccia deposited in a caldera lake environment (Fiske and Tobisch, 1978). Radiometric U–Pb dating of zircons from the ash-flow tuff and collapse deposits yielded ages of 101 and 98 Ma, respectively (errors not given; Fiske and Tobisch, 1994).

A detailed geochemical study by Lowe (1996) identified important vertical compositional changes in the caldera volcanics: (1) the total SiO_2 content in the ash flow tuff decreases up section from rhyolitic (74.6 % SiO_2) to rhyodacitic and dacitic compositions (67.5 % SiO_2); (2) this trend is accompanied by an increase in the proportion of lithic fragments which dramatically decreases across a sharp horizon; and (3) the abundance of phenocrysts drops at the base of the collapse deposits and is accompanied by a transition to less evolved compositions. On the other hand, the average Sri remains consistent across the ash-flow tuffs, implying a single large-scale caldera eruption from a stratified magma chamber (Lowe, 1996). These compositional shifts at the sharp horizon are explained as reflecting change in the eruptive rate, caused by intrusion of mafic magma into the sub-caldera magma chamber and by the caldera collapse itself. Hence, similarly to Fiske and Tobisch (1978), Lowe (1996) suggested that the lower rhyolitic ash-flow tuff corresponds to a pre-collapse eruption, which was followed by the deposition of the collapse, coarse collapse tuff-breccia reflecting the caldera collapse and by emplacement of post-collapse rhyodacitic to dacitic ash-flow tuffs. Finally, Lowe (1996) concluded that the Minarets caldera in its original extent as defined by Fiske and Tobisch (1994) merges two separate complexes (the other referred to as the Merced Peak caldera to the west), each having distinct geochemical compositions (Fig. 1B).

It remains unclear whether some of the plutonic units intruding the Minarets caldera (Fig. 1A) could potentially represent the sub-caldera magma chamber. Whereas most of these granitoids are clearly younger and postdate the caldera formation (McNulty et al., 1996, 2000; Memeti et al., 2010), the ~98 Ma Jackass Lake pluton to the W was broadly coeval with the caldera collapse (Fig. 1B). Indeed, the Jackass Lake pluton was first interpreted as a resurgent pluton that intruded into its own volcanic ejecta (Peck, 1980; McNulty et al., 1996; Fiske and Tobisch, 1994), and Lowe (1996) also inferred its genetic link to the Merced Peak caldera. In contrast, Pignotta et al. (2010) suggested a separate evolution of the pluton and the Merced Peak caldera. In the northeasterly Rush Creek pluton (99.9 ± 2.2 Ma; Rb–Sr whole-rock), Kistler and Swanson (1981) found a geochemical pattern similar to the caldera volcanic rocks and the Shellenbarger pluton. However, a spatial relation between there rocks is missing, and this interpretation is also challenged by recent radiometric dating of the Rush Creek pluton that determined a younger age of ~95–94 Ma (U–Pb on zircons; Black et al., 2010).

Transpressive shear zones

Volcanic rocks of the Minarets caldera have been affected by pervasive greenschist facies metamorphism, regional deformation, and localized ductile shearing along the Bench Canyon shear zone in the W part of the Minarets caldera (Fig. 1A, B; e.g., Fiske and Tobisch, 1978). This up to 3 km wide and ~20 km long ~NNW–SSE- to ~NW–SE- trending shear zone separates rocks of the Minarets caldera from the older volcanic basement (Fig. 1A, B). According to published data, the shear zone was episodically active in three stages, and in part synchronous with the caldera collapse (McNulty, 1995; Tobisch et al., 1995). (1) An early phase at ~101–95 Ma was possibly associated with the reactivation of the Minarets caldera ring fault (Fiske and Tobisch, 1994) and was completed by emplacement of the Red Devil Lake pluton and associated sills (95 ± 1 Ma; U–Pb on zircons, Tobisch et al., 1995). (2) The main phase of shearing continued at ~95–90 Ma in a ductile compressional regime and resulted in a pervasive overprint of the volcanic rocks. The deformation is bracketed by the emplacement of the syntectonic Red Devil Lake and posttectonic

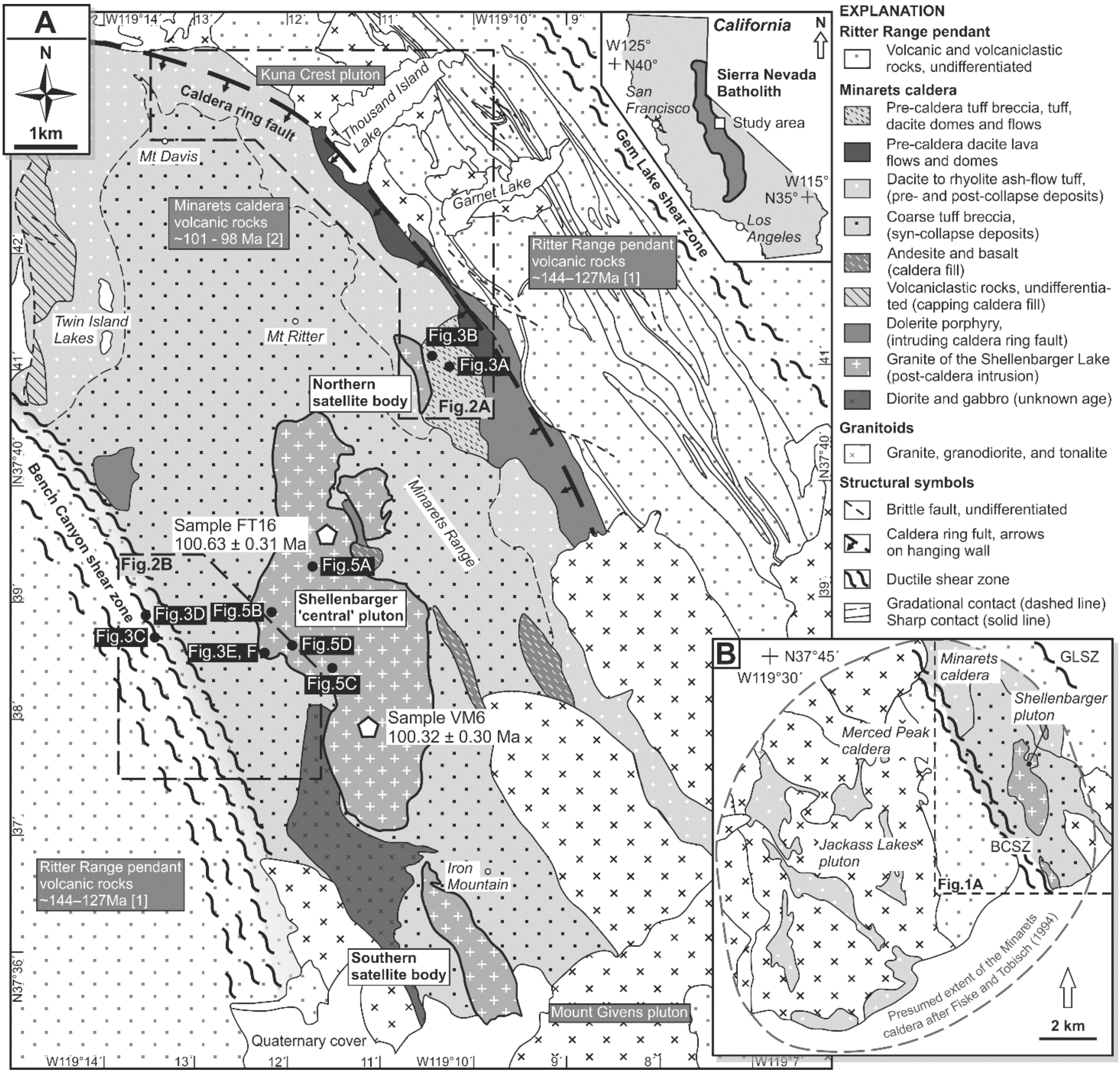

Figure 1 (A) Simplified geologic map of northeastern part of the Minarets caldera. Modified after Fiske and Tobisch (1994) and Hubert and Rinehart (1965). Note the position of new radiometric ages of Shellenbarger pluton (this study). Inset: position of studied area, Sierra Nevada, California. (B) The original extent of the Minarets caldera – the dashed line, after Fiske and Tobisch (1994), later reinterpreted by Lowe (1996) as representing two individual Minarets and Merced Peak calderas separated by the Bench Canyon shear zone (BCSZ). Radiometric dating: [1] Fiske and Tobisch (1978); [2] Fiske and Tobisch (1994).

Mount Givens plutons (90 ± 1 Ma; McNulty et al., 2000). (3) A late phase (~90–78 Ma) was weak, localized, and is marked by hydrothermal alteration and brittle faulting (McNulty, 1995; Tobisch et al., 1995).

About 3 km to the NE of the caldera, the Gem Lake shear zone cross-cuts the older volcanic rocks of the Northern Ritter Range pendant. The shear zone was active at ~94–80 Ma but may have started earlier (Greene and Schweickert, 1995; Memeti et al., 2010) at around 110 Ma (S.R. Paterson, unpublished data). This indicates that the deformation may have overlapped with the caldera collapse, however no direct evidence of caldera deformation by the Gem Lake shear zone was identified. The shear zone is ~30 km long, ~1 km wide, steep, ~NNW–SSE- to ~NW–SE-trending. It has been interpreted as a dextral transpressional shear zone with a minimum displacement of about 20 km (Fig. 1A; Greene and Schweickert, 1995). The Gem Lake shear zone is considered as one segment of the extensive ~NW–SE-trending Sierra Crest shear zone system which accommodated oblique convergence of the Pacific and North American plates at ~94–80 Ma (Tikoff and de Saint Blanquat, 1997; Tikoff and Greene, 1997; Tikoff and Teyssier, 1992).

The Shellenbarger pluton

The center of the Minarets caldera was intruded by the Shellenbarger pluton (previously referred to as granite of Shellenbarger Lake) which comprises a ‘central’ ~12.5 km2 pluton and two small satellite bodies exposed to the NE and S (Fig. 1A). Except for a small gabbro–diorite intrusion of uncertain age at the southwestern margin of the pluton, the granite was emplaced solely into the collapse deposits of the Minarets caldera (Fig. 1A, B; Fiske and Tobisch, 1994). The existing radiometric ages of the Shellenbarger pluton are imprecise and poorly constrained. Fiske and Tobisch (1994) obtained an age of 99 Ma (U–Pb on zircons, errors not given), Lowe (1996) constrained the age to 93 Ma with a 'large’ error (not given, U–Pb on zircons) and to 94.5 ± 1.2 Ma (Rb–Sr on whole rock), all indicating that the caldera deposits and the pluton are broadly coeval. Fiske and Tobisch (1994) also pointed out that the pluton may represent the source of the caldera deposits and was emplaced at a very shallow level into its own volcanic ejecta during caldera resurgence. Geochemical modeling by Lowe (1996) indicates that, rather than being equivalent to the ash-flow tuffs, the granite represents either a late melt formed after 70–75% equilibrium crystallization of residual rhyolite in the magma chamber or was derived by 25–30% partial melting of the still hot ash-flow tuff itself.

Mesoscopic deformational structures in the volcanic rocks

In this study, two areas in the Minarets caldera were mapped in detail: the NE portion of the caldera between Thousand Island and Garnet Lakes (Area 1, Fig. 2A) and the northern Bench Canyon area near Hemlock Crossing along the contact of volcanic rocks with the Shellenbarger pluton (Area 2; Figs. 2B).

In Area 1, the northern satellite body of the Shellenbarger pluton intrudes into ash-flow tuffs and collapse breccias (Fig. 2A). Both rock types are generally weakly metamorphosed and deformed and in some places preserve variably oriented original bedding and texture (Fig. 3A, B). ocally, the same rocks are strongly deformed and exhibit steep ~NW–SE striking foliation and associated stretching lineation plunging moderately to steeply to the ~WNW and ESE (Fig. 2A). In Area 2, the 'central' Shellenbarger pluton intruded volcanic breccias overprinted by intense ductile deformation along the Bench Canyon shear zone (Fig. 2B). The breccia west of Bench Canyon are composed of tuff and lapilli-tuff matrix containing basic to intermediate clasts (Fig. 3C) and also

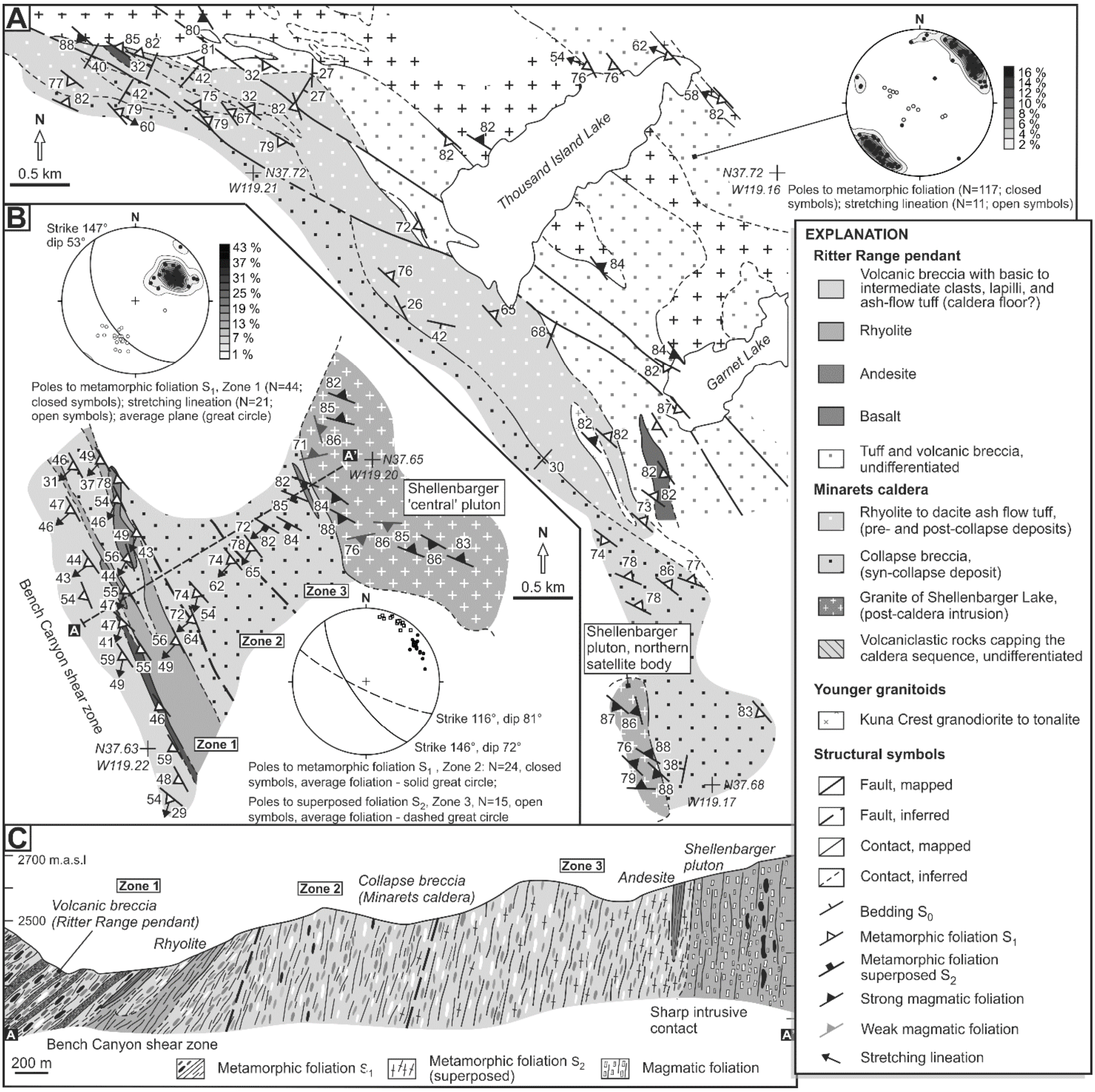

Figure 2 (A) Detailed geologic map to NNE from the Shellenbarger pluton – Area 1. (B) Detailed geologic map of the western margin of Shellenbarger pluton and its host rocks – Area 2. The white dashed line marks the position of the cross-section. Stereonets are equal-area, lower hemisphere. (C) An interpretative cross-section trough contact of the Shellenbarger pluton and its host rocks.

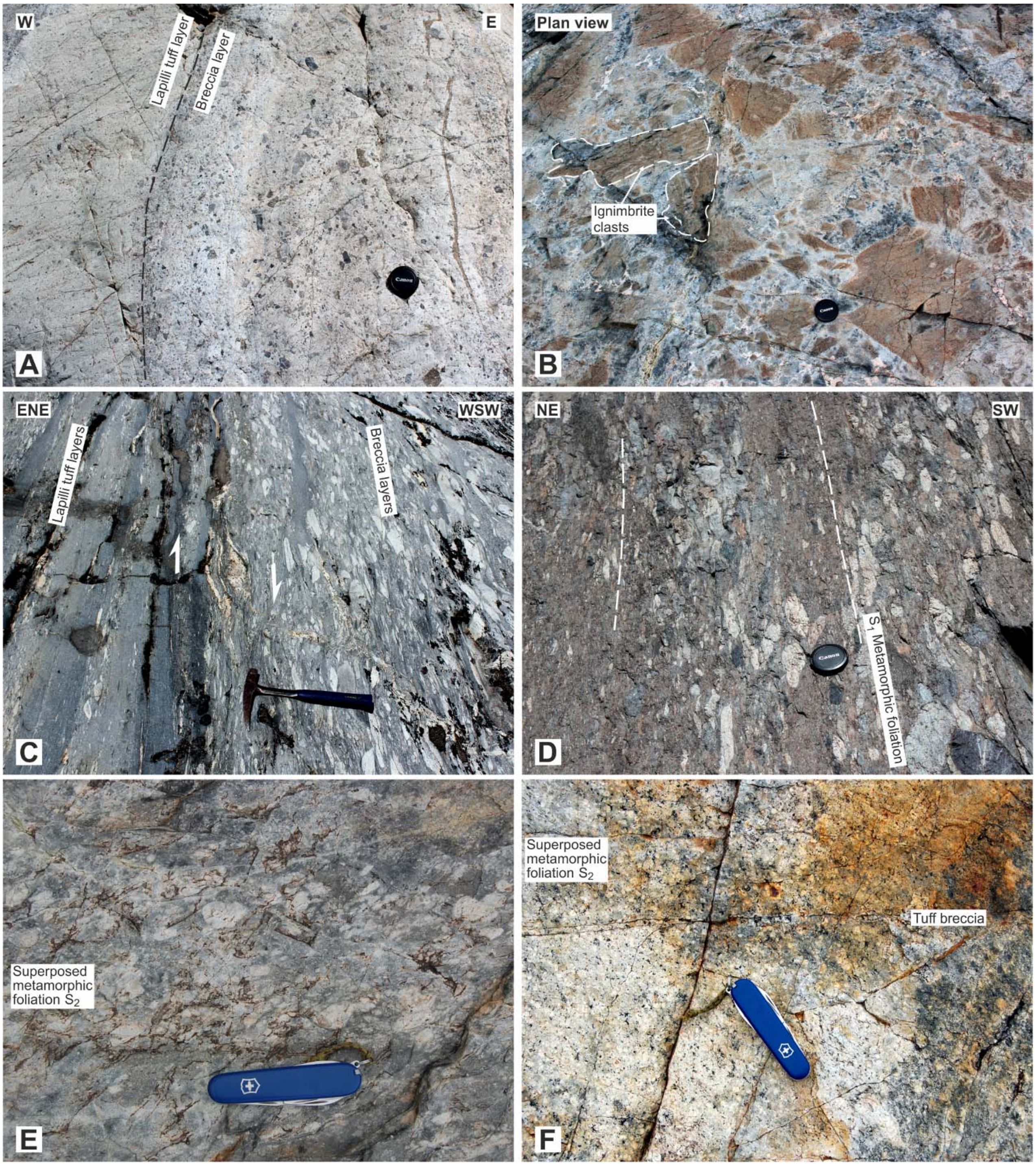

Figure 3 (A) Undeformed collapse breccia with large rhyolitic ash-flow clasts; station FT57, coordinates: N37.67993°, W119.17090°; camera lens cap for scale. (B) Undeformed, gently dipping sequence of intercalated lapilli tuff with blocky layers; station FT58, coordinates: N37.67984°; W119.17183°; camera lens cap for scale. (C) Steeply dipping, deformed (meta-) volcanic host rock, intercalation of fine ash and lapilli bands with coarse blocky layers. Dextral, top-to-the north kinematics; station FT25, coordinates: N37.64159°, W119.22652°; hammer for scale. (D) Steeply dipping, strongly deformed (meta-)volcanic breccia; station FT24, coordinates: N37.64739°, W119.22914°; camera lens cap for scale. (E) Superposition of S2 fabric on the lithological boundaries, parallel toS1 fabric. (F) S2 fabric overprinting pluton/host rock contact; Swiss army pocket knife for scale, both photos taken at station JZ7, coordinates: N37.64602°, W119.20565°; Swiss army pocket knife for scale. All coordinates are referenced to WGS84 datum.

host minor lenses of rhyolite, basaltic lavas, and andesite dikes (Fig. 2B, C). The breccia alternates with fine ash tuff and lapilli tuff layers in some places (Fig. 3C). East of Bench Canyon, the breccia contains intermediate to silicic and lithic clasts (Fig. 3D). A narrow andesite dike was also mapped near the contact with the Shellenbarger pluton (Fig. 2B).

All units in Area 2 are intensely deformed and display strong deformational fabric which leaves their original volcanic relations uncertain in many places. On the basis of fabric orientation and structural relations, three ~NW–SE-trending zones have been identified along a transect perpendicular to the western margin of the Shellenbarger pluton. In an outer zone (Zone 1 in Fig. 2B, C) in the middle of Bench Canyon, both compositional banding (referred to as S_0 for the purpose of this study) and a metamorphic foliation (S_1) strike ~NW–SE and dip moderately (mean dip is 53°) to the ~SW . The associated stretching lineation plunges moderately (42°) to the ~SSW (Fig. 2B). In an intermediate zone (Zone 2 in Fig. 2B), the bedding and foliation S_1 steepen to dips of about 70°, maintaining the same strike, and the stretching lineation plunges steeply to the SSW. The lineation is also commonly associated with a reverse sense of shear, documented by asymmetric winged clasts and asymmetrically folded quartz veins. In a ~0.5 km wide zone along the pluton margin (Zone 3 in Fig. 2B), foliation S1 has the same orientation as that in Zone 2, but is locally superimposed by a ~WNW–ESE subvertical foliation (S_2; Fig. 2B, C) which becomes more penetrative as the pluton margin is approached. The S_2 foliation overprints compositional banding (parallel to the S_1) in the collapse tuff-breccia (Fig. 3E) and is also at a high angle to the pluton/host rock contact (Fig. 3F).

THE SHELLENBARGER PLUTON

Field relationships, textural zoning, and structure

In map view, the 'central' pluton has a ~N–S elongated sigmoidal shape (Fig. 4A). Its outer contacts are intrusive, sharp, planar to gently curved, and vary in orientation from generally flat against the roof (Fig. 4B) to dipping steeply outward against the wall (Fig. 4C, D). On a decimeter scale, the contact may be highly irregular (Fig. 4F). The northern satellite body has also a ~NNW–SSE elongated shape in map-view and outward-dipping contacts (Fig. 4E). The southern body is also elongated in the same direction (Fig. 1A) but the contacts are not well exposed.

The granite is fine-grained, porphyritic with feldspar phenocrysts 1–10 mm in size (Fig. 5A, B), exhibits no significant macroscopic compositional variations, and lacks obvious sheeting and host rock xenoliths. Based on the groundmass microtexture, however, two granite facies can be identified in the pluton: fine-grained porphyritic and granophyric to micrographic (Fig. 6A, B). The former delineates the western pluton margin in an about 300 m wide zone, whereas the latter occupies the pluton center (Fig. 7A). These two facies thus define concentric textural zoning in the pluton with, gradational contacts

Mineral composition of both granite types is dominated by albitized plagioclase, K-feldspar, and quartz (Fig. 6A–D). On the microscale, glomerocrysts (1–6 mm in size, Fig. 6A, B) or individual crystals of albite are unzoned and clouded with minute grains of clay minerals, epidote-

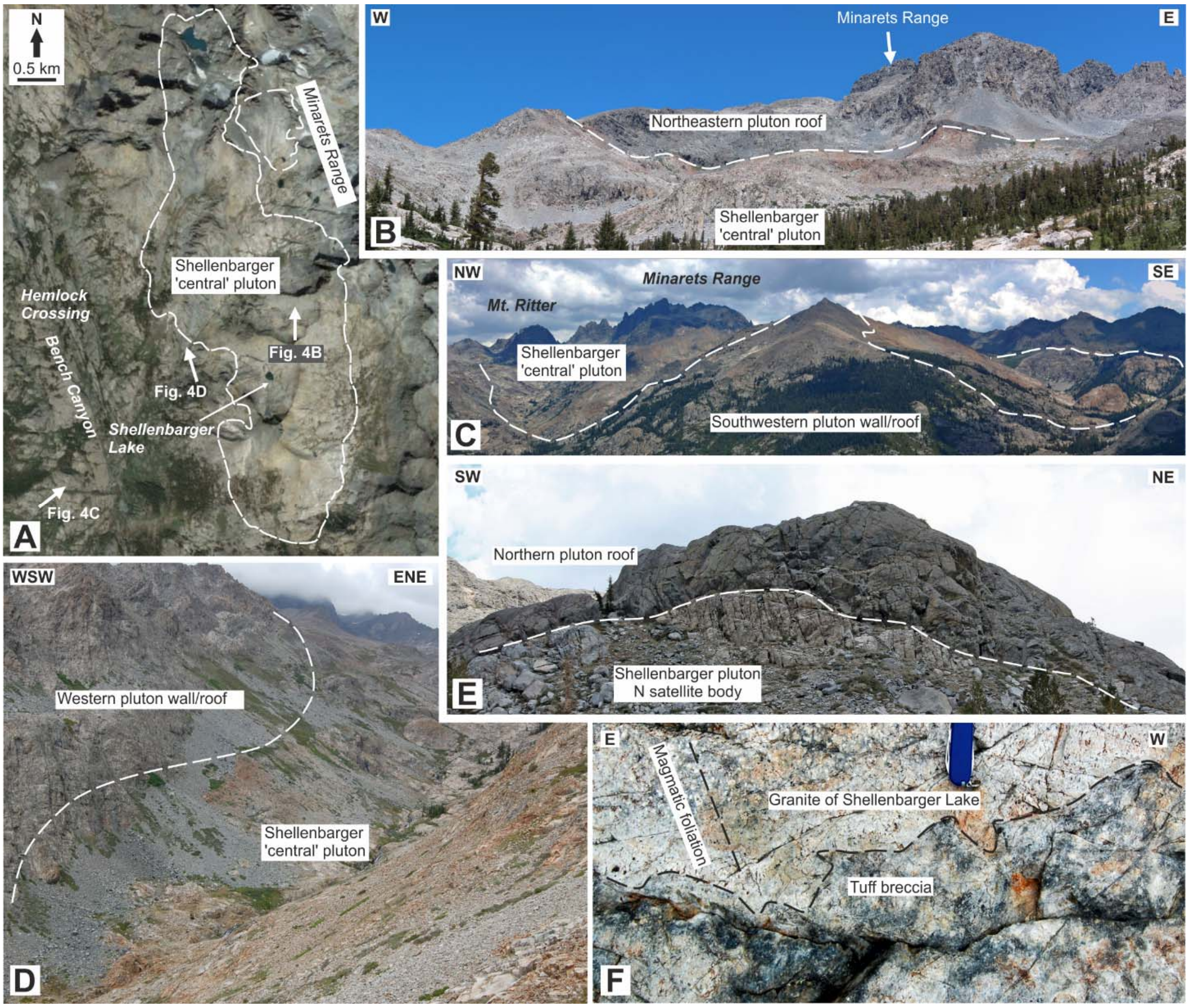

Figure 4 (A) Google Earth image of the Shellenbarger Lake pluton in the area between the Minarets and the Bench Canyon, Sierra Nevada, California. The arrows mark locations of next photos; (B) Panorama photo on the pluton/roof contact from the Iron Creek; station FT28, coordinates: N37.63639°, W119.18099°; (C) Panoramic view on the Shellenbarger pluton from the area of Lost Lake; (D) Outward dipping contact of the pluton and the host rock; station JZ07, coordinates: N37.64602°, W119.20565°; (E) Detail of contact of the granite and the host rock volcanic breccia; station JZ07, coordinates: N37.64602°, W119.20565°; (F) A dome-like pluton/roof contact near the Ediza Lake; station FT59, coordinates: N37.67988°, W119.17525°. All coordinates are referenced to WGS84 datum.

group minerals, and calcite in some places. Rarely, clouded albite was produced by partial albitization of K-feldspar. Similar alteration was described by Hanson et al. (2003) and Sorensen et al. (1998) in the volcanic rocks of the Ritter Range pendant. Another variety is nearly unclouded albite forming intergrowths with K-feldspar in the groundmass (Fig. 6C). The textural criteria prove that the intergrowths are formed by exsolution from original alkali-feldspars (sanidine?). Quartz forms isolated small grains (~200 μm in size) that commonly display undulatory extinction and chessboard pattern (Fig. 6C). Some of the examined thin sections revealed post-magmatic minerals in pseudomorphs, irregular clusters, and microcrack fillings. These minerals include aggregates of fine-grained dark micas, chlorite, individual grains or aggregates of epidote, magnetite, frequently also Ca-rich garnet, and titanite (Fig. 6D). Primary accessory minerals are

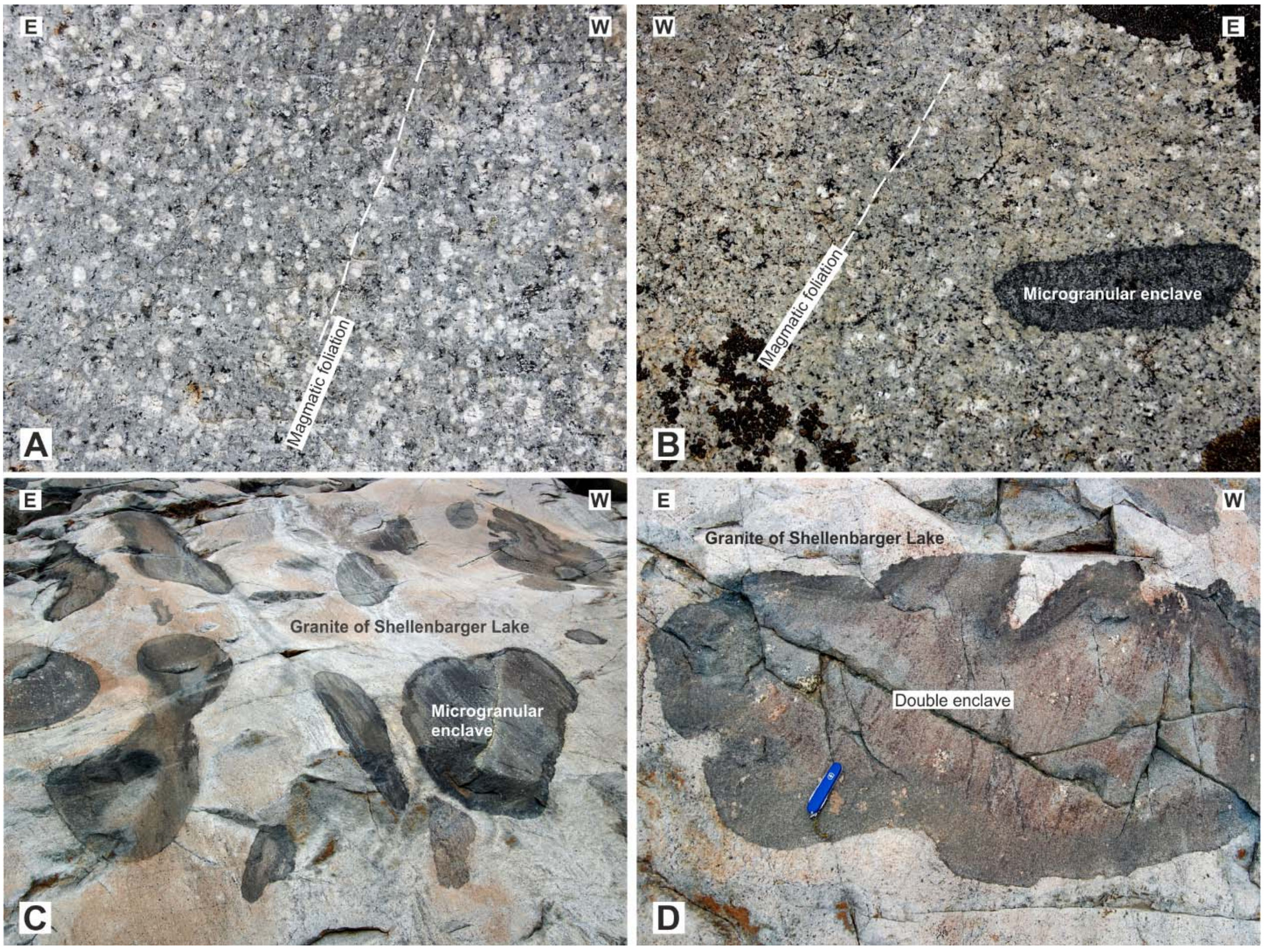

Figure 5 (A) A plan view of magmatic foliation in the Shellenbarger Lake granite; station FT15, coordinates: N37.65844°, W119.19765°; (B) Magmatic foliation in the granite and microgranular enclave; station FT4; coordinates: N37.64435°; W119.19888°; (C) Swarm of microgranular enclaves; (D) A mafic microgranular enclave close up with crenulation margins; both from station JZ3, coordinates: N37.64391°; W119.19770°; (E) Contact of porphyritic and fine-grained granite, magmatic foliation highlighted by black dashed line; station JZ6, coordinates: N37.64497°, W119.20318°. All coordinates are referenced to WGS84 datum.

represented by sporadic tiny apatite, zircon, and some magnetite grains (where not in association with post-magmatic minerals).

Microgranular enclaves, either scattered or in swarms, are abundant along the western margin of the pluton (Fig. 2C). The enclaves are either composed of sparse fine-grained porphyritic diorite or consist of two distinct textural and compositional varieties of diorite. They vary in size from a few centimeters to several meters and their shapes are rounded to highly flattened, commonly with lobate margins and with their long axes parallel to the nearby pluton margin (Fig. 5C, D).

Mesoscopic magmatic foliation in the granite is defined by planar shape-preferred orientation of albite and K-feldspar phenocrysts (Fig. 5A, B), whereas a lineation is generally absent. The foliation is subvertical and strikes ~WNW–ESE to ~NW–SE in the west-central and southern portions of the pluton, respectively. To the N, the pluton and the satellite body display both ~WNW–ESE and ~NW–SE foliation (Fig. 7B). The inferred foliation traces thus define chiefly a sigmoidal pattern in the 'central' pluton (highlighted by dashed lines in Fig. 7B) and are at a high

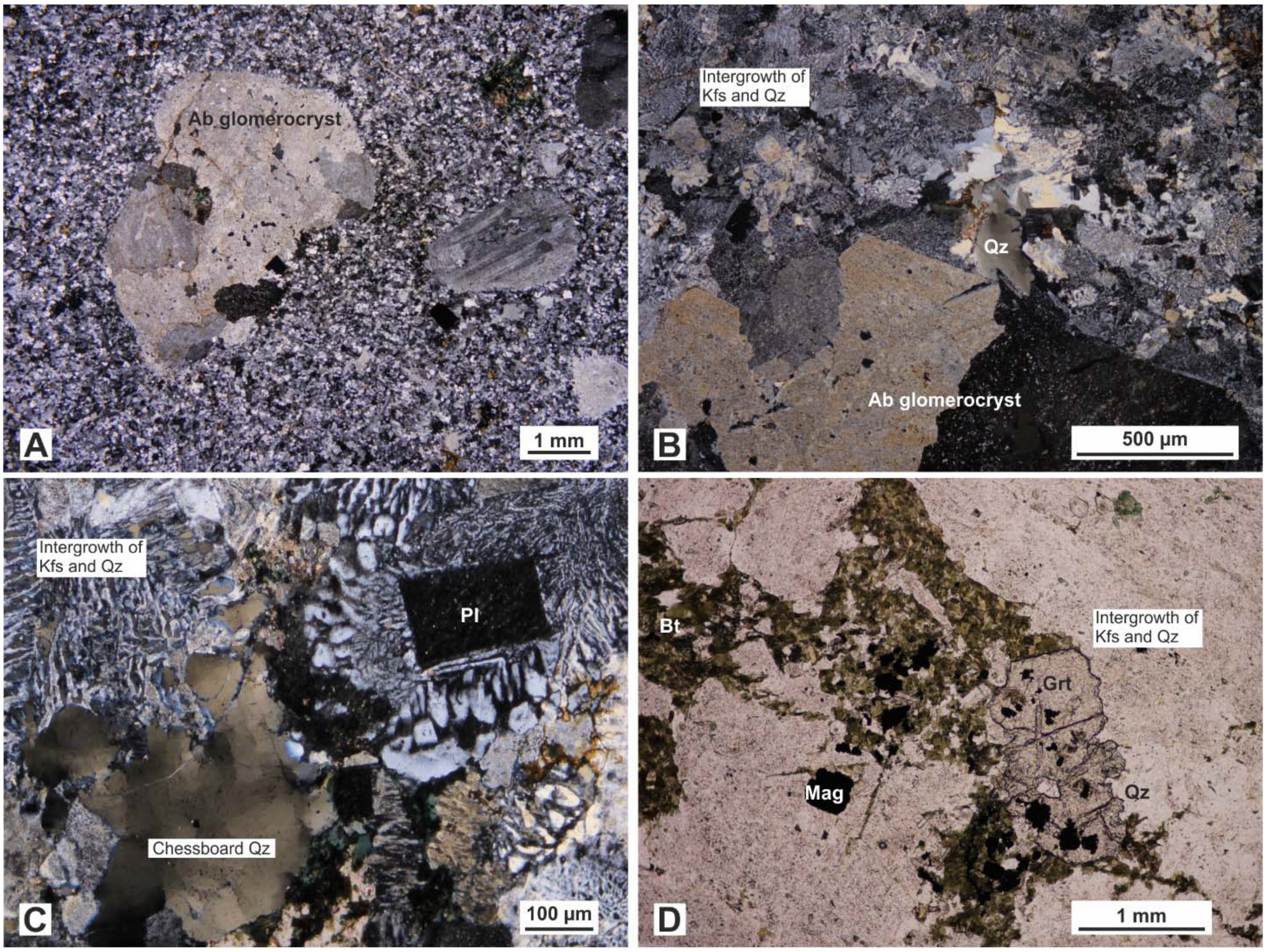

Figure 6 Photomicrographs of (A) porphyritic micrgranitic texture and (B) granophyric texture of the Shellenbarger pluton; crossed polar view. Stations JZ5 (coordinates: N37.64435°, W119.20275°) and FT1 (coordinates: N37.65742°, W119.19921°), respectively. (C) Detail of quartz and plagioclase intergrowths in the granophyric granite, crossed polar view. Station FT30, coordinates N37.62781°, W119.18235°. (D) Cluster of aggregates of secondary minerals; plane light view. Station JZ2, coordinates: N37.64398°, W119.19649°. Mineral abbreviations: Kfs – potassium feldspar, Plg – plagioclase, Ab – albite, Qz – quartz, Bt – biotite, Grt – garnet, Mag – magnetite (After Whitney and Evans, 2010).

angle both to internal textural zoning and to the outer pluton margin. The magmatic foliation is also parallel to the overprinting S2 foliation in the host rock in Zone 3 near the pluton margin (Fig. 2B).

Anisotropy of magnetic susceptibility (AMS)

Methodology

The anisotropy of magnetic susceptibility (AMS) was used to complement the structural data and to quantify fabric symmetry, intensity, and orientation across the pluton (see Hrouda, 1982; Tarling and Hrouda, 1993; Borradaile and Henry, 1997; Borradaile and Jackson, 2010 for reviews and principles of the method). The samples were collected at 23 stations as oriented blocks and then drilled using a hand-held gasoline drill, rotated back to their original (in situ) position, and the orientation of the drilled cores was measured using a standard orientation table. A total of 100 oriented cores were cut to 240 standard cylinder-shaped specimens (2.1 cm in height, 2.5 cm

Figure 7 Maps showing (A) textural zonation and (B) orientations magmatic foliation in the Shellenbarger pluton. The great circle represents average foliation plane and the stereonet is equal-area projected lower hemisphere.

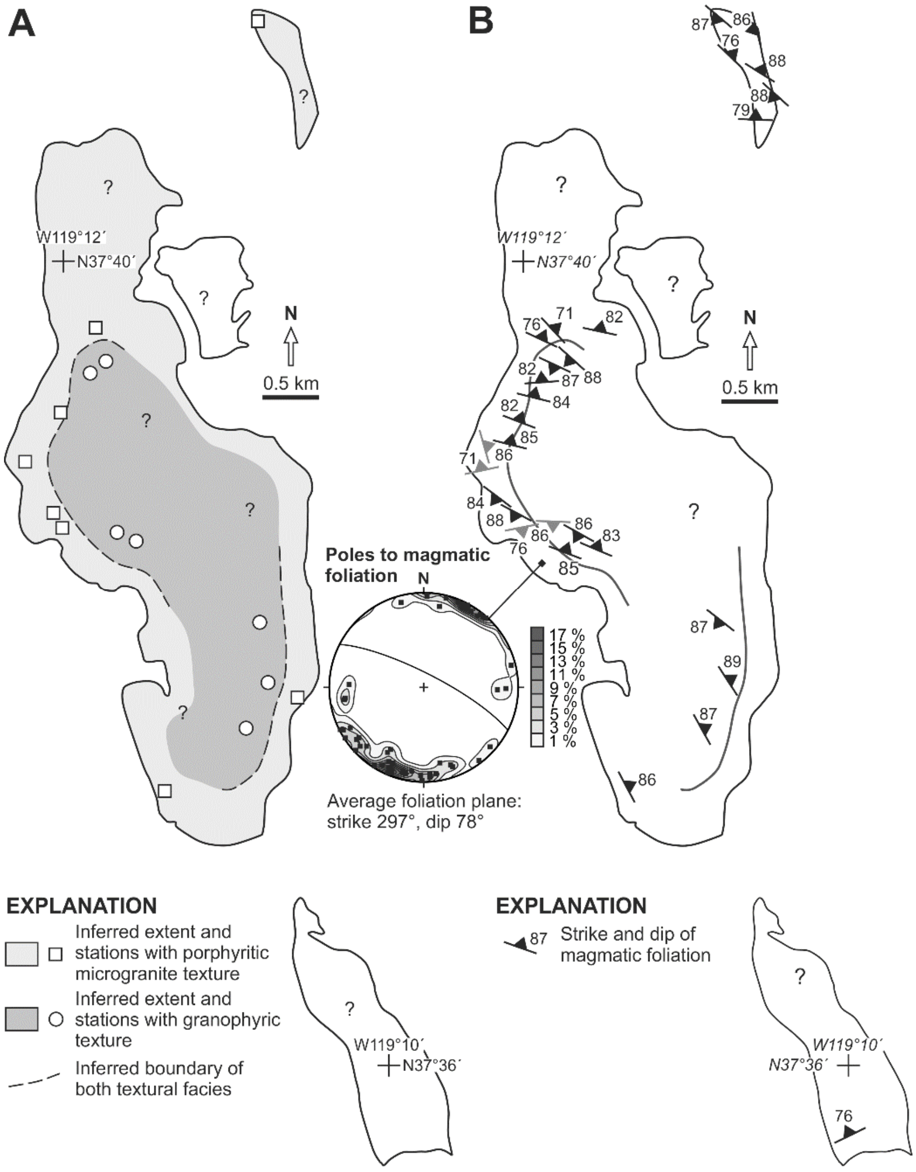

in diameter, and 10 cm3 in volume). AMS was measured at a low field of 450 Am–1 using a MFK1-A Kappabridge in the Laboratory of Rock Magnetism, Institute of Geology and Paleontology, Charles University in Prague. A statistical analysis of the data was carried out using the ANISOFT 4.2 software (www.agico.com; Chadima and Jelínek, 2009). The measured data and parameters are presented in Figs. 8–11 and listed full in the Appendix items 3/1 and 3/2.

Hereinafter, three parameters are used to characterize the magnetic fabric: (1) the mean susceptibility, $km = (k_1 + k_2 + k_3)/3$, reflecting the magnetic mineral species and their fraction, (2) the degree of anisotropy, $P = k_1/k_3$, which expresses the eccentricity of the AMS ellipsoid, and (3) the shape parameter, $T = 2\ln(k_2/k_3)/\ln(k_1/k_3) - 1$, which describes shape of the AMS ellipsoid; for $-1 \leq T < 0$ the ellipsoid is prolate, for $T = 0$ triaxial, and for $1 \geq T > 0$ oblate. The maximum, intermediate, and minimum susceptibility axes are k_1, k_2, and k_3, respectively. The maximum principal susceptibility (k_1) represents magnetic lineation, and the minimum principal susceptibility (k_3) represents a pole to magnetic foliation. The orientation of magnetic foliations and lineations is plotted in the lower hemisphere stereograms and as the station mean directions in the map.

Magnetic mineralogy and AMS carriers

Mean susceptibilities of the granite spans several orders of magnitude from 10^{-5} to 10^{-2} (SI units are used throughout this paper; Fig. 8A). Only a small number of specimens has low susceptibilities on the order of 10^{-5} and 10^{-4} (17 % of all specimens) whereas a great majority of specimens have higher susceptibilities (10^{-3} and 10^{-2}). The low and high susceptibilities indicate paramagnetic and ferromagnetic AMS carriers, respectively (Fig. 8A; e.g., Hrouda and Kahan, 1991).

In order to specify the AMS carriers, variation of the susceptibility with temperature was measured on four representative, coarsely powdered specimens using the CS-L Cryostat and CS-4 Furnace instruments (Hrouda, 1994) in the Laboratory of Rock Magnetism, Institute of Geology and Paleontology, Charles University in Prague. The data were statistically treated and plotted using the Cureval 8 software (Agico, Inc.).

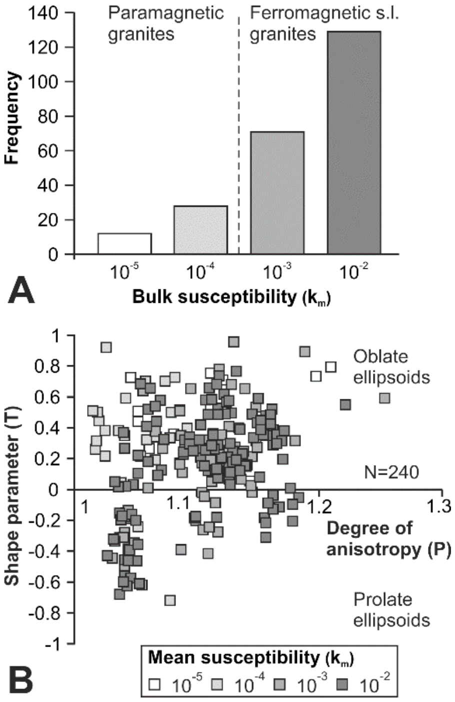

Figure 8. (A) Histogram of the bulk (mean) susceptibilities of all measured AMS specimens in the granite. (B) Magnetic anisotropy P–T plot summarizing all data for the granite of Shellenbarger Lake.

The thermomagnetic curves were obtained in two steps. First, specimens were cooled down to the temperature of liquid nitrogen (ca. –196 °C) and spontaneously heated to ~5 C°, while the magnetic susceptibility was measured at approximately every minute. Second, specimens were heated up from the room temperature up to ~700 °C and cooled back to ~40 °C at an approximate rate of 14 °C/min in argon atmosphere to minimize mineral changes due to oxidation.

Two types of thermomagnetic curves were obtained during the experiments. (1) The low-susceptibility specimens (JZ7/2/3 and FT2/2/2 with $km = 4.43 \times 10^{-5}$ *and* 2.25×10^{-4}, respectively) show a gradual hyperbolic decrease in the bulk susceptibility from –196 °C up to 400 °C (Fig. 9A, B). Such hyperbolic curves, where the magnetic susceptibility is inversely proportional to the absolute temperature according to the Curie–Weiss law, indicate paramagnetic minerals as the dominant AMS carriers. Above ~400 °C, the susceptibility increases up to ~580 °C and then abruptly decreases, indicating Currie temperature and thus the presence of magnetite. An additional increase on the cooling curves can be attributed to the growth of new magnetite as a result of decomposition and oxidation of Fe-bearing mineral phases with decreasing temperature (Fig. 9A, B). (2) Curves for the high-susceptibility specimens (FT16/1/2 and FT28/4/2 with $km = 2.81 \times 10^{-3}$ *and* 3.98×10^{-2}, respectively) show a susceptibility drop at –170 °C and ~580 °C both during heating and cooling, corresponding to the Verwey transition and Curie temperature, respectively (Fig. 9C, D). The measurements thus indicate that magnetic mineralogy of the granite is controlled by magnetite, however, a slight hyperbolic decrease from the Verwey transition temperature to ~300 °C also suggests a minor contribution of paramagnetic minerals to the bulk susceptibility. Small bumps at ~250–350 °C on the heating curves can be attributed to the presence of low-temperature maghemite (Fig. 9C, D). Both the heating and cooling curves do not follow the same trends suggesting specimen alteration or new magnetite growth during the experiment.

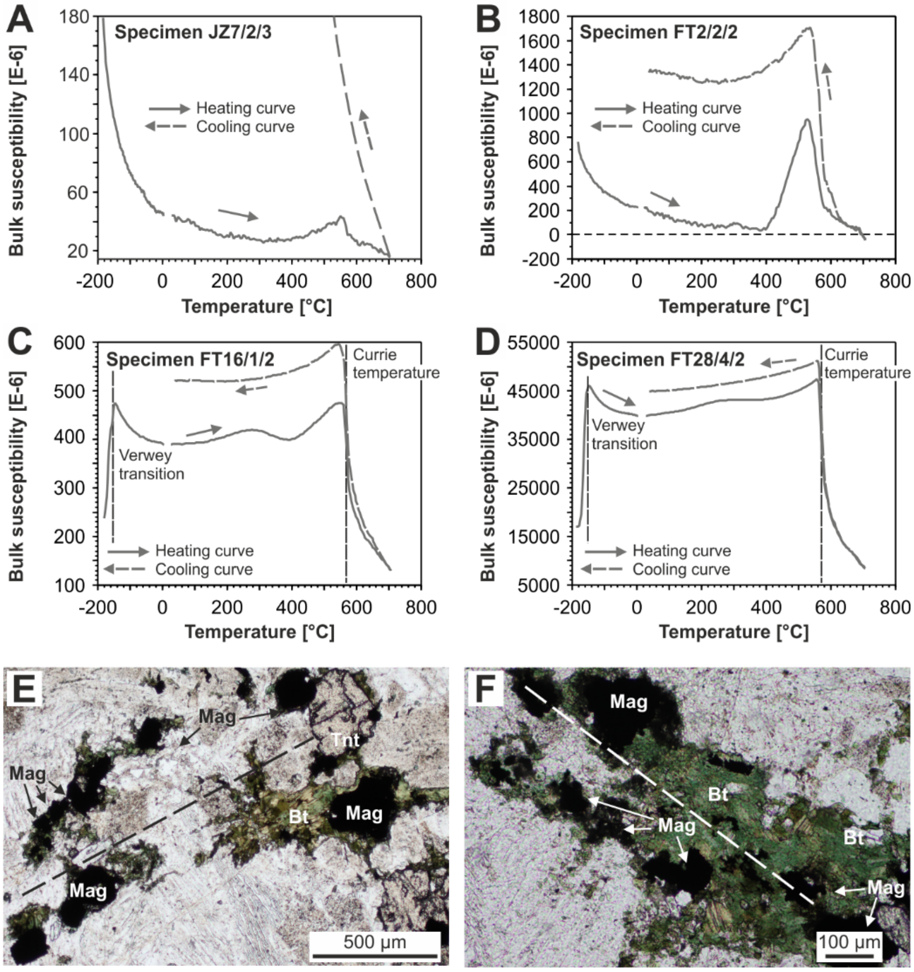

Figure 9 (A–D) Thermomagnetic curves representing magnetic susceptibility as a function of temperature for selected samples of the Granite of Shellenbarger Lake. Plane light view photomicrographs in XZ kinematic section of (E) specimens JZ6, coordinates: N37.64497° W119.20318° and (F) FT30, coordinates N37.62781° W119.18235°, show shape-preferred orientation and elongation of magnetite grains and aggregates along magmatic foliation (dashed line). All coordinates are referenced to WGS84 datum. Kfs – potassium feldspar, Qz – quartz, Bt – biotite, Mag – magnetite, Tnt – titanite (After Whitney and Evans, 2010).

On the microscale, magnetite shows two types of alignment: grains or aggregates have their long axes (in thin section) or form linear 'trains' parallel to magmatic foliation defined by biotite or feldspar (Fig. 9E, F).

Magnetic fabric parameters and orientation

The granite is relatively highly anisotropic, showing a large spread in the P parameter from 1.015 to 1.833 with two data peaks between 1.05 and 1.07 and between 1.12 and 1.17 (corresponding to 5, 7, 12, and 17% anisotropy, respectively; Fig. 8B, and Appendix item 3/1). The T parameter ranges from –0.715 to 0.957, but most specimens (75 %), and especially those with the anisotropy degree above 1.05, indicate oblate shapes of the AMS ellipsoid (Fig. 8B, and Appendix item 3/1). In

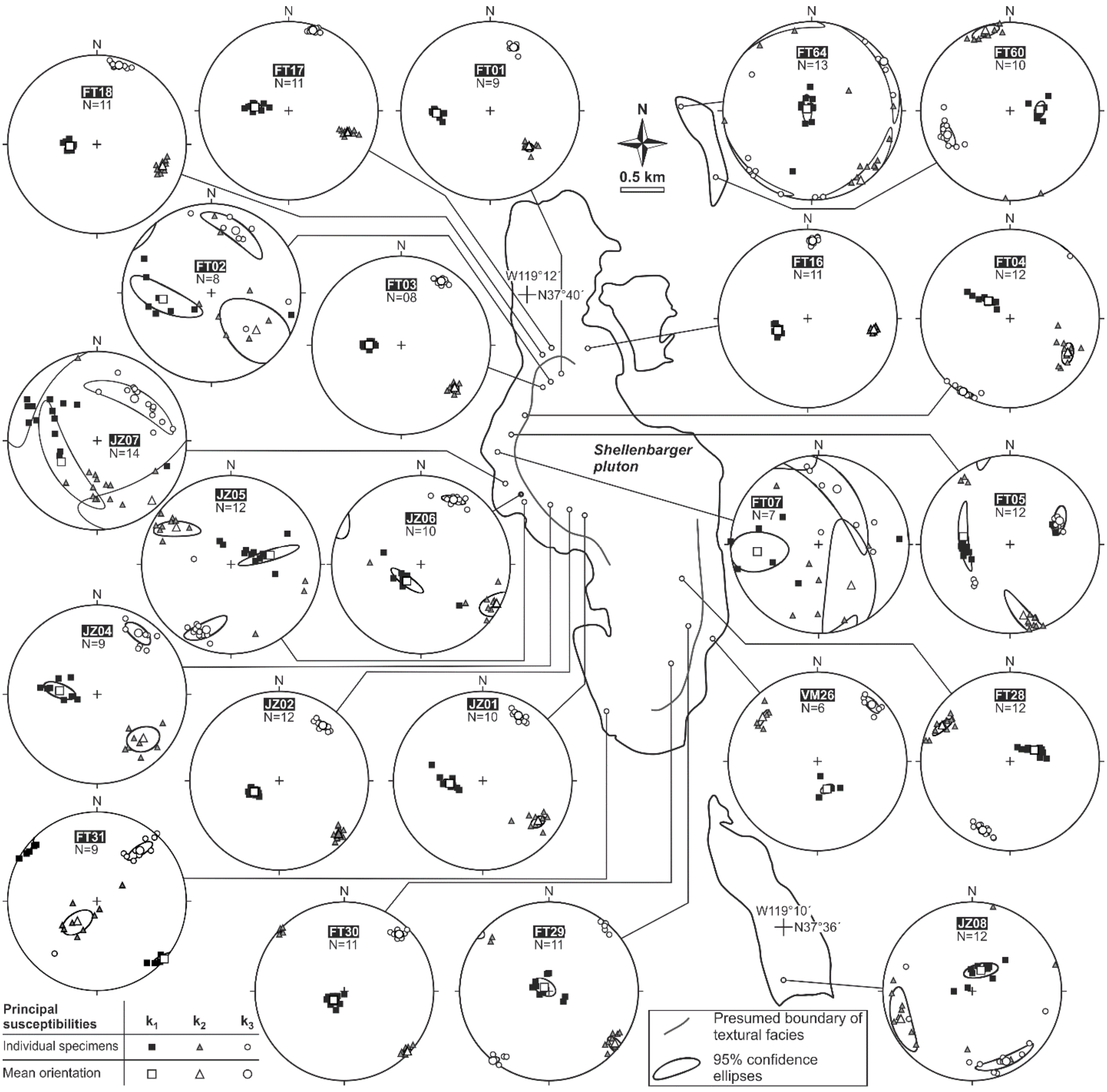

Figure 10 Maps showing orientation of the principal susceptibilities of individual specimens and station means in the Shellenbarger pluton. Stereonets are equal-area, lower hemisphere.

the map, the magnetic fabric parameters show no obvious spatial pattern (Appendix item 3/2).

On most stations, the measured orientations of the principal susceptibility axes are clustered, the site-mean directions are well defined (Fig. 10), and the mean magnetic foliation (Fig. 11A) corresponds to the mesoscopic feldspar phenocryst foliation (Fig. 7B). Magnetic foliations are steep and strike ~WNW–ESE in the northern and west-central portion of the pluton and ~NE–SW in its southern portion, thus at a high angle to the pluton margins (Fig. 11A). The statistical mean strike and dip of magnetic foliation in the pluton, calculated from all specimens using the method of Jelínek (1978, 1981), are 115° and 81°, respectively (Fig. 11A). The exceptions to this overall trend are two stations (FT60 and FT64) in the northern satellite body where foliations strike ~NNW–SSE and the southernmost station (JZ08) where foliations strike ~ENE–WSW (Fig. 11A). In most cases, magnetic lineations plunge steeply to the ~W with the mean trend and plunge of 269° and 69°, respectively (Fig. 11B). A few stations reveal other orientations than those described above: lineations plunge shallowly to the ~SE at station FT31 or steeply to the ~E, ~NE, and ~NNE at stations FT60, FT28, VM26, JZ04, and JZ08 (Fig. 11B).

Figure 11 Maps showing orientation of site-mean principal susceptibilities (A) poles to k_3, magnetic foliations and (B) k_1, magnetic lineations in the Shellenbarger pluton. Stereonets (equal-area, lower hemisphere) display orientation of the principal susceptibilities from all data. Full symbols indicate mean directions, black lines represent 95% confidence ellipses, and a dashed great circle is all-data mean magnetic foliation.

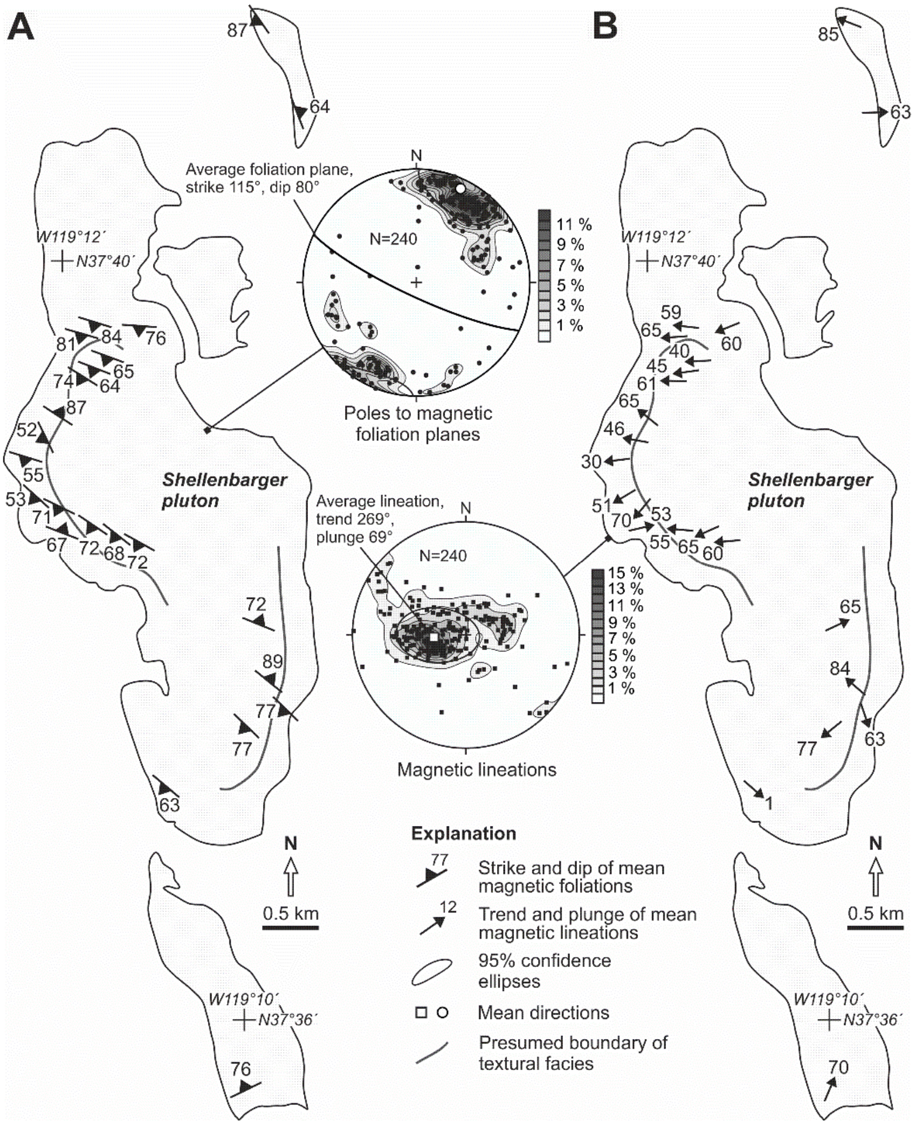

U–Th–Pb zircon geochronology using LA ICP-MS

Methodology

A Thermo-Finnigan Element 2 sector field ICP-MS coupled to a 193 nm ArF excimer laser (Resonetics RESOlution M-50 LR) at Bergen University, Norway, was used to measure Pb/U and Pb/Th isotopic ratios in zircons. The laser was fired at a repetition rate of 4.5 Hz and energy of 40 mJ with 19 μm spot size. Typical acquisitions consisted of 25 second measurements of blank followed by measurements of U, Th, and Pb signals from the ablated zircon for another 30 seconds. The data were acquired in time resolved – peak jumping – pulse counting mode with 1 point measured per peak for masses ^{204}Pb, ^{206}Pb, ^{207}Pb, ^{208}Pb, ^{232}Th, and ^{238}U. Data reduction was carried out off-line using the Iolite data reduction package version 2.5. Full details of the data reduction methodology can be found in Paton et al. (2010). It included correction for the gas blank, laser-induced elemental fractionation of Pb, Th, and U and instrument mass bias. For the data presented here, blank intensities and instrumental bias were interpolated using an automatic spline function while down-hole inter-element fractionation was corrected using an exponential function. No common Pb correction was applied to the data but the low concentrations of common Pb were controlled by observing ^{206}Pb/^{204}Pb ratio during measurements. Residual elemental fractionation and instrumental mass bias were corrected by normalization to the natural zircon reference material GJ-1 (Jackson et al., 2004). Zircon reference material 91500 (Wiedenbeck et al., 1995) was periodically analyzed during the measurement for quality control and the obtained mean value of 1063 ± 4 (2σ; n = 22) corresponds with the published reference values (1065 Ma; Wiedenbeck et al., 1995). The zircon Pb/U ages are presented as concordia diagrams, generated using the ISOPLOT program (v. 3.50; Ludwig, 2003).

Results

The cathodoluminescence (CL) imaging of short to long prismatic, faceted zircon prior to isotopic analysis revealed typical magmatic texture of multi-stage oscillatory and sector zoning in both samples VM6 and FT16 (Fig. 12). The minute, long-prismatic inclusions of apatite observed in most of the grains under binocular microscope reveal themselves in the CL images as tiny CL-bright spots located irregularly on the polished surface of the zircon grains (Fig. 12). Pb/U and Pb/Th ratios were measured in the inclusion-free. The darker inner parts of some of the grains (e.g., analysis 57; Fig. 12) yielded ages indistinguishable from other analyses indicating that the bulk of the zircons in the studied rocks represents a single magmatic zircon-forming event with no inherited component.

Zircons from both samples VM6 and FT16 are characterized by moderate to high U concentrations (averages of 515 ppm and 627 ppm, respectively) and moderate Th/U ratios (average value of 0.58 is identical for both samples) typical for magmatic zircons (Appendix item

3/3). The parts of the grains that are brighter on the CL images have generally lower U concentrations compared to those that are darker.

The pooled Pb/U isotopic data of samples VM6 and FT16 yielded well-defined concordia ages of 100.32 ± 0.30 Ma and 100.63 ± 0.31 Ma, respectively (2σ; Fig. 13A, B), identical within analytical uncertainties.

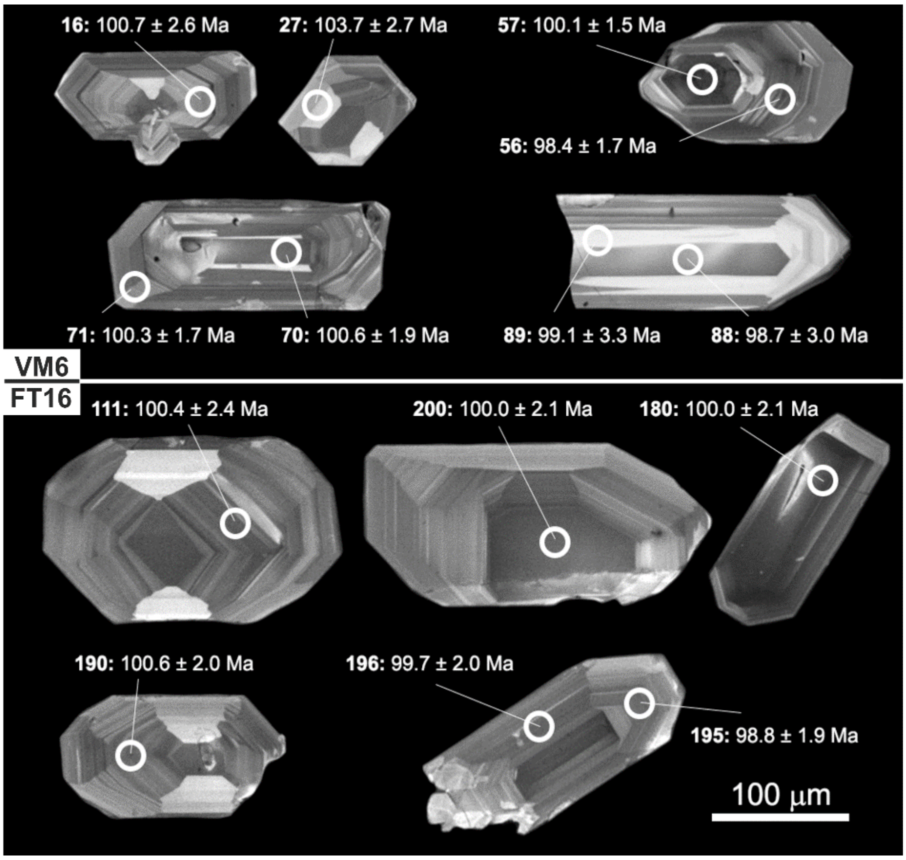

Figure 12 Representative cathodoluminescence images of zircon from samples VM6 and FT16. The spots where laser-ablation analysis was performed are indicated together with the obtained $^{206}Pb/^{238}U$ ages.

DISCUSSION

Origin of the magmatic and magnetic fabrics in the Shellenbarger pluton

We show that mesoscopic and magnetic foliations in the pluton are at high angle to the pluton margins, traverse the internal gradational boundary between the porphyritic and granophyric facies, and are continuous with the late S2 foliation which overprints the main ductile fabric of the Bench Canyon shear zone (Figs. 2B). Furthermore, the granite preserves a transition from magmatic to high-temperature subsolidus microstructures, significantly modified by hydrothermal fluid flow (Section 4). Although the latter could complicate the interpretation of AMS data, as hydrothermal alteration may induce changes in magnetic fabric orientation and parameters (e.g., Just et al., 2004; Krása and Herrero-Bervera, 2005; Petronis et al., 2011), the AMS data correspond well to the observed magmatic fabric. The data exhibit a systematic pluton-wide pattern, and the orientation of the principal susceptibilities is independent of the intensity of hydrothermal alteration as recorded by the two granite facies. Moreover, as the AMS signal is dominated by magnetite (Fig. 9C–F), we conclude that the Shellenbarger granite preserves two coaxial subfabrics: magmatic alignment of feldspar phenocrysts enhanced by the shape or distribution anisotropy fabric of magnetite single grains and aggregates (e.g., Hargraves et al., 1991; Archanjo et al., 1995; Cañón-Tapia, 2001). The late magnetite growth within elongated clusters of postmagmatic minerals is interpreted as resulting from the circulation of heated fluids in a post-magmatic stress field (Fig. 9E, F; e.g., Henry et al., 2003; Sizaret et al., 2003; Trindade et al., 2001).

Taken together, these observations indicate a post-emplacement (magmatic to solid state), tectonic origin of coaxial feldspar, biotite, and magnetite fabrics in the Shellenbarger pluton. Assuming that both the magmatic and magnetic foliations represent XY planes and lineations the X axis of the strain ellipsoid (e.g., Paterson et al., 1998), we interpret the down-temperature fabrics in the pluton as recording increments of tectonic strain of roughly constant orientation (~NNE–SSW horizontal shortening and steep to vertical stretching), imposed on the cooling magma across the hypersolidus/solidus transition and on the subsequent post-magmatic fluid flow focused particularly in the hotter pluton center (granophyric facies).

Figure 13 Concordia diagrams with zircon Pb/U isotopic data of samples VM6 and FT16.

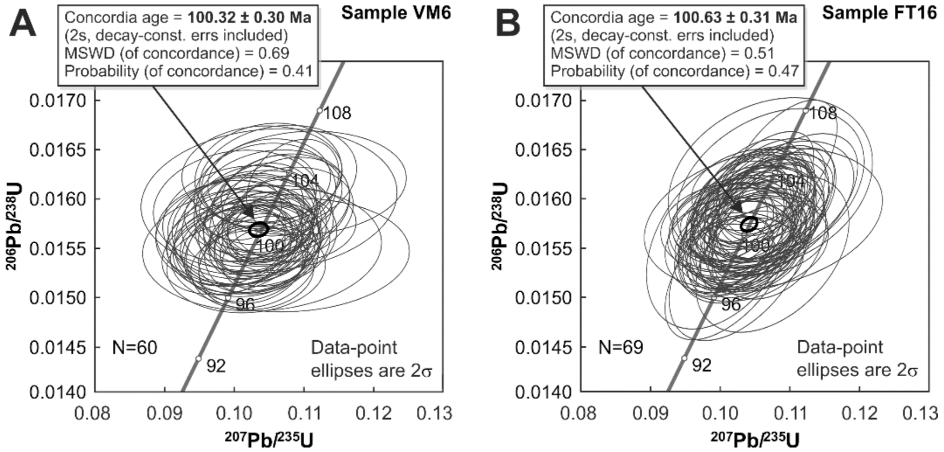

Volcano–tectonic evolution of the Minarets caldera

Based on the published information, combined with our new U–Pb zircon ages, field observations, and structural and AMS data, we present a refined model for the volcano–tectonic evolution of the Minarets caldera during ~101–96 Ma (Fig. 14).

(1) The pre-caldera stage is marked by the deposition of the basal volcanic layer on older, already tilted basement (Fiske and Tobisch, 1978, 1994). Although there is no direct field record of the pre-collapse volcanic forms, diverse lithologies of collapse breccia clasts point to a small felsic stratovolcano with lava domes, flows, and pyroclastic rocks eroded and destructed during eruptions and caldera collapse (Fig. 14A; Fiske and Tobisch, 1994). Subsequently, violent, possibly

Plinian eruption(s) produced the voluminous pre-collapse rhyolitic ash-flow tuff at around 101 Ma (Fig. 14a; Fiske and Tobisch, 1994).

(2) The caldera collapse is marked by the voluminous collapse breccia (Fig. 14B). The comparable Sri of the post-collapse rhyodacitic to dacitic ash-flow tuff was interpreted as recording continuous eruption during and after the collapse and deposition of post-collapse rhyodacitic to dacitic ash-flow tuff (Fig. 14b; Lowe, 1996).

(3) The whole volcanic sequence was then gently tilted to the SW and locally deformed during reverse transpressional shearing along the Bench Canyon shear zone (McNulty, 1995; Tobisch et al., 1995). The intensity of ductile strain and the tilt angle increase towards the shear zone or near the margin of the Shellenbarger pluton (Fig. 14C).

(4) A late event inside the caldera was magma resurgence at ~100 Ma as recorded by the emplacement of the subvolcanic Shellenbarger pluton (Fig. 14C; this study). Unlike Lowe (1996), who interpreted the Shellenbarger pluton as a horizontal sill, we argue that at least the upper part of the pluton has a domal shape (Fig. 4B, C, E). Although the floor is not exposed, the steep pluton/wall rock contacts and the extent and intensity of albitization provide indirect evidence for a voluminous, vertically extensive magma body. Importantly, we have shown that the S1 host rock foliation and lithological contacts are steepened in the pluton's structural aureole (Zones 2 and 3 in Fig. 2B, C). We explain this reorientation as resulting from emplacement-related strain that clearly postdated the main phase of ductile shearing along the Bench Canyon shear zone. Our new high-precision U–Pb zircon ages for the pluton thus constrain an upper age limit for the main deformation phase along the shear zone to ~101–100 Ma, at least in the area of the Bench Canyon, which is at variance with the previous age estimations of ~95–90 Ma (McNulty, 1995; Tobisch et al., 1995; 2000) and ~85 Ma (Titus et al., 2005).

After emplacement, but prior complete solidification, the Shellenbarger magma was overprinted by small increments of tectonic strain. Straining of the pluton continued even after solidification of the magma when the still hot pluton center was fluxed by hydrothermal fluids. The significance of this tectonic fabric is discussed below.

(5) Volcanic activity continued until at least 96.7 Ma, which is an age of rhyolitic tuff mapped close to the NE margin of the Minarets caldera (Fig. 14C; U–Pb on zircons, Paterson, unpublished data).

High-level intrusions as markers of crustal strain

A review of published structural and magnetic fabric data reveals that the ~WNW- to ~NW-striking foliations also occur in several other Mid to Late Cretaceous plutons in the central Sierra Nevada (Fig. 15A–H; and Appendix item 3/4). Except the Dinkey Creek and Bald Mountain plutons whose fabrics were previously explained as resulting from emplacement (Tobisch and

Cruden, 1995; Cruden et al., 1999), fabrics in the remaining plutons were interpreted as recording tectonic strain (Fig. 15B–H). Importantly, although the plutons' host rocks are dominated by 'Cordilleran' ~NNW–SSE structures (e.g., Schweickert et al., 1984; Tobisch et al., 1977, 1987), few locations in the Sierra Foothills and in the Eastern Metamorphic Belt also preserve ~NW–SE- to ~WNW–ESE-trending fabrics, overprinting the overall structural grain at a high angle (e.g., Tobisch and Fiske, 1978; Paterson, 1989; Paterson et al., 2003; Cao et al., 2015; this study; Fig. 15I). This implies that the ~NE–SW to ~NNE–SSW shortening is a regional tectonic event recorded domainally across a large portion of the Sierra Nevada magmatic arc.

The significance of this deformation has long remained unclear until Cao et al. (2015) directly linked the orientation of magmatic foliations and inferred principal shortening directions with the past plate-motion vectors (an approach discussed earlier in Benn et al., 2001). On the basis of fabric studies in four successively emplaced Sierran plutons Cao et al. (2015) proposed that (1) the mean foliation orientation rotated anti-clockwise from ~NW–SE to ~WNW–ESE during ~233 to ~86 Ma, (2) so did the associated principal incremental shortening direction (from ~NE–SW to ~NNE–SSW), and (3) this rotation was inferred to reflect a major change in plate kinematics from head-on to highly oblique eastward subduction of the Farallon plate beneath North America

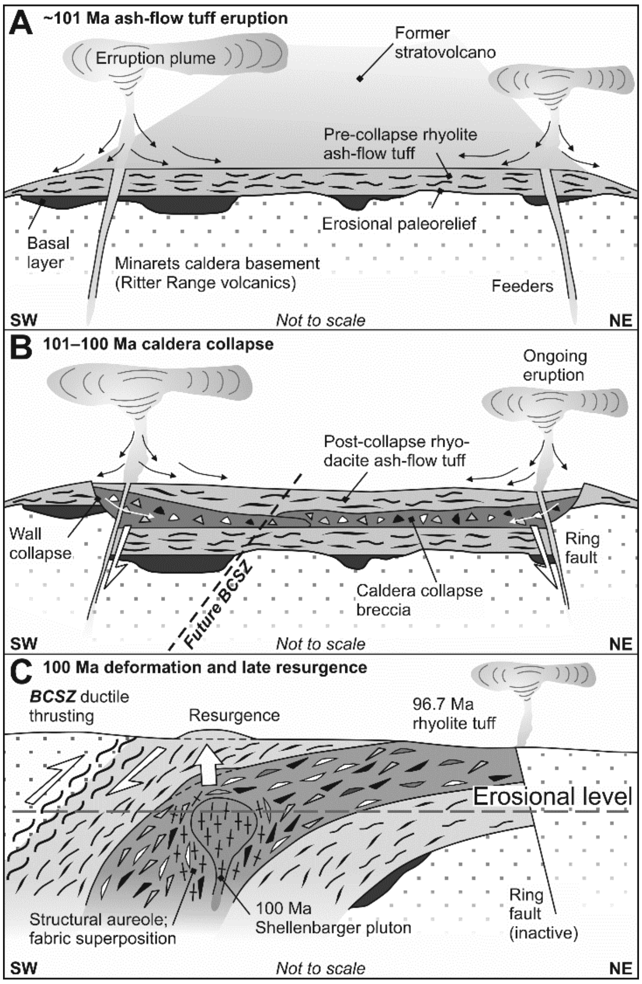

Figure 14 Interpretative illustration of evolution of the Minarets caldera. See the text for details.

at around 97–90 Ma (Engebretson at al., 1984, 1985; Cao et al., 2015). Similar switch in the plate convergence vector at ~110–100 Ma and at ~90 Ma was proposed by Greene and Schweickert (1995) and Tikoff and de Saint Blanquat (1997), respectively.

A compilation of structural and geochronological data from plutons of the central Sierra Nevada (Fig. 15B–H, and Appendix item 3/4) allows us to expand the previous models and provides some additional constrains on paleostrain fields and inferred plate kinematics during the Late Cretaceous Farallon/North America convergence. Interestingly, the mean orientation of magmatic and magnetic foliations in these plutons does not reveal a clear anti-clockwise rotation from older to younger plutons during ~102–86 Ma. Instead, foliations seem to vary non-systematically between the two main orientations (~NW–SE to ~WNW–ESE; Fig. 16A) which could be a result of small strain heterogeneity but also other additional effects (variable number of data compared, variable data scatter, measurements errors). In contrast, a significant change can be observed in the plunge of lineations (Fig. 16B). Magmatic and magnetic lineations are steep in plutons that were emplaced at ~102–86 Ma (Fig. 15B–G), whereas magnetic (mostly magnetite) lineations are subhorizontal to gently plunging in the three youngest, ~87–86 Ma subvolcanic plutons (Fig. 15F, H; Tab. 1). This trend is greatly exemplified in the Tuolumne batholith, where magmatic lineations associated with ~WNW–ESE foliation ('Type 4' of Žák et al., 2007) are subvertical in the ~94–93 Ma Kuna Crest, ~92–88 Ma Half Dome, and ~88–86 Ma Cathedral Peak units, but magnetic lineations in the latter are steep to moderate and shallow in the youngest, ~87 Ma Johnson Granite Porphyry (Fig. 15F, and Appendix item 3/4; Tikoff et al., 2005; Titus et al., 2005). As documented in this study, magnetite fabric in shallow-level intrusions may be acquired during focused postmagmatic fluid flow, implying that the inferred reorientation of the principal stretching direction may be younger than 86 Ma (note the published fabric data are only AMS from the younger plutons).

The presence of overprinting foliations in shallow (<2 km emplacement depth) subvolcanic intrusions (e.g., Shellenbarger granite) suggests that the crystallizing plutons behaved as rheologically weak inclusions in the stiff brittle crust where the contractional component of transpression was partitioned into active magma regions, recorded by magmatic and magnetic fabrics, and the wrench component was partitioned into shear zones or brittle faults (e.g., the Sierra Crest shear zone system; Tikoff and Greene, 1994; Tikoff and de Saint Blanquat, 1997). This inference challenges the common view that minor high-level intrusions (dikes, necks, small subvolcanic plutons) typically preserve only magma flow related fabrics as they solidify too fast to record the slow regional tectonic deformation (e.g., de Saint Blanquat et al., 2011). We thus conclude that fabrics in shallow-level intrusions may capture instantaneous tectonic strain in the upper crust as do large deeper granitoid plutons. From this perspective, magmatic fabrics in shallow-level intrusions may be used as tectonic markers in a similar way as joints (e.g., Engelder and Geyser, 1980; Pollard and Aydin, 1988); both form instantaneously, record only small

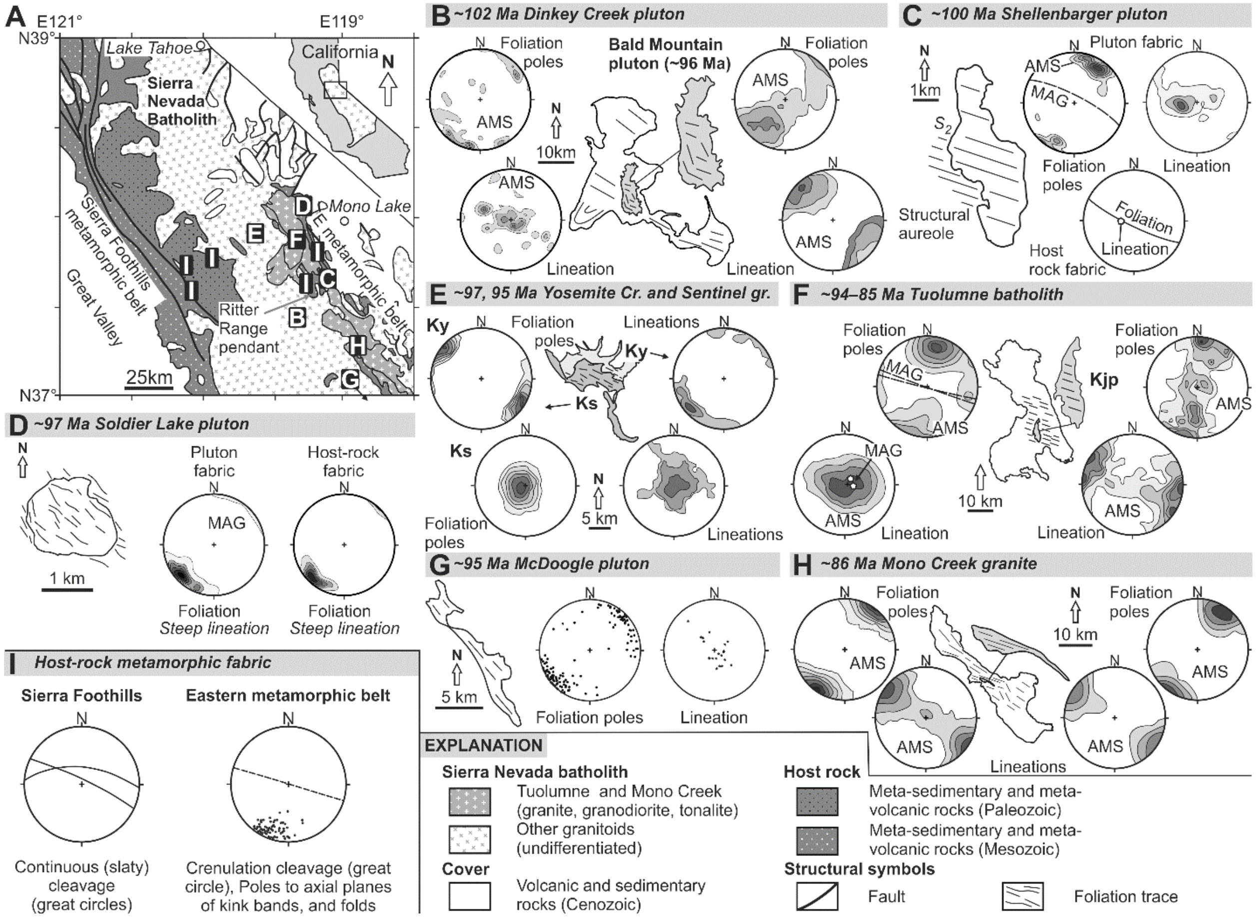

Figure 15 (A) Simplified geologic map of central Sierra Nevada (Gutierrez et al., 2010). See inset for map location. Position of Cretaceous plutons (B–H) and host rocks (I) with occurrence of NW- to WNW-striking fabrics are shown: (B) 102 ± 5 Ma Dinkey Creek and 95.9 ± 3 Bald Mountain plutons (Tobisch et al., 1993; Tobisch and Cruden, 1995; Cruden et al., 1999); (C) 100.32 ± 0.30 and 100.63 ± 0.31 Ma Shellenbarger pluton (this study); (D) ~97.4 ± 0.4 Ma Soldier Lake pluton (Paterson et al., 2003; Mundil et al., 2004; Cao et al., 2015); (E) ~97 Ma Yosemite Creek (Ky) and ~95 Ma Sentinel granodiorite (Ks; Petsche, 2008; Burgess et al., 2009; Johnson, 2013); (F) ~94-85 Ma Tuolumne batholith, composed of individual plutons: 94.4 ± 0.3, and 93.5 ± 0.7 Ma Kuna Crest, 92.8 ± 0.1, 91.7 ± 0.2, and 88.8 ± 0.8 Ma Half Dome, 88.1 ± 0.2 Ma, and 86 Ma Cathedral Peak granodiorites, and 87.5, and 85.4 ± 0.1 Ma Johnson Granite Porphyry (Kjp; Coleman et al., 2004; Tikoff et al., 2005; Titus et al., 2005; Matzel et al., 2005, 2006; Miller et al., 2007; Žák et al., 2007; Bracciali et al., 2008; Memeti et al., 2010); (G) ~95 Ma McDoogle pluton (Mahan et al., 2003); (H) ~86 Ma Mono Creek Granite and Silver Pass Porphyry (Stern et al., 1981; de Saint Blanquat and Tikoff, 1997; Titus et al., 2005); (I) Stereonets are showing orientation of ~WNW-ESE fabric in the Sierra Foothills and Eastern metamorphic belts (Tobisch and Fiske, 1976; Paterson, 1989). Stereonets are equal-area projections on the lower hemisphere. Except (c), all contoured stereonets are redrafted or calculated from data presented in cited papers. The contours indicate poles to foliation planes and lineation orientation. AMS – magnetic fabrics, MAG – magmatic fabrics).

increments of tectonic strain, and in simple strain regimes are perpendicular to the incremental maximum principal shortening or extension, respectively.

Late Cretaceous plate kinematics and shutdown of the Sierra Nevada magmatic arc

Provided that the construction of the Sierra Nevada magmatic arc occurred in an overall transpressional regime during the Late Cretaceous (e.g., Tikoff and Teyssier, 1992; Tikoff and de Saint Blanquat, 1997; de Saint Blanquat et al., 1998; Cao et al., 2015), the inferred reorientation of the principal stretching direction has significant implications for understanding the nature and kinematics of this transpressional deformation. Fossen and Tikoff (1994) and Tikoff and Greene (1997) showed that for the angle of convergence (α) less than 20°, transpression is wrench-dominated and the principal stretching direction (lineation) is horizontal whereas for $\alpha > 20°$ transpression is pure shear-dominated and the principal stretching is vertical (Fig. 16C). Alternatively, increasing strain magnitude can also cause switch in stretching direction for the same angle of convergence (Fig. 16C). Hence, we propose that the reorientation of lineation in the Late Cretaceous Sierran plutons (Fig. 15B–H, 16B, and Appendix item 3/4) can theoretically be attributed either to the decrease of strain recorded by younger plutons or to a change from pure shear- to wrench-dominated transpression (i.e., increasing the obliquity of plate convergence; Fig. 16C). Given that magmatic fabrics are generally weak, record only small amounts of strain (typically 5–10 % shortening; e.g., Benn, 1994; Paterson et al., 1998), and that no significant differences in finite strain have been described from the plutons in question, we favor the latter hypothesis and corroborate conclusions drawn by Cao et al. (2015).

Our data from the Shellenbarger granite, together with pluton fabric studies reviewed above (Fig. 15; and Appendix item 3/4), indicate decreasing magnitude of instantaneous strain and/or continuous change from pure shear-dominated to wrench-dominated transpression, where at around ~87 Ma the angle of convergence (α) decreased below 20° (Fig. 16C). Interestingly, this inferred switch in plate kinematic coincides with the end of the Late Cretaceous magmatic flare-up period in the Sierra Nevada magmatic arc (~85–82 Ma; e.g., Ducea, 2001; Ducea and Barton, 2007; DeCelles et al., 2009; Ducea et al., 2015; Paterson and Ducea, 2015). Plutons emplaced at ~88–86 Ma (e.g., Cathedral Peak, Johnson Granite Porphyry, Mono Creek, Silver Pass Porphyry, and Mount Whitney; Bateman, 1992) are the latest larger intrusions of this period and mark the onset of a magmatic lull in the region (note plutonism migrated eastward and continued in the Basin and Range Province during Tertiary; e.g., Armstrong and Ward, 1993). The end of voluminous the Late Cretaceous plutonism in the Sierra Nevada overlapping with a switch to highly oblique convergence disagrees with models of pluton emplacement facilitated by active strike-slip shear zones (e.g., Glazner, 1991; Tikoff and Teyssier, 1992; Tikoff and de Saint Blanquat, 1997; de Saint Blanquat, 1998), suggesting that changing plate-tectonic regimes do not dominantly control magma ascent. Instead, the inferences developed above suggest exactly the opposite, i.e., that arc magmatism may shut off if the plate convergence becomes highly oblique. This is perhaps due to dominantly trench-parallel horizontal material transport, which cannot supply sufficient amounts of fertile magma sourced from continental crust underthrusting beneath the arc as during high-magma-flux, frontal convergence periods (e.g., DeCelles et al., 2009). Alternatively, shutting off magmatism may be more controlled by either the shortening distance to slab and thus cooling the melting area, or thickening the root so that it approaches the subducting slab (e.g., Chin et al., 2015; Ducea et al., 2015; Paterson and Ducea, 2015).

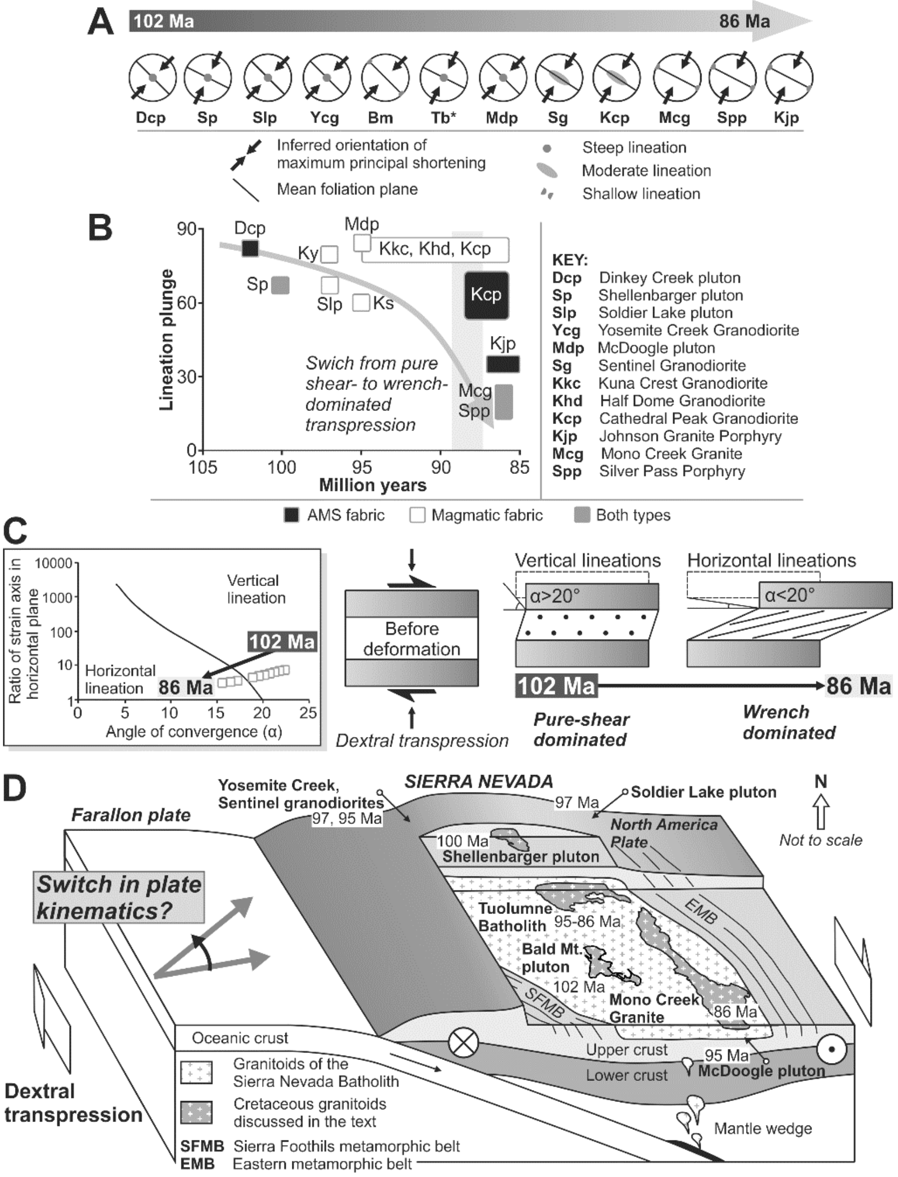

Figure 16 (A) Diagram showing foliation strike, lineation, and maximum principal shortening of Sierra Nevada Cretaceous plutons. (B) Diagram plotting lineation plunge against pluton ages. Note the decreasing plunge of lineation with younging age. (C) Left: Diagram plotting angle of convergence (α) against increasing magnitude of strain for transpression zones (after Tikoff and Greene, 1997). Note the position line separating vertical and horizontal lineations. Open squares mark individual plutons with steep or subhorizontal lineations. Right panel: plane-view illustration of deformation in dextral pure-shear and wrench- dominated transpression with an emphasis on lineation plunge. (D) 3D interpretative block-diagram illustrating magmatism of the North American active margin during Late Cretaceous. Our preferred hypothesis invokes switch in plate kinematics at <86 Ma. Subduction zone geometry is not precisely constrained.

CONCLUSIONS

A complex interaction of volcano–plutonic processes with regional tectonic deformation is recorded in the Mid-Cretaceous Minarets caldera and its resurgent Shellenbarger pluton. First, a pre-collapse edifice was built through the deposition of a basal volcanic layer and voluminous rhyolitic ash-flow tuff, possibly resulting from a large Plinian eruption at ~101 Ma. Second, the caldera collapse associated with the emplacement of a collapse breccia was followed by a volcanic eruption as evidenced by overlying rhyodacitic ash-flow tuff. The volcanic sequence was then overprinted by ductile transpressional shearing along the Bench Canyon shear zone in the western part of the caldera. Next, emplacement of the resurgent Shellenbarger pluton into the caldera center at ~100 Ma caused a steepening of the shear zone foliation and bedding in the volcanic host rock. Last, post-caldera volcanic activity continued at least untill ~96.7 Ma.

After emplacement, the granite magma was overprinted by ~NNE–SSW horizontal shortening, evidenced by ~WNW–ESE hypersolidus to solid state magmatic and late magnetic foliations. Same horizontal shortening is documented in several other Late Cretaceous syntectonic plutons of the central Sierra Nevada, however, they record two principal stretching directions: near-vertical in ~102–86 Ma plutons and subhorizontal to gently-plunging in ~87–86 Ma plutons. Provided that the Cretaceous Sierra Nevada magmatic arc was constructed during overall dextral transpression, we conclude that the change in the lineation plunge reflects a significant change in plate kinematics where older and younger plutons were emplaced during pure shear- ($\alpha > 20°$) and wrench-dominated transpression ($\alpha < 20°$), respectively. Such a switch in kinematics is explained as a result of progressively increasing relative convergence obliquity of the Farallon plate subducting beneath North American. The switch in type of deformation also overlaps with the termination of the Cretaceous magmatic flare-up period along the North American active margin.

ACKNOWLEDGEMENTS

We thank Scott Bogue for lending us his gasoline drill, U.S. National Forest Service for providing us with a research permit, packers at the Minarets Station for packing out our samples from the wilderness, Robert B. Miller, James Kirkpatrick for discussions, and Martin Chadima for help with processing the thermomagnetic curves. This study is part of the Ph.D. research of Filip Tomek, supported by the Grant Agency of the Czech Republic through Grant No. P210/12/1385 (to Jiří Žák) and by the Charles University research projects PRVOUK P44 and SVV261203. Filip Tomek and Jiří Sláma also acknowledge the Czech Academy of Sciences Research Plan RVO67985831.

REFERENCES

Armstrong, R.L., and Ward, P.L., 1993, Late Triassic to earliest Eocene magmatism in the North American Cordillera: Implications for the western interior basin, in Caldwell, W.G.E., Kauffman, E.G. eds., Evolution of the western interior basin: Geological Association of Canada Special Paper, v. 39, p. 49–72.

Archanjo, C.J., Launeau, P., and Bouchez, J.L., 1995, Magnetic fabric vs. magnetite and biotite shape fabrics of the magnetite-bearing granite pluton of Gameleiras (Northeast Brazil): Physics of the Earth and Planetary Interiors, v. 89, p. 63–75, doi: 10.1016/0031-9201(94)02997-P.

Bachmann, O., and Bergantz, G.W., 2004, On the Origin of Crystal-poor Rhyolites: Extracted from Batholithic Crystal Mushes: Journal of Petrology, v. 45, p. 1565–1582, doi: 10.1093/petrology/egh019.

Bachmann, O., and Bergantz, G.W., 2008, Rhyolites and their Source Mushes across Tectonic Settings: Journal of Petrology, v. 49, p. 2277–2285, doi: 10.1093/petrology/egn068.

Bateman, P.C., 1992, Plutonism in the Central Part of the Sierra Nevada Batholith, California: U.S. Geological Survey Professional Paper, v. 1483, p. 1–186.

Becker, T., and Faccenna, C., 2009, A Review of the Role of Subduction Dynamics for Regional and Global Plate Motions, in Lallemand, S. and Funiciello, F. eds., Subduction Zone Geodynamics, Frontiers in Earth Sciences, Springer Berlin Heidelberg, p. 3–34, doi: 10.1007/978-3-540-87974-9_1.

Benn, K., 1994, Overprinting of magnetic fabrics in granites by small strains: numerical modelling: Tectonophysics, v. 233, p. 153–162, doi: http://dx.doi.org/10.1016/0040-1951(94)90238-0.

Benn, K., Paterson, S.R., Lund, S.P., Pignotta, G.S., and Kruse, S., 2001, Magmatic fabrics in batholiths as markers of regional strains and plate kinematics: example of the Cretaceous Mt. Stuart batholith: Physics and Chemistry of the Earth, Part A: Solid Earth and Geodesy, v. 26, p. 343–354, doi: 10.1016/S1464-1895(01)00064-3.

Benn, K., 2004, Late Archaean Kenogamissi complex, Abitibi Subprovince, Ontario, Canada: doming, folding and deformation-assisted melt remobilisation during syntectonic batholith emplacement: Earth and Environmental Science Transactions of the Royal Society of Edinburgh, v. 95, p. 297–307, doi: 10.1017/S0263593300001085.

Black, C.J., Whitesides, A.S., Anderson, J.L., Culbert, K.N., Vandeveer, M., Cox, I.V., Cardamone, J., Torrez, G., Quirk, M., Memeti, V., Cao, W., and Paterson, S.R., 2010, Geochronology and structural studies in Northern Ritter Range: implications for the tectonic history of Mesozoic Sierra Nevada Arc: AGU annual meeting in San Francisco, Dec. 2010.

Borradaile, G.J., Henry, B., 1997, Tectonic applications of magnetic susceptibility and its anisotropy: Earth-Science Reviews, v. 42, p. 49–93, doi: 10.1016/S0012-8252(96)00044-X.

Borradaile, G.J., and Jackson, M., 2004, Anisotropy of magnetic susceptibility (AMS): magnetic petrofabrics of deformed rocks, in Martín-Hernández, F., Luneburg, C.M., Aubourg, C., and Jackson, M. eds., Magnetic fabric: methods and applications, Geological Society, London, Special Publications, 238, p. 299–323.

Borradaile, G.J., and Jackson, M., 2010, Structural geology, petrofabrics and magnetic fabrics (AMS, AARM, AIRM): Journal of Structural Geology, v. 32, p. 1519–1551, doi: 10.1016/j.jsg.2009.09.006.

Bouchez, J., 1997, Granite is never isotropic: an introduction to AMS studies of granitic rocks, in Bouchez, J.L., Hutton, D.H.W., and Stephens, W.E. eds., Granite: From Segregation of Melt to Emplacement Fabrics, Springer Netherlands, p. 95–112.

Bracciali, L., Paterson, S.R., Memeti, V., and Rocchi, S., 2008, Build-up of the Tuolumne batholith, California: The Johnson Granite Porphyry, in Rocchi, S., Dini, A., Mazzarini, F., and Westernman, D.S., eds., Laccoliths, Sills, and dykes III Conference Physical Geology of Subvolcanic Systems: p. 17–18.

Brandon, A.D., and Smith, A.D., 1994, Mesozoic granitoid magmatism in southeast British Columbia: Implications for the origin of granitoid belts in the North American Cordillera: Journal of Geophysical Research: Solid Earth, v. 99, p. 11879–11896, doi: 10.1029/94JB00336.

Burgess, S.D., Bowring, S.A., Petsche, J., Miller, R.B., Miller, J.S., 2009, High Precision U-Pb CA-TIMS Geochronology for the Sentinel and Yosemite Creek Granodiorites, Sierra Nevada Batholith, CA: A history of punctuated intrusion and protracted crystallization. AGU 2009, Geochemistry, Magma chamber processes.

Callahan, C.N., and Markley, M.J., 2003, A record of crustal-scale stress; igneous foliation and lineation in the Mount Waldo Pluton, Waldo County, Maine: Journal of Structural Geology, v. 25, p. 541–555, doi: http://dx.doi.org/10.1016/S0191-8141(02)00052-4.

Cao, W., Paterson, S., Memeti, V., Mundil, R., Anderson, J.L., Schmidt, K., 2015, Tracking paleodeformation fields in the Mesozoic central Sierra Nevada arc: Implications for intra-arc cyclic deformation and arc tempos: Lithosphere, p. 1–25, doi: 10.1130/L389.1.

Cañón-Tapia, E., 2001, Factors affecting the relative importance of shape and distribution anisotropy in rocks: Theory and experiments: Tectonophysics, v. 340, p. 117–131, doi: 10.1016/S0040-1951(01)00150-0.

Chadima M, Jelínek V. (2009) Anisoft 4.2: Anisotropy Data Browser for Windows." Agico, Inc.

Chardon, D., 2003, Strain partitioning and batholith emplacement at the root of a transpressive magmatic arc: Journal of Structural Geology, v. 25, p. 91–107, doi: http://dx.doi.org/10.1016/S0191-8141(02)00015-9.

Chin, E.J., Lee, C.T.A., and Blichert-Toft, J., 2015, Growth of upper plate lithosphere controls tempo of arc magmatism: Constraints from Al-diffusion kinetics and coupled Lu-Hf and Sm-Nd chronology: Geochemical Perspectives Letters, v. 1, p. 20–32, doi: 10.7185/geochemlet.1503.

Coleman, D.S., Gray, W., and Glazner, A.F., 2004, Rethinking the emplacement and evolution of zoned plutons: Geochronologic evidence for incremental assembly of the Tuolumne Intrusive Suite, California: Geology, v. 32, p. 433, doi: 10.1130/G20220.1.

Currie, C.A, Decelles, P.G., and Beaumont, C., 2015, Geodynamic models of Cordilleran orogens : Gravitational instability of magmatic arc roots: Geological Society of America Memoir, v. 1212, p. 1–22, doi: 10.1130/2015.1212(01).

Cruden, A.R.A., Tobisch, O.T., and Launeau, P., 1999, Magnetic fabric evidence for conduit-fed emplacement of a tabular intrusion: Dinkey Creek Pluton, central Sierra Nevada batholith, California: Journal of Geophysical Research, v. 104, p. 10511–10530, doi: 10.1029/1998JB900093.

Davies, J.H., and von Blanckenburg, F., 1995, Slab breakoff: A model of lithosphere detachment and its test in the magmatism and deformation of collisional orogens: Earth and Planetary Science Letters, v. 129, p. 85–102, doi: 10.1016/0012-821X(94)00237-S.

DeCelles, P.G., Ducea, M.N., Kapp, P., and Zandt, G., 2009, Cyclicity in Cordilleran orogenic systems: Nature Geosciences, v. 2, p. 251–257, doi: 10.1038/ngeo469.

DeCelles, P.G., Zandt, G., Beck, S.L., Currie, C.A., Ducea, M.N., Kapp, P., Gehrels, G.E., Carrapa, B., Quade, J., and Schoenbohm, L.M., 2015, Cyclical orogenic processes in the Cenozoic central Andes, in DeCelles, P.G., Ducea, M.N., Carrapa, B., and Kapp, P.A. eds., Geodynamics of a Cordilleran Orogenic System: The Central Andes of Argentina and Northern Chile, Geological Society of America Memoir 212, p. 459–490, doi: 10.1130/2015.1212(22).

de Saint Blanquat, M., Tikoff, B., 1997, Development of Magmatic to Solid-State Fabrics during Syntectonic

Emplacement of the Mono Creek Granite, Sierra Nevada Batholith, in Bouchez, J.L., Hutton, D.H.W., and Stephens, W.E. eds., Granite: From Segregation of Melt to Emplacement Fabrics, Petrology and Structural Geology, Springer Netherlands, p. 231–252, doi: 10.1007/978-94-017-1717-5_15.

de Saint Blanquat, Tikoff, B., Teyssier, C., Vigneresse, J.L., 1998, Transpressional kinematics and magmatic arcs, in Holdsworth, R.E., Strachan, R.A., and Dewey, J.F. eds., Continental pranspressional and transtensional tectonics, Geological Society, London, Special Publications, p. 327–340, doi: 10.1144/GSL.SP.1998.135.01.21.

de Saint Blanquat, M., Horsman, E., Habert, G., Morgan, S., Vanderhaeghe, O., Law, R., Tikoff, B., and de Saint Blanquat, M., 2011, Multiscale magmatic cyclicity, duration of pluton construction, and the paradoxical relationship between tectonism and plutonism in continental arcs: Tectonophysics, v. 500, p. 20–33, doi: 10.1016/j.tecto.2009.12.009.

Ducea, M., 2001, The California arc: Thick granitic batholiths, eclogitic residues, lithospheric-scale thrusting, and magmatic flare-ups: GSA today, p. 4–10.

Ducea, M.N., and Barton, M.D., 2007, Igniting flare-up events in Cordilleran arcs: Geology, v. 35, p. 1047, doi: 10.1130/G23898A.1.

Ducea, M.N., Paterson, S.R., and DeCelles, P.G., 2015, High-Volume Magmatic Events in Subduction Systems: Elements, v. 11, p. 99–104, doi: 10.2113/gselements.11.2.99.

Engebretson, D.C., Cox, A., and Gordon, R.G., 1984, Relative motions between oceanic plates of the Pacific Basin: Journal of Geophysical Research, v. 89, p. 10291, doi: 10.1029/JB089iB12p10291.

Engebretson, D.C., Cox, A., and Gordon, R.G., 1985, Relative Motions Between Oceanic and Continental Plates in the Pacific Basin: Geological Society of America Special Papers , v. 206 , p. 1–60, doi: 10.1130/SPE206-p1.

Engelder, T., and Geiser, P., 1980, On the use of regional joint sets as trajectories of paleostress fields during the development of the Appalachian Plateau, New York: Journal of Geophysical Research: Solid Earth, v. 85, p. 6319–6341, doi: 10.1029/JB085iB11p06319.

Fiske, R., and Tobisch, O., 1978, Paleogeographic significance of volcanic rocks of the Ritter Range pendant, central Sierra Nevada, California, in Howel, D. G., and McDougall, K. A., eds.: Mesozoic palogeografy of the western United States,, p. 209–221.

Fiske, R., and Tobisch, O., 1994, Middle Cretaceous ash-flow tuff and caldera-collapse deposit in the Minarets caldera, east-central Sierra Nevada, California: Geological Society of America Bulletin, v. 205, p. 582–593, doi: 10.1130/0016-7606(1994)106<0582:MCAFTA>2.3.CO;2.

Fossen, H., Tikoff, B., and Teyssier, C., 1994, Strain modeling of transpressional and transtensional deformation: Norsk Geologisk Tidsskrift, v. 74, p. 134–145.

Glazner, A.F., 1991, Plutonism, oblique subduction, and continental growth: an example from the Mesozoic of California: Geology, v. 19, p. 784–786, doi: 10.1130/0091-7613(1991)019<0784:POSACG>2.3.CO.

Gorton, M.P., and Schandl, E.S., 2000, From continents to island arcs: A geochemical index of tectonic setting for arc-related and within-plate felsic to intermediate volcanic rocks: The Canadian Mineralogist, v. 38, p. 1065–1073, doi: 10.2113/gscanmin.38.5.1065.

Greene, D., and Schweickert, R., 1995, The Gem Lake shear zone: cretaceous dextral transpression in the northern Ritter Range Pendant, eastern Sierra Nevada, California: Tectonics, v. 14, p. 945–961, doi: 10.1029/95TC01509.

Gutierrez, C., Bryant, W., Saucedo, G., Wills, C., 2010, Geologic Map of California 2010: California Department of Conservation, California Geological Survey, Geologic Map No. 2, scale 1:450,000.

Hamilton, W., 1969, Mesozoic California and the underflow of Pacific Mantle: Geological Society of America Bulletin, v. 80, p. 2409–2430, doi: 10.1130/0016-7606(1969)80[2409:MCATUO]2.0.CO;2.

Hanson, R.B., Sorensen, S.S., Barton, M.D., Fiske, R.S., 1993, Long-term evolution of fluid-rock interactions in magmatic arcs: Evidence from the Ritter Range pendant, Sierra Nevada, California, and numerical modeling: Journal of Petrology, v. 34, p. 23–62, doi:10.1093/petrology/34.1.23.

Hargraves, R.B., Johnson, D., and Chan, C.Y., 1991, Distribution anisotropy: The cause of AMS in igneous rocks?: Geophysical Research Letters, v. 18, p. 2193–2196, doi: 10.1029/91GL01777.

Haschke, M., Günther, A., Melnick, D., Echtler, H., Reutter, K.J., Scheuber, E., and Oncken, O., 2006, Central and Southern Andean Tectonic Evolution Inferred from Arc Magmatism, in Oncken, O., Chong, G., Franz, G., Giese, P., Götze, H.-J., Ramos, V., Strecker, M., and Wigger, P. eds., The Andes: active subduction orogeny, Frontiers in Earth Sciences, Springer Berlin Heidelberg, p. 337–353.

Henry, B., Jordanova, D., Jordanova, N., Souque, C., and Robion, P., 2003, Anisotropy of magnetic susceptibility of heated rocks: Tectonophysics, v. 366, p. 241–258, doi: 10.1016/S0040-1951(03)00099-4.

Heuret, A., Funiciello, F., Faccenna, C., and Lallemand, S., 2007, Plate kinematics, slab shape and back-arc stress: A comparison between laboratory models and current subduction zones: Earth and Planetary Science Letters, v. 256, p. 473–483, doi: 10.1016/j.epsl.2007.02.004.

Hrouda, F., 1982, Magnetic anisotropy of rocks and its application in geology and gephysics: Geophysical Surveys, v. 5, p. 37–82, doi: 10.1007/BF01450244.

Hrouda, F., 1994, A technique for the measurement of thermal changes of magnetic susceptibility of weakly magnetic rocks by the CS-2 apparatus and KLY-2 Kappabridge: Geophysical Journal International, p. 604–612, doi: 10.1111/j.1365-246X.1994.tb03987.x.

Hrouda, F., and Kahan, Š, 1991, The magnetic fabric relationship between sedimentary and basement nappes in the High Tatra Mountains, N. Slovakia: Journal of Structural Geology, v. 13, p. 431–442, doi: http://dx.doi.org/10.1016/0191-8141(91)90016-C.

Hubert, N.K., Rinehart, C.D., 1965, Geologic map of the Devils Postpile quadrangle, Sierra Nevada, California: U.S. Geological Survey, Geologic Quadrangle Map GQ-437, scale 1: 62,500.

Hutton, D.H.W., 1988, Granite emplacement mechanisms and tectonic controls: inferences from deformation studies: Earth and Environmental Science Transactions of the Royal Society of Edinburgh, v. 79, p. 245–25, doi: 10.1017/S0263593300014255.

Jackson, S.E., Pearson, N.J., Griffin, W.L., and Belousova, E.A., 2004, The application of laser ablation-inductively coupled plasma-mass spectrometry to in situ U-Pb zircon geochronology: Chemical Geology, v. 211, p. 47–69, doi: The application of laser ablation-inductively coupled plasma-mass spectrometry to in situ U-Pb zircon geochronology.

Jelínek, V., 1978, Statistical processing of anisotropy of magnetic susceptibility measured on groups of specimens: Studia Geophysica et Geodaetica, v. 22, p. 50–62, doi: 10.1007/BF01613632.

Jelínek V (1981) Characterization of the magnetic fabric of rocks. Tectonophysics 79:T63–T67, doi: 10.1016/0040-1951(81)90110-4.

John, B.E., Blundy, J.D., 1993, Emplacement-related deformation of granitoid magmas, southern Adamello Massif, Italy: Geological Society of America Bulletin, v. 105, p. 1517–1541, doi: 10.1130/0016-7606(1993)105<1517:ERDOGM>2.3.CO;2.

Johnson, B.L., 2013, Structure, Construction, and Emplacement of the Yosemite Valley Intrusive Suite and the Yosemite Creek Granodiorite in the Central Sierra Nevada Batholith, Master thesis, San Jose State University.

Jordan, T.E., Isacks, B.L., Allmendinger, R.W., Brewer, J. a., Ramos, V. A., and Ando, C.J., 1983, Andean tectonics related to geometry of subducted Nazca plate.: Geological Society of America Bulletin, v. 94, p. 341–361, doi: 10.1130/0016-7606(1983)94<341:ATRTGO>2.0.CO;2.

Just, J., Kontny, A., De Wall, H., Hirt, A.M., and Martín-Hernández, F., 2004, Development of magnetic fabrics during hydrothermal alteration in the Soultz-sous-Forêts granite from the EPS-1 borehole, Upper Rhine Graben: Geological Society, London, Special Publications , v. 238 , p. 509–526, doi: 10.1144/GSL.SP.2004.238.01.26 .

Karlstrom, L., Lee, C.T.A., and Manga, M., 2014, The role of magmatically driven lithospheric thickening on arc front migration: Geochemistry, Geophysics, Geosystems, v. 15, p. 2655–2675, doi: 10.1002/2014GC005355.

Kistler, R.W., and Swanson, S.E., 1981, Petrology and geochronology of metamorphosed volcanic rocks and a Middle Cretaceous volcanic neck in the east-central Sierra Nevada, California: Journal of Geophysical Research: Solid Earth, v. 86, p. 10489–10501, doi: 10.1029/JB086iB11p10489.

Krása, D., and Herrero-Bervera, E., 2005, Alteration induced changes of magnetic fabric as exemplified by dykes of the Koolau volcanic range: Earth and Planetary Science Letters, v. 240, p. 445–453, doi: 10.1016/j.epsl.2005.09.028.

Loock, S., Diot, H., Van Wyk de Vries, B., Launeau, P., Merle, O., Vadeboin, F., and Petronis, M.S., 2008, Lava flow internal structure found from AMS and textural data: An example in methodology from the Chaîne des Puys, France: Journal of Volcanology and Geothermal Research, v. 177, p. 1092–1104, doi: 10.1016/j.jvolgeores.2008.08.017.

Lowe, T.K., 1996, Petrogenesis of the Minarets and Merced Peak Volcanic-plutonic complexes, Sierra Nevada, California: PhD. thesis, Stanford University, California.

Ludwig, K.R., 2003, User's manual for Isoplot v. 3.00, a geochronological toolkit for Microsoft Excel: Berkeley Geochronological Center Special Publication no. 4.

Mahan, K.H., Bartley, J.M., Coleman, D.S., Glazner, A.F., and Carl, B.S., 2003, Sheeted intrusion of the synkinematic McDoogle pluton, Sierra Nevada, California: Geological Society of America Bulletin, v. 115, p. 1570, doi: 10.1130/B22083.1.

Marsh, B., 1981, On the crystallinity, probability of occurrence, and rheology of lava and magma: Contributions to Mineralogy and Petrology, v. 78, p. 85–98, doi: 10.1007/BF00371146.

Matzel, J.E.P., Mundil, R., Paterson, S.R, Renne, P., and Nomade, S., 2005, Evaluating pluton growth models using high resolution geochronology: Tuolumne intrusive suite, Sierra Nevada, CA: Geological Society of America Abstracts with Programs, v. 37, no. 7, p. 131.

Matzel, J.E.P., Miller, J.S., Mundil, R., and Paterson, S.R., 2006, Zircon saturation and the growth of the Cathedral Peak pluton, CA: Geochimica et Cosmochimica Acta, v. 70, p. A403, doi: 10.1016/j.gca.2006.06.813.

Memeti, V., Paterson, S.R, Matzel, J.E.P., Mundil, R., and Okaya, D., 2010, Magmatic lobes as “snapshots” of magma chamber growth and evolution in large, composite batholiths: An example from the Tuolumne intrusion, Sierra Nevada, California: Geological Society of America Bulletin, v. 122, p. 1912–1931, doi: 10.1130/B30004.1.

McNulty, B.A., 1995, Shear zone development during magmatic arc construction: The Bench Canyon shear zone, central Sierra Nevada, California: Geological Society of America Bulletin, v. 107, p. 1094–1107, doi:

10.1130/00167606(1995)107<1094:SZDDMA>2.3.CO;2.

McNulty, B.A., Tong, W., and Tobisch, O.T., 1996, Assembly of a dike-fed magma chamber: The Jackass Lakes pluton, central Sierra Nevada, California: Geological Society of America Bulletin, v. 108, p. 926–940, doi: 10.1130/0016-7606(1996)108<0926:AOADFM>2.3.CO;2.

McNulty, B.A., Tobisch, O.T., Cruden, a. R., and Gilder, S., 2000, Multistage emplacement of the Mount Givens pluton, central Sierra Nevada batholith, California: Geological Society of America Bulletin, v. 112, p. 119–135, doi: 10.1130/0016-7606(2000)112<119:MEOTMG>2.0.CO;2.

Miller, J.S., Matzel, J.E.P., Miller, C.F., Burgess, S.D., and Miller, R.B., 2007, Zircon growth and recycling during the assembly of large, composite arc plutons: Journal of Volcanology and Geothermal Research, v. 167, p. 282–299, doi: 10.1016/j.jvolgeores.2007.04.019.

Miller, C.F., Furbish, D.J., Walker, B.A., Claiborne, L.L., Koteas, G.C., Bleick, H.A., and Miller, J.S., 2011, Growth of plutons by incremental emplacement of sheets in crystal-rich host: Evidence from Miocene intrusions of the Colorado River region, Nevada, USA: Tectonophysics, v. 500, p. 65–77, doi: 10.1016/j.tecto.2009.07.011.

Mundil, R., Nomade, S., Paterson, S., and Renne, P.R., 2004, Geochronological constraints (40Ar/39Ar and U/Pb) on the thermal history of the Tuolumne intrusive suite (Sierra Nevada, California): Eos (Transactions, American Geophysical Union), v. 85, p. 47.

Park, Y., and Means, W.D., 1996, Direct observation of deformation processes in crystal mushes: Journal of Structural Geology, v. 18, p. 847–858, doi: 10.1016/S0191-8141(96)80017-4.

Paterson, S.R, 1989, A reinterpretation of conjugate folds in the central Sierra Nevada, California: Geological Society of America Bulletin, v. 101, p. 248–259, doi: 10.1130/0016-7606(1989)101<0248:AROCFI>2.3.CO;2.

Paterson, S.R., Vernon, R.H., Tobisch, O.T., and Vernont, R., 1989, A review of criteria for the identification of magmatic and tectonic foliations in granitoids: Journal of structural geology, v. 11, p. 349–363, doi: 10.1016/0191-8141(89)90074-6.

Paterson, S.R., Fowler, T.K., Schmidt, K.L., Yoshinobu, A.S., Yuan, E.S., and Miller, R.B., 1998, Interpreting magmatic fabric patterns in plutons: Lithos, v. 44, p. 53–82, doi: 10.1016/S0024-4937(98)00022-X.

Paterson, S.R, Onezime, J., Teruya, L., and Žák, J., 2003, Quadruple-pronged enclaves: their significance for the interpretation of multiple magmatic fabrics in plutons: Journal of the Virtual Explorer, v.10, p. 15–30.

Paterson, S.R., and Ducea, M.N., 2015, Arc Magmatic Tempos: Gathering the Evidence: Elements, v. 11, p. 91–98, doi: 10.2113/gselements.11.2.91.

Paton, C., Woodhead, J.D., Hellstrom, J.C., Hergt, J.M., Greig, A., and Maas, R., 2010, Improved laser ablation U-Pb zircon geochronology through robust downhole fractionation correction: Geochemistry, Geophysics, Geosystems, v. 11, p. Q0AA06, doi: 10.1029/2009GC002618.

Pearce, J.A., and Peate, D.W., 1995, Tectonic Implications of the Composition of Volcanic ARC Magmas: Annual Review of Earth and Planetary Sciences, v. 23, p. 251–285, doi: 10.1146/annurev.ea.23.050195.001343.

Peck, D.L., 1980, Geologic map of the Merced Peak Quad- rangle, central Sierra Nevada, California: U.S. Geological Survey, Geologic Quadrangle Map GQ-1531, scale 1: 62,500.

Petford, N., 2003, Rheology of granitic magmas during ascent and emplacement: Annual Review of Earth and Planetary Sciences, v. 31, p. 399–427, doi: 10.1146/annurev.earth.31.100901.141352.

Petford, N., Cruden, A.R., McCaffrey, K.J., and Vigneresse, J.L., 2000, Granite magma formation, transport and emplacement in the Earth’s crust.: Nature, v. 408, p. 669–73, doi: 10.1038/35047000.

Petronis, M.S., O’Driscoll, B., and Lindline, J., 2011, Late stage oxide growth associated with hydrothermal alteration of the Western Granite, Isle of Rum, NW Scotland: Geochemistry, Geophysics, Geosystems, v. 12, doi: 10.1029/2010GC003246.

Petronis, M.S., Delcamp, A., and van Wyk de Vries, B., 2013, Magma emplacement into the Lemptégy scoria cone (Chaîne Des Puys, France) explored with structural, anisotropy of magnetic susceptibility, and Paleomagnetic data: Bulletin of Volcanology, v. 75, p. 753, doi: 10.1007/s00445-013-0753-y.

Petsche, J.M., 2008, Structure of the Sentinel Granodiorite, Yosemite National Park, California. Master thesis, San Jose State University

Pignotta, G.S., Paterson, S.R., Coyne, C.C., Anderson, J.L., and Onezime, J., 2010, Processes involved during incremental growth of the Jackass Lakes pluton, central Sierra Nevada batholith: Geosphere, v. 6, p. 130–159, doi: 10.1130/GES00224.1.

Pilger, R.H., 1984, Cenozoic plate kinematics, subduction and magmatism: South American Andes: Journal of the Geological Society, v. 141, p. 793–802, doi: 10.1144/gsjgs.141.5.0793.

Pitcher, S.W., Berger, A.R., 1972, Geology of Donegal: A Study of Granite Emplacement and Unroofing: Regional Geology Series, John Wiley & Sons Inc, New York, pp. 435.

Pollard, D.D. and Aydin, A., 1988, Progress in understanding jointing over the past century: Geological Society of America Bulletin, v. 100, p. 1181–1204, doi: 10.1130/0016-

Silver, L.T., and Chappell, B.W., 1988, The Peninsular Ranges Batholith: an insight into the evolution of the Cordilleran batholiths of southwestern North America: Earth and Environmental Science Transactions of the Royal Society of Edinburgh, v. 79, p. 105–121, doi: 10.1017/S0263593300014152.

Sizaret, S., Chen, Y., Chauvet, A., Marcoux, E., and Touray, J., 2003, Magnetic fabrics and fluid flow directions in hydrothermal systems. A case study in the Chaillac Ba–F–Fe deposits (France): Earth and Planetary Science Letters, v. 206, p. 555–570, doi: 10.1016/S0012-821X(02)01112-3.

Snow, J.K., and Wernicke, B.P., 2000, Cenozoic tectonism in the central basin and range: Magnitude, rate, and distribution of upper crustal strain: American Journal of Science, v. 300, p. 659–719, doi: 10.2475/ajs.300.9.659.

Sorensen, S.S., Dunne, G.C., Hanson, R.B., Barton, M.D., Becker, J., Tobisch, O.T., Fiske, R.S., 1998, From Jurassic shores to Cretaceous plutons: Geochemical evidence for paleoalteration environments of metavolcanic rocks, eastern California: Geological Society of America Bulletin, v. 110, no. 3, p. 326–343, doi:10.1130/0016-7606(1998)110<0326:FJSTCP>2.3 .CO;2

Schweickert, R.A., Bogen, N.L., Girty, G.H., Hanson, R.E., and Merguerian, C., 1984, Timing and structural expression of the Nevadan orogeny, Sierra Nevada, California: Geological Society of America Bulletin, v. 95, p. 967–979, doi: 10.1130/0016-7606(1984)95<967:TASEOT>2.0.CO;2.

Stern, T., 1981, Isotopic U-Pb ages of zircon from the granitoids of the central Sierra Nevada, California: Geological Survey Professional Paper, v. 1185, p. 1–17.

Tarling, D., and Hrouda, F., 1993, Magnetic Anisotropy of Rocks: Chapman & Hall.

Tatsumi, Y. (2005). The subduction factory: How it operates in the evolving Earth. GSA Today, 15, 4. doi:10.1130/1052-5173(2005)015[4:TSFHIO]2.0.CO;2

Tatsumi, Y., and Eggins, S., 1985, Subduction Zone Magmatism: Blackwell Science, Frontiers in Earth Sciences, 211 pp.

Tatsumi, Y., and Kogiso, T. (2003). The subduction factory: its role in the evolution of the Earth's crust and mantle. Geological Society, London, Special Publications , 219, 55–80. doi:10.1144/GSL.SP.2003.219.01.03

Thorkelson, D.J., 1996, Subduction of diverging plates and the principles of slab window formation: Tectonophysics, v. 255, p. 47–63, doi: 10.1016/0040-1951(95)00106-9.

Tikoff, B., and Teyssier, C., 1992, Crustal-scale, en echelon" P-shear" tensional bridges: A possible solution to the batholithic room problem: Geology, v. 20, p. 927–930, doi: 10.1130/0091-7613(1992)020<0927:CSEEPS>2.3.CO;2.

Tikoff, B., and Greene, D., 1994, Transpressional deformation within the Sierra Crest Shear zone system, Sierra Nevada, California (92-80 Ma): Vertical and horizontal stretching lineations within a single shear zone. Geological Society, America Abstracts with Programs Annual Meetings, 385.

Tikoff, B., and Greene, D., 1997, Stretching lineations in transpressional shear zones: an example from the Sierra Nevada Batholith, California: Journal of Structural Geology, v. 19, p. 29–39, doi: http://dx.doi.org/10.1016/S0191-8141(96)00056-9.

Tikoff, B., and de Saint Blanquat, M., 1997, Transpressional shearing and strike-slip partitioning in the Late Cretaceous Sierra Nevada magmatic arc, California: Tectonics, v. 16, p. 442–459, doi: 10.1029/97TC00720.

Tikoff, B., and Greene, D., 1997, Stretching lineations in transpressional shear zones: an example from the Sierra Nevada Batholith, California: Journal of Structural Geology, v. 19, p. 29–39, doi: http://dx.doi.org/10.1016/S0191-8141(96)00056-9.

Tikoff, B., Davis, M.R., Teyssier, C., De Saint Blanquat, M., Habert, G., and Morgan, S., 2005, Fabric studies within the Cascade Lake shear zone, Sierra Nevada, California: Tectonophysics, v. 400, p. 209–226, doi: 10.1016/j.tecto.2005.03.003.

Titus, S.J., Clark, R., and Tikoff, B., 2005, Geologic and geophysical investigation of two fine-grained granites, Sierra Nevada Batholith, California: Evidence for structural controls on emplacement and volcanism: Geological Society of America Bulletin, v. 117, p. 1256–1271, doi: 10.1130/B25689.1.

Tobisch, O., and Fiske, R., 1976, Significance of conjugate folds and crenulations in the central Sierra Nevada, California: Geological Society of America Bulletin, v. 87, p. 1411–1420, doi: 10.1130/0016-7606(1976)87<1411:SOCFAC>2.0.CO;2.

Tobisch, O.T., and Cruden, A.R., 1995, Fracture-controlled magma conduits in an obliquely convergent continental magmatic arc: Geology, v. 23, p. 941–944, doi: 10.1130/0091-7613(1995)023<0941:FCMCIA>2.3.CO;2.

Tobisch, O., and Fiske, R., 2000, Steep tilting of metavolcanic rocks by multiple mechanisms, central Sierra Nevada, California: Geological Society of America Bulletin, p. 1043–1058, doi: doi: 10.1130/0016-7606(2000)112<1043:STOMRB>2.0.CO;2.

Tobisch, O.T., Fiske, R.S., Sacks, S., and Taniguchi, D., 1977, Strain in metamorphosed volcaniclastic rocks and its bearing on the evolution of orogenic belts: Geological Society of America Bulletin, v. 88, p. 23–40, doi: 10.1130/0016-7606(1977)88<23:SIMVRA>2.0.CO;2.

Tobisch, O.T., Paterson, S.R., Longiaru, S., and Bhattacharyya, T., 1987, Extent of the Nevadan orogeny, central Sierra

Nevada, California: Geology , v. 15 , p. 132–135, doi: 10.1130/0091-7613(1987)15<132:EOTNOC>2.0.CO;2 .

Tobisch, O.T., Renne, P.R., and Saleeby, J.B., 1993, Deformation resulting from regional extension during pluton ascent and emplacement, central Sierra Nevada, California: Journal of Structural Geology, v. 15, p. 609–628, doi: 10.1016/0191-8141(93)90151-Y.

Tobisch, O.T., Saaleby, J.., Renne, P.R., and Mcnulty, B., 1995, Variations in deformation fields during development of a large- volume magmatic arc, central Sierra Nevada , California: Geological Society of America Bulletin, v. 107, p. 148–166, doi: 10.1130/0016-7606(1995)107<0148:VIDFDD>2.3.CO;2.

Trindade, R., Bouchez, J., Bolle, O., Nédélec, A., Peschler, A., and Poitrasson, F., 2001, Secondary fabrics revealed by remanence anisotropy: methodological study and examples from plutonic rocks: Geophysical Journal International, v. 147, p. 310–318, doi: 10.1029/2001GL013218.

Vernon, R.H., and Paterson, S.R., 2006, Mesoscopic structures resulting from crystal accumulation and melt movement in granites: Transactions of the Royal Society of Edinburgh-Earth Sciences, v. 97, p. 369–381, doi: 10.1017/S0263593300001516.

Wiedenbeck, M., Alle, P., Corfu, F., Griffin, W.L., Meier, M., Oberli, F., Vonquadt, A., Roddick, J.C., and Speigel, W., 1995, 3 Natural Zircon Standards for U-Th-Pb, Lu-Hf, Trace-Element and Ree Analyses: Geostandards Newsletter, v. 19, no. 1, p. 1-23, doi: 10.1111/j.1751-908X.1995.tb00147.x.

Whitney, D.L., and Evans, B.W. (2010). Abbreviations for names of rock-forming minerals. American Mineralogist, 95, 185–187. doi:10.2138/am.2010.3371

Žak, J., Paterson, S.R., and Memeti, V., 2007, Four magmatic fabrics in the Tuolumne batholith, central Sierra Nevada, California (USA): Implications for interpreting fabric patterns in plutons and evolution of magma chambers in the upper crust: Geological Society of America Bulletin, v. 119, p. 184–201, doi: 10.1130/B25773.1.

Chapter *4:*

SIMULTANEOUS BATHOLITH EMPLACEMENT, TERRANE/CONTINENT COLLISION, AND OROCLINAL BENDING IN THE BLUE MOUNTAINS PROVINCE, NORTH AMERICAN CORDILLERA

by Jiří Žák, Kryštof Verner, Filip Tomek, František V. Holub, Kenneth Johnson, and Joshua J. Schwartz

a paper published in **Tectonics** (2015), 34, doi: 10.1002/2015TC003859

(additional information are listed in supplementary material part 2 and appendix item 4)

KEY WORDS

◇ Anisotropy of magnetic susceptibility (AMS)

◇ North American Cordillera

◇ Orocline

◇ Pluton emplacement

◇ Terrane accretion

◇Terrane/continental collision

SIMULTANEOUS BATHOLITH EMPLACEMENT, TERRANE/CONTINENT COLLISION, AND OROCLINAL BENDING IN THE BLUE MOUNTAINS PROVINCE, NORTH AMERICAN CORDILLERA

ABSTRACT

The North American Cordillera is a classic example of accretionary orogen, consisting of multiple oceanic terranes attached to the western margin of Laurentia during the Mesozoic times. Although the Cordillera is linear for most parts, terrane boundaries are at a high angle to the overall structural grain in several segments of the orogen, which has been a matter of longstanding controversy as to how and when these orogenic curvatures formed. This paper discusses mechanisms, kinematics, and timing of initiation of one of these major curvatures, the Blue Mountains Province in northeastern Oregon. Here, magmatic fabric patterns and anisotropy of magnetic susceptibility (AMS) in the Wallowa batholith record three phases of progressive deformation of the host Wallowa terrane during Early Cretaceous. First is terrane-oblique ~NE–SW shortening, interpreted as recording attachment of the amalgamated oceanic and fringing, continental-margin terranes to the continental margin during dextral convergence at ~140 Ma. Deformation subsequently switched to pure shear-dominated ~NNE–SSW shortening associated with crustal thickening, caused by continued impingement of the amalgamated Blue Mountains superterrane into a presumed westward-concave reentrant in the continental margin at ~135–128 Ma. Upon impingement (at ~126 Ma), the northern portion of the superterrane became 'locked', leading to reorientation of the principal shortening direction to ~NNW–SSE while its still deformable southern portion rotated clockwise about a vertical axis. We thus propose oblique bending as the main mechanism of the orocline formation whereby horizontal compressive forces resulting from plate convergence acted at an angle to the terrane boundaries.

INTRODUCTION

The North American Cordillera developed as an accretionary orogen along the western margin of Laurentia during the Mesozoic to Cenozoic times (Figure 1) (e.g., Coney et al., 1980; Monger, 1997; Dickinson, 2004; Piercey and Colpron, 2009; and Hildebrand, 2013). Though the polarity and significance of the past subductions have been a matter of debate (e.g., Johnston, 2008; Hildebrand, 2009, 2013; Sigloch and Mihalynuk, 2013), the prevailing view is that the overall eastward motion of the paleo-Pacific basin (e.g., Hamilton, 1969; Atwater, 1970; Engebretson et al., 1985), itself composed of several oceanic plates, brought a number of Late Paleozoic to Early Mesozoic intraoceanic-arc systems and associated sedimentary basins (in some reconstructions inferred to compose a large ribbon continent) (e.g., Johnston, 2001, 2008; Hildebrand, 2009, 2013) to the proximity of the Laurentian margin. These oceanic units were then successively attached to and variously displaced along this continental margin as tectonostratigraphic terranes (Figure 1). Though much of the western North American Cordillera is linear and roughly parallels the leading continental edge, some portions exhibit a significant curvature and are at a high angle to the overall ~NNW–SSE tectonic grain (Figure 1; present-day coordinates are used throughout this paper). From north to south, the major Cordilleran orogenic curvatures include the Bering Strait region northwest of Alaska (e.g., Patton and Tailleur, 1977; Amato et al., 2004; not shown in Figure 1), several oroclines in central and southern Alaska (e.g., Johnston, 2001; Glen, 2004), the Southern Vancouver Island orocline (Johnston and Acton, 2003), the Blue Mountains Province (BMP in Figure 1), forming what was variously referred to as the

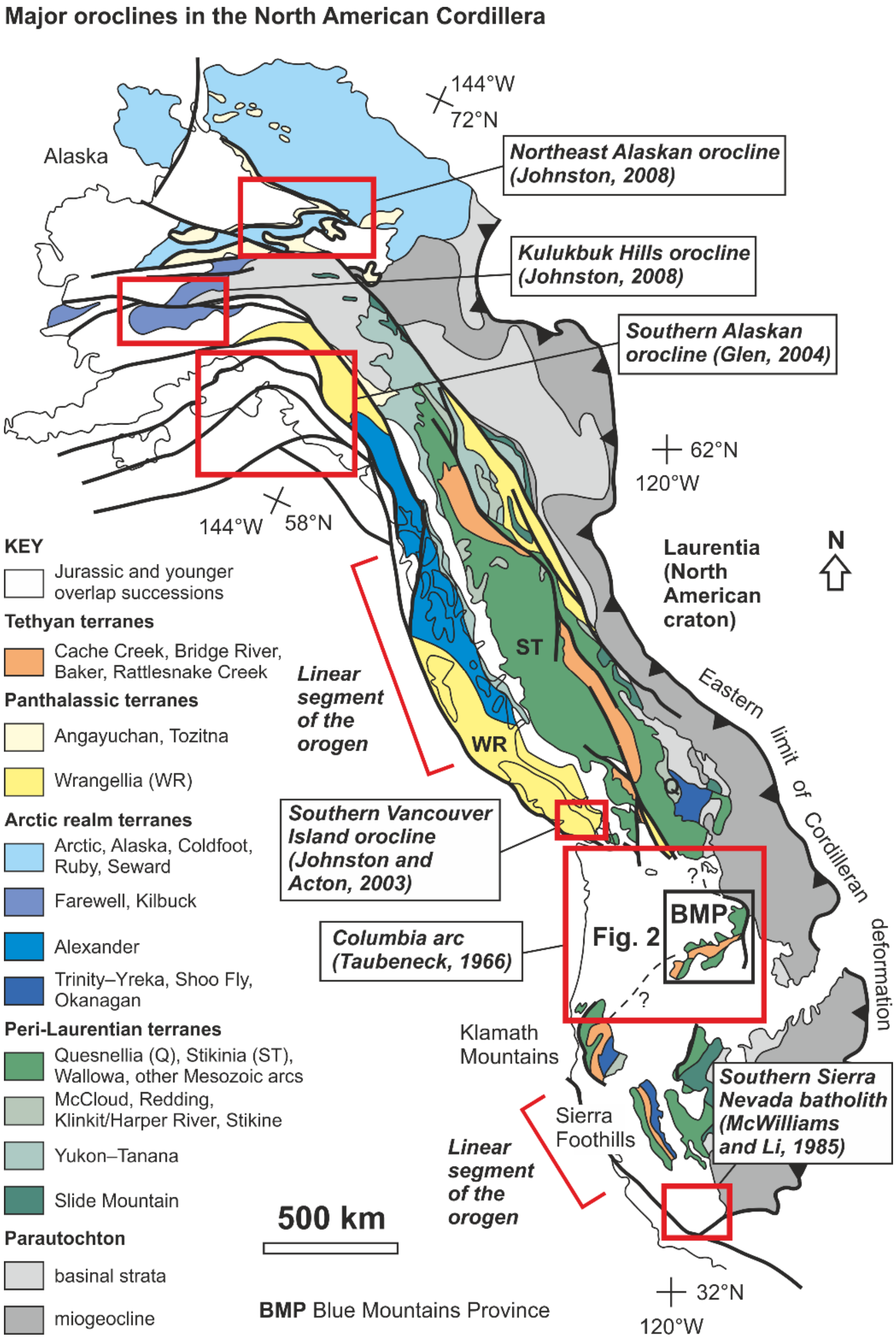

Figure 1. Schematic geologic map showing the principal tectonostratigraphic terranes, their inferred afinities, and major oroclines in the North American Cordillera. Base map modified from Piercey and Colpron [2009].

Columbia or Idaho orocline (e.g., Carey, 1958; Hamilton and Myers, 1966; Taubeneck, 1966; Greenwood and Reid, 1969) around an area covered by Tertiary volcanic and sedimentary rocks (Figure 1), and an orocline at the southern termination of the Sierra Nevada batholith (McWilliams and Li, 1985).

As exemplified by the Blue Mountains Province, large uncertainty persists regarding the driving forces, kinematics, exact amount of rotation, and timing of formation of these orogenic curvatures. In this paper, we examine in detail a portion of the Early Cretaceous Wallowa batholith that, on a regional scale, intrudes into the 'hinge' of the Blue Mountains orocline (Figures 2, 3). Furthermore, the existing structural and geochronologic data establish that batholith emplacement was broadly coeval with collision of the previously amalgamated oceanic terranes ('the Blue Mountains superterrane'; Figure 2) with the North American craton. The Wallowa batholith is thus one of the key areas to explore the nature of crustal deformation, kinematics, and temporal relations of plutonism to terrane/continent collision and to vertical-axis lithospheric rotations in the Cordilleran orogen.

Below, we first briefly review the principal tectonic elements of the Blue Mountains Province and geology of the Wallowa batholith and then concentrate on the host rock deformation structures and multiple magmatic to solid-state fabrics recorded in the batholith. The field observations are complemented by a magnetic fabric analysis in three main component plutons of the batholith to obtain an independent quantitative information on their internal structure and to infer possible strain patterns recorded by these plutons. Finally, we use these data sets as a background for discussion on kinematics and potential geodynamic causes of the vertical-axis lithospheric rotations in the North American Cordillera.

PRINCIPAL LITHOTECTONIC ELEMENTS OF THE BLUE MOUNTAINS PROVINCE

Overview

The Blue Mountains Province is an erosional inlier that exposes the uplifted late Paleozoic to Mesozoic variably metamorphosed basement rocks from beneath Tertiary and Quaternary deposits and Columbia River flood basalts. The basement comprises the following principal lithotectonic units (e.g., Dorsey and LaMaskin, 2007, 2008; LaMaskin et al., 2009, 2011; Schwartz et al., 2010, 2011a):

(1) The outboard Wallowa terrane (Figure 2) is an oceanic island-arc assemblage consisting of Permian and Triassic volcanic and volcaniclastic rocks. The island-arc volcanic complex is overlain unconformably by Triassic to Lower Jurassic siliciclastic and limestone successions of the Hurwal and Martin Bridge formations, respectively (e.g., Stanley et al., 2008), and these rocks are in turn unconformably overlain by a Middle to Upper Jurassic flysch-like succession (LaMaskin et al., 2008). The Wallowa terrane was correlated with the Wrangellia or Stikinia terranes farther

north in the Canadian Cordillera (e.g., Sarewitz, 1983; Mortimer, 1986; Wernicke and Klepacki, 1988; Schwartz et al., 2011a).

(2) The less extensively exposed, inboard Olds Ferry terrane (Figure 2) is also an island-arc complex that consists of Middle Triassic to Lower Jurassic weakly metamorphosed volcanic and volcaniclastic rocks of chiefly andesitic composition (Brooks and Vallier, 1978; Vallier, 1995). This terrane was interpreted as a fringing arc complex that developed along the North American passive margin (e.g., Ferns and Brooks, 1995).

(3) The Baker terrane (Figure 2) is a subduction–accretionary wedge–forearc complex located between the two island-arc assemblages and was thrust over the Wallowa terrane during Mid- to Late-Jurassic terrane convergence (Ferns and Brooks, 1995; Schwartz et al., 2010; Žák et al., 2012a). The terrane contains fault-bounded island-arc igneous and sedimentary rocks ranging in age from Middle Devonian to Early Jurassic and extensively disrupted fragments of ocean floor, including mélanges with blocks of moderate-pressure metamorphic rocks (Schwartz et al., 2011a). Part of the Baker terrane is overlain unconformably by a Permian to Triassic siliciclastic succession (Ferns and Brooks, 1995; Schwartz et al., 2011a).

(4) The Izee unit (Figure 2) comprises Triassic and Jurassic sedimentary successions that can be divided into two marine siliciclastic Upper Triassic to Early to early-Late Lower Jurassic megasequences separated by an angular unconformity (Dorsey and LaMaskin, 2007). The Izee basin was earlier interpreted as a separate forearc basin terrane (Dickinson, 1979) but recently was reinterpreted as a regional overlap succession that rests unconformably upon the Baker and Olds Ferry terranes (Dorsey and LaMaskin, 2007).

(5) To the east, the Blue Mountains oceanic terranes are juxtaposed against the western margin of the North American craton (Laurentia) along the Salmon River suture zone (Figure 2). This zone comprises several west-dipping thrust sheets derived from the Wallowa terrane, pinches out the Baker and Olds Ferry terranes, and is separated from the easterly Cretaceous–Tertiary plutons of the Idaho batholith along the Western Idaho shear zone. The Salmon River suture zone also coincides with the 0.706Sr line which marks an abrupt increase in contamination of plutonic rocks by radiogenic Precambrian continental crust (e.g., Armstrong et al., 1977; Manduca et al., 1992, 1993; Giorgis et al., 2005).

Though the Salmon River suture zone records a protracted kinematic history (e.g., Manduca et al., 1993; McClelland et al., 2000; Gray and Oldow, 2005; Giorgis et al., 2008), most relevant for this study are the Early Cretaceous events coeval with emplacement of the Wallowa batholith. Recent petrologic data and Sm–Nd garnet ages suggest prograde amphibolite-facies metamorphism and garnet growth at ~141–124 Ma and were interpreted as recording crustal thickening via stacking of thrust sheets and dating the collision of the previously amalgamated terranes with the western North American margin (Selverstone et al., 1992; Getty et al., 1993; McKay, 2011; Stowell et al., 2014).

(6) To the northeast, the Wallowa terrane, Salmon River belt, and Western Idaho shear zone abut against the North American craton margin. In the map (Figure 2), all these units as well as the Sri isopleth take an abrupt, approximately 90° bend from ~NNE–SSW in the east to ~E–W in the north; the bend has been referred to as the Syringa embayment. The origin of the bend has been a matter of controversy (see Lund et al., 2008 for discussion). In one view, the embayment is an inherited pre-accretion feature of the rifted North American craton margin (Schmidt et al., 2003, 2009) with the ~E–W segment representing a transform fault and the ~NNE–SSW segment representing part of the now shortened rift structure (Tikoff et al., 2014). Recent paleomagnetic data suggest that the original orientation of the two segments may have been 60° and 330°, respectively (Tikoff et al., 2014). In an opposite view, formation of the bend is a result of sinistral transpressional shearing where the NNE–SSW-trending assemblages have been truncated along the Late Cretaceous ~NW–SE to ~E–W-trending Orofino shear zone (Figure 2; active from ~90 to ~70 Ma) (McClelland and Oldow, 2007).

Geometry of the terrane boundaries and vertical-axis block rotations

In a regional map view, the terrane boundaries in the Blue Mountains Province generally trend ~E–W in the west and then continuously reorient to the ~NNE–SSW trend in the east (Figure 2). The ~E–W trend of the Blue Mountains terranes is at a high angle to the ~NNW–SSE trend of the Sierra Nevada and Canadian Cordillera terranes (Figure 1). The curved terrane boundaries in the Blue Mountains Province are thus suggestive of significant clockwise vertical-axis rotation (Figure 2), a notion that is supported by several paleomagnetic studies (see Housen and Dorsey, 2005 for discussion). Wilson and Cox (1980) inferred rotation by 60° ± 29° on the basis of samples from plutonic and contact metamorphic rocks of the Wallowa batholith and Baker terrane. Similarly, Hillhouse et al. (1982) estimated rotation by 66° ± 21° from Upper Triassic volcanogenic rocks of the Wallowa terrane. Cretaceous sedimentary rocks of the Mitchell Inlier (Figure 2), recently interpreted by Schwartz and Johnson (2014) as separated from the central Blue Mountains by a large-magnitude shear zone, indicate a lesser amount of rotation of 37° ± 7°. The rotation was resolved into 21° from the mid-Cretaceous to early/middle Eocene and an additional 16° after Eocene (Housen and Dorsey, 2005; see also Grommé et al., 1986). It follows from the above that the paleomagnetic data from igneous and metamorphic rocks lack paleohorizontal control and involve an unknown amount of tilt of the sampled units and that large rotations are consistently derived from older rocks in the Blue Mountains Province, thus all of the above estimates may be correct.

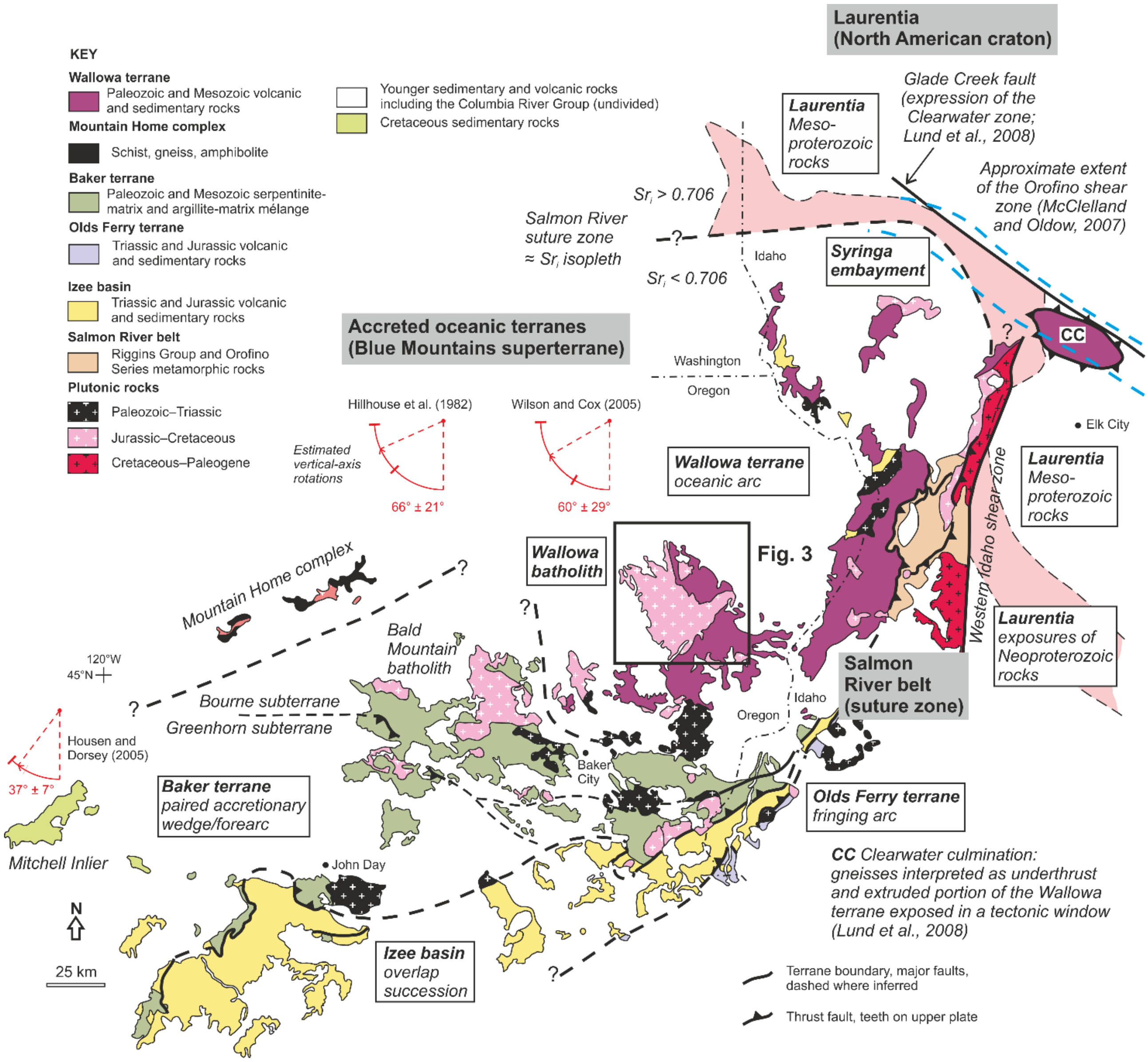

Figure 2. Simplified geologic map showing terranes, their boundaries, other principal tectonic features, and main plutonic units in the Blue Mountains Province accreted to the North American craton. The Wallowa batholith intruded into the hinge of the orogenic curvature. Redrafted from Schwartz et al. [2011a].

GEOLOGY OF THE WALLOWA BATHOLITH

The Wallowa batholith is the largest (~620 km2) of multiple compositionally diverse plutonic bodies that intruded the Blue Mountains Province (Figure 2) (Krauskopf, 1943). The batholith is composite and from north to south consists of four main plutons (Figures 3, 4) (Taubeneck, 1987; Johnson et al., 2011): Pole Bridge (140.2 ± 1.4 Ma), Hurricane Divide (130.2 ± 1.0 Ma), Craig Mountain (125.6 ± 0.6 Ma), and Needle Point (130.8 ± 1.5 Ma; not examined in this study). Overlapping ages and identical compositions of the ~130 Ma Hurricane Divide and Needle Point plutons (K. Johnson, unpublished data) suggest that they are virtually the same intrusion bifurcated by the younger Craig Mountain pluton (Figure 3). From north to south, the inter-pluton contacts change orientation from ~NE–SW to ~E–W and define a fan-like pattern, with the youngest Craig Mountain pluton in the middle tapered westward. In addition, the Sawtooth stock dated at 129.9 ± 2.1 Ma (all ages are based on U–Pb SHRIMP-RG measurements of igneous zircons) (Johnson et al., 2011) intruded the easterly batholith host rock and is correlative both in terms of composition and age with the Hurricane Divide pluton (Figures 3, 4).

Rocks from the Pole Bridge, Hurricane Divide, and Sawtooth plutons are broadly of the same lithology, ranging from low-silica tonalite along pluton margins to amphibole–biotite granodiorite in pluton cores. Minor hornblende gabbro bodies intrude all of the tonalite–granodiorite plutons. These plutons are interpreted to be derived from a depleted-mantle source during Late Jurassic–Early Cretaceous crustal thickening broadly coeval with thrust loading in the Salmon River belt (Johnson et al., 2011). On the other hand, the Craig Mountain pluton is compositionally more felsic, and primarily granodiorite. Rocks of the Craig Mountain pluton are consistent with partial melting of thickened crust (Johnson et al., 2011) following attachment of the Blue Mountains superterrane to the continental margin at ~141–124 Ma. The last stage of Wallowa magmatism is represented by small satellite bodies of cordierite-bearing trondhjemite to the south of the main batholith (e.g., Taubeneck, 1964; Johnson et al., 1997, 2002).

In summary, existing geochemical data indicate that the Wallowa batholith formed in a supra-subduction setting associated with amalgamation of the Blue Mountains superterrane to the North American craton (Johnson et al., 2011). However, it remains unclear, and beyond the scope of this paper, whether Wallowa plutonism formed above an oceanic plate subducting eastward (Farallon plate) or westward (oceanic basin once underlying the Salmon River belt) beneath the Blue Mountains superterrane. Contrasting views regarding subduction zone polarity are presented in Selverstone et al. (1992), McClelland et al. (2000), Dorsey and LaMaskin (2007, 2008), and Schwartz et al. (2011b, 2014, and references therein).

The remainder of the Wallowa batholith is largely concealed by basalt flows of the Miocene Columbia River Group; intrusive contacts against the host rocks of the Wallowa oceanic arc terrane are exposed only along its northeastern and southeastern margins (Figures 3, 4) (Krauskopf, 1943; Weis et al., 1976). In a stratigraphic order, these variably metamorphosed volcanic and sedimentary arc-related host rocks comprise (1) a Triassic succession, the base of which is not exposed, of altered basic to intermediate volcanic rocks and marine mudstones, sandstones, and conglomerates, overlain conformably by (2) a ~300–460 m thick succession of Upper Triassic (Carnian–Norian) limestone and calcareous shales of the Martin Bridge Formation, and by (3) Upper Triassic to Lower Jurassic (Norian–Sinemurian) bedded siliciclastic sedimentary rocks of the Hurwal Formation comprising shales, siltstones, and quartzites of unknown total thickness (Weis et al., 1976; Stanley et al., 2008). Both successions have been heterogeneously overprinted by contact metamorphism which produced a variety of hornfels from siliciclastic protoliths and was most intense in the carbonate lithologies. The latter are commonly recrystallized to marbles and calc-silicate rocks with tremolite, garnet, epidote, diopside, and wollastonite (Krauskopf, 1943). Away from the batholith, the degree of regional metamorphism is low in general and does not exceed greenschist-facies conditions, consistent with Al-in hornblende barometry indicating a shallow emplacement depth of less than 7 km (Žák et al., 2012b).

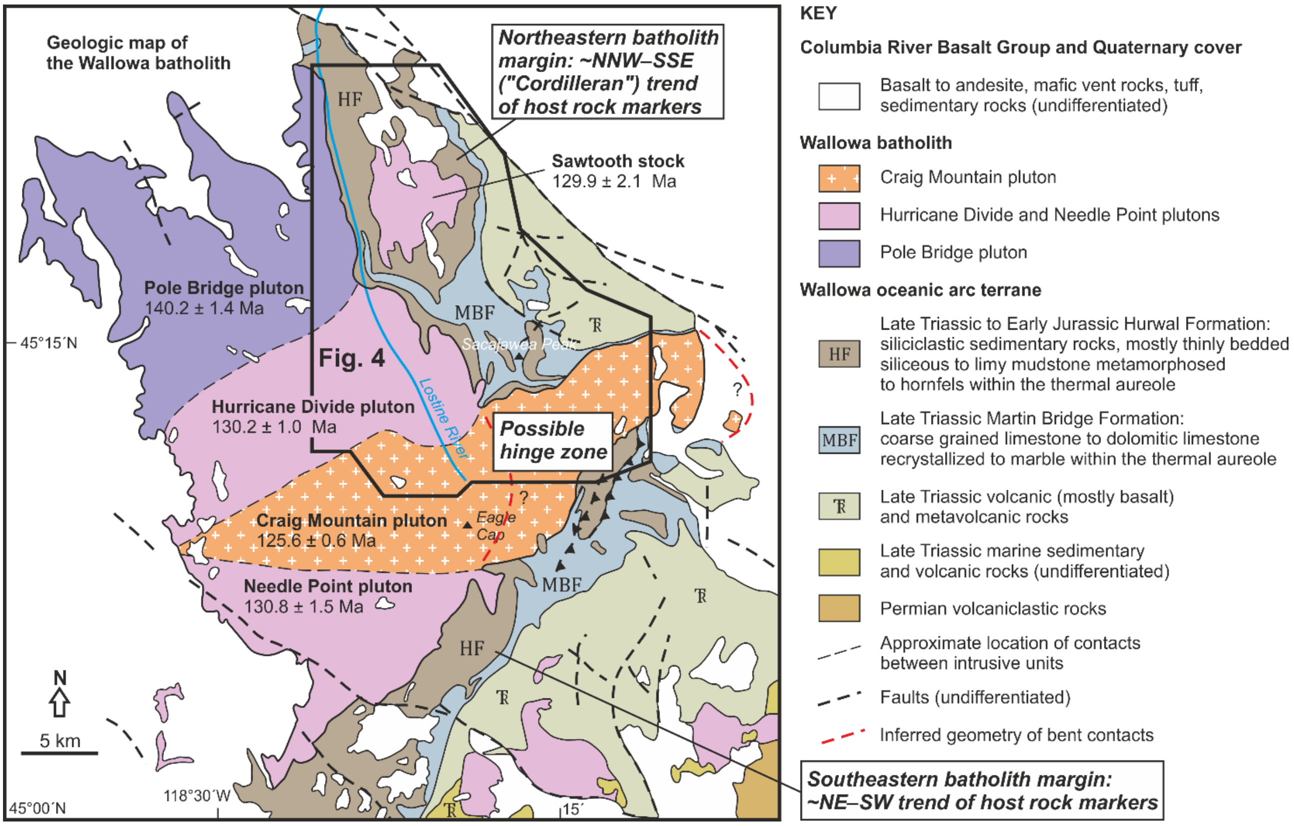

Figure 3. Simplified geologic map of the Wallowa batholith, which is largely concealed beneath the Tertiary Columbia River Basalt Group. The batholith is composite and consists of four component intrusions emplaced over a time span of about 15 M.y. during Early Cretaceous. Geology compiled from Walker [1979] and Taubeneck [1987], radiometric ages from Johnson et al. [2011].

STRUCTURE OF THE BATHOLITH HOST ROCK

On a regional map scale, lithologic contacts between the Late Triassic (meta-)volcanic rocks and the Martin Bridge and Hurwal formations define an arc with a ~NNW–SSE-trending limb roughly parallel to the northeastern batholith margin, hinge zone located within the northeastern off-shoot of the Craig Mountain pluton, and a ~NNE–SSW-trending limb parallel to the southeastern batholith margin (Figures 3, 4). At this scale, the outer batholith margin is largely discordant to bedding and foliation in the host rock and the inter-pluton contacts are at a high angle to the regional curvature of host rock markers (Figures 3, 4).

This tens of kilometers scale structure contains folds on a scale of kilometers to hundreds meters with the fold geometry and fabric orientation varying along strike; in some places, fold limbs have been overturned (Figures 4–6, 7a, b). Below, the fabrics and folds are described in four domains from the northwest to the southeast along the batholith margin (Domains 1–4; Figure 4).

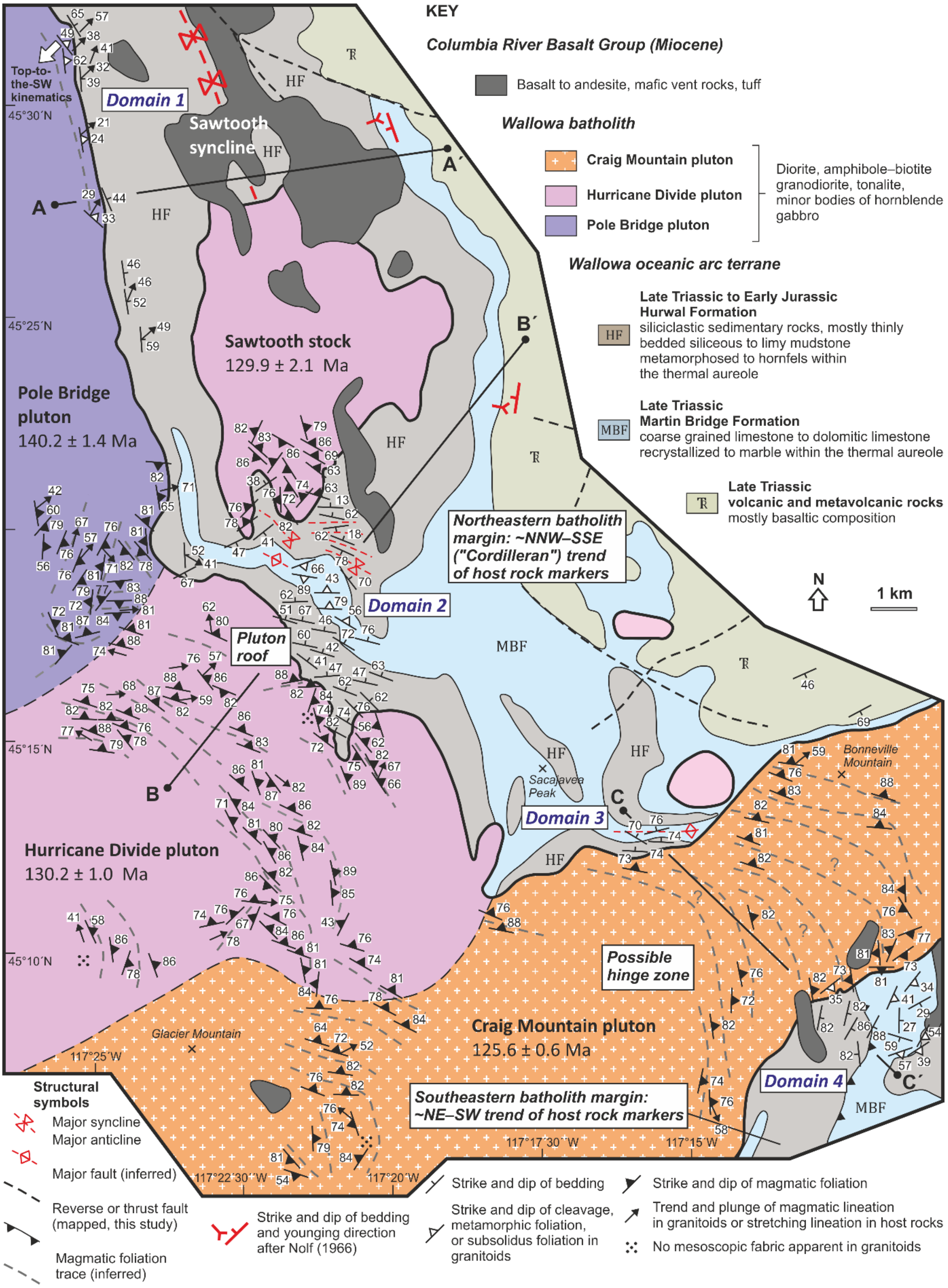

Figure 4. Structural map of the northeastern portion of the Wallowa batholith and its host rocks. Note different magmatic to solid-state fabric patterns in each pluton.

In Domain 1, bedding is well preserved, chiefly planar, and oriented uniformly over large regions in the siliciclastic rocks of the Hurwal Formation (Figures 4, 5, 6c). Near the Pole Bridge pluton, the bedding strikes parallel to the pluton margin and dips at moderate angle to the ~ENE to ~E, slickenside-type striations on the bedding planes plunge at moderate angle to the ~NNE to ~NE (Figures 4, 5). This easterly-dipping strata are part of a major ~NNW–SSE-trending Sawtooth syncline (Nolf, 1966; not mapped in this study; Figures 4, 5).

In Domain 2, significant vertical relief establishes that the northeastern margin of the Hurricane Divide pluton is a flat-lying batholith roof (Figure 6a) rolling over into a steep wall (see Žák et al., 2012b for details). The overall synclinal architecture described above is here superposed by smaller-scale folds with their axial planes at a high angle to the ~NNW–SSE structural grain (Figures 4, 6b). For instance, we mapped a steeply inclined, tight to isoclinal, ~NNW–SSE to ~NW–SE-trending anticline facing towards the pluton, where the marbles and calc-silicate rocks of the Martin Bridge Formation occupy the core and the overlying siliciclastic rocks of the Hurwal Formation are exposed in the limbs (Figures 4, 5, 6b). Furthermore, another anticlines and

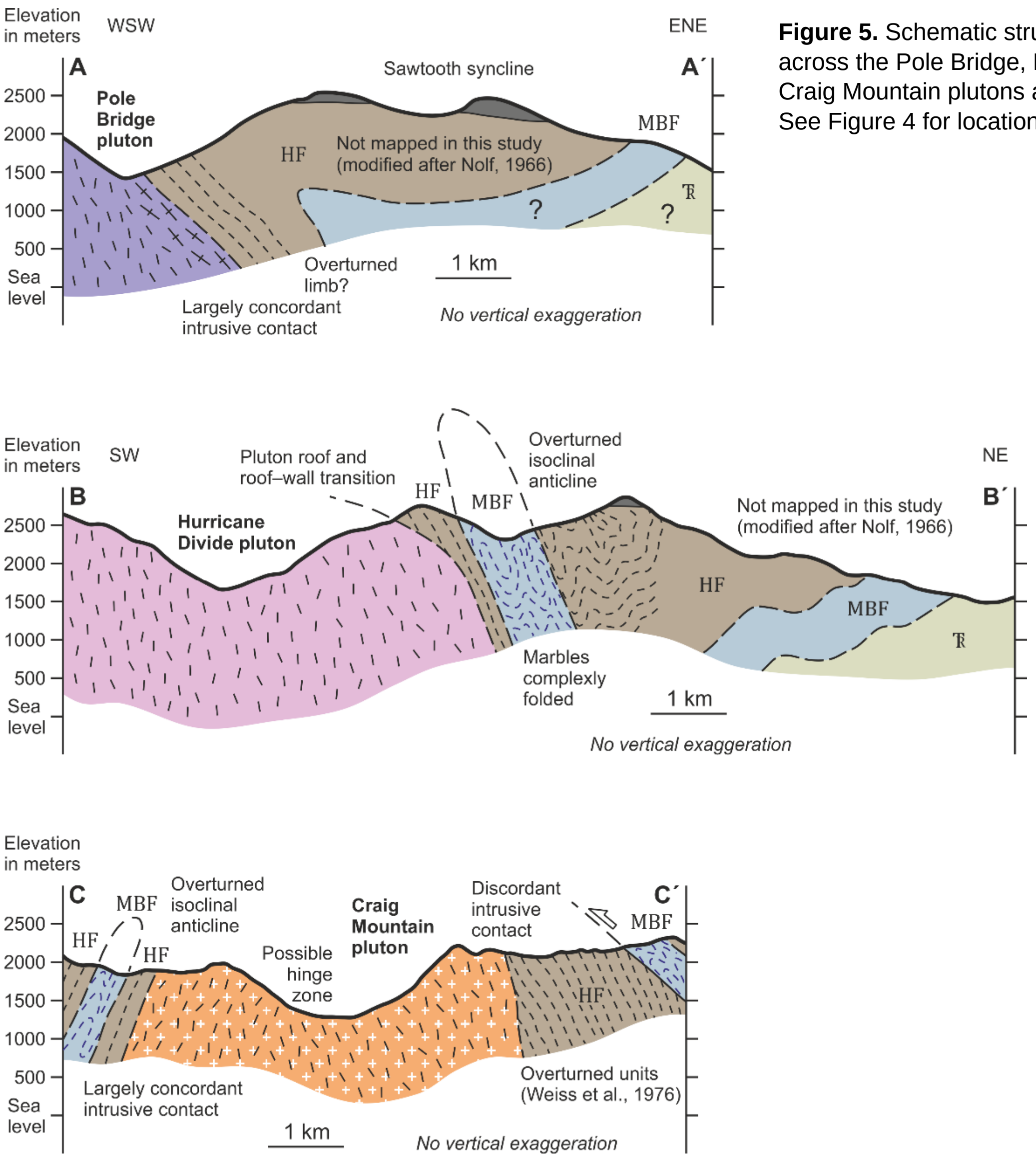

Figure 5. Schematic structural cross-sections across the Pole Bridge, Hurricane Divide, and Craig Mountain plutons and their host rocks. See Figure 4 for location.

synclines occur in the nearby Hurwal Formation (Figures 4, 5). The exception to this generally simple fold style is seen in the marbles where boudins of calc-silicate rocks have been folded more complexly. On outcrops, both formations exhibit remarkably contrasting patterns of deformation (Figure 6c, d). The marbles exhibit pervasive metamorphic foliation and compositional banding (Figure 6d), and have well developed mineral and stretching lineation defined by elongated or fibrous grains and aggregates of calcite, tremolite, and epidote. Foliation commonly encloses boudins of competent calc-silicate rocks and is axial-planar to minor tight to isoclinal folds defined

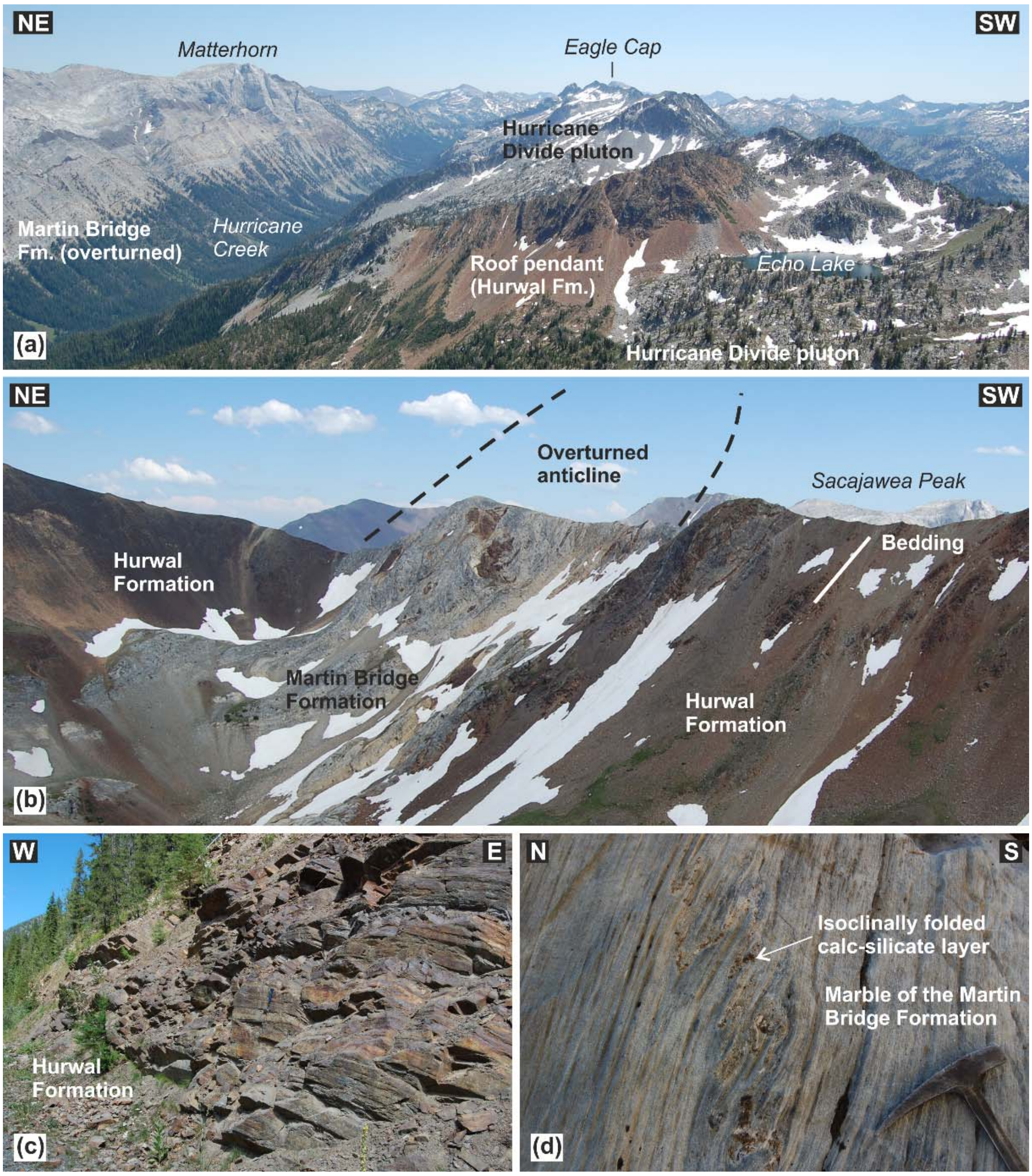

Figure 6. Host rock structures along the northeastern margin of the Wallowa batholith. (a) Distant view to the SE on top of the Wallowa batholith with a flat roof pendant made up of the siliciclastic rocks of the Hurwal Formation and east-dipping marbles of the Martin Bridge Formation in the far left background; view from a ridge in the Hurricane Divide. (b) Overturned NW–SE-trending isoclinal anticline cored by marbles of the Martin Bridge Formation, looking SE; ridge 2.2 km SSE of Frances Lake. (c) East-dipping bedded siliciclastic succession of the Hurwal Formation; hammer for scale. WGS coordinates: N45.340177°, W117.410447°. (d) Minor isoclinal folds with their axial planes parallel to pervasive metamorphic foliation in marble of the Martin Bridge Formation; hammer for scale. WGS coordinates: N45.27841455°, W117.35172400°.

by folded calcite veins or quartzite and calc-silicate intercalations (Figure 6d). Farther south, bedding in the siliciclastics and metamorphic foliation and banding in the marbles strike ~E–W to ~NW–SE and dip moderately to steeply to the ~N to ~NE (Figures 4, 5, 7a). Mineral lineation in the marbles tend to plunge moderately to the ~NE (Figures 4, 7a).

In Domain 3 along the northwestern margin of the Craig Mountain pluton, lithologic contacts between the Martin Bridge and Hurwal formations, as well as steep metamorphic foliation and bedding, dip steeply to the N and, again, appear deflected from the ~NNW–SSE to the ~E–W strike, i.e., towards parallelism with the nearby pluton margin (Figures 4, 5). Similarly to Domain 2, the units here define an overturned steep isoclinal anticline cored by the marbles and facing towards the pluton (Figures 4, 5).

In the southeasterly Domain 4, a limb-parallel, ~NNE–SSW-trending reverse to thrust fault was mapped that separates siliciclastic rocks of the Hurwal Formation from the Martin Bridge marbles (Figures 4, 5). Bedding and foliation dip moderately to steeply to the ~ESE to ~SE (Figures 4, 5, 7b), and mineral and stretching lineations are rare. In contrast to Domain 3, the intrusive pluton/host rock contact is discordant and truncates both the thrust fault and mesoscopic fabrics in the host rock.

MULTIPLE MAGMATIC TO SOLID STATE FABRICS IN THE WALLOWA BATHOLITH

Mesoscopic magmatic foliation in the Pole Bridge, Hurricane Divide, and Craig Mountain plutons is commonly defined by planar shape-preferred orientation of biotite, hornblende, and feldspar grains or aggregates (Figure 8a) and by the alignment of flattened microgranular enclaves and elongated host rock xenoliths (Figure 8a–d). Lineation is defined by linear shape-preferred orientation of euhedral to subhedral hornblende crystals or elongated biotite aggregates in the foliation plane. On many outcrops, however, lineation is difficult to measure due to the lack of suitably oriented, foliation-parallel surfaces.

A similar feature of all plutons in the batholith is a moderately to steeply plunging lineation (~60–90° plunge) and a steep foliation (~70–90° dip), the strike and statistical orientation distribution of which varies among the individual plutons (Figures 4, 7c–f). In most cases, poles to foliation tend to concentrate around the periphery of the stereonets with multiple maxima and submaxima (Figure 7c–f) and thus define a girdle around the steeply plunging lineation. The Pole Bridge pluton is characterized by margin-parallel, ~N to ~NNW-striking subsolidus foliation in the north and two distinct foliations (~NNE–SSW and ~E–W) in its southeastern portion (Figures 4, 7c). Broadly similar to the latter is the Sawtooth stock with dominant ~NE–SW and less pronounced ~NW–SE foliations (Figures 4, 7d). In the Hurricane Divide pluton, foliation strikes predominantly ~WNW–ESE and ~NW–SE but also ~N–S to ~NNE–SSW in a domain near its southern margin (Figures 4, 7e). In contrast, a map analysis reveals a pronounced arcuate foliation pattern in the Craig Mountain pluton, where foliations are at a low angle to the nearby pluton

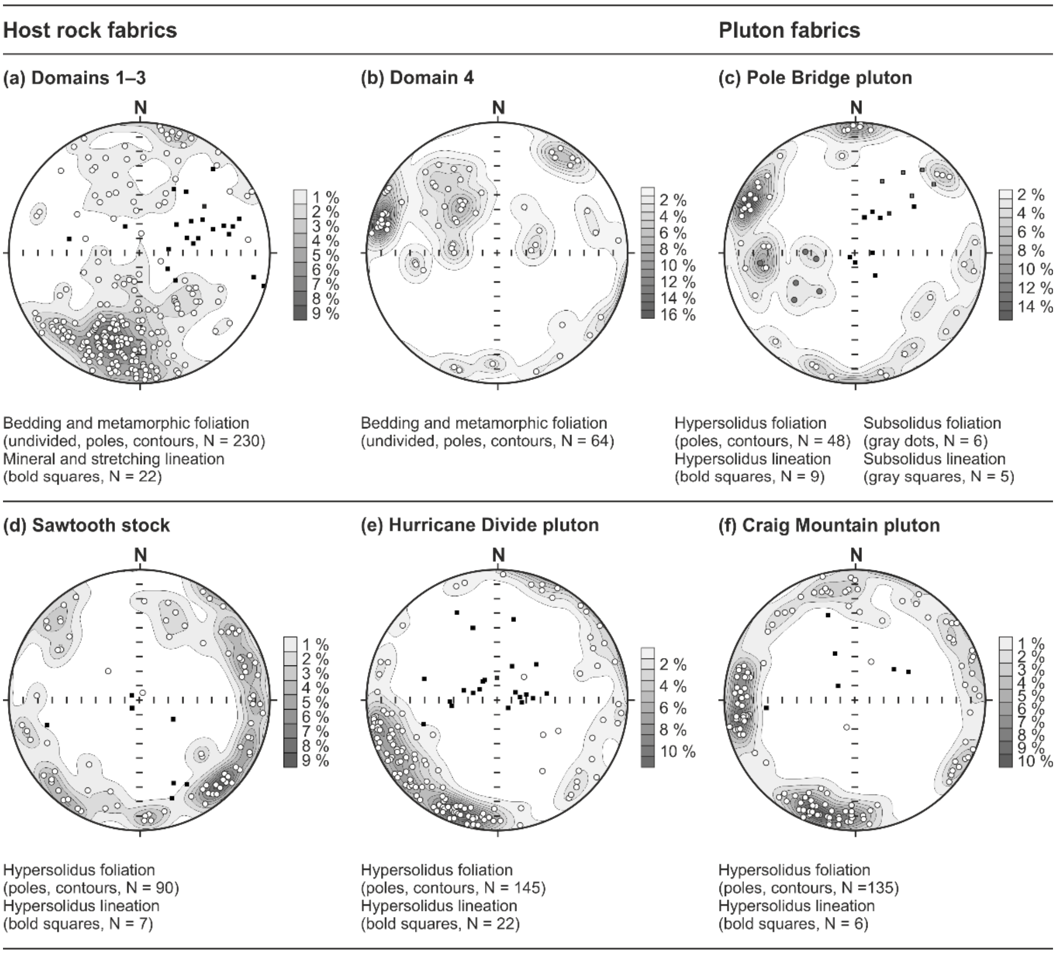

Figure 7. Stereonets (equal area projection, lower hemisphere) showing orientation of fabric elements in the Wallowa terrane and in component plutons of the Wallowa batholith.

margin and appear to continuously reorient to an almost perpendicular strike in the pluton center (Figures 4, 7f).

On some outcrops, relative geometric and temporal relations of mineral fabric to other magmatic structures can be established. For instance, magmatic mineral foliation, in some cases also defined by the alignment of micrstill granular enclaves, is seen to traverse, with little to no change in orientation, felsic and hornblende–biotite cumulate layers or irregular patches with lobate, diffuse to sharp margins (Figure 8e) and composite mafic–felsic dikes with knife-sharp, planar margins (Figure 8d). In other cases, mineral foliation is axial-planar to gently folded aplite dikes (Figure 8f).

At map scale, internal pluton foliations are oriented at a high angles to both the Pole Bridge/Hurricane Divide and Hurricane Divide/Craig Mountain interplutonic contacts. On the other hand, magmatic foliations are, in terms of orientation, continuous with host rock markers (lithologic contacts, bedding, metamorphic foliation; Figure 4) and are thus examples of coupled fabric patterns of Paterson et al. (1998). Local complexities and exceptions to the above do exist, as exemplified by foliations parallel to the local intrusive margin and discordant to host rock

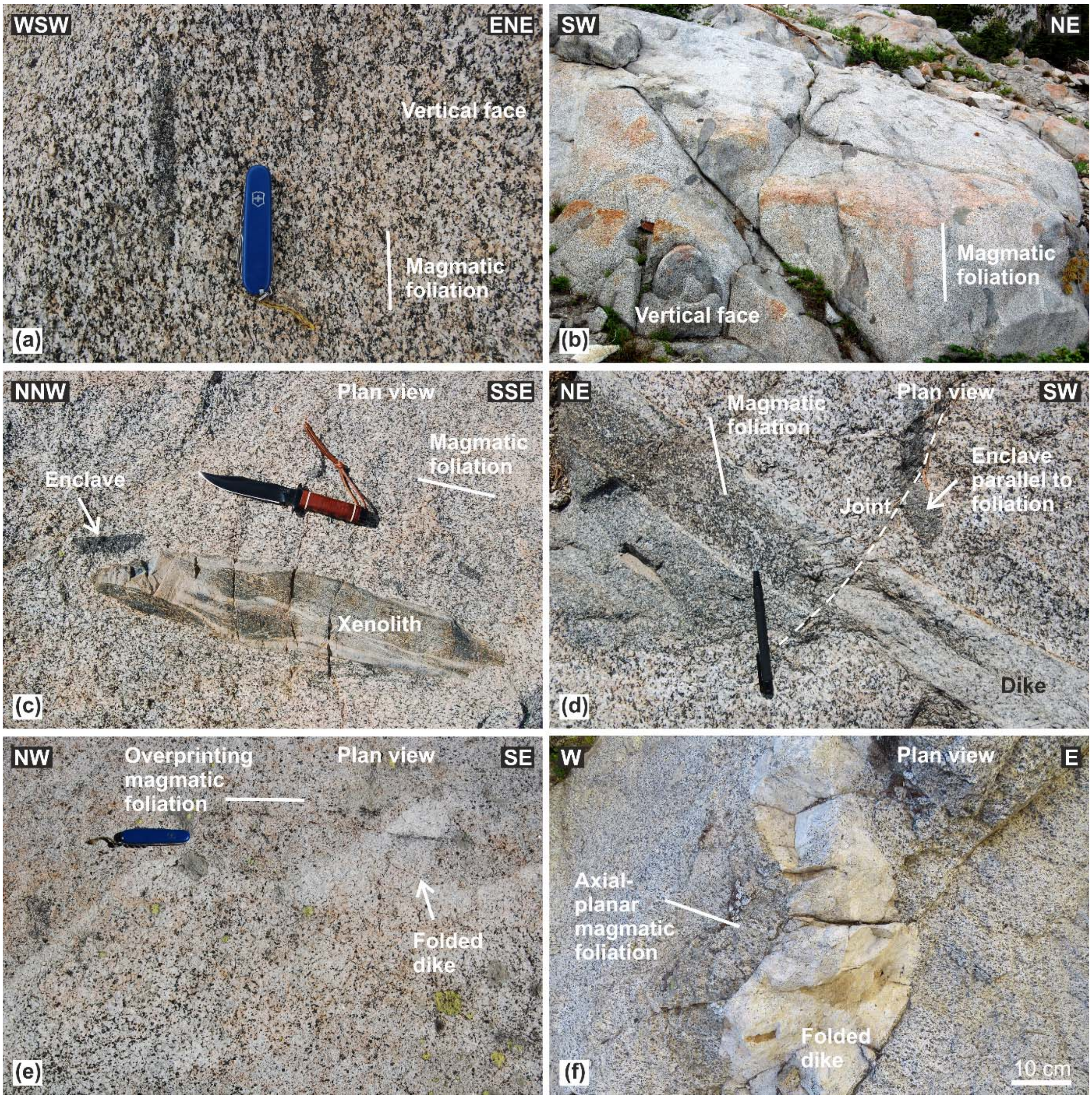

Figure 8. Field examples of magmatic fabrics in the Wallowa batholith and their geometric and temporal relations to other magmatic structures. (a) Close-up of subvertical mineral foliation in the Hurricane Divide pluton, defined mainly by amphibole and biotite. Stretched microgranular enclave is aligned parallel to the mineral fabric in the host granodiorite. Swiss Army penknife for scale is 9 cm long. WGS84 coordinates: N45.24463205°, W117.34662060°. (b) Steeply-dipping swarm of flattened microgranular enclaves aligned parallel to mineral foliation in the host granodiorite of the Hurricane Divide pluton. WGS84 coordinates: N45.25134667°, W117.4067383°. (c) Microgranular enclave near larger host rock xenolith, both with their long axes parallel to mineral foliation in the host granodiorite of the Hurricane Divide pluton. SOG 2.0 Bowie knife for scale is 28 cm long. WGS84 coordinates: N45.24509900°, W117.34090380°. (d) Close-up of mineral fabric overprinting at a high angle a composite aplitic–mafic cumulate dike. Note microgranular enclave parallel to the host mineral fabric; the Hurricane Divide pluton. Pencil for scale is 14 cm long. WGS84 coordinates: N45.24362002°, W117.34236385°. (e) Mineral fabric in the host granodiorite overprinting a folded aplitic dike. Swiss Army penknife for scale is 9 cm long. WGS84 coordinates: N45.21056347°, W117.3931542°. (f) Aplitic dike folded into an open magmatic fold, magmatic foliation in the host granodiorite is axial-planar to this fold; the Craig Mountain pluton pluton. WGS coordinates: N45.201704°, W117.208478°.

structures or by foliations at a high angle to the overall, pluton-wide foliation pattern (Figure 4).

On the micro-scale, fabrics in the batholith are magmatic to submagmatic in most cases (Appendix item 4/1) as defined using criteria in Paterson et al., (1989) and Vernon (2000). The tonalites (e.g., sample JZ146) typically contain euhedral to subhedral zoned andesine phenocrysts up to 7 mm in size, whereas K-feldspar is rare. Amphibole and biotite grains are mostly subhedral with variable size, not exceeding 4.5 mm. Quartz is anhedral and fills the space between other minerals. The quartz grains or aggregates may locally exhibit undulatory extinction and chessboard pattern. The granodiorites (e.g., sample JZ216) show similar microstructure, but contain abundant euhedral to subhedral, patchy zoned tabular grains of K-feldspar and oligoclase, up to 4 mm in size.

The exception is tonalite (sample JZ91) from the eastern margin of the Pole Bridge pluton, which exhibits S–C fabric (e.g., Berthé et al., 1979) defined by two oblique shape-preferred orientations of quartz, plagioclase, amphibole, and biotite grains and aggregates. Consistent with this S–C fabric are also asymmetric sigmoidal grains of plagioclase and biotite fish (e.g., Lister and Snoke, 1984), all indicating reverse, top-to-the-SW kinematics during submagmatic to high-temperature subsolidus deformation of the tonalite. A similar case is fine-grained amphibole–biotite microtonalite to microdiorite (e.g., sample KV112) possibly representing the chilled margin of the Pole Bridge pluton deformed at submagmatic to high-temperature subsolidus conditions.

ANISOTROPY OF MAGNETIC SUSCEPTIBILITY (AMS)

Methodology

The anisotropy of magnetic susceptibility (e.g., Hrouda, 1982; Tarling and Hrouda, 1993; Bouchez, 1997; Borradaile and Henry, 1997; Borradaile and Jackson, 2004, 2010) was used to describe quantitatively gradients in fabric symmetry, intensity, and orientation in the Wallowa batholith (Figure 9; and Appendix items 4/3–4/6). The AMS samples were taken at 42 stations: 7 in the Pole Bridge pluton, 15 in the Hurricane Divide pluton, 2 in the Sawtooth stock, and 18 in the Craig Mountain pluton (Appendix item 4/2). The samples were taken as oriented blocks and then drilled using a hand-held gasoline drill, rotated back to their original (in situ) position, and the orientation of the drilled cores was measured using the standard orientation table. After cutting, the cores yielded 466 standard specimens (cylinder-shaped, 2.1 cm in height and 2.5 cm in diameter; 112 in the Pole Bridge pluton, 20 in the Sawtooth stock, 167 in the Hurricane Divide and 167 in the Craig Mountain plutons). The AMS was measured using an Agico MFK1-A Multi-function Kappabridge in the Laboratory of Rock Magnetism, Institute of Geology and Paleontology, Charles University in Prague, and statistical treatment and analysis of the AMS data was carried out using the ANISOFT 4.2 program.

The AMS data are represented by the mean magnetic susceptibility (*km*), degree of anisotropy (*P*), and shape parameter (*T*) defined as follows (Jelínek, 1981; Hrouda, 1982): $km = (k_1 + k_2 + k_3)/3$; $P = k_1/k_3$; $T = 2ln(k_2/k_3)/ln(k_1/k_3) - 1$, where $k_1 > k_2 > k_3$ are the principal susceptibilities. The orientations of the magnetic lineations (k_1) and magnetic foliation poles (k_3) are presented in stereonets in the geographic coordinates and as mean values for individual stations on the maps.

Magnetic mineralogy

The mean magnetic susceptibility is high, on the orders of 10^{-3} to 10^{-2} in all units (Appendix item 4/3) and thus these granitoids (tonalites to granodiorites) can be broadly regarded as ferromagnetic (Hrouda and Kahan, 1991; Bouchez, 1997) with the main carriers of the AMS being ferromagnetic minerals. However, on five stations (FT96, KV112, JZ106, JZ236, JZ251), the granitoids have lower susceptibilities on the order of 10^{-4}, suggesting paramagnetic mineralogy.

In order to determine the AMS carriers, variation of susceptibility with temperature was measured on 6 coarsely powdered specimens in the temperature range from –194 °C to 700 °C and back to ca. 40 °C using the CS-L and CS-4 instruments (Hrouda, 1994). Argon atmosphere was applied to avoid oxidation during heating, the heating rate was ca. 10 °C per minute. Measurements were performed in the Laboratory of Rock Magnetism, Institute of Geology and Paleontology, Charles University in Prague, the data were statistically treated and plotted using the Cureval software (Agico, Inc.). The resulting thermomagnetic curves are provided in Appendix item 4/4.

The analysis corroborates that the main AMS carrier in specimens with high susceptibilities (JZ224/2/2, JZ16/3/4, JZ103/2/1, KV132/1/1) is magnetite, detected by significant drop in the bulk susceptibility at temperatures from –180 °C to –160 °C and of 580 °C, corresponding to the Verwey transition and Curie temperature of magnetite, respectively. On the other hand, low-susceptibility specimens (KV112/1/1, FT96/2/1) exhibit hyperbolic thermomagnetic curves typical of paramagnetic minerals. Both paramagnetic specimens also showed an increase in the bulk susceptibility during cooling suggesting growth of a secondary ferromagnetic component.

Magnetic fabric parameters and orientation

The degree of anisotropy of the Pole Bridge pluton specimens ranges widely from 1.025 to 1.929, but the P parameter for most of the specimens (82 %) is below 1.256 (Appendix item 4/5 and 4/6). The susceptibility ellipsoid shapes are almost evenly distributed between oblate (61 % of the specimens) and prolate. The exception to the above are two stations, JZ91 and JZ94, where the granitoids have a higher P parameter associated with a predominantly prolate AMS ellipsoids (T down to –0.161). The other plutons show the P parameter mostly not exceeding 1.3, but, unlike the Pole Bridge pluton, most of the specimens in each of these units are oblate (Sawtooth stock, 80 %; Hurricane Divide, 87 %; Craig Mountain, 72 %) especially those with $P > 1.2$ (Appendix items 4/5 and 4/6). The exception is station JZ224 in the Hurricane Divide pluton with high P (1.236–1.459) and mostly oblate ellipsoids.

For the high bulk susceptibilities of 10^{-3} to 10^{-2}, the P and T parameters exhibit systematic spatial variations in the Hurricane Divide and Craig Mountain plutons (Appendix items 4/3, 4/5, and 4/6). In the former, the degree of anisotropy and oblateness of the AMS ellipsoid decrease from the pluton/roof contact inward, defining ~NW–SE-trending zones at a high angle to the interpluton contacts. In the latter, zones of comparable P and T parameters trend ~NE–SW, parallel to the pluton margin, however, the spatial pattern is more irregular. The degree of anisotropy decreases inward from a narrow zone of highly anisotropic granitoids along the southern margin passing into a broad zone of moderately anisotropic granitoids in the pluton center. These variations in the P parameter are associated with an increase in the degree of oblateness of the AMS ellipsoids from near-triaxial to weakly oblate. The exception to this trend are two stations with paramagnetic and weakly anisotropic granitoids (Appendix items 4/3 and 4/4).

The four plutons also differ significantly in the orientation of magnetic fabric. Magnetic foliations in the Pole Bridge pluton strike ~N–S to ~NW–SE and dip moderately to steeply outward, i.e., to the W to NE (Figure 9a). The foliations are thus roughly subparallel to the pluton/host rock contact and to the bedding in siliciclastic metasedimentary rocks of the Hurwal Formation (Figures 4, 9a). Only along the southern margin of the pluton, magnetic foliations are at a high angle to both the pluton/host rock and Pole Bridge/Hurricane Divide interpluton contact, dipping at an angle of about 30° to the SW (Figure 9a). Magnetic lineations exhibit moderate plunges and their trends scatter widely to almost all directions, but predominantly to the ~NNE (parallel to lineation on bedding planes) and ~SSE (Figure 9b).

In the Hurricane Divide pluton, our analysis revealed two distinct orientations of magnetic fabric. In a northeasterly domain, magnetic foliations are steep and strike ~NW–SE to ~WNW–ESE. They are thus at a high angle to the nearby flat-lying pluton/roof contact but, at the same time, roughly concordant with foliations in the pluton roof (Figures 4, 9a). Lineations vary from mostly subvertical to shallowly plunging to the ~ESE or ~WNW (Figure 9b). In a southerly domain along the Hurricane Divide/ Craig Mountain interpluton contact, magnetic foliations are almost perpendicular to the above, striking ~NE–SW and being associated with variably trending lineations (Figure 9a). Similarly, on the two stations in the Sawtooth stock, magnetic fabric is discordant to the pluton/roof contact: magnetic foliations strike ~WNW–ESE and ~NE–SW and are associated with lineations moderately plunging to the ~SW and ~S, respectively (Figure 9a, b).

An entirely different fabric pattern is observed in the Craig Mountain pluton. Along both pluton margins, magnetic foliations are oriented systematically at an angle of about 30°–45° to the nearby pluton/host rock contact and this angle increases toward pluton center (Figure 9a). In the majority of cases, lineations plunge moderately outward and their trends are oblique to the contacts (Figure 9b). Altogether, the foliations and lineations define a pronounced asymmetric arcuate pattern in the map with a narrow southeastern and broad northwestern 'limbs'. This arcuate pattern seems to be continuous with deflected lithologic contacts, bedding, and metamorphic foliation in the host rock on both sides of the pluton (Figure 9a).

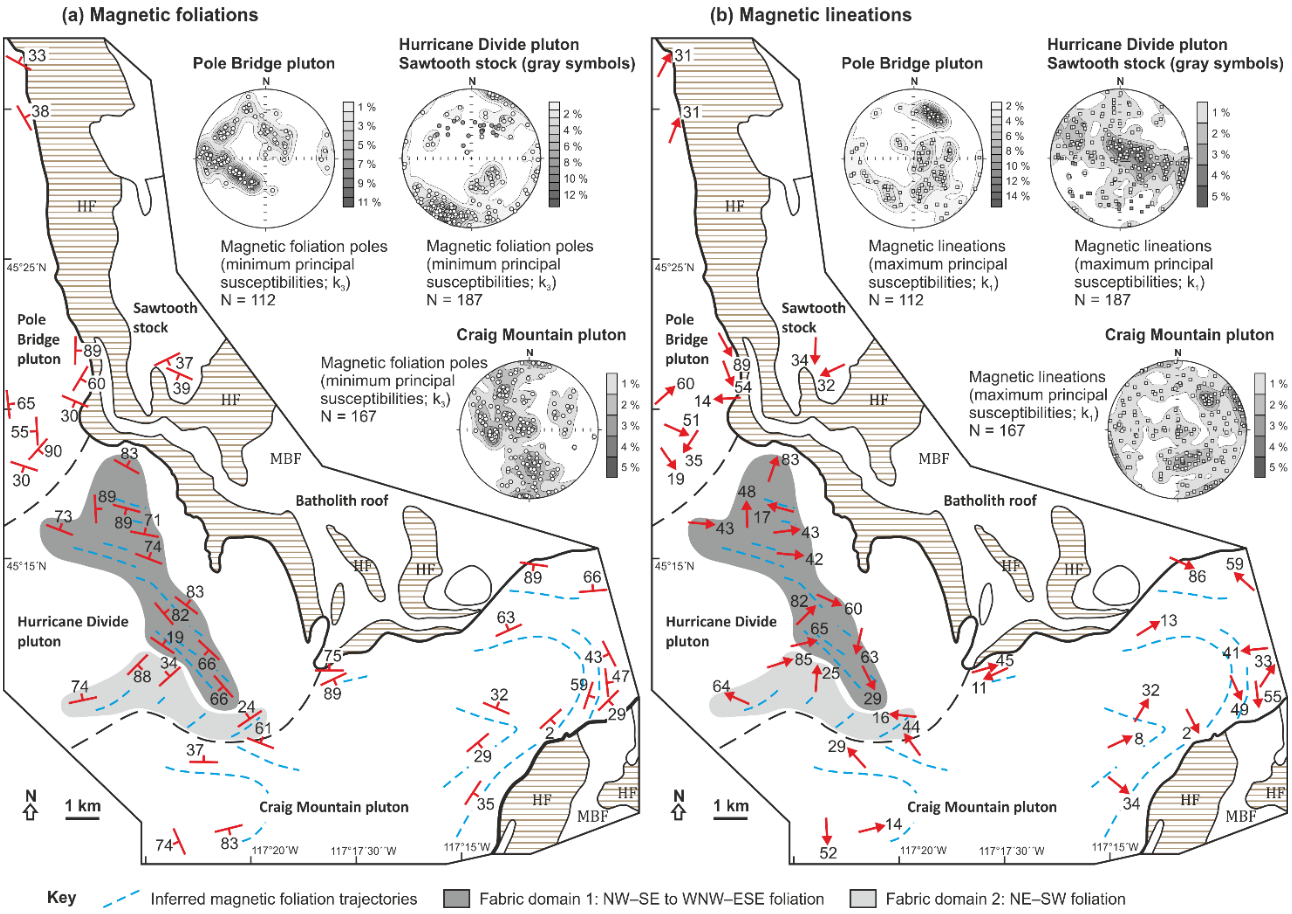

Figure 9. Maps of magnetic foliations and lineations in the component plutons of the northeastern Wallowa batholith. Stereonets (equal area projection, lower hemisphere) show orientations of the maximum and minimum principal susceptibilities. HF – Hurwal Formation, MBF – Martin Bridge Formation.

DISCUSSION

Structural interpretation

In terms of orientation of fabric axes, the mesoscopic foliation and lineation defined mostly by paramagnetic mafic minerals (Figure 8a) correspond well to the measured AMS in all three plutons (Figures 4, 9). The AMS data are interpreted as representing the shape or distribution anisotropy of magnetite grains or aggregates, corroborated by the high bulk susceptibility of most analyzed specimens and by the thermomagnetic measurements (Appendix item 4/4). Furthermore, the relative geometric and temporal relations of mineral fabric to other magmatic and host rock structures (Figure 8d–f) indicate that both the mesoscopic fabrics and AMS in the three plutons record syn- to post-emplacement increments of regional tectonic strain. Hence, in combination with the existing $^{206}Pb/^{238}U$ ages, our structural and AMS data suggest that the successively emplaced plutons of the Wallowa batholith record three strain regimes, each of unknown duration but certainly active at ~140 Ma, ~131–130 Ma, and ~126 Ma (Figure 10), allowing inferences on the progressive tectonic history of and strain partitioning in the Wallowa terrane during the Early Cretaceous times.

In the northerly ~140 Ma Pole Bridge pluton, mesoscopic and magnetic foliations are subparallel to both the intrusive contact and bedding in the Hurwal Formation, whereas slickenside-type striation on bedding surfaces (inferred to result from simple shear on the bedding planes) and magnetic lineations are oblique to this structural grain (Figures 4, 7, 9). Together with reverse, top-to-the-SW kinematics observed in the deformed granitoids along pluton margin (supporting material, Part 2), this fabric is interpreted as recording early, perhaps pre-emplacement ~ENE–WSW principal shortening to form the Sawtooth syncline in Domain 1, continued as dip-oblique ~NE–SW shortening and reverse slip during and after final solidification of the northwestern pluton margin (Figure 10a).

In contrast, fabric in the ~130 Ma Hurricane Divide pluton is dominated by ~WNW–ESE foliation and variably, but in most instances steeply, plunging lineation along the mean foliation plane (Figures 4, 7e, 9b). The inferred synmagmatic strain was oblate, with the fabric intensity and degree of oblateness decreasing from the pluton/host contact inwards (Appendix item 4/5), and associated with ~NNE–SSW shortening and a vertical stretching component. In the host rock (Domain 2), the latter fabric corresponds to the steepened to overturned bedding and steep metamorphic foliation in the Hurwal and Martin Bridge formations, respectively, and was associated with refolding of the Sawtooth syncline into ~NW–SE to ~WNW–ESE upright tight to isoclinal folds developed especially in the weak marbles, with fold axial planes subparallel to the magmatic foliation in the pluton (Figures 4, 10b). In a small domain near the southern margin of the pluton, mesoscopic and magnetic foliations strike ~NE–SW (Figures 4, 9a), suggesting that the synmagmatic strain was locally more complex. Based on the available information, it is difficult to distinguish whether this latter fabric represents a relic of earlier emplacement-related strain or records two broadly simultaneous but nearly orthogonal shortening directions, ~NW–SE and dominant ~NE–SW, swinging around a common vertical stretching axis (e.g., Paterson et al., 2003).

The structural relations indicate that the youngest, 126 Ma Craig Mountain pluton is elongated and axial-planar with a regional map-scale bend of host rock markers from the ~NNW–SSE into ~NE–SW trend, tapers southwestward, and bifurcates an originally single unit represented by the coeval Hurricane Divide and Needle Point plutons (Figure 3). Together with the arcuate magmatic and magnetic foliation patterns (Figures 4, 9a), this suggests that the pluton intruded during increment(s) of crustal-scale folding of the adjacent Wallowa terrane about a vertical axis (Figure 10c). Sharp and largely discordant contacts (Figure 4) suggest that emplacement of the pluton was dominated by brittle processes (into a growing crack?) but also by some ductile shortening in marble-dominated lithologies. The latter is evidenced by contact-parallel deflection of host rock markers in concordant portions of the northeastern pluton margin

(Figure 4). The internal arcuate fabric pattern is likely composite, resulting from simple shear magma flow into a tensional region along the axial plane of the fold combined with some amount of tectonic shortening across the already emplaced magmatic sheet. The former is consistent with higher-intensity plane-strain fabric along the southeastern margin whereas the latter produced oblate fabrics along both sides of the pluton (Appendix item 4/5). The observed internal fabric pattern is thus more complex than simple theoretical strain variations as predicted for various types of folds (e.g., Hobbs, 1971; Twiss and Moores, 1992, p. 314–321, and references therein).

In summary, fabric analysis in the three plutons and their host rocks of the Wallowa terrane suggests that (1) the magmatic and ductile deformation at the exposed shallow crustal level was heterogeneous and largely partitioned into rheologically weak active plutons and their aureoles, (2) deformation was time-transgressive, progressing from north to south following the general pattern of magmatic emplacement, and (3) the principal shortening axis rotated counter-clockwise from ~NE–SW (in the ~140 Ma Pole Bridge pluton) through ~NNE–SSW (in the ~130 Ma Hurricane Divide pluton) to ~NNW–SSE (in the ~126 Ma Craig Mountain pluton; Figure 10).

Inferred plate kinematics during terrane convergence

Previous structural and geochronologic studies in the Blue Mountains Province suggested (1) amalgamation of the Wallowa and Baker terranes at ca. 162–154 Ma, (2) folding and faulting of the Wallowa–Baker–Olds Ferry terranes and Izee basin by 154 Ma (e.g., Schwartz et al., 2010, 2011a, b), (3) thrust loading in the Salmon River belt interpreted as recording collision and final attachment of the Blue Mountains superterrane to cratonic North America at ca. 144–128 Ma (Selverstone et al., 1992; Getty et al., 1993; McKay et al., 2011), and (4) post-collisional intracontinental shearing along the eastern margin of the accreted terranes spanning from ca. 120 to 80 Ma (e.g., McClelland et al., 2000; Giorgis et al., 2005, 2008). Although these studies provided a broad tectonic scenario for the Blue Mountains province, details of the resulting deformation, changes in regional strain fields through time, and exact timing of these events still remain poorly constrained (see, e.g., Avé Lallemant 1995; Gray and Oldow, 2005 for discussion).

On the basis of the inferred temporally evolving strain regimes and rotation of the principal strain axes, we propose the following kinematic history of the Wallowa terrane at the time of emplacement of the Wallowa batholith.

The ~NE–SW shortening recorded in the ~140 Ma Pole Bridge pluton and its host rock is broadly coeval with the K–Ar and Sm–Nd garnet ages indicating crustal thickening and thrusting over a time span of about 141–124 Ma in the Salmon River belt (Selverstone et al., 1992; Getty et al., 1993; Snee et al., 1995; McKay, 2011; Stowell et al., 2014). We thus interpret this deformation as an early phase of the prolonged attachment of the Blue Mountains 'superterrane' to the North American continental margin. The obliquity of the inferred principal shortening direction with respect to the terrane boundaries also implies an overall dextral plate convergence at around 140

Ma (Figures 10a, 11a).

Subsequently, a change in the strain regime and reorientation of the regional strain axes must have occurred between ~140 and ~130 Ma. This can be inferred from fabrics in the ~130 Ma Hurricane Divide pluton which record pure shear with dominant ~NNE–SSW shortening and vertical stretching (thickening) of the crust (Figure 10b). We envisage that the superterrane impinged into a westward-concave reentrant in the continental margin as represented by the Syringa embayment (Figures 2, 11b) (see also Strayer et al., 1989). Our structural data thus indirectly support the notion that the embayment was an inherited, pre-accretion feature in the rifted margin of the North American craton (e.g., Lund et al., 2008), presumably later reactivated by sinistral transpressional shearing along the ca. 90–70 Ma Orofino shear zone (Figure 2) (McClelland and Oldow, 2007).

As a consequence of squeezing the Blue Mountains superterrane into the presumed continental margin reentrant, its northern portion must have become 'locked' and difficult to further deform (Figures 10c, 11c). Hence, we assume that the continuing oblique convergence was accommodated by crustal-scale folding about a vertical axis, thereby rotating clockwise the southern, still deformable portion of the superterrane (Figures 10c, 11c). The Craig Mountain pluton was emplaced into a local tensional domain along the axial plane and its internal magmatic fabric records strain increment during progressive development of this crustal-scale fold at around 126 Ma (Figure 10c). Subsequently, ductile deformation became localized mainly along the dextral transpressive Western Idaho shear zone (Figure 2), accommodating continued subduction outboard the Blue Mountains province until Late Cretaceous times (McClelland et al., 2000). No ductile structures related to these younger events have been identified as yet in the examined portion of the Wallowa terrane, suggesting eastward stepping of deformation through time.

The above inferred strain patterns fit well a general model of granitoid plutonism in developing oroclines (e.g., Gutiérrez-Alonso et al., 2011a; Pastor-Galán et al., 2012; Johnston et al., 2013) whose inner arcs undergo vertical stretching (the Hurricane Divide pluton) and outer arcs undergo horizontal extension (the Craig Mountain pluton). Given that the voluminous plutonism and deformation are closely spatially associated in the Wallowa batholith and that emplacement of the ~140–130 Ma plutons preceded initiation of the orocline, we suggest that thermal weakening from magma emplacement may have played an important role in localizing the hinge of this crustal-scale fold. Progressive orocline development commonly triggers delamination of the underlying lithospheric mantle beneath the inner arc (e.g., Gutiérrez-Alonso et al., 2004, 2011b; Weil et al., 2013). Mantle delamination beneath the Blue Mountains Province and surrounding areas has been proposed to explain the Miocene flood basalt volcanism of the Columbia River Group (e.g., Camp and Hanan, 2008; Eagar et al., 2010; Darold and Humphreys, 2013, and references therein), and it remains an open question whether this process could have occurred also as early as during the Early/mid-Cretaceous phase of the orocline development.

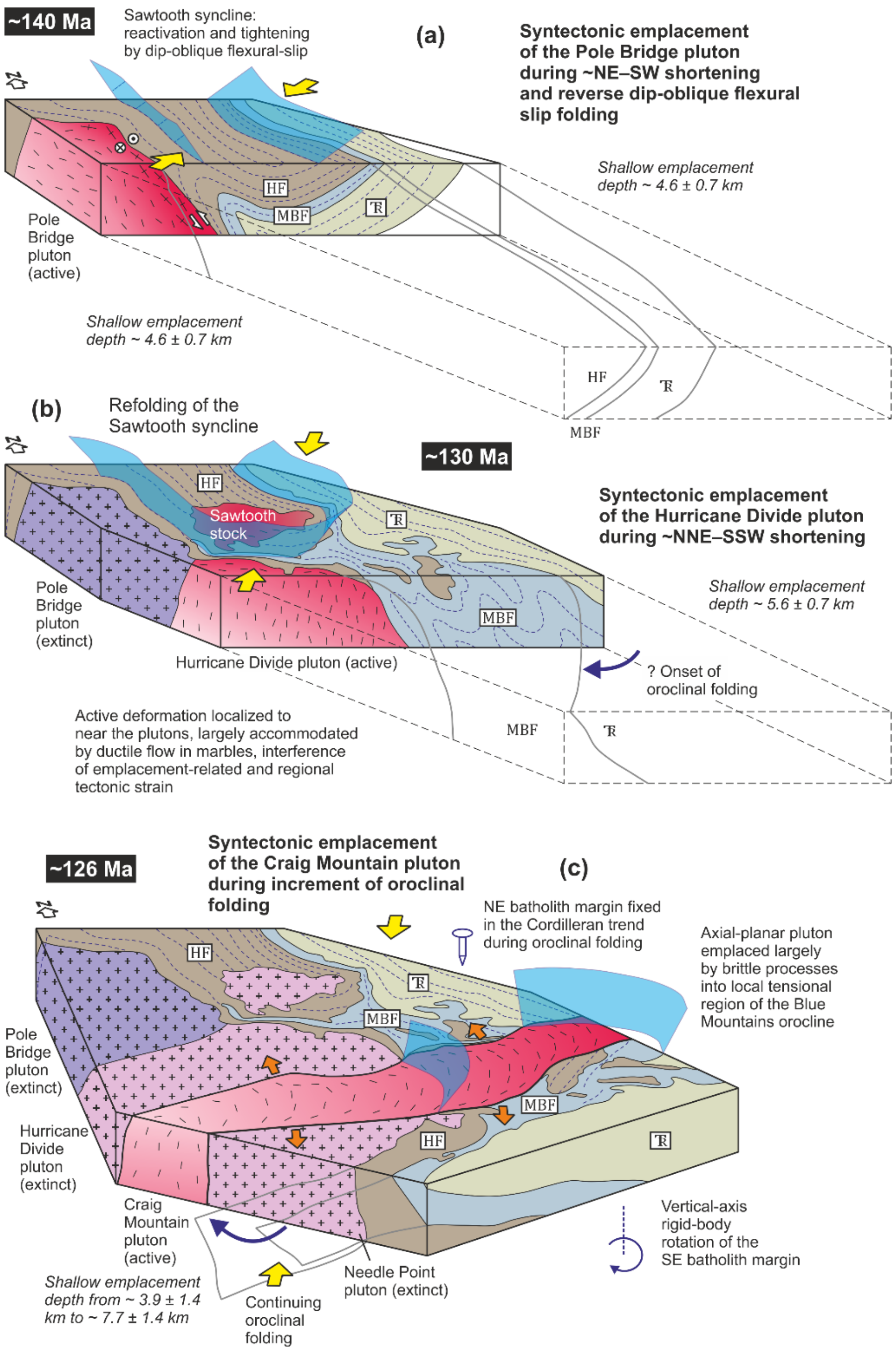

Figure 10. Schematic blockdiagrams showing the inferred structural and emplacement history of the northeastern Wallowa batholith during the Early Cretaceous times; see text for discussion.

Implications for timing and mechanism of rotation of Cordilleran terranes

The proposed timing and geodynamic causes of the ~E–W bend in terrane boundaries in the Blue Mountain Province have been controversial. The orocline was variously interpreted as (1) being a primary feature and thus recording no rotation (Taubeneck, 1966), or resulting from (2) post-middle Eocene oroclinal bending (Carey, 1958), (3) Middle Jurassic to Early Cretaceous indentation of the Wrangellia terrane causing lateral escape and rotation of the Stikine (including Wallowa) terrane (Wernicke and Klepacki, 1988), (4) Early Cretaceous westward displacement of the Klamath Mountains salient along strike-slip faults (Ernst, 2012), (5) Late Cretaceous–Early Tertiary terrane collision (Tikoff et al., 2014), or (6) post-Cretaceous Basin-and-Range regional extension (e.g., Wilson and Cox, 1980; Dickinson, 2002).

Our structural and AMS data and interpretations provide some new temporal and mechanical constraints on this oroclinal rotation. First, we have argued above that the main cause of the fold development, at least during its incipient stages, was oblique oroclinal bending whereby horizontal compressive forces resulting from overall plate convergence acted at an angle to the terrane boundaries (Figures 10, 11). Second, we propose that the emplacement of the ~130 Ma Hurricane Divide pluton may represent a lower age limit for the oroclinal bending (Figure 11). It remains unresolved whether the vertical stretching as documented in this pluton (Figures 7e, 9b) may represent onset of this process. Nevertheless, we have shown that the progressive folding predated and was active during emplacement of the Craig Mountain pluton (Figures 10c). In summary, these pluton–deformation relationships corroborate that the Blue Mountains orocline probably initiated and at least partly developed earlier than previously thought, during mid-early Cretaceous times between ca. 130–126 Ma (Figures 10, 11).

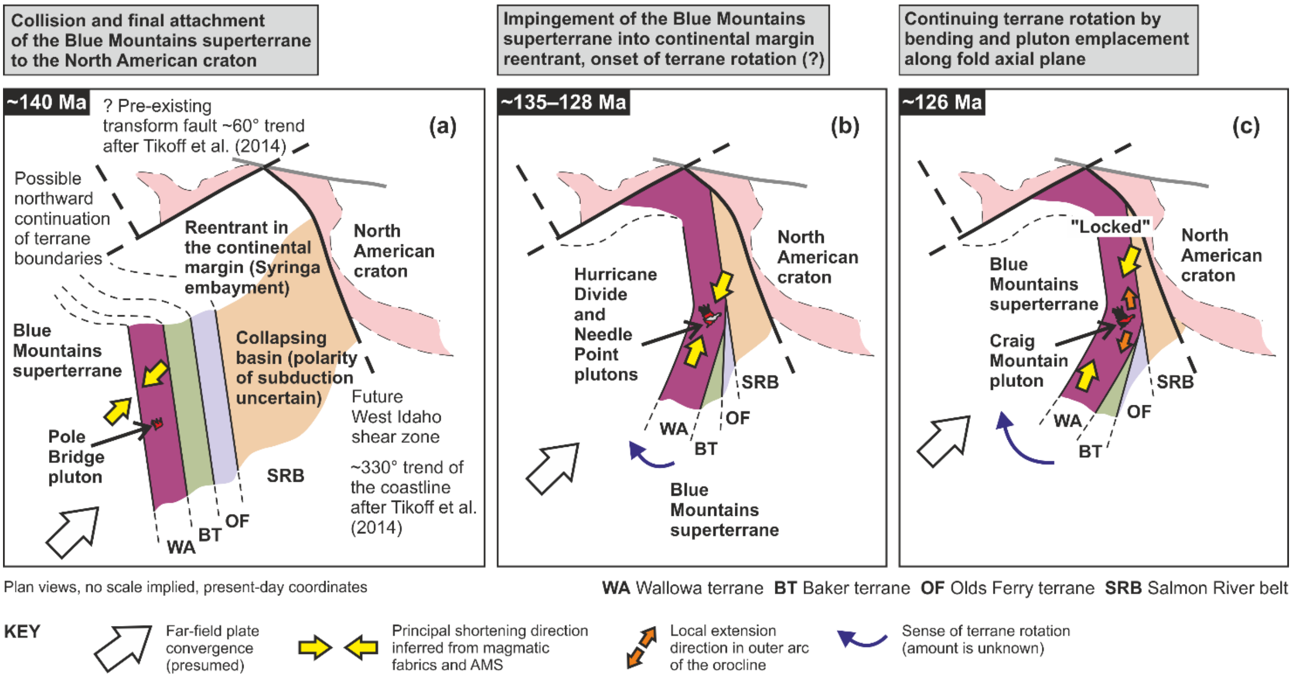

Figure 11. The proposed kinematic model for successive pluton emplacement during terrane collision, impingement into a reentrant in the margin of the North American craton, and incipient oroclinal bending of the Blue Mountains Province during Early Cretaceous right-oblique plate convergence; see text for discussion

CONCLUSIONS

Magmatic to solid state fabrics in the Pole Bridge, Hurricane Divide, and Craig Mountain plutons and coeval deformational structures in their host rocks record three phases of progressive regional deformation in the Wallowa terrane during Early Cretaceous times:

(1) The early ~NE–SW terrane-oblique principal shortening is interpreted as recording an early stage of attachment of the welded Blue Mountains superterrane to the North American continental margin during overall right-oblique convergence at around 140 Ma.

(2) This deformation switched to pure shear ~NNE–SSW shortening associated with vertical stretching (crustal thickening) and refolding of an earlier kilometer-scale syncline into a series of almost perpendicular smaller-scale tight folds. This event is related to the continued impingement of the superterrane into a westward-concave reentrant in the North American continental margin at around 135–128 Ma.

(3) Upon impingement, the northern portion of the superterrane became 'locked' and difficult to further deform. The 'lock-up' led to reorientation of the principal shortening direction to ~NNW–SSE and the still deformable southern portion of the superterrane rotated clockwise about vertical axis at around 126 Ma.

The above inferences imply that the main mechanism of the crustal-scale fold development was oblique oroclinal bending whereby lateral compressive forces resulting from overall plate convergence acted at an angle to the terrane boundaries and to the continental margin. Pluton fabrics indicate the onset of oroclinal bending at around 130–125 Ma.

ACKNOWLEDGEMENTS

We greatly appreciate the detailed and constructive comments by Stephen Johnston, Associate Editor, and three anonymous reviewers which helped to improve the original manuscript significantly. Martin Chadima is thanked for help with processing the thermomagnetic curves. This study is part of the Ph.D. research of Filip Tomek, supported by the Grant Agency of the Czech Republic through Grant No. P210/12/1385 (to Jiří Žák), by the Charles University research projects PRVOUK P44 and SVV261203, and by the Czech Academy of Sciences Research Plan RVO67985831. Partial financial support for this work was provided by National Science Foundation Grant EAR-0911681 (to Joshua J. Schwartz) and National Science Foundation Grant EAR-0911735 (to Kenneth Johnson).

REFERENCES

Amato, J. M., J. Toro, and T. E. Moore (2004), Origin of the Bering Sea salient, in Orogenic curvature: integrating paleomagnetic and structural analyses, Geol. Soc. Am. Spec. Pap., vol. 383, edited by Sussmann, A. J., and A. B., Weil, pp. 131–144, doi:10.1130/0-8137-2383-3(2004)383(131:OOTBSS)2.0.CO;2.

Armstrong, R. L., W. H. Taubeneck, and P. O. Hales (1977), Rb–Sr and K–Ar geochronometry of Mesozoic granitic rocks and their Sr isotopic composition, Oregon, Washington, and Idaho, Geol. Soc. Am. Bull., 88(3), 397–411, doi:10.1130/0016-7606(1977)88<397:RAKGOM>2.0.CO;2.

Atwater, T. (1970), Implications of plate tectonics for the Cenozoic tectonic evolution of western North America, Geol. Soc. Am. Bull., 81, 3513–3236, doi:10.1130/0016-7606(1970)81(3513:IOPTFT)2.0.CO;2.

Avé Lallemant, H. G. (1995), Pre-Cretaceous tectonic evolution of the Blue Mountains Province, northeastern Oregon, in: Geology of the Blue Mountains Region of Oregon, Idaho and Washington: petrology and tectonic evolution of pre-Tertiary rocks of the Blue Mountains region, U.S. Geol. Surv. Prof. Pap., vol. 1438, edited by T. L. Vallier, and H. C. Brooks, pp. 271–304.

Berthé, D., Choukroune, P. and P. Jegouzo (1979), Orthogneiss, mylonite and non coaxial deformation of granites: the example of the South Armorican Shear Zone, J. Struct. Geol., 1, 31–42, doi: 10.1016/0191-8141(79)90019-1.

Borradaile, G. J., and B. Henry (1997), Tectonic applications of magnetic susceptibility and its anisotropy, Earth Sci. Rev., 42(1–2), 49–93, doi:10.1016/S0012-8252(96)00044-X.

Borradaile, G. J., and M. Jackson (2004), Anisotropy of magnetic susceptibility (AMS): magnetic petrofabrics of deformed rocks, in Magnetic fabric: methods and application, Geol. Soc. London Spec. Publ., vol. 238, edited by F. Martín-Hernández, C. M. Loneburg, C. Aubourg, and M. Jackson, pp. 299–360, doi:10.1144/GSL.SP.2004.238.01.18.

Borradaile, G. J., and M. Jackson (2010), Structural geology, petrofabrics and magnetic fabrics (AMS, AARM, AIRM), J. Struct. Geol., 32(10), 1519–1551, doi:10.1016/j.jsg.2009.09.006.

Bouchez, J. L. (1997), Granite is never isotropic: an introduction to AMS studies of granitic rocks, in Granite: from segregation of melt to emplacement fabrics, edited by. J. L. Bouchez, D. Hutton, and S. Stephens, pp. 95–112, Kluwer Academic Publishers, Amsterdam, doi:10.1007/978-94-017-1717-5_6.

Brooks, H.C., and T.L. Vallier (1978), Mesozoic rocks and tectonic evolution of eastern Oregon and western Idaho, in Mesozoic paleogeography of the western United States, edited by D.G. Howell and K.A. McDougall, pp. 133–145, The Pacific Section, Society of Economic Paleontologists and Mineralogists, Los Angeles.

Camp, V. E., and B. B. Hanan (2008), A plume-triggered delamination origin for the Columbia River Basalt Group, Geosphere, 4(3), 480–495, doi:10.1130/GES00175.1.

Carey, S. W. (1958), The tectonic approach to continental drift, in Continental Drift – A Symposium, edited by S. W. Carey, pp 177–363, University of Tasmania, Hobart.

Coney, P.J., Jones, J.L., and J.W.H. Monger (1980), Cordilleran suspect terranes, Nature, 288, 329–333, doi: 10.1038/288329a0.

Darold, A., E. Humphreys (2013), Upper mantle seismic structure beneath the Pacific Northwest: a plume-triggered delamination origin for the Columbia River flood basalt eruptions, Earth Planet. Sci. Lett., 365, 232–242, doi:10.1016/j.epsl.2013.01.024.

Dickinson, W. R. (1979), Mesozoic forearc basin in central Oregon. Geology, 7, 166–170, doi: 10.1130/0091-7613(1979)7<166:MFBICO>2.0.CO;2.

Dickinson, W. R. (2002), The Basin and Range province as a composite extensional domain, Int. Geol. Rev., 44(1), 1–38, doi:10.2747/0020-6814.44.1.1.

Dickinson, W. R. (2004), Evolution of the North American Cordillera, Ann. Rev. Earth Planet. Sci., 32, 13–45, doi:10.1146/annurev.earth.32.101802.120257.

Dorsey, R. J., and T. A. LaMaskin (2007), Stratigraphic record of Triassic–Jurassic collisional tectonics in the Blue Mountains province, northeastern Oregon, Am. J. Sci., 307, 1167–1193, doi: 10.2475/10.2007.03.

Dorsey, R. J., and T. A. LaMaskin (2008), Mesozoic collision and accretion of oceanic terranes in the Blue Mountains province of northeastern Oregon: new insights from the stratigraphic record, in Circum-Pacific tectonics, geologic evolution, and ore deposits, Arizona Geol. Soc. Digest, vol. 22, edited by J. E. Spencer, and S. R. Titley, pp. 325–332

Eagar, K. C., M. J. Fouch, and D. E. James (2010), Receiver function imaging of upper mantle complexity beneath the Pacific Northwest, United States, Earth Planet. Sci. Lett., 297, 141–153, doi:10.1016/j.epsl.2010.06.015.

Engebretson, D. C., A. Cox, and R. G. Gordon (1985), Relative motions between oceanic and continental plates in the Pacific basin. Geol. Soc. Am. Spec. Pap., 206, 1–59, doi:10.1130/SPE206-p1.

Ernst, W. G. (2012), Earliest Cretaceous Pacificward offset of the Klamath Mountains salient, NW California–SW Oregon, Lithosphere, 5(1), 151–159, doi:10.1130/L247.1.

Ferns, M. L., and H. C. Brooks, (1995), The Bourne and Greenhorn subterranes of the Baker Terrane, northeastern Oregon; implications for the evolution of the Blue Mountains island-arc system, in: Geology of the Blue Mountains

Region of Oregon, Idaho and Washington: petrology and tectonic evolution of pre-Tertiary rocks of the Blue Mountains region, U.S. Geol. Surv. Prof. Pap., vol. 1438, edited by T. L. Vallier, and H. C. Brooks, pp. 331–358.

Getty, S. R., J. Selverstone, B. P. Wernicke, S. B. Jacobsen, and E. Aliberti (1993), Sm–Nd dating of multiple garnet growth events in an arc–continent collision zone, northwestern U.S. Cordillera, Contrib. Mineral. Petrol., 115, 45–47, doi:10.1007/BF00712977.

Giorgis, S., Tikoff, B., and W. McClelland (2005), Missing Idaho arc: transpressional modification of the 87Sr/86Sr transition on the western edge of the Idaho batholith, Geology, 33, 469–472, doi: 10.1130/G20911.1.

Giorgis, S., W. C. McClelland, A. Fayon, B. S. Singer, and B. Tikoff (2008), Timing of deformation and exhumation in the western Idaho shear zone, McCall, Idaho, Geol. Soc. Am. Bull., 120(9–10), 1119–1133, doi:10.1130/B26291.1.

Glen, J. M. G. (2004), A kinematic model for the southern Alaska orocline based on regional fault patterns, in Orogenic curvature: integrating paleomagnetic and structural analyses, Geol. Soc. Am. Spec. Pap., vol. 383, edited by A. J. Sussmann, and A. B., Weil, pp. 161–172, doi:10.1130/0-8137-2383-3(2004)383(161:AKMFTS)2.0.CO;2.

Gray, K. D., and J. S. Oldow (2005), Contrasting structural histories of the Salmon River belt and Wallowa terrane: implications for terrane accretion in northeastern Oregon and west-central Idaho, Geol. Soc. Am. Bull., 117(5–6), 687–706, doi: 10.1130/B25411.1.

Greenwood, W.R., and R.R. Reid (1969), The Columbia Arc: new evidence for pre-Tertiary rotation, Geol. Soc. Am. Bull., 80, 1797–1800, doi: 10.1130/0016-7606(1969)80(1797:TCANEF)2.0.CO;2.

Grommé, C. S., M. E. Beck, and D. C. Engebretson (1986), Paleomagnetism of the Tertiary Clarno Formation of central Oregon and its significance for the tectonic history of the Pacific Northwest, J. Geophys. Res., 91, B14, 14089–14103, doi:10.1029/JB091iB14p14089.

Gutiérrez-Alonso, G., J. Fernández-Suárez, A. B. Weil (2004), Orocline triggered lithospheric delamination, Geol. Soc. Am. Spec. Pap., vol. 383, edited by A. J. Sussmann, and A. B., Weil, pp. 121–130, doi:10.1130/0-8137-2383-3(2004)383(121:OTLD)2.0.CO;2.

Gutiérrez-Alonso, G., J. Fernández-Suárez, T. E. Jeffries, S. T. Johnston, D. Pastor-Galán, J. B. Murphy, M. P. Franco, and J. C. Gonzalo (2011a), Diachronous post-orogenic magmatism within a developing orocline in Iberia, European Variscides, Tectonics, 30, TC5008, doi:10.1029/2010TC002845.

Gutiérrez-Alonso, G., J. B. Murphy, J. Fernández-Suárez, A. B. Weil, M. Piedad Franco, and J. C. Gonzalo (2011b), Lithospheric delamination in the core of Pangea: Sm–Nd insights from the Iberian mantle, Geology, 39(2), 155–158, doi:10.1130/G31468.1.

Hamilton, W. (1969), Mesozoic California and the underflow of Pacific mantle, Geol. Soc. Am. Bull., 80, 2409–2430, doi: 10.1130/0016-7606(1959)70(1119:COGFWL)2.0.CO;2

Hamilton, W., and W. B. Myers (1966), Cenozoic tectonics of the western United States, Rev. Geophys., 4(4), 509–549, doi:10.1029/RG004i004p00509.

Hildebrand, R.S. (2009), Did westward subduction cause Cretaceous–Tertiary orogeny in the North American Cordillera? Geol. Soc. Am. Spec. Pap., 457, 1–71, doi: 10.1130/2009.2457.

Hildebrand, R.S. (2013), Mesozoic assembly of the North American Cordillera, Geol. Soc. Am. Spec. Pap., 495, 1–169, doi: 10.1130/9780813724959.

Hillhouse, J. W., C. S. Grommé, and T. L.Vallier (1982), Paleomagnetism and Mesozoic tectonics of the Seven Devils volcanic arc in northeastern Oregon, J. Geophys. Res., 87, B5, 3777–3794, doi: 10.1029/JB087iB05p03777.

Hobbs, B. E. (1971), The analysis of strain in folded layers, Tectonophysics, 11(5), 329–375, doi:10.1016/0040-1951(71)90025-4.

Housen, B. A., and R. J. Dorsey (2005), Paleomagnetism and tectonic significance of Albian and Cenomanian turbidites, Ochoco Basin, Mitchell Inlier, central Oregon. J. Geophys. Res., 110, B07102, doi:10.1029/2004JB003458.

Hrouda, F. (1982), Magnetic anisotropy of rocks and its application in geology and geophysics, Geophysical Surv., 5(1), 37–82, doi:10.1007/BF01450244.

Hrouda, F. (1994), A technique for the measurement of thermal changes of magnetic susceptibility of weakly magnetic rocks by the CS-2 apparatus and KLY-2 Kappabridge, Geophys. J. Int., 118(3), 604–612, doi:10.1111/j.1365-246X.1994.tb03987.x.

Hrouda, F., and Š. Kahan (1991), The magnetic fabric relationship between sedimentary and basement nappes in the High Tatra Mountains, N. Slovakia, J. Struct. Geol., 13(4), 431–442, doi:10.1016/0191-8141(91)90016-C.

Jelínek V (1981) Characterization of the magnetic fabric of rocks. Tectonophysics 79, T63–T67.

Johnson, K., C. G. Barnes, and C. A. Miller (1997), Petrology, geochemistry, and genesis of high-Al tonalite and trondhjemites of the Cornucopia stock, Blue Mountains, northeastern Oregon, J. Petrol., 38, 1585–1611, doi: 10.1093/petroj/38.11.1585.

Johnson, K., C. G. Barnes, J. M. Browning, and H. R. Karlsson (2002), Petrology of iron-rich magmatic segregations associated with strongly peraluminous trondhjemite in the Cornucopia stock, northeastern Oregon, Contrib. Mineral. Petrol., 142, 564–581, doi: 10.1007/s00410-001-0311-z.

Johnson, K., J. J. Schwartz, J. L. Wooden, L. J. O'Driscoll, and R. C. Jeffcoat (2011), The Wallowa batholith: new Pb/U (SHRIMP–RG) ages place constraints on arc magmatism and crustal thickening in the Blue Mountains Province, NE Oregon. Geol. Soc. Am. Abstracts with Programs 43(4), 5.

Johnston, S. T. (2001), The Great Alaskan Terrane Wreck: reconciliation of paleomagnetic and geological data in the northern Cordillera, Earth Planet. Sci. Lett., 193, 259–272, doi: 10.1016/S0012-821X(01)00516-7.

Johnston, S.T. (2008), The Cordilleran ribbon continent of North America, Ann. Rev. Earth Planet. Sci., 36, 495–530, doi: 10.1146/annurev.earth.36.031207.124331.

Johnston, S.T., and S. Acton (2003), The Eocene Southern Vancouver Island Orocline – a response to seamount accretion and the cause of fold-and-thrust belt and extensional basin formation, Tectonophysics, 365(1–4), 165–183, doi: 10.1016/S0040-1951(03)00021-0

Johnston, S. T., A. B. Weil, and G. Gutiérrez-Alonso (2013), Oroclines: thick and thin, Geol. Soc. Am. Bull, 125(5–6), 643–663, doi: 10.1130/B30765.

Krauskopf, K. B. (1943), The Wallowa batholith, Am. J. Sci., 241(10), 607–628, doi:10.2475/ajs.241.10.607.

LaMaskin, T. A., R. J. Dorsey, and J. D. Vervoort (2008), Tectonic controls on mudrock geochemistry, mesozoic rocks of eastern Oregon and western Idaho, U.S.A.: implications for Cordilleran tectonics, J. Sedim. Res., 78(12), 765–783, doi: 10.2110/jsr.2008.087.

LaMaskin, T. A., J. J. Schwartz, R. J. Dorsey, A. W. Snoke, K. Johnson, and J. D. Vervoort (2009), Mesozoic sedimentation, magmatism, and tectonics in the Blue Mountains Province, northeastern Oregon, Geol. Soc. Am. Field Guide, 15, 1–17, doi: 10.1130/2009.fld015(09).

LaMaskin, T. A., J. D. Vervoort, R. J. Dorsey, and J. E. Wright (2011), Early Mesozoic paleogeography and tectonic evolution of the western United States: insights from detrital zircon U–Pb geochronology, Blue Mountains Province, northeastern Oregon, Geol. Soc. Am. Bull., 123 (9–10), 1939–1965, doi: 10.1130/B30260.1.

Lister, G.S., and A.W. Snoke (1984), S–C mylonites, J. Struct. Geol., 6, 617–638, doi: 10.1016/0191-8141(84)90001-4

Lund, K., Aleinikoff, J.N., Yacob, E.Y., Unruh, D.M., and C.M. Fanning (2008), Coolwater culmination: Sensitive high-resolution ion microprobe (SHRIMP) U-Pb and isotopic evidence for continental delamination in the Syringa Embayment, Salmon River suture, Idaho, Tectonics, 27, TC2009, doi:10.1029/2006TC002071.

Manduca, C.A., L.T. Silver, and H.P. Taylor (1992), 87Sr/86Sr and 18O/16O isotopic systematics and geochemistry of granitoids plutons across a steeply-dipping boundary between contrasting lithospheric blocks in western Idaho, Contrib. Mineral. Petrol., 109, 355–372, doi:10.1007/BF00283324.

Manduca, C. A., M. A. Kuntz, and L. T. Silver (1993), Emplacement and deformation history of the western margin of the Idaho batholith near McCall, Idaho: influence of a major terrane boundary, Geol. Soc. Am. Bull., 105(6), 749–765, doi: doi: 10.1130/0016-7606(1993)105<0749:EADHOT>2.3.CO;2.

McClelland, W. C., B. Tikoff, and C. A. Manduca (2000), Two-phase evolution of accretionary margins: examples from the North American Cordillera, Tectonophysics, 326, 37–55, doi: 10.1016/S0040-1951(00)00145-1.

McClelland, W. C., and J. S. Oldow (2007), Late Cretaceous truncation of the western Idaho shear zone in the central North American Cordillera, Geology, 35(8), 723–726, doi: 10.1130/G23623A.1.

McKay, M. P. (2011), Pressure–temperature–time paths, prograde garnet growth, and protolith of tectonites from a polydeformational, polymetamorphic terrane: Salmon River suture zone, west-central Idaho. M.S. thesis, Univ. of Alabama.

McWilliams, M., and Y.P. Li (1985), Oroclinal bending of the southern Sierra Nevada batholith, Science, 230, 172–175, doi: 10.1126/science.230.4722.172.

Monger, J.W.H. (1997), Plate tectonics and northern Cordilleran geology: an unfinished revolution, Geosci. Canada, 24, 189–198, doi: 10.12789/gs.v24i4.3953.

Mortimer, N. (1986), Late Triassic, arc-related, potassic igneous rocks in the North American Cordillera, Geology, 14(12), 1035–1038, doi:10.1130/0091-7613(1986)14<1035:LTAPIR>2.0.CO;2.

Nolf, B. (1966), Structure and stratigraphy of part of the northern Wallowa Mountains, northeast Oregon, Ph.D. dissertation, Princeton University, New Jersey.

Pastor-Galán, D., G. Gutiérrez-Alonso, G. Zulauf, and F. Zanella (2012), Analogue modeling of lithospheric-scale orocline buckling: constraints on the evolution of the Iberian–Armorican Arc, Geol. Soc. Am. Bull., 124(7–8), 1293–1309, doi: 10.1130/B30640.1.

Paterson, S. R., R. H. Vernon, and O. T. Tobisch (1989), A review of criteria for identification of magmatic and tectonic foliations in granitoids, J. Struct. Geol., 11(3), 349–363, doi:10.1016/0191-8141(89)90074-6.

Paterson, S. R., T. K. Fowler, K. L. Schmidt, A. S. Yoshinobu, E. S. Yuan, and R. B. Miller (1998), Interpreting magmatic fabric patterns in plutons, Lithos, 44(1–2), 53–82, doi:10.1016/S0024-4937(98)00022-X.

Paterson, S. R., Onézime, J., Teruya, L., and J. Žák (2003), Quadruple-pronged enclaves: their significance for the interpretation of multiple magmatic fabrics in plutons, J. Virt. Explor., 10, 15–30.

Patton, W.W., and I.L. Tailleur (1977), Evidence in the Bering Strait region for differential movement between North America and Eurasia, Geol. Soc. Am. Bull., 88, 1298–1304, doi: 10.1130/0016-7606(1977)88<1298:EITBSR>2.0.CO;2.

Piercey, S. J., and M. Colpron (2009), Composition and provenance of the Snowcap assemblage, basement to the Yukon–Tanana terrane, northern Cordillera: implications for Cordilleran crustal growth, Geosphere, 5(5), 439–464, doi:10.1130/GES00505.1.

Sarewitz, D. (1983), Seven Devils terrane: is it really a piece of Wrangellia? Geology, 11(11), 634–637, doi:10.1130/0091-7613(1983)11<634:SDTIIR>2.0.CO;2.

Selverstone, J., B. P. Wernicke, and E. A. Aliberti (1992), Intracontinental subduction and hinged unroofing along the Salmon River suture zone, west central Idaho, Tectonics, 11(1), 124–144, doi: 10.1029/91TC02418.

Schmidt, K.L., Burmeister, R.F., Link, P.K., and C.M. Fanning (2003), New constraints on the western Idaho orocline: a primary feature in the Mesozoic collision zone or result of strike-slip modification? Geol. Soc. Am. Abstracts with Programs, 35, 559

Schmidt, K.L., Lewis, R.S., Gaschnig, R.M., and J. Vervoort (2009), Testing hypotheses on the origin of the Syringa embayment in the Salmon River suture zone, western Idaho, USA, Geol. Soc. Am. Abstracts with Programs, 41, 223.

Schwartz, J. J., and K. Johnson (2014), Construction of Phanerozoic continental crust in the Blue Mountains province by tectonic assembly and magmatic addition. Geol. Soc. Am. Abstracts with Programs 43(5), 647.

Schwartz, J. J., A. W. Snoke, C. D. Frost, C. G. Barnes, L. P. Gromet, and K. Johnson (2010), Analysis of the Wallowa–Baker terrane boundary: implications for tectonic accretion in the Blue Mountains province, northeastern Oregon, Geol. Soc. Am. Bull., 122(3–4), 517–536, doi:10.1130/B26493.1.

Schwartz, J. J., A. W. Snoke, F. Cordey, K. Johnson, C. D. Frost, C. G. Barnes, T. A. LaMaskin, and J. L. Wooden (2011a), Late Jurassic magmatism, metamorphism, and deformation in the Blue Mountains province, northeast Oregon, Geol. Soc. Am. Bull., 123(9–10), 2083–2111, doi: 10.1130/B30327.1.

Schwartz, J. J., K. Johnson, E. A. Miranda, and J. L. Wooden (2011b), The generation of high Sr/Y plutons following Late Jurassic arc–arc collision, Blue Mountains province, NE Oregon, Lithos, 126, 22–41, doi: 10.1016/j.lithos.2011.05.005.

Schwartz, J.J., Johnson, K., Mueller, P., Valley, J., Strickland, A., and J.L. Wooden (2014), Time scales and processes of Cordilleran batholith construction and high-Sr/Y magmatic pulses: evidence from the Bald Mountain batholith, northeastern Oregon. Geosphere, 10, 1456–1481, doi: 10.1130/GES01033.1.

Sigloch, K., and M.G. Mihalynuk (2013), Intra-oceanic subduction shaped the assembly of Cordilleran North America, Nature, 496, 50–56, doi: 10.1038/nature12019.

Snee, L. W., K. Lund, J. F. Sutter, D. E. Balcer, and K. V. Evans (1995), An 40Ar/39Ar chronicle of the tectonic development of the Salmon River suture zone, western Idaho, in: Geology of the Blue Mountains Region of Oregon, Idaho and Washington: petrology and tectonic evolution of pre-Tertiary rocks of the Blue Mountains region, U.S. Geol. Surv. Prof. Pap., vol. 1438, edited by T. L. Vallier, and H. C. Brooks, pp. 359–414.

Stanley, G. D., C. A. McRoberts, and M. T. Whalen (2008), Stratigraphy of the Triassic Martin Bridge Formation, Wallowa terrane: stratigraphy and depositional setting, in The terrane puzzle: new perspectives on paleontology and stratigraphy from the North American Cordillera, Geol. Soc. Am. Spec. Pap., vol. 442, edited by R. B. Blodgett, and G. D. Stanley, pp. 227–250.

Stowell, H., M. P. McKay, J. J. Schwartz, and D. R. Gray (2014), Loading and metamorphism within the Salmon River suture zone, west-central Idaho. Geol. Soc. Am. Abstracts with Programs, 43(5), 647.

Strayer, L. M., D. W. Hyndman, J. W. Sears, and P. E. Myers (1989), Direction and shear sense during suturing of the Seven Devils–Wallowa terrane against North America in western Idaho, Geology, 17(11), 1025–1028, doi:10.1130/0091-7613(1989)017<1025:DASSDS>2.3.CO;2.

Tarling, D. H., and F. Hrouda (1993), The magnetic anisotropy of rocks, Chapman and Hall, London.

Taubeneck, W. H. (1964), Cornucopia stock, Wallowa Mountains, northeastern Oregon: field relationships, Geol. Soc. Am. Bull., 75(11), 1093–1116, doi:10.1130/0016-7606(1964)75(1093:CSWMNO)2.0.CO;2.

Taubeneck, W. H. (1966), An evaluation of tectonic rotation in the Pacific Northwest, J. Geophys. Res., 71(8), 2113–2120, doi: 10.1029/JZ071i008p02113.

Taubeneck, W. H. (1987), The Wallowa Mountains, northeast Oregon, in Geol. Soc. Am. Centennial Field Guide – Cordilleran Section, edited by M. L. Hill, pp. 327–332.

Tikoff, B., P. Kelso, T., Stetson-Lee, A. Byerly, R. M. Gaschnig, J. D. Vervoort, and A. P. Rinna (2014), The role of the Precambrian rifted margin on Cretaceous-aged deformation. Geol. Soc. Am. Abstracts with Programs, 46(5), 18.

Twiss, R.J., and E.M. Moores (1992), Structural geology, W.H. Freeman and Company, New York, 532 pp.

Vallier, T.L. (1995), Petrology of pre- Tertiary igneous rocks in the Blue Mountains region of Oregon, Idaho, and Washington: implications for the geologic evolution of a complex island arc, in: Geology of the Blue Mountains Region of Oregon, Idaho and Washington: petrology and tectonic evolution of pre-Tertiary rocks of the Blue Mountains region, U.S. Geol. Surv. Prof. Pap., vol. 1438, edited by T. L. Vallier, and H. C. Brooks, pp. 125–219.

Vernon, R. H. (2000), Review of microstructural evidence of magmatic and solid-state flow, Electronic Geosci., 5(2), 1–23, doi: 10.1007/s10069-000-0002-3.

Walker, G. W. (1979), Reconnaissance geologic map of the Oregon part of the Grangeville quadrangle, Baker, Union, Umatilla, and Wallowa Counties, Oregon, scale 1:250,000. U.S. Geol. Surv. miscellaneous investigations series map No. I-1116.

Weil, A. B., G. Gutiérrez-Alonso, S. T. Johnston, and D. Pastor-Galán (2013), Kinematic constraints on buckling a lithospheric-scale orocline along the northern margin of Gondwana: a geologic synthesis, Tectonophysics, 582, 25–49, doi:10.1016/j.tecto.2012.10.006.

Weis, P.L., Gualtieri, J.L., Cannon, W.F., Tuchek, E.T., McMahan, A.B., and F.E. Federspiel (1976), Mineral resources of the Eagle Cap Wilderness and adjacent areas, Oregon, U. S. Geol. Surv. Bull., 1385–E, 1–100.

Wernicke, B., and D. W. Klepacki (1988), Escape hypothesis for the Stikine block, Geology, 16(5), 461–464, doi: doi: 10.1130/0091-7613(1988)016<0461:EHFTSB>2.3.CO;2.

Wilson, D., and A. Cox (1980), Paleomagnetic evidence for tectonic rotation of Jurassic plutons in Blue Mountains, eastern Oregon, J. Geophys. Res., 85, NB7, 3681–3689, doi: 10.1029/JB085iB07p03681.

Žák, J., K. Verner, K. Johnson, and J. J. Schwartz (2012a), Magnetic fabric of Late Jurassic arc plutons and kinematics of terrane accretion in the Blue Mountains, northeastern Oregon, Gondwana Res., 22(1), 341–352, doi: 10.1016/j.gr.2011.09.013.

Žák, J., K. Verner, K. Johnson, and J. J. Schwartz (2012b), Magma emplacement process zone preserved in the roof of a large Cordilleran batholith, Wallowa Mountains, northeastern Oregon, J. Volcanol. Geotherm. Res., 227–228, 61–75, doi: 10.1016/j.jvolgeores.2012.03.001.

Chapter 5:

GRANITIC MAGMA EMPLACEMENT AND DEFORMATION DURING EARLY-OROGENIC SYN-CONVERGENT TRANSTENSION: THE STARÉ SEDLO COMPLEX, BOHEMIAN MASSIF

by Filip Tomek, Jiří Žák, and Martin Chadima

a paper published in **Journal of Geodynamics** (2015) 87:50–66

(additional information are listed in supplementary material part 3 and appendix item 5)

GRAPHICAL ABSTRACT

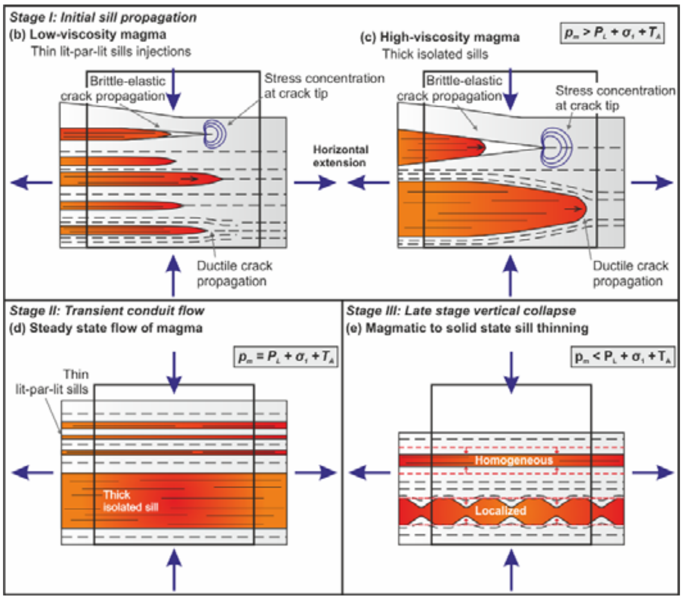

KEY WORDS

◇ Anisotropy of magnetic susceptibility (AMS)

◇ Bohemian Massif ◇ Pluton emplacement

◇ Granite

◇ Transtension

◇ Variscan orogeny

GRANITIC MAGMA EMPLACEMENT AND DEFORMATION DURING EARLY-OROGENIC SYN-CONVERGENT TRANSTENSION: THE STARÉ SEDLO COMPLEX, BOHEMIAN MASSIF

ABSTRACT

The Late Devonian Staré Sedlo complex, Bohemian Massif, was emplaced as a subhorizontal sheeted sill pluton into a transtension zone. The transtensional setting is documented by strong constrictional fabric, corroborated by the anisotropy of magnetic susceptibility (AMS), with variably developed subhorizontal magmatic to solid-state foliation suggesting vertical shortening. Intrusive contacts of the granitoids with metapelitic screens and tapered sill tips indicate that magma wedging was the dominant process of sill propagation. The sills exhibit two intrusive styles, ranging from thin lit-par-lit injections to widely spaced meter-thick sills. These two styles are interpreted as reflecting variable viscosities of intruding magma where low-viscosity magma percolated along foliation planes whereas high-viscosity magma produced more localized thicker sills. We propose that the magma/host rock system in transtension must have evolved from initial crack tip propagation and vertical expansion due to new magma additions through conduit flow to ductile thinning after the magma input had ceased. The sill emplacement and their subsequent deformation are then interpreted as recording early-orogenic syn-convergent sinistral transtension along the rear side of an upper-crustal wedge, which was extruded both upward and laterally in response to subduction and continental underthrusting.

INTRODUCTION

Transtension is a deformation regime resulting from oblique divergence where the transport direction is at an acute angle (α) to the deforming zone boundary, leading to a simultaneous combination of coaxial vertical shortening (thinning) with non-coaxial horizontal simple shear (e.g., Dewey, 2002; Dewey et al., 1998; Fossen and Tikoff, 1998; Fossen et al., 1994, 2013; Tikoff and Fossen, 1993). As such, transtension is a consequence of obliquely divergent motion of lithospheric plates (e.g., McCaffrey, 1992; Teyssier et al., 1995) but may also operate in ‛second-order’ transtensional domains in otherwise convergent settings. The former class includes obliquely divergent continental rifts and mid-ocean ridges (e.g., Acosta and Uchupi, 1996; Baines et al., 2003; John et al., 2004; Kashintsev et al., 2008; Kidane et al., 2009; Rotstein and Schaming, 2011; Tommasi and Vauchez, 2001; Wilson et al., 2006) whereas the latter can be found within arc and back-arc regions along active plate margins (e.g., Creixell et al., 2006, 2011; Dewey, 2002; Kirsch et al., 2012) and even in collisional orogenic belts (e.g., Andronicos et al., 2003; Hou et al., 2006; Murphy and Copeland, 2005; Murphy and Burgess, 2006). Transtensional deformation also characterizes releasing bends in transform and strike-slip fault zones (e.g., Garcia et al., 2002; Teyssier and Tikoff, 1998; Thybo, 1997; Wesnousky, 2005).

Active transtension zones may also represent favorable sites for magma transport and emplacement. Based on external intrusion geometry and internal fabrics, two end-member magma emplacement modes into transtension zones have been proposed in the literature.

First, magma may migrate through tensile (T) or Riedel (R) and anti-Riedel (R') shear fractures. This mechanism results in the formation of vertical intrusive sheets that are oblique to the deforming zone boundary (e.g., Altenberger et al., 2001; Brown et al., 2008; Pereira et al., 2013; Rossetti et al., 2000; Scarrow et al., 2011; Soper and Woodcock, 2003; Vaughan, 1996). Magmatic to solid state fabric is typically asymmetric in these cases, oblique to the sheet walls, and characterized by sigmoidally curved subvertical foliations and subhorizontal lineations (e.g., Correa-Gomes et al., 2001; Creixell et al., 2006, 2011; Zulauf and Helferich, 1997). In addition, examples of larger, steep granitoid plutons the emplacement of which was variously controlled by, or interacted with, regional transtension were reported by Bolle et al. (2010), Krohe (1991), Salazar et al. (2013), Venera et al. (2000), and Zulauf et al. (1997).

Second, magma may intrude into transtension zones as horizontal sheets if the physical conditions, such as the stress state, the presence of horizontal host rock anisotropy, or a rheological barrier, force the feeder dikes to propagate horizontally (e.g., Aranguren et al., 1997; Cook et al., 1964; Gudmundsson, 2011; Krohe, 1991; Sadeghian et al., 2005). Common to these intrusions are subhorizontal magmatic foliations and lineations and plane-strain to prolate fabrics. Lineations are typically parallel to the principal stretching direction but may variously reorient depending on the amount of total strain recorded by the magma (e.g., Sadeghian et al., 2005) or due to strain partitioning (e.g., Kratinová et al., 2007). Sill complexes may also develop through intrusion along flat-lying detachments within active transtensional zones (e.g., Crawford et al., 1999; Hollister and Andronicos, 2006; Klepeis and Crawford, 1999).

Despite the number of examples listed above, many issues regarding the mechanisms of magma emplacement into active transtension zones remain unclear. These include the exact nature of interactions between the buoyant overpressurized magma and transtensional deformation, the means whereby host rock is displaced along the advancing magma process zone, the role of mechanical host rock anisotropy and its reactivation during magma emplacement, and the influence of changing magma/host rock rheology on fabric development during progressive magma crystallization.

This paper addresses some of the above issues in the Late Devonian Staré Sedlo complex, central Bohemian Massif (Fig. 1), which provides excellent exposures to study granitic magma emplacement into actively deforming, highly anisotropic host rock during transtension. After a brief introduction into geologic setting, we concentrate in detail on intrusive contacts, microstructures and internal fabric of the (meta-)granitoids, including detailed quantification of fabric parameters using the anisotropy of magnetic susceptibility (AMS). Based on this example, we present a model for emplacement of magmatic sheets during vertical shortening, which is characteristic of active transtension zones, emphasizing the complex interplay among magma pressure, viscosity, and mechanical host rock anisotropy. We then discuss the significance of magmatic to solid state fabrics in the Staré Sedlo complex and some implications for syn-convergent transtensional deformation in the interior of the Variscan orogenic belt.

GEOLOGY AND TECTONIC SETTING OF THE STARÉ SEDLO COMPLEX

The Bohemian Massif of central Europe is the largest inlier of the once continuous but now largely dismembered or concealed Ouachita–Appalachian–Variscan orogenic belt (Fig. 1a) that formed during the Devonian to Carboniferous closure of the Rheic Ocean by convergence of Gondwana and Laurussia (e.g., Nance et al. 2010; Kroner and Romer, 2013 and references therein). Shortly after the onset of the Variscan orogeny as marked by an abrupt change in the sedimentary record during Givetian (~388–383 Ma; flysch siliciclastics deposited over limestones; e.g., Chlupáč et al., 1998; Strnad and Mihaljevič, 2005), the orogenic upper crust of the central

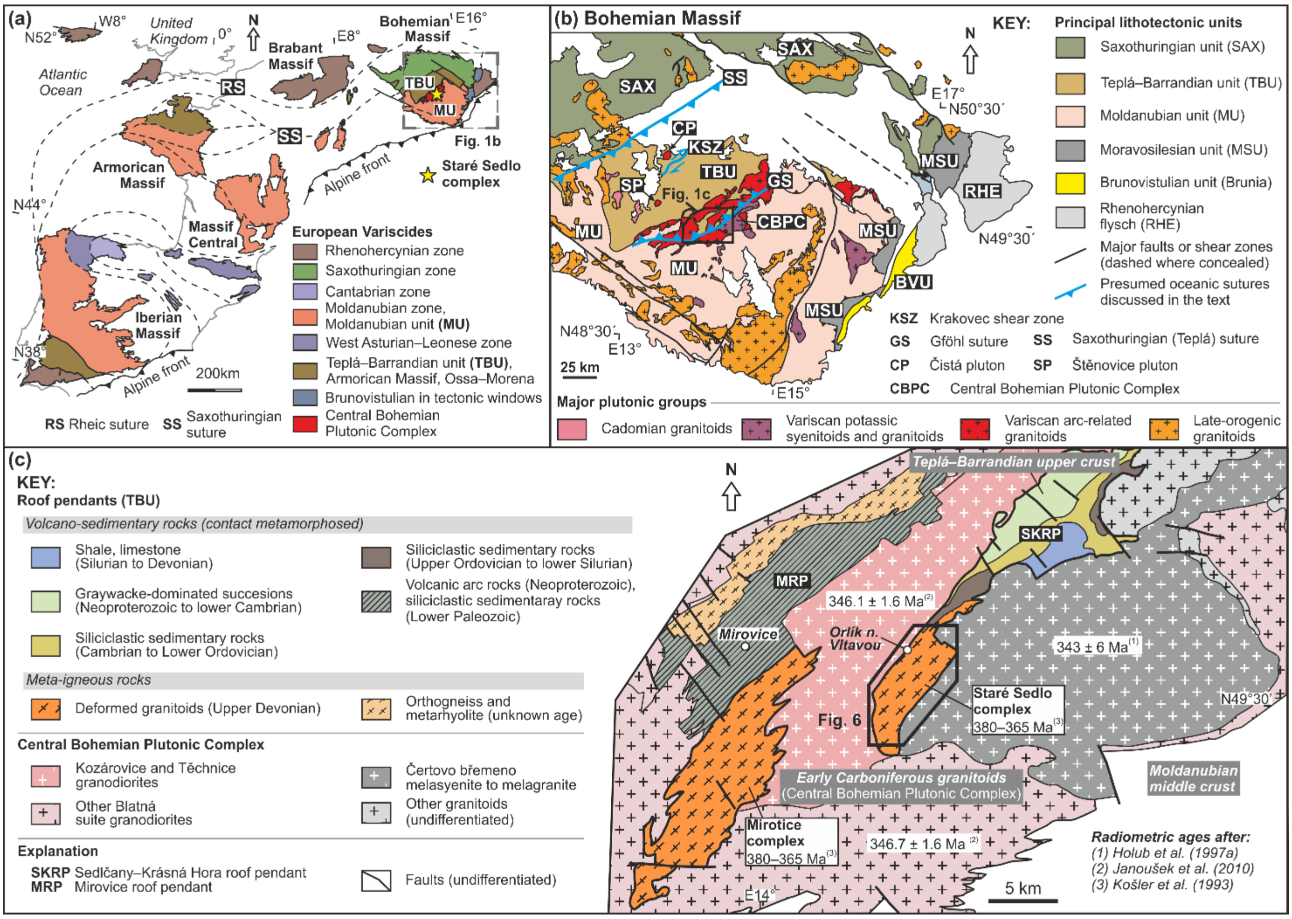

Fig. 1. (a) Overview geologic map of Europe showing the main basement outcrop areas and principal lithotectonic zones and sutures of the Variscan orogenic belt; Bohemian Massif is the easternmost exposure of the orogen. Compiled from Winchester (2002), Asch (2003), and Martínez Catalán (2011, 2012). (b) Simplified geologic map of the interior Bohemian Massif emphasizing principal lithotectonic units and plutonic groups. Compiled from Fusán et al. (1967) and Cháb et al. (2007). (c) Geologic map of the central Bohemian Massif showing the boundary between the Teplá–Barrandian and Moldanubian units largely intruded by the Central Bohemian Plutonic Complex; simplified after Kodym (1996). Radiometric dating after (1) Košler et al. (1993), (2) Janoušek et al. (2010), and (3) Holub et al. (1997a).

Bohemian Massif plutons include two ~375–373 Ma small stocks in the center of the Teplá–Barrandian unit (the Čistá and Štěnovice plutons in Fig. 1b; Klomínský, 1963, 1965; Kopecký et al., 1997; Venera et al., 2000; Žák et al., 2011) and the ~380–365 Ma Staré Sedlo and Mirotice complexes (Fig. 1c; Košler et al., 1993). The latter two complexes were emplaced into the Neoproterozoic and Early Paleozoic metasedimentary successions along a tectonic boundary now separating the orogenic upper crust from the mid- to lower-crustal rocks (the Teplá–Barrandian and Moldanubian units, respectively; Fig. 1a–c). All the Late Devonian plutons are composed of calc-alkaline, peraluminous to metaluminous I-type (magnetite-series) granodiorites to tonalites and their whole-rock and isotopic compositions point to a magmatic arc origin above a subduction zone (Košler, 1993; Košler and Farrow, 1994; Košler et al., 1993; Žák et al., 2011). However, linking these granitoids to a particular subduction zone within the Bohemian Massif remains unresolved. For instance, the Staré Sedlo complex was variously explained to form above the SE-directed subduction of the Saxothuringian Ocean (e.g., Janoušek and Holub, 2007; Schulmann et al., 2009) or opposite, NW-directed subduction of the Moldanubian (Gföhl) Ocean (e.g., Babuška and Plomerová, 2013; Faryad et al., 2015; Franke, 1999, 2006), both beneath the overriding Teplá–Barrandian upper crust (Fig. 1b). Especially reconstruction of the hypothetic Moldanubian (Gföhl) suture is hindered by the extensive early Carboniferous, ~354–337 Ma Central Bohemian Plutonic Complex which intruded into a broad zone along the Teplá–Barrandian/Moldanubian boundary (Fig. 1a, b; see Holub et al., 1997a, 1997b; Janoušek et al., 1995, 2000, 2010 for overview and references).

This paper deals with the Staré Sedlo complex which occupies portion of a major roof pendant in younger granitoids (Fig. 1c). The complex is superbly exposed in a ~10 km long section along the Vltava River valley and comprises several petrographic and textural varieties of variously deformed amphibole–biotite and biotite granodiorites to tonalites (also referred to as 'orthogneisses') separated by gradational or sharp contacts (Košler et al., 1993; Waldhausrová, 1986, 1987). To the northeast, the granitoids are in intrusive contact with the host metasedimentary and metavolcanic rocks of presumably Ordovician to mid-Devonian age (Chlupáč, 1989), represented by spotted schists, paragneisses, quartzites, and lenses of amphibolites. Except for this northeastern end, the granitoids have been intruded from all sides by the ~346 Ma Kozárovice granodiorite and by ~343 Ma Čertovo Břemeno durbachite (Fig. 1b, c; Holub et al., 1997a; Janoušek and Gerdes, 2003; Janoušek et al., 2010; Žák et al., 2005a).

FIELD RELATIONSHIPS, INTRUSIVE CONTACTS, AND MAGMA MINGLING STRUCTURES

The southern portion of the Staré Sedlo complex has been little affected by syn-emplacement deformation from the surrounding younger plutons. Here, the complex preserves the original intrusive contacts of the granitoids with the metasedimentary host rocks as well as a variety of structures resulting from mafic–felsic magma interactions. The granitoids form a sheeted complex that consists of abundant subhorizontal sills separated by tabular host rock septa (Figs. 2a–d, 3a–d). The sills are parallel to subhorizontal relic bedding or to metamorphic foliation in the metasedimentary rocks (Figs. 2a–c, 3a, c). In terms of the sill thickness, two end-member cases were observed. (1) Thicker sills of several decimeters to several meters thickness alternate with comparably thick, or even thicker, septa (Fig. 2b–d). These sills may also locally pass into dikes where they have segments discordant to the host rock foliation (Fig. 2c). (2) Extremely thin, vein-like sills with a thickness of several millimeters to several centimeters at most are always parallel to the pervasive foliation in the host rock (Fig. 3a, b). These thin sills occur in swarms, splitting the host rock along the foliation planes into numerous cm-thick screens (Fig. 3b). The thin-sill tips, if preserved on an outcrop, are tapered (Fig. 3c, d).In some places, the granitoids also contain metasedimentary xenoliths up to several decimeters in size. Some xenoliths have a rectangular shape, are irregularly fractured, and exhibit knife-sharp margins that truncate the internal xenolith foliation (Fig. 3e) whereas other xenoliths, or relic septa, are strongly elongated and show signs of mechanical disruption by the granitic/tonalitic magma (Fig. 3f).

The granitoids are associated with bodies of basic to intermediate rocks mostly of gabbro to diorite compositions which vary in size, degree of deformation, and structural relation to their host. In the southern and central portion of the complex, they form either synplutonic sheets up to

Fig. 2. Intrusive relationships in the Staré Sedlo complex. (a, b) Granitic sills intruding the host metapelite along subhorizontal foliation planes and splitting the host rock into thin septa. Swiss Army penknife for scale. WGS84 coordinates: N49.49641563°, E14.17661173°. (c) Thick sill with a subhorizontal intrusive contact (close-up). Thinner granitic veins are boudinaged. WGS84 coordinates: N49.51228500°, E14.17840688°. (d) Screens of host metapelite alternating with sills of deformed granitoids; hammer for scale. WGS84 coordinates: N49.49921091°, E14.18375077°.

several meters thick (Fig. 4a, b) or swarms of microgranular enclaves (Fig. 4c, d). In some cases observed in low-strain domains, the synplutonic sheets are disrupted and grade into enclave swarms (Fig. 4a, b).

The shape, texture, and degree of magmatic to solid-state deformation of micrograngular enclaves varies from rounded ellipsoidal enclaves with preserved magmatic texture in low-strain domains (Fig. 4c, d) to strongly deformed enclaves in high-strain domains, where the enclaves are extremely flattened parallel to foliation and elongated parallel to lineation in the host deformed granitoid (Fig. 4e). Some synplutonic sheets are composite and have been boudinaged (Fig. 4f).

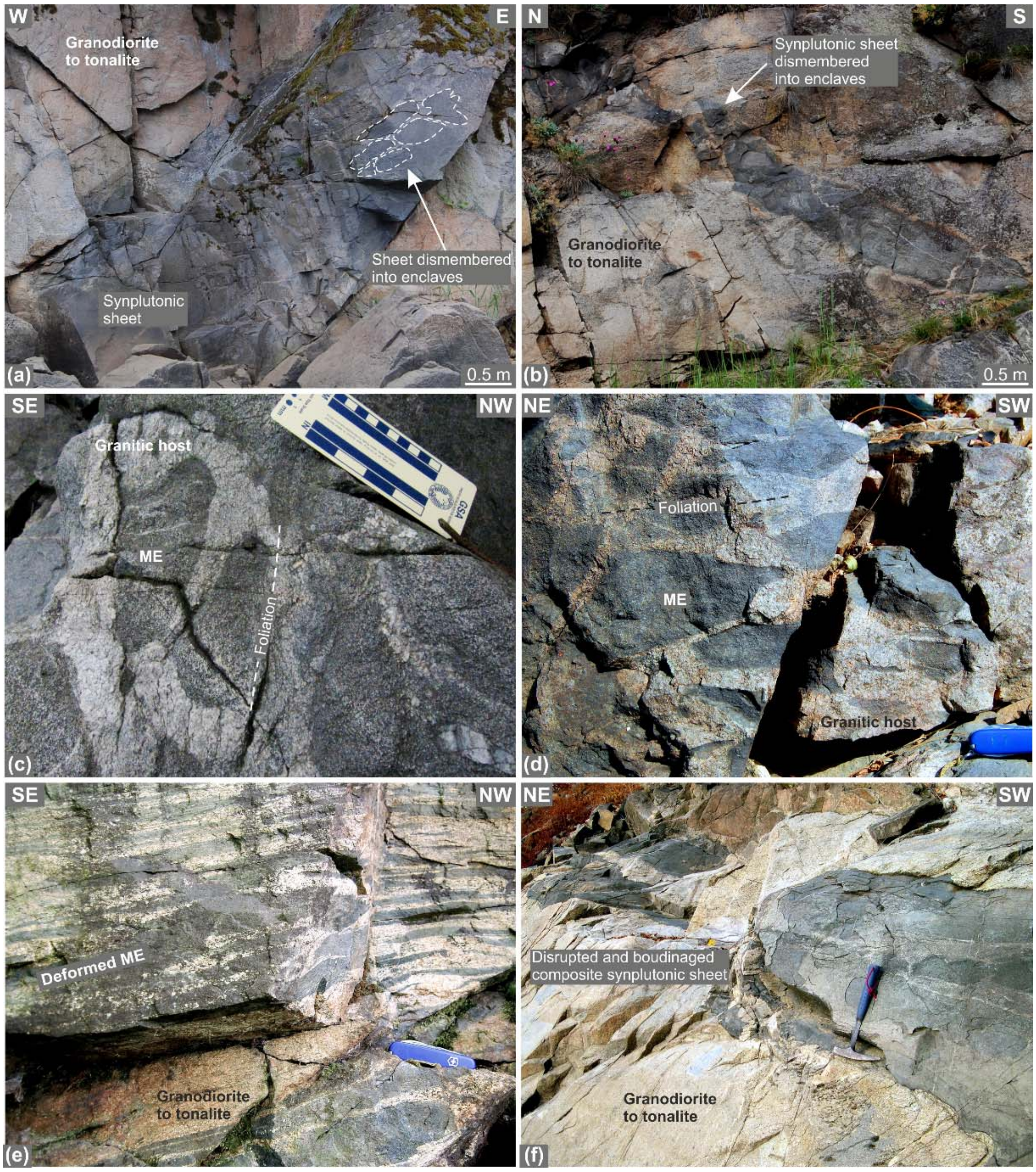

Fig. 4. Structures resulting from magma mingling in the Staré Sedlo complex. (a, b) Composite synplutonic basic sheets dismembered into microgranular enclaves. WGS84 coordinates: N49.50762793°, E14.17922965°. (c) Weakly aligned micrograngular enclaves (ME) in a low strain domain. The granitic host exhibits undeformed magmatic texture. WGS84 coordinates: N49.48714457°, E14.18030304°. (d) Weakly deformed micrograngular enclaves showing subhorizontal magmatic foliation. Swiss Army penknife for scale. WGS84 coordinates: N49.47555877°, E14.16505619°. (e) Strongly deformed micrograngular enclaves exhibiting subhorizontal foliation. Swiss Army penknife for scale. WGS84 coordinates: N49.49641563°, E14.17661173°. (f) Disrupted and boudinaged composite synplutonic sheet in intensely deformed granitic host. Hammer for scale. WGS84 coordinates: N49.48714457°, E14.18030304°.

MESOSCOPIC FABRICS

The Staré Sedlo granitoids preserve a continuum from magmatic to high-temperature solid-state fabric (as defined in Paterson et al., 1989, 1998; and Vernon, 2000). The former is defined by relic mineral fabric and by the alignment of micrgranular enclaves (Fig. 4c, d) whereas the latter, dominant solid-state foliation and/or lineation is defined by the shape-preferred orientation of quartz, feldspar, biotite, and amphibole grains (Fig. 5a–c; Section 5). Three structural domains (referred to as Domains 1–3 in this paper) were distinguished in the complex on the basis of fabric orientation and shape of the fabric ellipsoid, as determined from relative importance of foliation and lineation (Figs. 6, 7):

(1) The Domain 1 in the south–central portion of the complex is characterized by subhorizontal to moderately-dipping (<40° dip) magmatic to solid-state foliation (Figs. 4d, 6a, c). This foliation in both granitoids and in the host rock screens dips either to the ~NW or ~SE and is associated with a subhorizontal ~NE–SW stretching lineation (Fig. 6b). Although the shape of the fabric ellipsoid may vary, this flat fabric is predominantly strongly prolate (Fig. 7). Asymmetric structures are generally absent in both lineation-parallel and lineation-perpendicular sections. This observation is consistent with thin quartz veins which have been folded into symmetric isoclinal

Fig. 5. Mesoscopic fabrics in the Staré Sedlo complex. (a) Subhorizontal solid-state foliation and lineation in the deformed granitoids. Swiss Army penknife for scale. WGS84 coordinates: N49.49413600°, E14.17524045°. (b) Solid state foliation in the deformed granitoids. Swiss Army penknife for scale. WGS84 coordinates: N49.51319788°, E14.18221646°. (c) Close up of solid-state foliation in the deformed granitoids. WGS84 coordinates: N49.49085549°, E14.17488716°. (d) Isoclinally folded granitic vein with its axial plane parallel to the foliation in the granitic host. Coin for scale. WGS84 coordinates: N49.46936899°, E14.16478629°.

folds with their axial planes parallel to the foliation (Fig. 5d).

(2) In the approximately 100–200 m wide Domain 2 along the northwestern margin of the complex, the intrusive contacts, host rock screens, and foliation in the granitoids and their host rocks steepen to about 40–75° dip (to the ~SE and NW) while maintaining the same ~NE–SW strike and being associated with the subhorizontal ~NE–SW lineation (Fig. 6a–c).

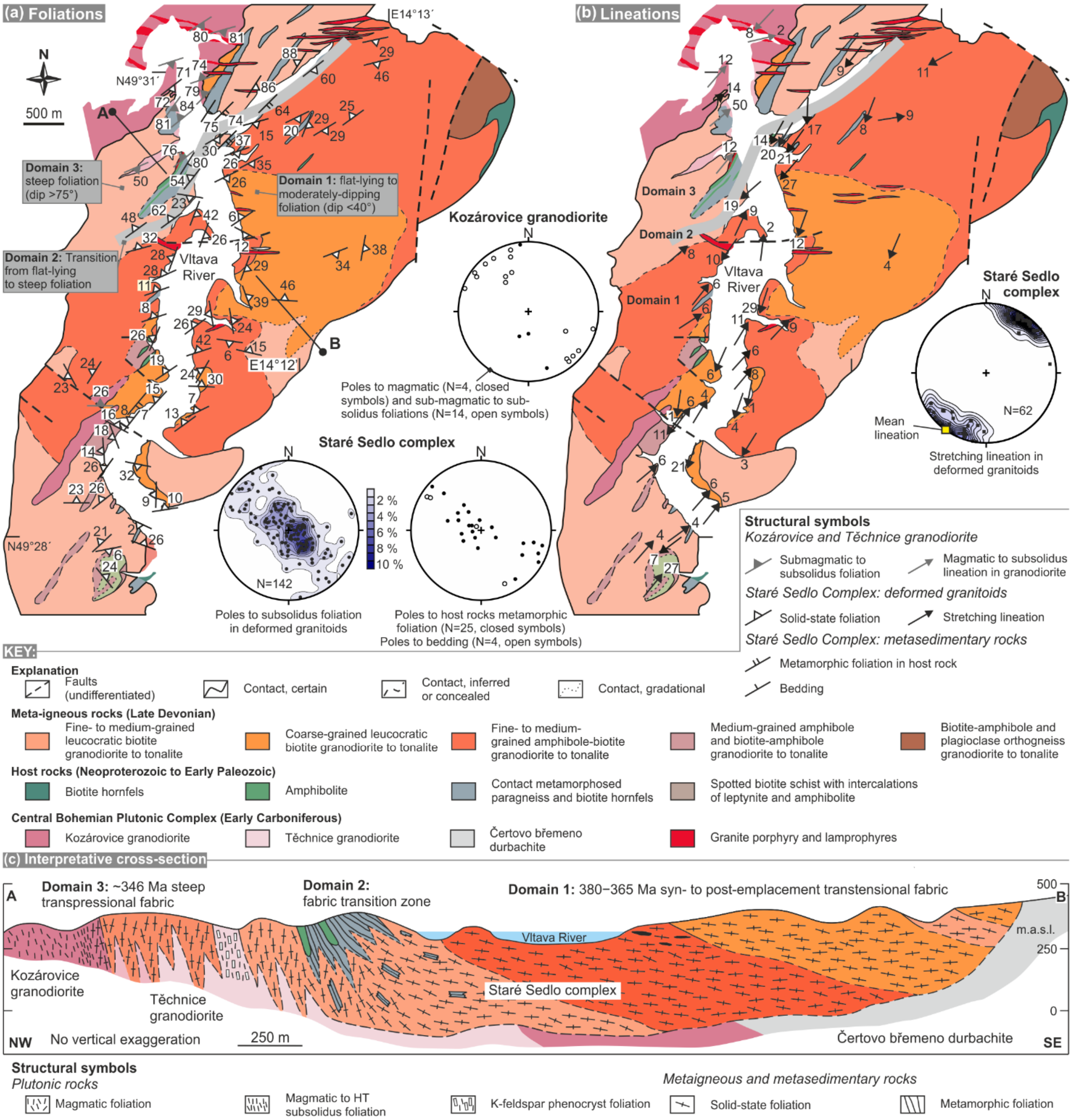

Fig. 6. Structural map of the Staré Sedlo complex; geology based on Waldhausrová (1986). Stereonets (equal area projection, lower hemisphere) show orientation of solid-state foliations of the Staré Sedlo granitoids, host rock metamorphic foliations and bedding, and magmatic to submagmatic foliations in the Kozárovice granodiorite. (a) Foliations in the Staré Sedlo complex. (b) Lineations in the Staré Sedlo complex. (c) Schematic interpretive cross-section along line A–B (location shown in Fig. 7a).

(3) In the northwesterly Domain 3 along the contact with the Kozárovice granodiorite, the host rock screens become particularly abundant, have a steep attitude, and both the granitoids and metasedimentary rocks exhibit a steep foliation (75–90° dip) associated with a subhorizontal ~NE–SW lineation (Fig. 6a–c).

Fig. 7. Map of mesoscopic fabric ellipsoids in the Staré Sedlo complex; prolate fabrics are highlighted.

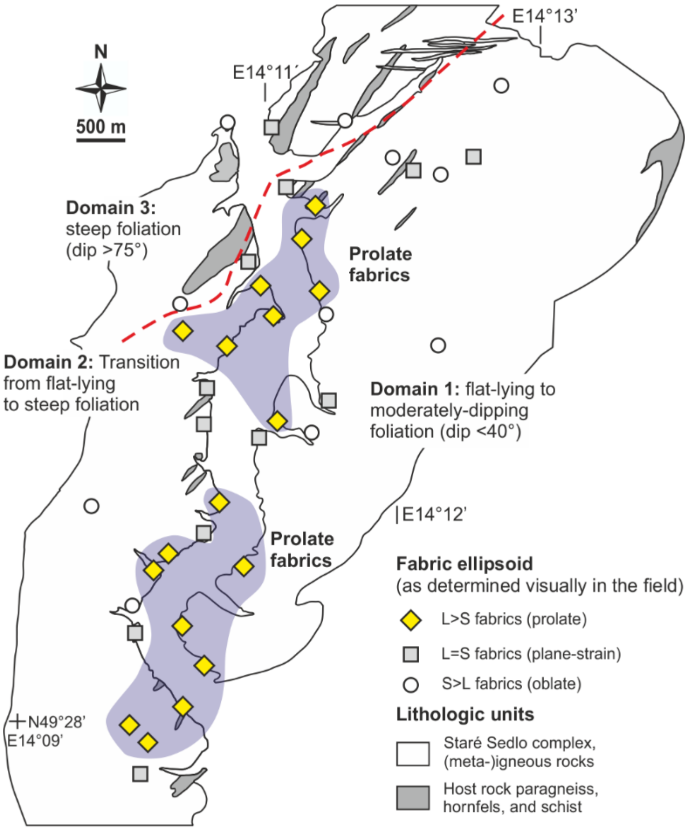

DEFORMATION MICROSTRUCTURES

For a microstructural study, 26 oriented samples were collected on 22 stations in the Staré Sedlo complex and examined in the lineation-parallel and foliation-perpendicular section. The granitoids reveal three distinct stages in their microstructural evolution.

(1) The low-strain domains preserve abundant roughly subhedral plagioclase (oligoclase to andesine) phenocrysts up to ~3 mm in size exhibiting oscillatory and normal zoning and rare, up to 0.5 mm large grains of K-feldspar with twin lamellae (Fig. 8a). These features are relics of magmatic crystallization (e.g., Allègre et al., 1981; Shore and Fowler, 1996; Vernon, 1983, 2000) whereas the interstitial quartz has been largely recrystallized (Fig. 8a–e).

(2) The subsequent stage in the microstructural evolution of the granitoids is characterized by solid-state ductile deformation leading to the development of penetrative foliation, mineral lineation, and dynamic recrystallization of the main rock-forming minerals. The plagioclase grains exhibit core-and-mantle microstructure (Fig. 8b; e.g., Passchier and Trouw, 2005; White, 1976, 1977). The newly recrystallized outer grains have been rotated and stretched parallel to foliation

whereas the cores are frequently at an angle to foliation (Fig. 8b). Plagioclase is largely sericitized along foliation-perpendicular microfractures (Fig. 8a, e). Potassium-feldspar exhibits similar deformation microstructures. Quartz grains show undulatory extinction and a chessboard pattern (Fig. 8c; e.g., Kruhl, 1996). The recrystallization also resulted in the development of subgrains and reorientation of aggregates parallel to foliation (Fig. 8c, d). Some quartz aggregates also display highly irregular, sutured grain boundaries (Fig. 8d). Biotite grains have been completely recrystallized, stretched, and merged into thin folia parallel to foliation and alternating with

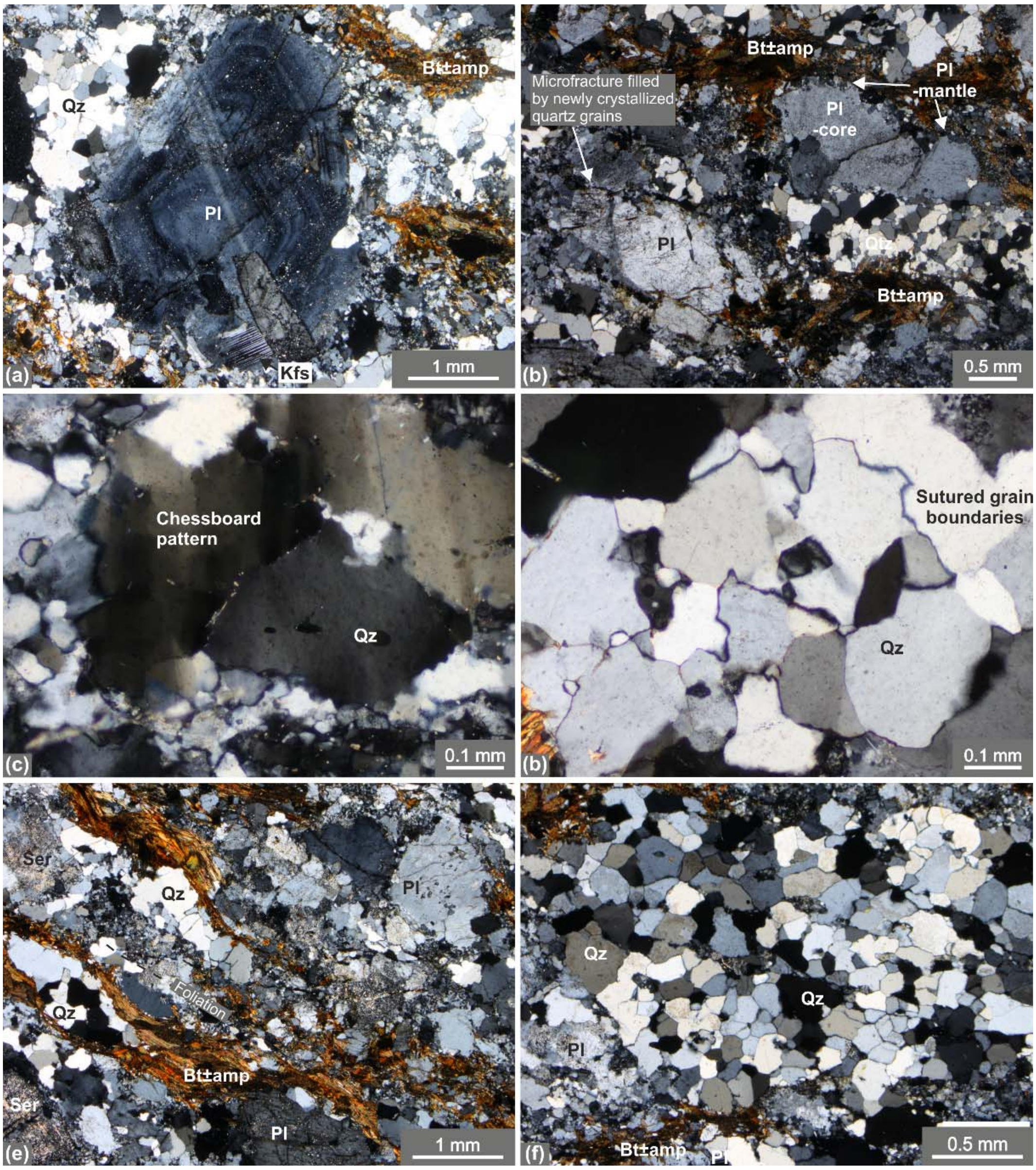

Fig. 8. Deformational microstructures in granitoids of the Staré Sedlo complex (all photomicrographs in crossed polars). (a) Oscillatory zoning in relic magmatic plagioclase. WGS84 coordinates: N49.49921091°, E14.18375077°. (b) Core-and-mantle structure of plagioclase. Note the microfractures filled by newly crystallized quartz grains. WGS84 coordinates: N49.49921091°, E14.18375077°. (c) Chessboard pattern in quartz. WGS84 coordinates: N49.48714457°, E14.18030304°. (d) Sutured grain boundaries in quartz. WGS84 coordinates: N49.51100°, E14.17865°. (e) Solid-state foliation (dashed line) defined by alignment of rotated quartz and feldspar grains/subgrains into bands parallel with thinner folia of recrystallized amphibole and biotite. WGS84 coordinates: N49.51100°, E14.17865°. (f) Large polygonal quartz aggregates. WGS84 coordinates: N49.46913°, E14.17070°. Mineral abbreviations after Whitney and Evans (2010): Amp – amphibole, Bt – biotite, Kfs – K-feldspar, Pl – plagioclase, Ser – sericite, Qz – quartz.

recrystallized quartz and feldspar aggregate bands. Biotite is commonly replaced by a mixture of chlorite and titanite. Together with biotite, recrystallized amphibole constitutes the thin foliation-parallel folia which may in some cases wrap around the feldspar and quartz porphyroclasts (Fig. 8e). Amphibole grains are progressively replaced by biotite, epidote, and/or chlorite with magnetite and ilmenite.

At this stage, the fabric is thus characterized by shape-preferred orientation of elongated recrystallized grains and by thin biotite–amphibole folia alternating with wider bands of feldspar and quartz aggregates (Fig. 8b, e). Micro-scale asymmetric structures have not been observed.

(3) The final stage of granitoid evolution is best documented in quartz aggregates growing on older foliation and consisting of large polygonal grains up to 0.5 mm in size (Fig. 8f). The polygonal grains exhibit neither undulatory extinction nor shape-preferred orientation and their boundaries are straight and in many cases at a high angle to the foliation (Fig. 8f). The microfractures in the recrystallized plagioclase grains are also filled by small (<1 μm in size) polygonal quartz grains (Fig. 8b).

ANISOTROPY OF MAGNETIC SUSCEPTIBILITY (AMS)

A total of 38 oriented cores were sampled using a hand-held gasoline-powered drill at 13 stations in the Staré Sedlo complex. These cores yielded 125 standard cylinder-shaped specimens (approximately 10 cm^3 in volume). The AMS was measured with a MFK1-A Kappabridge in the Laboratory of Rock Magnetism, Institute of Geology and Paleontology, Charles University in Prague. A statistical analysis of the data was performed using the ANISOFT software (www.agico.com). The measured data and parameters are presented in Figs. 9–13 and listed in full in the Appendix item 5/1.

The AMS tensor is represented by an ellipsoid with the principal susceptibility axes $k_1 \geq k_2 \geq k_3$ where the maximum principal susceptibility (k_1) represents magnetic lineation and the minimum principal susceptibility (k_3) indicates the pole to magnetic foliation. The AMS can be further characterized by several parameters (Hrouda, 1982; Tarling and Hrouda, 1993). We use (1) the bulk (mean) susceptibility $(k_m = (k_1 + k_2 + k_3)/3)$ which reflects the type and volume fraction of magnetic minerals, (2) the degree of anisotropy $(P = k_1/k_3)$ which indicates the eccentricity of the AMS ellipsoid and may be thus related to the intensity of the shape-preferred orientation of magnetic minerals (Nagata, 1962), and (3) the shape parameter $(T = 2\ln(k_2/k_3)/\ln(k_1/k_3) - 1)$ which describes shape of the AMS ellipsoid. For $-1 \leq T < 0$ the ellipsoid is prolate, for $T = 0$ triaxial, and for $1 \geq T > 0$ oblate (Jelínek, 1981).

Magnetic mineralogy

The bulk (mean) susceptibility of the granitoids spans four orders of magnitude from 10^{-5} to 10^{-2} (Figs. 10a, 11a and Appendix item 5/1; SI units are used throughout this paper). In order to better constrain the carriers of the AMS, magnetic susceptibility of five representative powdered specimens (Fig. 9) was measured as a function of temperature using an Agico MFK1-FA Kappabridge connected to a CS4 temperature control unit. Complete thermomagnetic curves from −196 °C to 700 °C and back were obtained in three steps. First, samples were cooled down to the temperature of liquid nitrogen (ca. −196 °C) and heated to the room temperature (ca. 20 °C), magnetic susceptibility was measured approximately every minute. Second, samples were heated up in argon atmosphere (to minimize mineral changes due to oxidation) from the room temperature to 700 °C and cooled back at an approximate rate of 14 °C/min. Third, the previously heated samples were cooled down to the temperature of liquid nitrogen and heated to the room temperature.

The thermomagnetic curves of the low-susceptibility specimens (k_m < *10–4*; FT105/2/1 and FT53/1/2) show a nearly hyperbolic decrease in susceptibility from the temperature of liquid nitrogen up to ~400 °C (Fig. 9a). This feature is characteristic of paramagnetic minerals where magnetic susceptibility is inversely proportional to the absolute temperature according to the Curie–Weiss law. The susceptibility increase observed above 400 °C and also further increase on the cooling curves (Fig. 9a) can be attributed to the growth of new magnetite as a result of alteration of Fe-bearing mineral phases with increasing temperature.

The newly-grown magnetite is indicated by the Curie temperature on the heating curves (an abrupt susceptibility drop at ~580 °C) and by the Verwey transition in the end of the cooling curves (a slight susceptibility decrease at –170 °C; Fig. 9a).

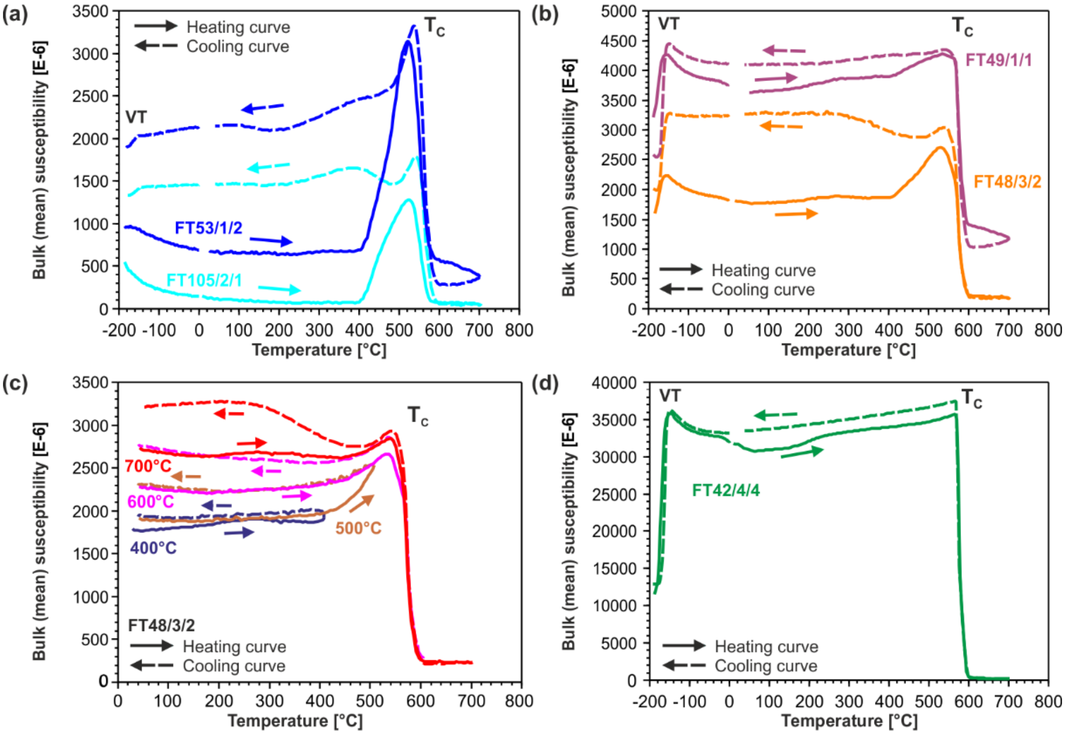

Fig. 9. Magnetic susceptibility as a function of temperature for (a) low-, (b) intermediate-, and (c) high-susceptibility specimens. VT – Verwey transition, Tc – Curie temperature.

Magnetic mineralogy of the moderate-susceptibility specimens ($10–3 \le k_m < 10–2$; FT48/3/2 and FT49/1/1) is controlled both by paramagnetic minerals, detected by the nearly hyperbolic decrease in susceptibility, and by magnetite as demonstrated by the Verwey transition in the beginning of the heating curves (Fig. 9b). Further increase in temperature induces alterations in magnetic mineralogy as reflected by the susceptibility increase above ca. 400 °C. A repeated heating experiment (FT48/3/2, Fig. 9c) shows that the susceptibility increase is gradual; each subsequent heating curve follows, in its initial part, the course of the previous cooling curve. The last heating/cooling cycle shows a slight susceptibility increase just below the Curie temperature which may be attributed to the Hopkinson effect. The newly-grown magnetite is evidenced by the Curie temperature on the heating curves and by the pronounced Verwey transition in the end of the cooling curves (Fig. 9b; specimen FT48/3/2). The cooling curve does not follow the course of the heating curve implying that additional growth of magnetite occurred above the Curie temperature. In a specimen with a slightly higher susceptibility (FT49/1/1), the cooling curve follows more or less the same course as the heating curve, implying no mineral changes during the experiment (Fig. 9b).

Magnetic mineralogy of the highest-susceptibility specimen ($k_m \ge 10^{-2}$; FT42/4/4) is controlled solely by pure magnetite, proved by a Verwey transition on both heating and cooling curves and by the Curie temperature of pure magnetite on the heating curves. Both heating and cooling curves follow almost the same course implying that no magnetite grew during the experiment (Fig. 9d).

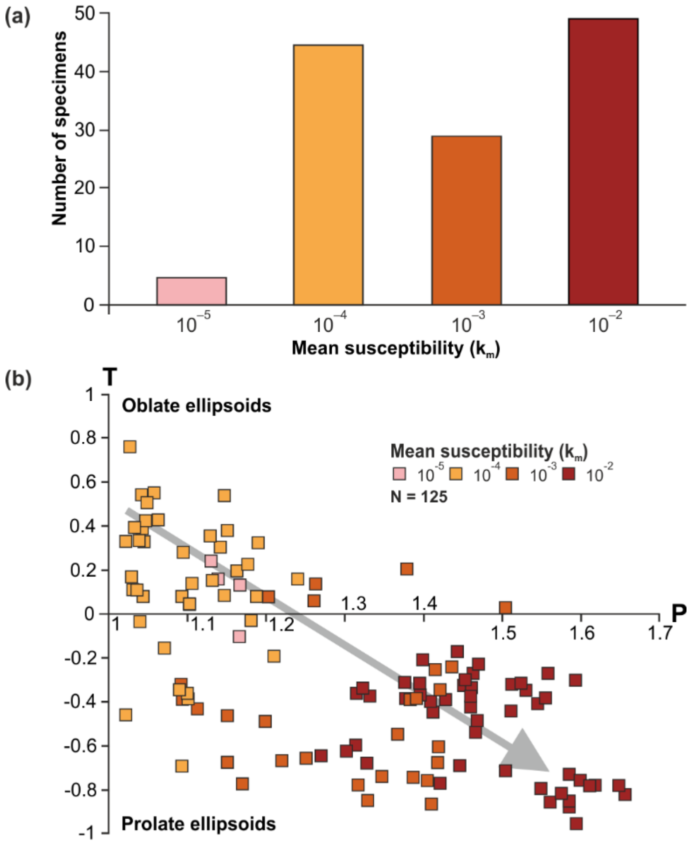

Fig. 10. (a) Histogram of the bulk (mean) susceptibilities of all measured AMS specimens of the Staré Sedlo complex. (b) Magnetic anisotropy P–T plot summarizing all data from the Staré Sedlo complex.

Magnetic fabric parameters and orientation

The degree of anisotropy ranges from 1.022 to 1.656, with two peaks around 1.075 and 1.450 (Fig. 10b). The shape parameter ranges from −0.953 to 0.759, 65 % of specimens indicate prolate fabrics (Fig. 10b). In the P–T plot, the data exhibit a clear trend from weakly anisotropic oblate specimens with low bulk susceptibilities (10^{-5} to 10^{-4}) to strongly anisotropic prolate specimens with bulk susceptibilities as high as 10–2 (Fig. 10b). This is consistent with the spatial pattern of site-averaged k_m, P, and T parameters (Fig. 11), where the center of the Staré Sedlo complex is characterized by high bulk susceptibilities, prolate AMS ellipsoids, and high degree of anisotropy.

Orientation of the principal susceptibilities is rather homogeneous and corresponds well to the mesoscopic foliation and lineation (Fig. 7a, b). Magnetic foliations are subhorizontal (Figs. 12, 13a) and the associated magnetic lineations plunge shallowly to the ~NE or ~SW (Figs. 12, 13b). The exceptions from this uniform orientation distribution and mesoscopic/magnetic fabric relationships are stations FT14 and FT11. On station FT14, mesoscopic foliation dips gently to the ~SE whereas magnetic foliations dip steeply to the ~NW. Magnetic and mesoscopic (mineral) lineations are here roughly of the same orientation, plunging shallowly with opposite trends (Figs. 6b, 12, 13b). Station FT11 is in the fabric transition zone (Domain 2; Figs. 6, 12, 13) and exhibits steep magnetic foliation and subhorizontal ~WNW–ESE magnetic lineation.

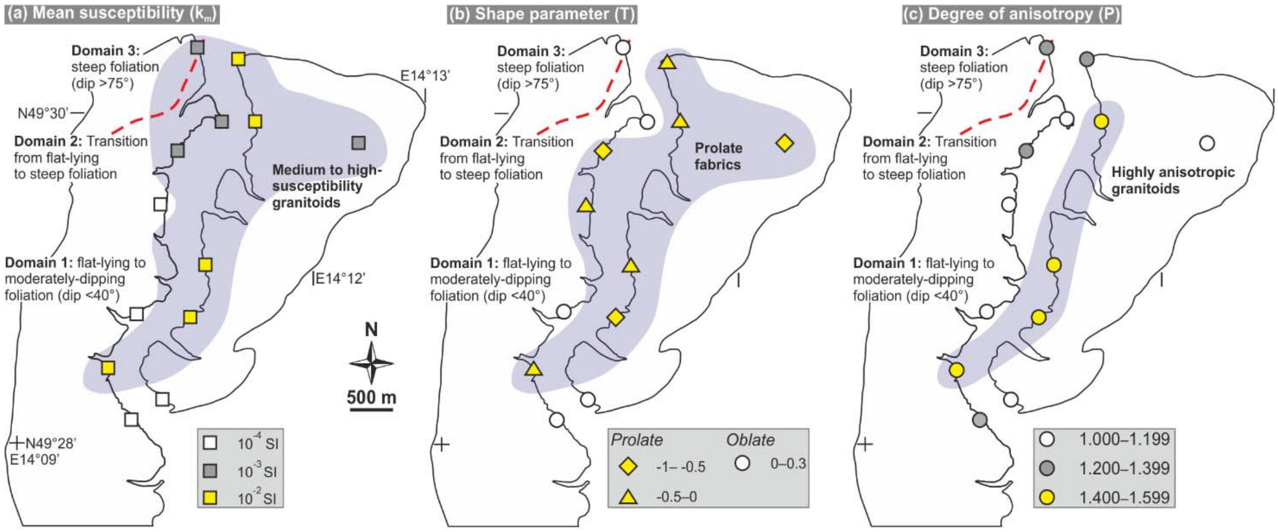

Fig. 9. Magnetic susceptibility as a function of temperature for (a) low-, (b) intermediate-, and (c) high-susceptibility specimens. VT – Verwey transition, Tc – Curie temperature.

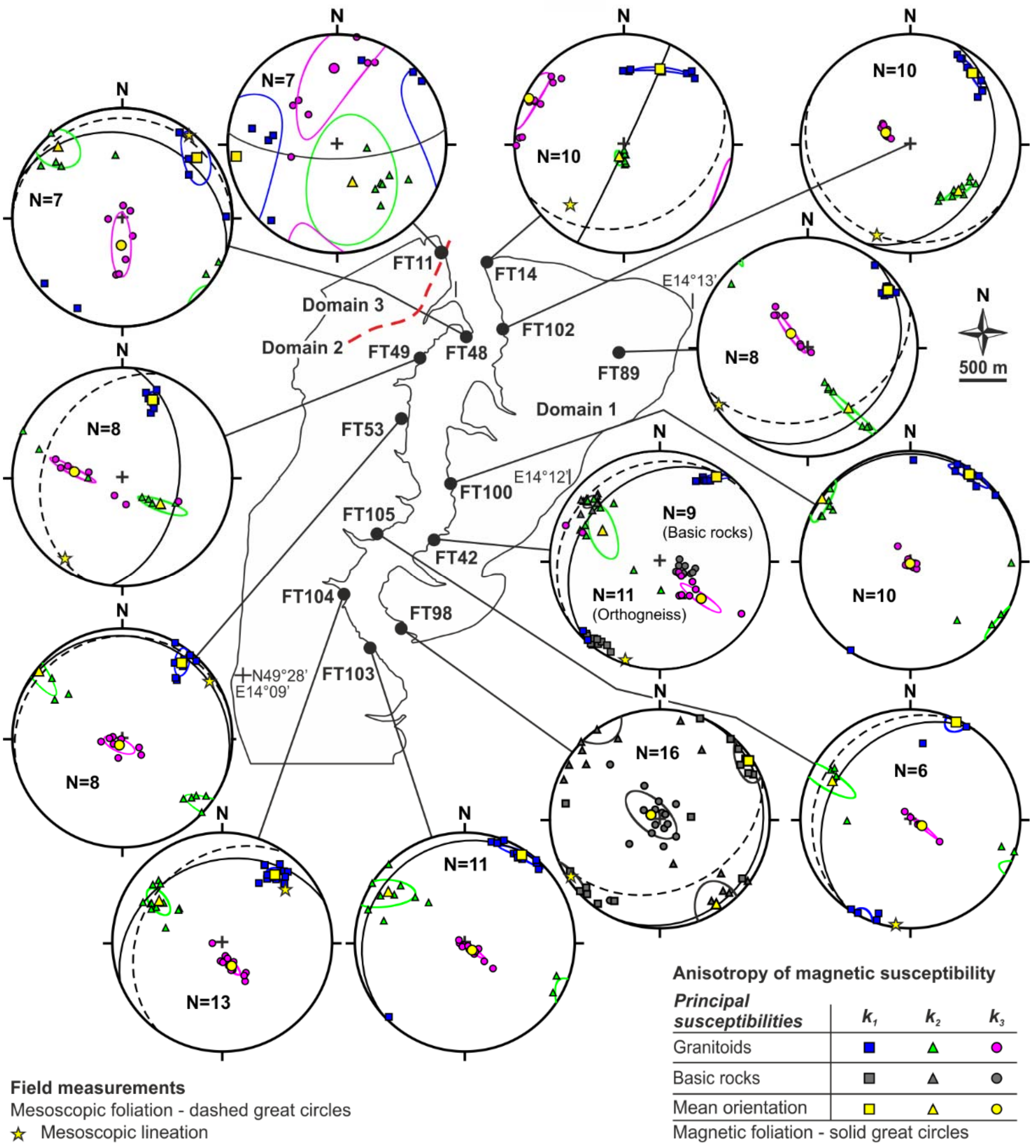

Fig. 12. Map showing orientation of the principal susceptibilities in the south-central portion of the Staré Sedlo complex.

DISCUSSION

Emplacement of the Staré Sedlo complex

In the southern portion of the Staré Sedlo complex, the deformed granitoids occur as subhorizontal sheets parallel to bedding or to foliation in the metasedimentary septa (Figs. 2, 3a–d). This suggests that, at least in part, the complex was assembled as a sheeted pluton consisting of a series of sills, in which the granitoid magma was driven into pre-existing subhorizontal anisotropy of the host rock during vertical shortening. In detail, the tapered sill tips (Fig. 3c, d) suggest magma wedging (e.g., Hutton, 1992; Ingram and Hutton, 1994; Miller and Paterson, 2001; Weinberg, 1999) along bedding or foliation planes in the host rock as the main emplacement mechanism. Furthermore, hotter magmas of gabbroic to dioritic composition intruded simultaneously the granitoid sill interiors to form synplutonic sheets, concordant with, or slightly oblique to, the sill margins, and were frequently disintegrated into microgranular enclaves (Fig. 4a–e).

From a mechanical point of view, the presumed magma wedging mechanism during vertical shortening requires that the magma was overpressurized so its pressure (p_m) exceeded the lithostatic load (P_L), vertical tectonic stress (σ_1), and the tensile strength of the rock along its mechanical anisotropy (T_A; e.g., Hutton, 1992; Price and Cosgrove, 1990; Vigneresse et al., 1999). We propose that this type of syntectonic magma emplacement likely occurred in three stages (Fig. 14).

First, it is inferred that stress must have been concentrated at crack tips to facilitate propagation of overpressurized magma along host rock foliation planes (Fig. 14a–c; e.g., Clemens and Mawer, 1992; Jin and Johnson, 2008; Kavanagh et al., 2006; Menand, 2008; Rubin, 1995; Takada, 1989). In the Staré Sedlo complex, two distinct intrusive styles were observed differing in the sill thickness and volumetric proportion of magma and host rock: pervasive lit-par-lit melt injection of thin ~1–2 cm thick veins (Fig. 3b, c) and intrusion of decimeters to several meters thick sills (Fig. 2a, c). We suggest that these two styles may have been controlled by one of the three main parameters, or their combination: different volumes of magma additions, variable magma driving pressure, and variable viscosities of intruding magma (e.g., Wada, 1994). Especially the latter seems to explain well our field observations: we envision that the low-viscosity, mobile magmas percolated along foliation planes (Fig. 14b) whereas high-viscosity magmas produced more localized and thicker sills (Fig. 14c). The presumed viscosity fluctuations could be attributed to variable content of volatiles (e.g., Baker, 1998), compatible with little variations in the bulk magma compositions (tonalitic to granodioritic; Košler, 1993; Košler and Farrow, 1994). Despite the active

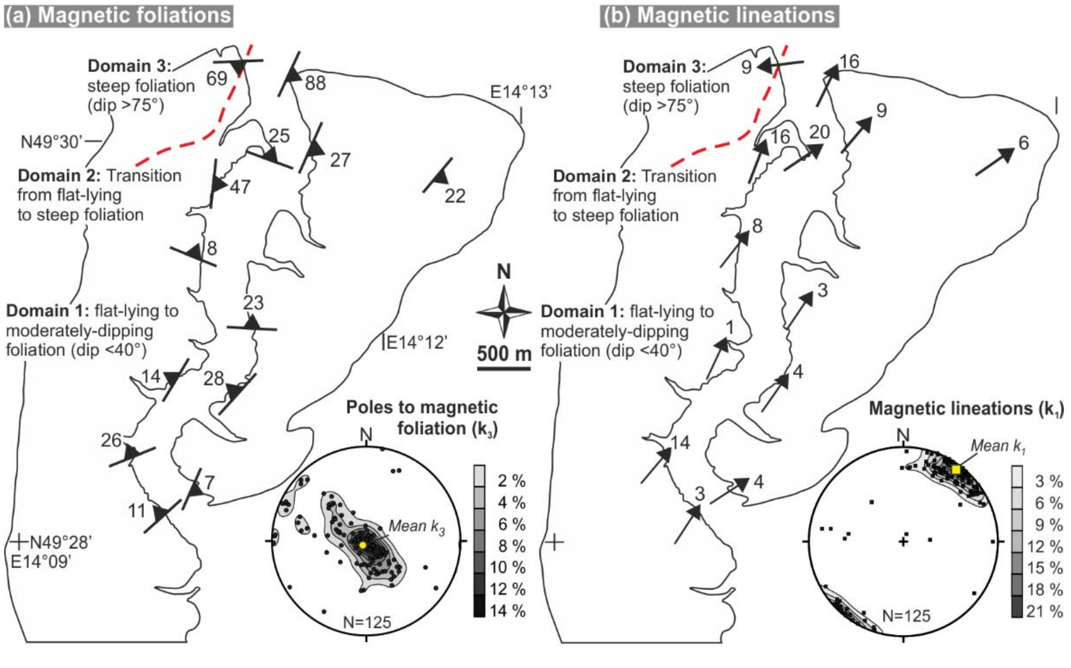

Fig. 13. Map of magnetic foliations (a) and magnetic lineations (b) in the south-central portion of the Staré Sedlo complex. Stereonets (equal area, projection on the lower hemisphere) show orientation of the maximum (k_1) and minimum (k_3) principal susceptibilities including mean values (yellow symbols).

vertical tectonic shortening, this initial stage must have led to a transient vertical expansion of the magma/host rock system (Fig. 14b, c).

The second stage is magma flow through already established planar conduits but still during vertical shortening (Fig. 14d). In general, if the pressure of the flowing magma was steady and compensated both the additive lithostatic load (P_L) and vertical tectonic stress (σ_1) to produce sills of constant thickness, the variable sill/host rock ratio may reflect the three factors discussed above (Fig. 14d).

Finally, the cessation of magma flow and drop in the magma overpressure, which now becomes overridden by lithostatic load and vertical tectonic stress, will give way to a vertical collapse of the whole magma/host rock system (Fig. 14e). This case would result either in homogeneous or localized thinning of the sills, the latter possibly reflecting lateral variations in viscosity contrasts between magma and host rock (Fig. 14e). The third stage is well documented in the Staré Sedlo complex where the sheets underwent vertical shortening during and after cooling below the solidus temperature as evidenced by boudinage and the pervasive magmatic to solid state fabrics (Figs. 4d–f, 5, 6a, c, 8a–e, 13a). In general, this late-stage deformation is strongly controlled by the evolving viscosity contrasts and strain partitioning between the cooling magma and heated host rock (e.g., Pavlis, 1996; Teyssier and Tikoff, 1999).

In three-dimensions, the presumed vertical collapse of magma in the sills will largely depend on the direction in which the low-viscosity magma could flow/stretch in the horizontal plane as magma may spread either in one or all directions. Theoretically, the former case would result in plane strain or constriction, if the sills were subjected to simultaneous horizontal shortening or have initial tube-like shapes, whereas the latter case would produce flattening type strain in the magma. It is difficult to evaluate these two possible cases in the Staré Sedlo complex despite the constrictional type seems more likely as suggested by the widespread prolate fabrics. However, it should be noted that the three-dimensional pre- and post-collapse shapes of the sills are difficult to establish and the prolate fabrics, as detailed below, are interpreted as resulting from regional tectonic deformation.

The significance of magmatic to solid state fabrics in the Staré Sedlo complex

We have shown that magma intrusion along the subhorizontal foliation planes implies that the metasedimentary host rock experienced significant pre-emplacement vertical shortening and that the whole complex, except for low strain domains (e.g., Fig. 4c, d), underwent pervasive magmatic to solid state overprint. This interpretation is documented by mesoscopic fabric and microstructures indicating progressive down-temperature deformation from a magmatic stage (Fig. 8a) through high-temperature solid state down to the greenschist facies conditions (Fig. 8b–e). Above all, core-and-mantle microstructures (Fig. 8b), chessboard patterns (Fig. 8c), and sutured grain boundaries (Fig. 8d) point to dynamic recrystallization, subgrain rotation and grain-boundary migration, respectively, under decreasing temperature (e.g., Hirth and Tullis, 1992; Jessell, 1987; Knipe and Law, 1987; Kruhl, 1996; Passchier and Trouw, 2005; Urai et al., 1986; White, 1976, 1977).

A late reheating of the northern part of the Staré Sedlo complex by younger plutons (Fig. 1b, c) caused significant static recrystallization of the previously dynamically recrystallized quartz and plagioclase aggregates. This process led to rearranging grain boundaries and an increase in the grain size through grain boundary area reduction (Fig. 8f; e.g., Bons and Urai, 1992; Passchier and Trouw, 2005).

Our detailed fabric and AMS analysis provides further details on the nature of the post-emplacement deformation of the Staré Sedlo complex. It is important to note that our interpretations concern only its south-central portion, excluding the near-contact zone with the younger plutons where the flat-lying sills have likely been reoriented into a steep attitude (Fig. 6a–c; AMS stations FT11 and FT14 in Figs. 12, 13). This reorientation is interpreted as a result of syn-tectonic emplacement of the ~346 Ma Kozárovice granodiorite (foliation in the Staré Sedlo complex is concordant with that of in the granodiorite) and thus is not dealt with in this paper (see Žák et al., 2005a, 2009 for details).

On the basis of the structural and AMS data, the subhorizontal fabric of the Staré Sedlo complex could be interpreted as recording a variable combination of vertical shortening with horizontal ~NE–SW stretching. However, prolate fabrics, corroborated by the AMS (Figs. 10b, 11b),

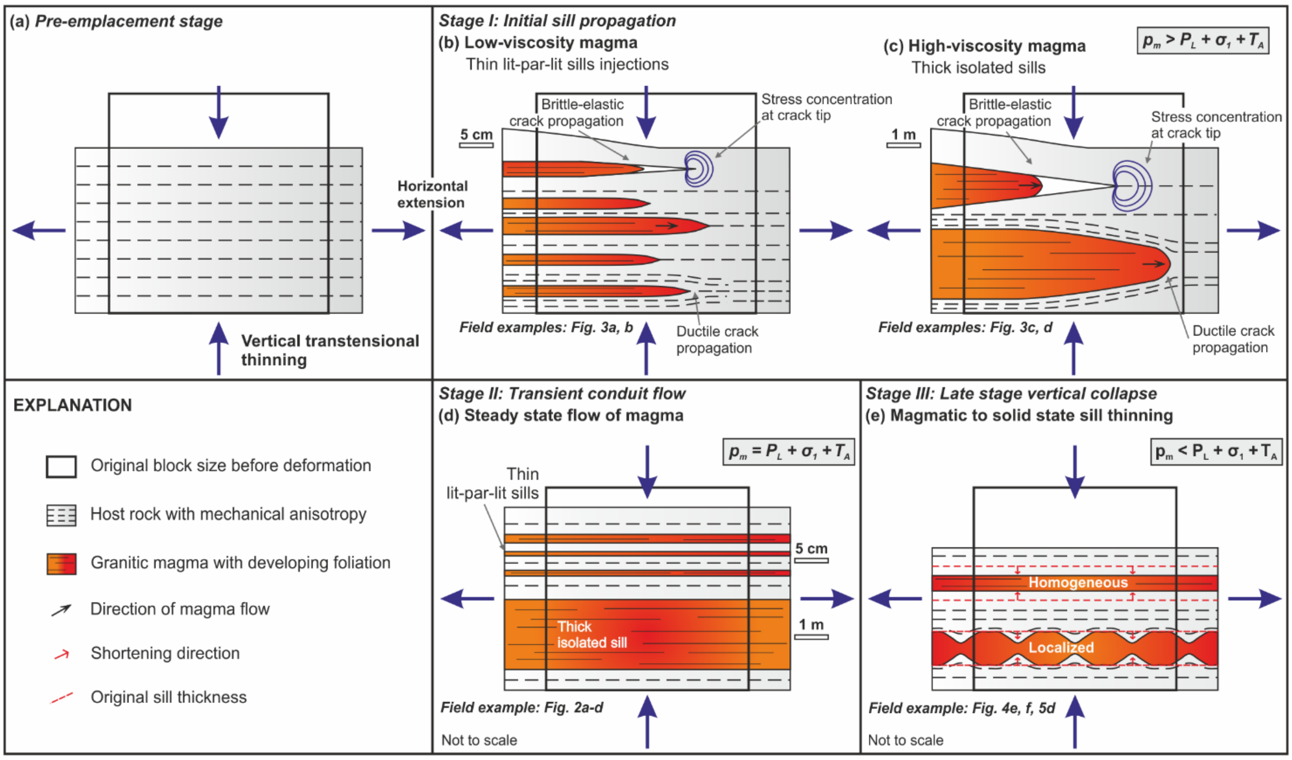

Fig. 14. Proposed two-dimensional model (shown in a vertical plane) of initial sill propagation, emplacement, and deformation in the horizontally foliated host rock. The bold rectangle indicates host rock before transtensional deformation. Panels b and c based on Wada (1994) and Clemens and Mawer (1992). See text (section 7.1.) for discussion.

are found on most outcrops (Fig. 7) implying that horizontal constriction was the dominant strain regime. The local deviations from the prolate fabric can be interpreted in terms of heterogeneous deformation where vertical shortening contributed to horizontal stretching (e.g., Fossen et al., 1994). Another complexity is the mineralogical control (perhaps due to primary compositional variations) on the AMS, in addition to strain regime. Stations with low bulk susceptibility and paramagnetic lithologies exhibit weakly oblate AMS ellipsoids (Fig. 11), thus the magnetic fabric may be interpreted as being dominated by oblate magnetocrystalline anisotropy of biotite (e.g., Martín-Hernández and Hirt, 2003; Zapletal, 1990). The 'true' strain in these cases may be, however, shifted towards the plane-strain type as these rocks are typically LS tectonites. The exception is station FT53 with weakly prolate fabric (but clustered distribution of the principal susceptibilities; Fig. 12) which may represent a biotite zone axis parallel to the principal stretching direction (Henry, 1997). On the other hand, magnetic fabric on stations with high bulk susceptibility and prolate ellipsoids (Fig. 11) may reflect the prolate shape-anisotropy (e.g., Mamtani et al., 2011) or linear distribution anisotropy of magnetite (Hargarves et al., 1991) and may thus better reflect the inferred constrictional strain regime.

The prolate fabrics are at variance with vertical collapse (ductile thinning) of the crust as a plausible explanation for it would lead to a predominantly flattening to plane-strain fabric ellipsoid. Thus considering prolate strains only, they may form (1) in specific transpression zones (e.g., Dias and Ribeiro, 1994; Fossen and Tikoff, 1998), (2) by superposition of horizontal onto vertical foliation (e.g., Kratinová et al., 2010; Schulmann and Ježek, 2011; Sullivan, 2013), and (3) in transtension zones (e.g., Dewey, 2002 and references therein). We can exclude the first two cases for the following reasons. First, foliations, if developed, are subhorizontal in the southern Staré Sedlo complex and thus they cannot record transpression which is by definition associated with horizontal shortening of the deforming zone and thus vertical foliation (e.g., Sanderson and Marchini, 1984; Teyssier and Tikoff, 1999). Second, we documented only a single phase of ductile deformation associated with the prolate fabrics and no earlier vertical foliation was found in the complex. Hence, we argue that the observed fabric parameters strengthen the case for 'true' constrictional strain and are compatible only with transtensional setting during emplacement of the Staré Sedlo complex. When compared with theoretical models, our fabric data indicate sinistral pure shear dominated transtension as there is no evidence for anomalously high finite strains in the Staré Sedlo complex, required to produce horizontal foliation during wrench dominated transtension (Dewey et al., 1998; Dewey, 2002; Fossen and Tikoff, 1998; McCoss, 1986; Teyssier and Tikoff, 1999; Tikoff and Fossen, 1993; Tikoff and Teyssier, 1994).

Implications for early Variscan orogenic deformation in the Bohemian Massif

Košler et al. (1995) interpreted the Staré Sedlo complex as emplaced along a flat of a major listric thrust zone, recording Late Devonian SE-directed thrusting of the upper-crustal Teplá–

Barrandian unit onto a high-grade core of the orogen as represented by the Moldanubian unit (Fig. 1a). The inferences developed above challenge this interpretation and point to a transtensional regime with an orogen-parallel, ~NE–SW principal stretching direction. The question thus arises of how to explain the inferred transtensional deformation in the interior of the Variscan orogen during early stages of its development in an overall compressional setting, which was governed by the Late Devonian to early Carboniferous convergence of the Saxothuringan, Teplá–Barrandian, and Moldanubian units (e.g., see Hajná et al., 2012; Schulmann et al., 2009; and Zulauf, 1997 for details).

Given that the Staré Sedlo complex is engulfed in voluminous ~20 M.y. younger granitoids (Fig. 1b, c), we are left with large uncertainties regarding the original boundaries, orientation, and regional extent and significance of the inferred Late Devonian transtensional zone. Similarly, the structural data presented in this paper do not provide a definitive answer to the question raised in Section 2 (and neither do the published geochemistry and geochronology), i.e., which subduction zone is the Staré Sedlo complex linked to. Below we thus evaluate three hypotheses which could explain this enigmatic transtensional event, taking into account only what has been well established: first, that the Teplá–Barrandian unit is the upper plate for all the hypothetic subduction zones and, second, that it has a wedge shape in an orogen-perpendicular section (Figs. 1b, 15). The hypotheses are discussed from the least to the most likely in light of the available structural and geochronologic data.

One of the possible explanations could be slab roll-back generating extension/transtension in the back-arc region (e.g., Collins, 2002; Jolivet et al., 2003). However, no evidence has been found as yet to prove that this process operated either during the SE-directed subduction/underthrusting of the Saxothuringian Ocean and passive margin or during the hypothetic NW-directed subduction of the Moldanubian (Gföhl) Ocean beneath the Teplá–Barrandian unit (Figs. 1b, 15).

Alternatively, the transtensional deformation could have been generated in a local releasing bend in a major strike-slip shear zone. Indeed, both dextral (e.g., Matte et al., 1990; Rajlich, 1987) and sinistral (e.g., Pitra et al., 1999) strike-slip movements were invoked to explain juxtaposition of the Teplá–Barrandian against the Moldanubian units. However, the existince of such a large-scale, thoroughgoing strike-slip shear zone during Late Devonian has recently been questioned (e.g., Žák et al., 2009) and is not well supported by structural and kinematic data.

Last, numerous studies documented that the Teplá–Barrandian unit underwent overall thickening with a component of dextral shear during the Late Devonian times (e.g., Hajná et al., 2012; Zulauf, 1997, 2001 and references therein). It should be emphasized that the upper crust also recorded significant orogen-parallel horizontal extension, which lasted from Late Devonian (~380–370 Ma; Hajná et al., 2012; this study) till the Early Carboniferous (~346 Ma; Žák et al., 2005a, 2005b, 2009). Hence, the response of the Teplá–Barrandian upper crust to the plate convergence involved a complex three-dimensional deformation further complicated by strain partitioning (Fig. 15). To account for simultaneous sinistral transtensional deformation in the orogen's interior at around 380–365 Ma, we suggest that the Teplá–Barrandian unit represented an orogenic wedge which was thrust to the WNW to NW over the Saxothuringian unit but was also extruded southward while the rear portion of the wedge recorded sinistral transtension (Fig. 15). Such syn-convergent extrusion wedges with thrust faults on their pro-side and normal faults on their retro-side have been postulated as accommodating exhumation of (U)HP rocks also in other convergent orogens (e.g., Platt, 1993; Ring et al., 2007; Ring and Glodny, 2010; Seyferth and Henk, 2004). Compared to these models, which mostly consider displacement only along a vertical plane perpendicular to the subduction zone, we argue for a significant component of orogen-parallel stretching during plate convergence. The latter could account for the limited amount of vertical exhumation and thus generally only supracrustal rocks being exposed at the present-day erosion level of the Teplá–Barrandian unit (Fig. 15).

During early Carboniferous, the Teplá–Barrandian/Moldanubian boundary was intruded by voluminous early Carboniferous (~354–337 Ma) arc plutons of the Central Bohemian Plutonic Complex (Fig. 1b, c), which largely obliterated the early sinistral transtension stage. These plutons recorded ~WNW–ESE horizontal shortening and dextral transpression from at least ~354 Ma to ~346 Ma, with roughly same principal stretching direction as that of recorded in the Staré Sedlo complex, and then vertical collapse of the whole Teplá–Barrandian and exhumation of the high-grade Moldanubian unit from ~346 to ~337 Ma (Dörr and Zulauf, 2010; Žák et al., 2005a, 2005b, 2009, 2012). In summary, the newly recognized and defined transtensional deformation event extends our knowledge of evolution of the Teplá–Barrandian/Moldanubian boundary, an important tectonic element of the European Variscides, to Late Devonian times, i.e., towards the early development of the orogen.

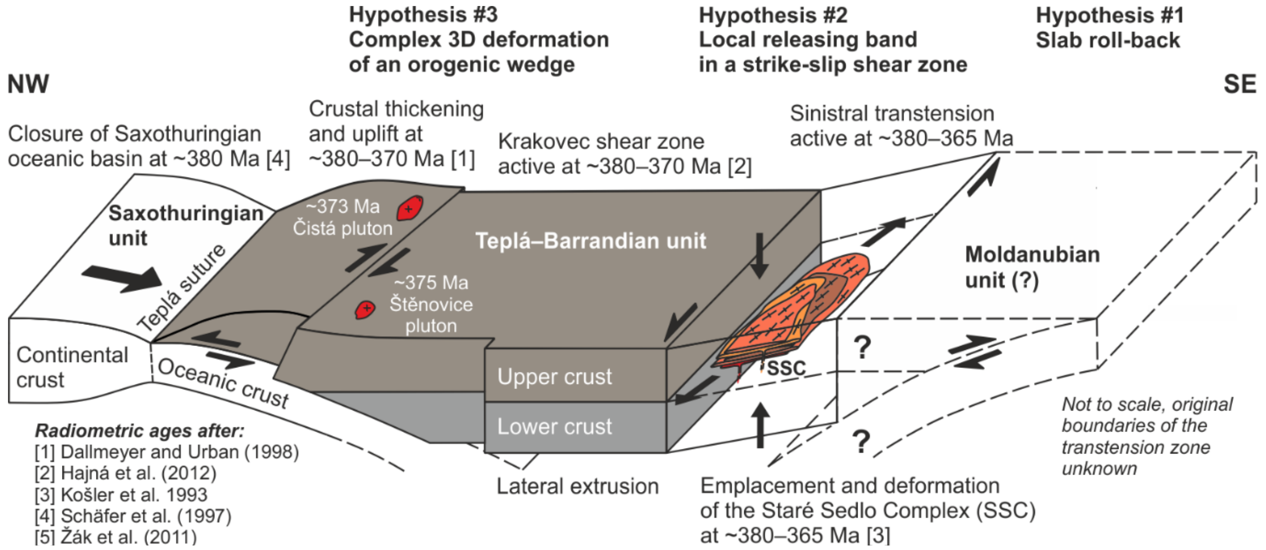

Fig. 15. Interpretive block-diagram illustrating three possible hypotheses for transtensional emplacement of the Late Devonian Staré Sedlo sill complex in the rear side of the extrusion upper-crustal wedge as represented by the Teplá–Barrandian unit (present-day coordinates). See text (section 7.3.) for discussion. References: (1) Dallmeyer and Urban (1998), (2) Hajná et al. (2012), (3) Košler et al. (1993), (4) Schäfer et al. (1997), (5) Žák et al. (2011).

CONCLUSIONS

Granitoids of the Late Devonian Staré Sedlo complex were emplaced as a subhorizontal sheeted sill pluton into an active transtension zone. The intrusive contacts against the metapelitic host rocks indicate that magma wedging was the dominant process of sill propagation along subhorizontal foliation planes. The sills exhibit two end-member styles of thickness and frequency, ranging from thin interconnected lit-par-lit injections to spaced meter-thick sills, interpreted to reflect variations in magma viscosity caused by the variable volatile contents. We have also shown that the magma/host rock system in transtension evolves from initial crack tip propagation and vertical expansion due to new magma additions through conduit flow to final vertical collapse after the magma input ceased. Finally, the sill emplacement and subsequent deformation of the granitoids are interpreted as recording syn-convergent, early-orogenic sinistral transtension along the rear side of an upward and laterally extruded upper-crustal wedge as represented by the Teplá–Barrandian unit. This previously unrecognized tectonic event sheds some new light on the protracted kinematic evolution of a boundary between the upper crust and exhumed mid- to lower crustal rocks in the Bohemian Massif.

ACKNOWLEDGEMENTS

We thank Bernard Henry, Alexander R. Cruden, and an anonymous reviewer for their detailed and constructive reviews which helped to improve the manuscript significantly. We also thank Michel de Saint Blanquat, Jean-Luc Bouchez, and three other anonymous reviewers for reviews of earlier versions of the manuscript. František Hrouda, Marta Chlupáčová, František Holub, Kryštof Verner, Vladislav Babuška, Vojtěch Janoušek, and Václav Kachlík are thanked for valuable discussions. We acknowledge financial support from the Grant Agency of the Czech Republic through grants No. P210/12/1385 and P210/11/1168 (to Jiří Žák). This study is part of the Ph.D. research of Filip Tomek, supported by the Charles University projects PRVOUK P44 and SVV261203.

REFERENCES

Acosta, J., Uchupi, E., 1996. Transtensional tectonics along the south Scotia Ridge, Antarctica. Tectonophysics 267, 31–56.

Allègre, C.J., Provost, A., Jaupart, C., 1981. Oscillatory zoning: a pathological case of crystal growth. Nature 294, 223–228.

Altenberger, U., Oberhänsli, R., Stein, E., Moghni, M., 2001. Geochemistry, tectonic setting and geodynamic significance of late orogenic dikes in the Melibocus Massif, Bergsträsser Odenwald. Mineral. Petrol. 72, 209–228.

Andronicos, C.L., Chardon, D.H., Hollister, L.S., Gehrels, G.E., Woodsworth, G.J., 2003. Strain partitioning in an obliquely convergent orogen, plutonism, and synorogenic collapse: Coast Mountains Batholith, British Columbia, Canada. Tectonics 22, 1012, doi: 10.1029/2001TC001312, 2.

Aranguren, A., Larrea, F.J., Carracedo, M., Cuevas, J., Tubía, J.M., 1997. The Los Pedroches batholith (Southern Spain): polyphase interplay between shear zones in transtension and setting of granites, in: Bouchez, J.L., Hutton, D., Stephens, W.E. (Eds.), Granite: from segregation of melt to emplacement fabrics. Kluwer Academic Publishers, Netherlands, pp. 215–229.

Asch, K., 2003. The 1:5 million international geological map of Europe and adjacent areas: development and implementation of a GIS-enabled concept. Geologisches Jahrbuch, Sonderhefte, A3. E. Schweizerbart'sche Verlagsbuchhandlung, Stuttgart.

Babuška, V., Plomerová, J., 2013. Boundaries of mantle–lithosphere domains in the Bohemian Massif as extinct exhumation channels for high-pressure rocks. Gondwana Res. 23, 973–987.

Baines, A.G., Cheadle, M.J., Dick, H.J.B., Scheirer, A.H., John, B.E., Kusznir, N.J., Matsumoto, T., 2003. Mechanism for generating the anomalous uplift of oceanic core complexes: Atlantis Bank, southwest Indian Ridge. Geology 31, 1105–1108.

Baker, D.R., 1998. Granitic melt viscosity and dike formation. J. Struct. Geol. 20, 1395–1404.

Bolle, O., Diot, H., Liégeois, J.P., Auwera, J.V., 2010. The Farsund intrusion (SW Norway): a marker of late-Sveconorwegian (Grenvillian) tectonism emplaced along a newly defined major shear zone. J. Struct. Geol. 32, 1500–1518.

Bons, P.D., Urai, J.L., 1992. Syndeformational grain growth: microstructures and kinetics. J. Struct. Geol. 14, 1101–1109.

Brown, P.E., Ryan, P.D., Soper, N.J., Woodcock, N.H., 2008. The Newer Granite problem revisited: a transtensional origin for the Early Devonian Trans-Suture Suite. Geol. Mag. 145, 235–256.

Cháb, J., Stráník, Z., Eliáš, M., 2007. Geological map of the Czech Republic 1:500,000. Czech Geological Survey, Prague.

Chlupáč, I., 1989. Stratigraphy of the Sedlčany–Krásná Hora metamorphic "Islet" in Bohemia (Proterozoic? to Devonian). J. Min. Geol. 34, 1–15.

Chlupáč, I., Havlíček, V., Kříž, J., Kukal, Z., Štorch, P., 1998. Palaeozoic of the Barrandian (Cambrian to Devonian). Czech Geological Survey, Prague.

Clemens, J.D., Mawer, C.K., 1992. Granitic magma transport by fracture propagation. Tectonophysics 204, 339–360.

Collins, W.J., 2002. Hot orogens, tectonic switching, and creation of continental crust. Geology 30, 535–538.

Cook, J., Gordon, J.E., Evans, C.C., Marsh, D.M., 1964. A mechanism for the control of crack propagation in all-brittle systems. Proc. R. Soc. London. Ser. A. Math. Phys. Sci 282, 508–520.

Correa-Gomes, L.C., Souza Filho, C.R., Martins, C.J.F.N., Oliveira, E.P., 2001. Development of symmetrical and asymmetrical fabrics in sheet-like igneous bodies: the role of magma flow and wall-rock displacements in theoretical and natural cases. J. Struct. Geol. 23, 1415–1428.

Crawford, M.L., Klepeis, K.A., Gehrels, G., Isachsen, C., 1999. Batholith emplacement at mid-crustal levels and its exhumation within an obliquely convergent margin. Tectonophysics 312, 57–78.

Creixell, C., Parada, M.A., Roperch, P., Morata, D., Arriagada, C., De Arce, C.P., 2006. Syntectonic emplacement of the Middle Jurassic Concón Mafic Dike Swarm, Coastal Range, central Chile (33° S). Tectonophysics 425, 101–122.

Creixell, C., Parada, M.A., Morata, D., Vásquez, P., de Arce, C.P., Arriagada, C., 2011. Middle–Late Jurassic to Early Cretaceous transtension and transpression during arc building in Central Chile: evidence from mafic dike swarms. Andean Geol. 38, 37–63.

Dallmeyer, R.D., Urban, M., 1998. Variscan vs Cadomian tectonothermal activity in northwestern sectors of the Teplá–Barrandian zone, Czech Republic: constraints from 40Ar/39Ar ages. Geol. Rundsch. 87, 94–106.

Dewey, J.F., 2002. Transtension in arcs and orogens. Int. Geol. Rev. 44, 402–439.

Dewey, J.F., Holdsworth, R.E., Strachan, R.A., 1998. Transpression and transtension zones, in: Holdsworth, R.E., Strachan, R.A., Dewey, J.F. (Eds.), Continental transpressional and transtensional tectonics. Geol. Soc. London, Spec. Publ. 135, pp. 1–14.

Dias, R., Ribeiro, A., 1994. Constriction in a transpressive regime: an example in the Iberian branch of the Ibero-Armorican arc. J. Struct. Geol. 16, 1543–1554.

Dörr, W., Zulauf, G., 2010. Elevator tectonics and orogenic collapse of a Tibetan-style plateau in the European Variscides: the role of the Bohemian shear zone. Int. J. Earth Sci. 99, 299–325.

Faryad, S.W., Kachlík, V., Sláma, J., Hoinkes, G., 2015. Implication of corona formation in a metatroctolite to the granulite facies overprint of HP–UHP rocks in the Moldanubian

Zone (Bohemian Massif). J. Met. Geol., doi: 10.1111/jmg.12121.

Fossen, H., Tikoff, B., 1998. Extended models of transpression and transtension, and application to tectonic settings, in: Holdsworth, R.E., Strachan, R.A., Dewey, J.F. (Eds.), Continental transpressional and transtensional tectonics. Geol. Soc. London, Spec. Publ. 135, pp. 15–33.

Fossen, H., Tikoff, B., Teyssier, C., 1994. Strain modeling of transpressional and transtensional deformation. Nor. Geol. Tidsskr. 74, 134–145.

Fossen, H., Teyssier, C., Whitney, D.L., 2013. Transtensional folding. J. Struct. Geol. 56, 89–102.

Franke, W., 1999. Tectonic and plate tectonic units at the north Gondwana margin: evidence from the central European Variscides. Abh. geol. Bundesanst. 54, 7–13.

Franke, W., 2006. The Variscan orogen in Central Europe: construction and collapse, in: Gee, D.G., Stephenson, R.A (Eds.), European lithosphere dynamics. Geol. Soc. London, Mem., pp. 333–343.

Fusán, O., Kodym, O., Matějka, A., Urbánek, L., 1967. Geological map of Czechoslovakia 1:500,000. Central Geological Survey, Prague.

Garcia, S., Angelier, J., Bergerat, F., Homberg, C., 2002. Tectonic analysis of an oceanic transform fault zone based on fault-slip data and earthquake focal mechanisms: the Húsavík–Flatey Fault zone, Iceland. Tectonophysics 344, 157–174.

Gudmundsson, A., 2011. Deflection of dykes into sills at discontinuities and magma chamber formation. Tectonophysics 500, 50–64.

Hargraves, R.B., Johnson, D., Chan, C.Y., 1991. Distribution anisotropy: the cause of AMS in igneous rocks. Geophys. Res. Lett 18, 2193–2196.

Hajná, J., Žák, J., Kachlík, V., Chadima, M., 2012. Deciphering the Variscan tectonothermal overprint and deformation partitioning in the Cadomian basement of the Teplá–Barrandian unit, Bohemian Massif. Int. J. Earth Sci. 101, 1855–1873.

Henry, B., 1997. The magnetic zone axis: a new element of magnetic fabric for the interpretation of the magnetic lineation. Tectonophysics 271, 325–331.

Hirth, G., Tullis, J., 1992. Dislocation creep regimes in quartz aggregates. J. Struct. Geol. 14, 145–158.

Hollister, L.S., Andronicos, C.L., 2006. Formation of new continental crust in Western British Columbia during transpression and transtension. Earth Planet. Sci. Lett. 249, 29–38.

Holub, F.V., Cocherie, A., Rossi, P., 1997a. Radiometric dating of granitic rocks from the Central Bohemian Plutonic Complex (Czech Republic): constraints on the chronology of thermal and tectonic events along the Moldanubian–Barrandian boundary. Compt. Rend. Acad. Sci. Ser. IIA Earth Planet. Sci. 325, 19–26.

Holub, F.V., Machart, J., Manová, M., 1997b. The Central Bohemian Plutonic Complex: geology, chemical composition and genetic interpretation. J. Geol. Sci., Econ. Geol. 31, 27–50.

Hou, Z., Tian, S., Yuan, Z., Xie, Y., Yin, S., Yi, L., Fei, H., Yang, Z., 2006. The Himalayan collision zone carbonatites in western Sichuan, SW China: petrogenesis, mantle source and tectonic implication. Earth Planet. Sci. Lett. 244, 234–250.

Hrouda, F., 1982. Magnetic anisotropy of rocks and its application in geology and geophysics. Geophys. Surv. 5, 37–82.

Hutton, D.H.W., 1992. Granite sheeted complexes: evidence for the dyking ascent mechanism. Trans. R. Soc. Edin. Earth Sci. 83, 377–382.

Ingram, G., Hutton, D., 1994. The Great Tonalite Sill: emplacement into a contractional shear zone and implications for Late Cretaceous to early Eocene tectonics in southeastern Alaska and British Columbia. Geol. Soc. Am. Bull. 106, 715–728.

Janoušek, V., Gerdes, A., 2003. Timing the magmatic activity within the Central Bohemian Pluton, Czech Republic: conventional U–Pb ages for the Sázava and Tábor intrusions and their geotectonic significance. J. Czech Geol. Soc. 48, 70–71.

Janoušek, V., Holub, F.V., 2007. The causal link between HP–HT metamorphism and ultrapotassic magmatism in collisional orogens: case study from the Moldanubian Zone of the Bohemian Massif. Proc. Geol. Assoc. 118, 75–86.

Janoušek, V., Rogers, G., Bowes, D.R., 1995. Sr–Nd isotopic constraints on the petrogenesis of the Central Bohemian Pluton, Czech Republic. Geol. Rundsch. 84, 520–534.

Janoušek, V., Bowes, D.R., Rogers, G., Farrow, C.M., Jelínek, E., 2000. Modelling diverse processes in the petrogenesis of a composite batholith: the Central Bohemian Pluton, Central European Hercynides. J. Petrol. 41, 511–543.

Janoušek, V., Wiegand, B.A., Žák, J., 2010. Dating the onset of Variscan crustal exhumation in the core of the Bohemian Massif: new U–Pb single zircon ages from the high-K calc-alkaline granodiorites of the Blatná suite, Central Bohemian Plutonic Complex. J. Geol. Soc. London 167, 347–360.

Jelínek, V., 1981. Characterization of the magnetic fabric of rocks. Tectonophysics 79, T63–T67.

Jessell, M.W., 1987. Grain-boundary migration microstructures in a naturally deformed quartzite. J. Struct. Geol. 9, 1007–1014.

Jin, Z.H., Johnson, S.E., 2008. Magma-driven multiple dike propagation and fracture toughness of crustal rocks. J. Geophys. Res. 113, B03206, doi:10.1029/2006JB004761.

Jolivet, L., Facenna, C., Goffe, B., Burov, E., Agard, P., 2003. Subduction tectonics and exhumation of high-pressure metamorphic rocks in the Mediterranean orogens. Am. J. Sci. 303, 353–349.

John, B.E., Foster, D.A., Murphy, J.M., Cheadle, M.J., Baines, A.G., Fanning, C.M., Copeland, P., 2004. Determining the cooling history of in situ lower oceanic crust – Atlantis Bank, SW Indian Ridge. Earth Planet. Sci. Lett. 222, 145–160.

Kashintsev, G.L., Shreider, A.A., Maksimochkin, V.I., Bulychev, A.A., Gilod, D.A., 2008. Transtension and alkaline magmatism of the Romanche Fracture Zone. Geotectonics 42, 318–323.

Kavanagh, J.L., Menand, T., Sparks, R.S.J., 2006. An experimental investigation of sill formation and propagation in layered elastic media. Earth Planet. Sci. Lett. 245, 799–813.

Kidane, T., Otofuji, Y.I., Komatsu, Y., Shibasaki, H., Rowland, J., 2009. Paleomagnetism of the Fentale magmatic segment, main Ethiopian Rift: new evidence for counterclockwise block rotation linked to transtensional deformation. Phys. Earth Planet. Inter. 176, 109–123.

Kirsch, M., Keppie, J.D., Murphy, J.B., Lee, J.K.W., 2012. Arc plutonism in a transtensional regime: the late Palaeozoic Totoltepec pluton, Acatlán Complex, southern Mexico. Int. Geol. Rev. 55, 263–286.

Klepeis, K.A., Crawford, M.L., 1999. High-temperature arc-parallel normal faulting and transtension at the roots of an obliquely convergent orogen. Geology 27, 7–10.

Klomínský, J., 1963. Geology of the Čistá massif. J. Geol. Sci. Geol. 3, 7–27.

Klomínský, J., 1965. The Štěnovice granodiorite massif. J. Geol. Sci. Geol. 8, 75–98.

Knipe, R.J., Law, R.D., 1987. The influence of crystallographic orientation and grain boundary migration on microstructural and textural evolution in an S–C mylonite. Tectonophysics 135, 155–169.

Kodym, O., 1996. Geological map of the Czech Republic 1:200,000, sheet Tábor. Czech Geological Survey, Prague.

Kopecký, L., Chlupáčová, M., Klomínský, J., Sokol, A., 1997. The Čistá–Jesenice pluton in western Bohemia: geochemistry, geology and ore potential. J. Geol. Sci. Econ. Geol. Mineral. 31, 97–127.

Košler, J., 1993. Age and geochemistry of the Staré Sedlo and Mirotice complexes, Bohemian Massif, Czech Republic. PhD Thesis, University of Glasgow.

Košler, J., Farrow, C.M., 1994. Mid-late Devonian arc-type magmatism in the Bohemian massif: Sr and Nd isotope and trace element evidence from the Staré Sedlo and Mirotice gneiss complexes, Czech Republic. J. Czech Geol. Soc. 39, 56–58.

Košler, J., Aftalion, M., Bowes, D.R., 1993. Mid-late Devonian plutonic activity in the Bohemian Massif: U–Pb zircon isotopic evidence from the Staré Sedlo and Mirotice gneiss complexes, Czech Republic. Neues Jahrb. Mineral. Monatsh. 9, 417–431.

Košler, J., Rogers, G., Roddick, J.C., Bowes, D.R., 1995. Temporal association of ductile deformation and granitic plutonism: Rb–Sr and 40Ar–39Ar evidence from roof pendants above the Central Bohemian Pluton, Czech Republic. J. Geol. 103, 711–717.

Kratinová, Z., Schulmann, K., Edel, J.B., Ježek, J., Schaltegger, U., 2007. Model of successive granite sheet emplacement in transtensional setting: integrated microstructural and anisotropy of magnetic susceptibility study. Tectonics 26, TC6003, doi:10.1029/2006TC002035.

Kratinová, Z., Machek, M., Kusbach, V., 2010. Fabric transpositions in granite plutons – an insight from non-scaled analogue modelling. J. Geol. Soc India 75, 267–277.

Krohe, A., 1991. Emplacement of synkinematic plutons in the Variscan Odenwald (Germany) controlled by transtensional tectonics. Geol. Rundsch. 80, 391–409.

Kroner, U., Romer, R.L., 2013. Two plates – many subduction zones: the Variscan orogeny reconsidered. Gondwana Res. 24, 298–329.

Kruhl, J.H., 1996. Prism-and basal-plane parallel subgrain boundaries in quartz: a microstructural geothermobarometer. J. Metam. Geol. 16, 581–589.

Mamtani, M.A., Piazolo, S., Greiling, R.O., Kontny, A., Hrouda, F., 2011. Process of magnetite fabric development during granite deformation. Earth Planet. Sci. Lett. 308, 77–89.

Martínez Catalán, J.R., 2011. Are the oroclines of the Variscan belt related to late Variscan strike-slip tectonics? Terra Nova 23, 241–247.

Martínez Catalán, J.R., 2012. The Central Iberian arc, an orocline centered in the Iberian Massif and some implications for the Variscan belt. Int. J. Earth Sci. 101, 1299–1314.

Martín-Hernández, F., Hirt, A.M., 2003. The anisotropy of magnetic susceptibility in biotite, muscovite and chlorite single crystals. Tectonophysics 367, 13–28.

Matte, P., Maluski, H., Rajlich, P., Franke, W., 1990. Terrane boundaries in the Bohemian Massif: result of large-scale Variscan shearing. Tectonophysics 177, 151–170.

McCaffrey, R., 1992. Oblique plate convergence, slip vectors, and forearc deformation. J. Geophys. Res. 97, 8905–8915.

McCoss, A.M., 1986. Simple constructions for deformation in transpression/transtension zones. J. Struct. Geol. 8, 715–718.

Menand, T., 2008. The mechanics and dynamics of sills in layered elastic rocks and their implications for the growth of laccoliths and other igneous complexes. Earth Planet. Sci. Lett. 267, 93–99.

Miller, R.B., Paterson, S.R., 2001. Construction of mid-crustal sheeted plutons: examples from the North Cascades, Washington. Geol. Soc. Am. Bull. 113, 1423–1442.

Murphy, M.A., Copeland, P., 2005. Transtensional deformation in the central Himalaya and its role in accommodating growth of the Himalayan orogen. Tectonics 24, TC4012, doi:10.1029/2004TC001659.

Murphy, M.A., Burgess, W.P., 2006. Geometry, kinematics, and landscape characteristics of an active transtension zone, Karakoram fault system, Southwest Tibet. J. Struct. Geol. 28, 268–283.

Nagata, T., 1962. Rock magnetism. Maruzen, Tokyo.

Nance, R.D., Gutierréz-Alonso, G., Keppie, J.D., Linnemann, U., Murphy, J.B., Quesada, C., Strachan, R.A., Woodcock, N.H., 2010. Evolution of the Rheic Ocean. Gondwana Res. 17, 194–222.

Passchier, C.W., Trouw, R.A.J., 2005. Microtectonics. Springer, Berlin, Heidelberg, New York.

Paterson, S.R., Vernon, R.H., Tobisch, O.T., 1989. A review of criteria for identification of magmatic and tectonic foliations in granitoids. J. Struct. Geol. 11, 349–363.

Paterson, S.R., Fowler, T.K., Schmidt, K.L., Yoshinobu, A.S., Yuan, E.S., Miller, R.B., 1998. Interpreting magmatic fabric patterns in plutons. Lithos 44, 53–82.

Pavlis, T.L., 1996. Fabric development in syn-tectonic intrusive sheets as a consequence of melt-dominated flow and thermal softening of the crust. Tectonophysics 253, 1–31.

Pereira, M.F., Chichorro, M., Fernández, C., Silva, J.B., Matias, F.V, 2013. The role of strain localization in magma injection into a transtensional shear zone (Variscan belt, SW Iberia). J. Geol. Soc. London 170, 93–105.

Platt, J.P., 1993. Exhumation of high-pressure rocks: a review of concepts and processes. Terra Nova 5, 119–133.

Price, N.J., Cosgrove, J.W., 1990. Analysis of geological structures. Cambridge University Press, Cambridge.

Rajlich, P., 1987. Variscan ductile tectonics in the Bohemian Massif. Geol. Rundsch. 76, 755–786.

Ring, U., Glodny, J., 2010. No need for lithospheric extension for exhuming (U)HP rocks by normal faulting. J. Geol. Soc. London 167, 225–228.

Ring, U., Will, T., Glodny, J., Kumerics, C., Gessner, K., Thomson, S., Güngör, T., Monié, P., Okrusch, M., Drüppel, K., 2007. Early exhumation of high-pressure rocks in extrusion wedges: Cycladic blueschist unit in the eastern Aegean, Greece, and Turkey. Tectonics 26, TC2001.

Rossetti, F., Storti, F., Salvini, F., 2000. Cenozoic noncoaxial transtension along the western shoulder of the Ross Sea, Antarctica, and the emplacement of McMurdo dyke arrays. Terra Nova 12, 60–66.

Rotstein, Y., Schaming, M., 2011. The Upper Rhine Graben (URG) revisited: Miocene transtension and transpression account for the observed first-order structures. Tectonics 30, TC3007, doi:10.1029/2010TC002767.

Rubin, A.M., 1995. Propagation of magma-filled cracks. Annu. Rev. Earth Planet. Sci. 23, 287–336.

Sadeghian, M., Bouchez, J.L., Nédélec, A., Siqueira, R., Valizadeh, M.V., 2005. The granite pluton of Zahedan (SE Iran): a petrological and magnetic fabric study of a syntectonic sill emplaced in a transtensional setting. J. Asian Earth Sci. 25, 301–327.

Salazar, C.A., Archanjo, C.J., Rodrigues, S.W.D.O., Hollanda, M.H.B.M., Liu, D., 2013. Age and magnetic fabric of the Três Córregos granite batholith: evidence for Ediacaran transtension in the Ribeira Belt (SE Brazil). Int. J. Earth Sci. 102, 1563–1581.

Sanderson, D.J., Marchini, W.R.D., 1984. Transpression. J. Struct. Geol. 6, 449–458.

Scarrow, J.H., Molina, J.F., Bea, F., Montero, P., Vaughan, A.P.M., 2011. Lamprophyre dikes as tectonic markers of late orogenic transtension timing and kinematics: a case study from the Central Iberian Zone. Tectonics 30, TC4007, doi:10.1029/2010TC002755.

Schäfer, J., Neuroth, H., Ahrendt, H., Dörr, W., Franke, W., 1997. Accretion and exhumation at a Variscan active margin, recorded in the Saxothuringian flysch. Geol. Rundsch. 86, 599–611.

Schulmann, K., Ježek, J., 2011. Some remarks on fabric overprints and constrictional AMS fabrics in igneous rocks. Int. J. Earth Sci. 101, 705–714.

Schulmann, K., Konopásek, J., Janoušek, V., Lexa, O., Lardeaux, J.M., Edel, J.B., Štípská, P., Ulrich, S., 2009. An Andean type Palaeozoic convergence in the Bohemian Massif. Compt. Rend. Geosci. 341, 266–286.

Seyferth, M., Henk, A., 2004. Syn-convergent exhumation and lateral extrusion in continental collision zones–insights from three-dimensional numerical models. Tectonophysics 382, 1–29.

Shore, M., Fowler, A.D., 1996. Oscillatory zoning in minerals: a common phenomenon. Can. Mineral. 34, 1111–1126.

Soper, N.J., Woodcock, N.H., 2003. The lost Lower Old Red Sandstone of England and Wales: a record of post-Iapetan flexure or Early Devonian transtension? Geol. Mag. 140, 627–647.

Strnad, L., Mihaljevič, M., 2005. Sedimentary provenance of Mid-Devonian clastic sediments in the Teplá–Barrandian Unit (Bohemian Massif): U–Pb and Pb–Pb geochronology of detrital zircons by laser ablation ICP-MS. Mineral. Petrol. 84, 47–68.

Sullivan, W.A., 2013. L tectonites. J. Struct. Geol. 50, 161–175.

Takada, A., 1989. Magma transport and reservoir formation by a system of propagating cracks. Bull. Volcanol. 52, 118–126.

Tarling, D., Hrouda, F., 1993. Magnetic anisotropy of rocks. Chapman and Hall, London.

Teyssier, C., Tikoff, B., 1998. Strike-slip partitioned transpression of the San Andreas fault system: a lithospheric-scale approach, in: Holdsworth, R.E., Strachan, R.A., Dewey, J.F. (Eds.), Continental transpressional and transtensional tectonics. Geol. Soc. London, Spec. Publ. 135, pp. 143–158.

Teyssier, C., Tikoff, B., 1999. Fabric stability in oblique convergence and divergence. J. Struct. Geol. 21, 969–974.

Teyssier, C., Tikoff, B., Markley, M., 1995. Oblique plate motion and continental tectonics. Geology 23, 447–450.

Thybo, H., 1997. Geophysical characteristics of the Tornquist fan area, northwest Trans-European suture zone: indication of Late Carboniferous to Early Permian dextral transtension. Geol. Mag. 134, 597–606.

Tikoff, B., Fossen, H., 1993. Simultaneous pure and simple shear: the unifying deformation matrix. Tectonophysics 217, 267–283.

Tikoff, B., Teyssier, C., 1994. Strain modeling of displacement-field partitioning in transpressional orogens. J. Struct. Geol. 16, 1575–1588.

Tommasi, A., Vauchez, A., 2001. Continental rifting parallel to ancient collisional belts: an effect of the mechanical anisotropy of the lithospheric mantle. Earth Planet. Sci. Lett. 185, 199–210.

Urai, J.L., Means, W.D., Lister, G.S., 1986. Dynamic recrystallization of minerals, in: Hobbs, B.E., Heard, H.C. (Eds.), Mineral and rock deformation: laboratory studies. Geophysical Monograph 36, pp. 161–199

Vaughan, A.P.M., 1996. A tectonomagmatic model for the genesis and emplacement of Caledonian calc-alkaline lamprophyres. J. Geol. Soc. London 153, 613–623.

Venera, Z., Schulmann, K., Kröner, A., 2000. Intrusion within a transtensional tectonic domain: the Čistá granodiorite (Bohemian Massif) – structure and rheological modelling. J. Struct. Geol. 22, 1437–1454.

Vernon, R.H., 1983. Metamorphic processes: reactions and microstructure development. George Allen and Unwin, London, Great Britain.

Vernon, R.H., 2000. Review of microstructural evidence of magmatic and solid-state flow. El. Geosci. 5, 1–23.

Vigneresse, J.L., Tikoff, B., Améglio, L. 1999. Modification of the regional stress field by magma intrusion and formation of tabular granitic plutons. Tectonophysics 302, 203–224.

Wada, Y., 1994. On the relationship between dike width and magma viscosity. J. Geophys. Res. 99, 17743–17755.

Waldhausrová, J., 1986. Geological map of Czechoslovakia 1:25,000, sheet 22-232 Kostelec nad Vltavou. Central Geological Survey, Prague.

Waldhausrová, J., 1987. Explanations to Geological map of Czechoslovakia 1:25,000, sheet 22-232 Kostelec nad Vltavou. Central Geological Survey, Prague.

Weinberg, R.F., 1999. Mesoscale pervasive felsic magma migration: alternatives to dyking. Lithos 46, 393–410.

Wesnousky, S.G., 2005. The San Andreas and Walker Lane fault systems, western North America: transpression, transtension, cumulative slip and the structural evolution of a major transform plate boundary. J. Struct. Geol. 27, 1505–1512.

White, S.H., 1976. The role of dislocation processes during tectonic deformation with special reference to quartz, in: Strens, R.J. (Ed.), The physics and chemistry of minerals and rocks. Wiley, London, pp. 75–91.

White, S., 1977. Geological significance of recovery and recrystallization processes in quartz. Tectonophysics 39, 143–170.

Whitney, D.L, Evans, B.W., 2010. Abbreviations for names of rock-forming minerals. American Mineralogist, 95, 185–187.

Wilson, R.W., McCaffrey, K.J.W., Holdsworth, R.E., Imber, J., Jones, R.R., Welbon, A.I.F., Roberts, D., 2006. Complex fault patterns, transtension and structural segmentation of the Lofoten Ridge, Norwegian margin: using digital mapping to link onshore and offshore geology. Tectonics 25, TC4018, doi: 10.1029/2005TC001895.

Winchester, J.A. 2002. Palaeozoic amalgamation of Central Europe: new results from recent geological and geophysical investigations. Tectonophysics 360, 5–21.

Žák, J., Holub, F.V., Verner, K., 2005a. Tectonic evolution of a continental magmatic arc from transpression in the upper crust to exhumation of mid-crustal orogenic root recorded by episodically emplaced plutons: the Central Bohemian Plutonic Complex (Bohemian Massif). Int. J. Earth Sci. 94, 385–400.

Žák, J., Schulmann, K., Hrouda, F., 2005b. Multiple magmatic fabrics in the Sázava pluton (Bohemian Massif, Czech Republic): a result of superposition of wrench-dominated regional transpression on final emplacement. J. Struct. Geol. 27, 805–822.

Žák, J., Dragoun, F., Verner, K., Chlupáčová, M., Holub, F.V., Kachlík, V., 2009. Forearc deformation and strain partitioning during growth of a continental magmatic arc: the northwestern margin of the Central Bohemian Plutonic Complex, Bohemian Massif. Tectonophysics 469, 93–111.

Žák, J., Kratinová, Z., Trubač, J., Janoušek, V., Sláma, J., Mrlina, J., 2011. Structure, emplacement, and tectonic setting of Late Devonian granitoid plutons in the Teplá–Barrandian unit, Bohemian Massif. Int. J. Earth Sci. 100, 1477–1495.

Žák, J., Verner, K., Holub, F. V., Kabele, P., Chlupáčová, M., Halodová, P. 2012. Magmatic to solid state fabrics in syntectonic granitoids recording early Carboniferous orogenic collapse in the Bohemian Massif. J. Struct. Geol. 36, 27–42.

Žák, J., Verner, K., Janoušek, V., Holub, F.V., Kachlík, V., Finger, F., Hajná, J., Tomek, F., Vondrovic, L., Trubač, J., Kachlík, V., Hajná, J., Trubač, J., 2014. A plate-kinematic model for the assembly of the Bohemian Massif constrained by structural relationships around granitoid plutons, in: Schulmann, K., Oggiano, G., Lardeaux, J.M., Janoušek, V., Martínez Catalán, J.R. (Eds.), The Variscan orogeny: extent, timescale and the formation of the European crust. Geol. Soc. London, Spec. Publ. 405, pp. 169–196.

Zapletal, K., 1990. Low-field susceptibility anisotropy of some biotite crystals. Phys. Earth Planet. Inter. 63, 85–97.

Zulauf, G., 1997. From very low-grade to eclogite-facies metamorphism: tilted crustal sections as a consequence of Cadomian and Variscan orogeny in the Teplá–Barrandian unit (Bohemian Massif). Geotekt. Forsch. 89, 1–302.

Zulauf, G., 2001. Structural style, deformational mechanisms and paleodifferential stress along an exposed crustal section: constraints on the rheology of quartzofeldspathic rocks at supra- and infrastructural levels (Bohemian Massif). Tectonophysics 332, 211–237.

Zulauf, G., Helferich, S., 1997. Strain and strain rate in a synkinematic trondhjemitic dike: evidence for melt-induced strain softening during shearing (Bohemian Massif, Czech Republic). J. Struct. Geol. 19, 639–652.

Zulauf, G., Dörr, W., Fiala, J., Vejnar, Z., 1997. Late Cadomian crustal tilting and Cambrian transtension in the Teplá–Barrandian unit (Bohemian Massif, Central European Variscides). Geol. Rundsch. 86, 571–584.

EXECUTIVE SUMMARY

Specific studies: magma emplacement dynamics in shallow volcano–plutonic systems

In the Miocene Štiavnica volcano–plutonic complex, complex fabric patterns of three lava domes (Domes 1–3) and shallow plutons were interpreted as recording magma flow paths and strain patterns during lava dome growth and magma chamber construction.

(1) Spatial and temporal association of collapse caldera and the andesite lava domes emplaced along a ring-fault suggest that the dome growth was controlled by caldera floor subsidence. Dome 1 is characterized as a lava coulee which flowed down the hinged floor of a trap-door caldera. Dome 2 represents a single elongated, ring-fault-parallel dome with short lava outflow emplaced on a flat floor during piston collapse. Dome 3 was fed by multiple linear fissures at a high angle to the ring fault in the collapsing caldera floor and was later intruded by ring-fault-parallel dikes representing potential feeders for younger lava domes and flows. It is inferred that each dome reflects snapshots of a continuous succession of various modes of caldera collapse from piston (Dome 2) through trap-door (Dome 1) to piecemeal (Dome 1).

(2) Magnetic fabric study of two deeper, sub-volcanic diorite and granodiorite plutons revealed contrasting mechanisms of their construction. The diorite was emplaced as a steep-sided ~WNW–ESE elongated stock. The voluminous granodiorite has a 'layered' architecture and was presumably emplaced in two stages. First, an upper 'layer' was emplaced as a thin sill along a major sub-horizontal basement/cover detachment followed subsidence of the pluton floor along ~NNE–SSW to ~NE–SW faults. This process created space for a lower 'layer' causing thickening the original sill into a tabular pluton. Based on this case example, various models for magma flow and resulting fabrics during various modes of pluton floor subsidence were developed.

Specific studies: arc volcanism, plutonism, and tectonic deformation

(1) The mid-Cretaceous Minarets caldera of the Sierra Nevada magmatic arc greatly exemplifies complex interactions between volcanism, plutonism and tectonic deformation. The original volcanic edifice was built by Plinian ash-flow tuff eruptions followed by caldera collapse marked by deposition of collapse mega-breccia and post collapse ash-flow tuff. The whole sequence was then deformed along a ductile transpressive shear zone and intruded by very shallow, resurgent Shellenbarger granite pluton within the caldera interior.

Magmatic and metamorphic fabrics in the pluton and its aureole, respectively record regional dextral transpressional deformation. The same deformation has been documented in several other Late Cretaceous syntectonic plutons of the Sierra Nevada indicating two principal stretching directions: near-vertical magmatic stretching in ~102–86 Ma plutons and subhorizontal late magmatic to subsolidus stretching in ~87–86 Ma plutons. It was inferred that the rotation of the principal stretching direction at around 87–86 Ma reflects a continuous change in plate kinematics and resulting arc deformation from pure shear-dominated to wrench-dominated dextral transpression suggesting increased obliquity of converging Farallon and North American plates.

(2) In the Wallowa batholith, northeastern Oregon, host-rock structures and multiple magmatic to solid state fabrics in the Pole Bridge, Hurricane Divide, and Craig Mountain plutons record three phases of progressive regional deformation in the Wallowa terrane during Early Cretaceous times (~140–126 Ma). The fabrics indicate early ~NE–SW terrane-oblique principal shortening recording attachment of the Blue Mountains superterrane to the North American continental. This deformation switched to ~NNE–SSW shortening associated with vertical stretching related to the continued impingement of the superterrane into the North American margin at around 135–128 Ma. The northern portion of the superterrane became 'locked' and difficult to further deform. The 'lock-up' impingement of superterrane led to reorientation of the principal shortening direction to ~NNW–SSE and the still deformable southern portion of the superterrane rotated clockwise about vertical axis at around 126 Ma.

(3) In the Late Devonian Staré Sedlo complex, central Bohemian Massif, granodiorites to tonalites were emplaced as a subhorizontal sheeted sill complex into an active transtension zone. This deformation is evidenced by subhorizontal magmatic to solid state foliations and NE–SW stretching lineations associated with overall prolate shapes of fabric ellipsoid and concordant metamorphic fabrics in their host-rock. The magma/host rock system in transtension evolved from initial crack tip propagation by magma wedging and vertical expansion due to new magma additions through stable conduit flow to final vertical collapse after the magma input ceased. Finally, the sill emplacement and subsequent deformation of the granitoids were interpreted as recording syn-convergent, early orogenic sinistral transtension along the rear side of an upward and laterally extruded upper-crustal wedge as represented by the Teplá–Barrandian unit.

General implications

The thesis has documented how tectonic inheritance (faults, detachment zones) and active faulting (caldera collapse) in volcano–plutonic systems may control emplacement of volcanic and plutonic rocks as exemplified by the dynamics of growth and construction of lava domes and subvolcanic magma chambers. Furthermore, as opposed to theoretical models, it has been demonstrated that even very shallow-level small-scale intrusions are capable of recording even subtle tectonic strains still in magmatic state. Although fabrics in plutons preserve only a snapshot of the total strain, detailed analysis of syntectonic plutons with developed hypersolidus fabrics together with precise radiometric dating is a powerful tool in unraveling complex deformation histories (transpression, transtension, crustal-scale folding, and lithospheric block rotations) at regional scale over a long period of time. Finally, it has been proposed that pluton fabrics may be used to decipher kinematics of lithospheric plate convergence or divergence and changes in their past relative motions.